

Plasmons in Gold-Induced Quantum Wires

Von der Fakultät für Mathematik und Physik
der Gottfried Wilhelm Leibniz Universität Hannover

zur Erlangung des Grades
Doktor der Naturwissenschaften
Dr. rer. nat.

genehmigte Dissertation von

M. Sc. Timo Lichtenstein

2017

Referent: Prof. Dr. Herbert Pfnür *Gottfried Wilhelm Leibniz Universität Hannover*

Korreferent: Prof. Dr. Simone Sanna *Justus-Liebig-Universität Gießen*

Korreferent: Prof. Dr. Mario Rocca *Università degli Studi di Genova*

Tag der Promotion: 11. August 2017

Keywords: *collective excitations, electronic correlations, atomic wires*

Schlagworte: *kollektive Anregungen, elektronische Korrelationen, atomare Drähte*

Abstract

For future plasmonic devices, the understanding of low-dimensional collective excitations is indispensable. Nevertheless, although fundamental theories of the properties of low-dimensional plasmons exist for many years, their predictions of the behavior are still rather unsatisfactory. Several key aspects of the influences in real world systems such as, e.g., many-body effects, Coulomb screening, as well as the general impact of the surrounding structural elements are still rather unexplored. Furthermore, quasi-one-dimensional electronic systems show exceptional transport properties such as Peierls transition or Tomonaga-Luttinger liquid (TLL) behavior that may have a strong influence on the plasmonic properties.

For the investigations, the wire quality was checked with spot profile analysis in low energy electron diffraction (SPA-LEED). A combination of an electron energy loss spectrometer (EELS) and SPA-LEED providing both high energy and momentum resolution gave access to the plasmon dispersion.

As quasi-one-dimensional structures, Au-induced wires on regularly stepped Si(hhk) offer the perfect playground for systematic investigations with their varying terrace widths. Therefore, in the first part of this work, the systems were prepared to a state, where each of these terraces hosts a gold chain of either single or double atomic width. Although 1D metallicity is observed, the plasmon dispersion strongly depends on two-dimensional crossover. On the one hand, this crossover is caused by the feedback of the spacing of the wires, a so-called interwire correlation. On the other hand, the distribution of the 1D electronic band structure is both affected by the terrace width as well as by the additional structural elements. Modifications of a quasi-free electron gas plasmon model including calculated electronic band structures were able to describe the observed plasmon dispersions qualitatively. Widths of the plasmon loss peaks revealed broadening beyond merely an effect of the lifetime. Adsorption measurements with molecular oxygen and atomic hydrogen showed the possibility to change the energy of the plasmons. Though their changes were counterintuitive with an increase of the energy upon oxygen adsorption and a decrease by hydrogen, the introduced modified model can explain this behavior by changes in their band structures.

The other system in this thesis is Ge(100)-Au that became renowned in the literature due to its proposed TLL behavior. However, the atomistic structure of these wires is still controversially discussed. After the optimization of the preparation of the germanium substrate, a detailed analysis of the diffraction profiles of the gold-induced wire structure highly supports a corrugated structure comparable to the giant missing row model. Plasmon investigations only showed loss peaks of low intensity. Both a TLL and a quasi-1D plasmon model were inapplicable for the explanation of the experimental data. A qualitative description was possible after a modification of the quasi-1D approach to a high lateral overlap of the density of states with the adjacent wires. This picture highly indicates the system to be of anisotropic two-dimensional nature instead of a TLL candidate.

Zusammenfassung

Für zukünftige plasmonische Bauteile ist das Verständnis von niedrigdimensionalen kollektiven Anregungen unentbehrlich. Obwohl grundlegende Theorien der Eigenschaften von niedrigdimensionalen Plasmonen seit vielen Jahre existieren, sind ihre Vorhersagen dennoch ziemlich unbefriedigend. Mehrere Schlüsselaspekte der Einflüsse in realen Systemen, wie z.B. Vielteilcheneffekte, Coulomb-Screening oder der Einfluss der umgebenden Strukturelemente sind noch relativ unerforscht. Darüber hinaus zeigen quasi-eindimensionale elektronische Systeme außergewöhnliche Transporteigenschaften. Dazu gehören unter anderem der Peierls-Übergang oder ein Verhalten als Tomonaga-Luttinger-Flüssigkeit (TLL), die einen starken Einfluss auf die plasmonischen Eigenschaften haben können.

Die Drahtqualität wurde mit niederenergetischer Elektronenbeugung (SPA-LEED) überprüft. Eine Kombination aus einem Elektronenenergieverlust-Spektrometer (EELS) und SPA-LEED, die sowohl eine hohe Energie- als auch Impulsauflösung liefert, erlaubte die Messung von Plasmonendispersionen.

Durch ihre unterschiedlichen Terrassenbreiten bieten Au-induzierte Drähte auf regelmäßig gestuftem Si(hhk) den perfekten Spielplatz für systematische Untersuchungen in quasi-eindimensionale Strukturen. Daher wurden sie im ersten Teil so präpariert, dass jede dieser Terrassen eine Goldkette von einem oder zwei atomaren Breiten beherbergt. Trotz 1D-Metallizität hängt die Plasmonendispersion stark von einem 2D-Übersprechen ab. Dieser Dimensional Crossover wird einerseits durch die Rückkopplung der Drähte zueinander, einer sogenannten Interwire-Korrelation, verursacht. Andererseits wird die 1D-Bandstruktur sowohl von der Terrassenbreite als auch von zusätzlichen Strukturelementen beeinflusst. Modifikationen eines Plasmonenmodells für quasi-freie Elektronengase, die berechnete Bandstrukturen berücksichtigt, konnten die beobachteten Plasmonendispersionen qualitativ beschreiben. Die Plasmonenverlustspitzen zeigten eine Verbreiterung, die nicht bloß durch Lebensdauern erklärt werden konnte. Adsorptionsmessungen mit molekularem Sauerstoff und atomarem Wasserstoff zeigten die Möglichkeit, die Eigenschaften der Plasmonen zu verändern. Obwohl ihre Veränderungen mit einer Zunahme der Energie bei der Sauerstoffadsorption und einer Abnahme durch Wasserstoff kontraintuitiv waren, kann das eingeführte modifizierte Modell dieses Verhalten über ihre Bandstrukturen erklären.

Das andere System in dieser Arbeit ist Ge(100)-Au, das in der Literatur aufgrund seines vorgeschlagenen TLL-Verhaltens bekannt wurde. Allerdings wird die atomistische Struktur dieser Drähte noch kontrovers diskutiert. Nach der optimierten Präparation des Germaniumsubstrats legte eine detaillierte Analyse der Beugungsprofile der goldinduzierten Drahtstruktur eine Struktur mit tiefen Rillen nah, die dem Giant-Missing-Row-Modell ähnelt. Plasmonenuntersuchungen zeigten nur Verlustspitzen geringer Intensität. Sowohl ein TLL- als auch ein Quasi-1D-Plasmonen-Modell konnten die experimentellen Daten nicht sinnvoll erklären. Eine qualitative Beschreibung war nach einer Modifikation des Quasi-1D-Ansatzes in Form einer starken lateralen Überlappung der Zustandsdichten von benachbarten Drähten möglich. Dieses Bild weist anstelle einer TLL stark auf eine anisotrope zweidimensionale Natur hin.

Contents

I Physical Principles and Theory	19
1. Motivation and Introduction	21
1.1. Realization of Low-Dimensional Wires on Surfaces	22
1.2. Structure of This Thesis	24
2. Low Energy Electron Diffraction	27
2.1. Kinematic Approximation	28
2.2. Spot Profile Analysis	29
2.2.1. Lateral Roughness	30
2.2.2. Vertical Roughness	31
2.3. Inelastic Scattering of Electrons	32
2.3.1. Small-Angle Inelastic Scattering by Dipole Fields	33
2.3.2. Impact Scattering Regime	35
3. Plasmons in Low Dimensions	37
3.1. Theoretical Determination of Plasmons in Quasi-Free Electron Gases	38
3.2. Quasi-One-Dimensional Approach	39
3.3. Arrays of Quasi-One-Dimensional Wires	43
3.4. Plasmons in Tomonaga-Luttinger Liquids	45
4. The Vacuum Chamber Setup	49
4.1. SPA-LEED	50
4.2. EELS-LEED	52
4.3. Gold Evaporator	53
4.4. Hydrogen Source	55

II	Gold-Induced Wires on Si(hhk)	57
5.	A Golden Playground on Vicinal Silicon Surfaces	59
5.1.	The System Si(hhk)	59
5.2.	Structural Resemblances in Si(hhk)-Au	61
5.2.1.	Si(553)-Au – Double Gold Chain	62
5.2.2.	Si(775)-Au – Double Gold Chain and Adatom Chain	65
5.2.3.	Si(335)-Au – Single Gold Chain	66
5.2.4.	Si(557)-Au – Single Gold Chain and Adatom Chain	66
5.3.	Discrepancy between Photoemission Data and Electronic Band Structure Calculations	67
6.	Structural Properties of Si(hhk)-Au	69
6.1.	Sample Preparation	69
6.2.	Surface Properties Probed by Electron Diffraction	70
6.3.	Spot Profile Analysis of Si(553)-Au	74
7.	Plasmonic Excitations in Si(hhk)-Au	79
7.1.	Electron Energy Loss Spectra	79
7.2.	Two-Dimensional Crossover of One-Dimensional Electron Density	82
7.3.	Deviations from the Quasi-Free Electron Character	87
7.4.	Computation of the Electron-Hole Pair Continuum Boundary	89
7.4.1.	Si(553)-Au in High and Low Coverage Phase	90
7.4.2.	Si(775)-Au	93
7.4.3.	Si(557)-Au	95
7.4.4.	Si(335)-Au	97
7.4.5.	Conclusions from the Excitation Spectrum Calculations	98
7.5.	Further Insight – Excitation Probabilities and Lifetimes	99
7.6.	Conclusions from the Plasmon Investigations	104
8.	Chemisorption-Induced Modification of the Electronic Structure	107
8.1.	Adsorption of Molecular Oxygen	107
8.2.	Oxygen-Induced Modifications of the Electronic Band Structure	112
8.3.	Adsorption of Atomic Hydrogen on Si(553)-Au	115
8.4.	Conclusion from the Adsorption Experiments	118
III	Gold-Induced Wires on Ge(100)	121
9.	Introduction to Ge(100)-Au	123
9.1.	The Pristine Ge(100) Surface	123

9.2. Structure upon Adsorption of Au	125
9.3. Electronic Properties of Ge(100)-Au	129
10. Structural Investigation of Ge(100)-Au	131
10.1. Pristine Ge(100)	131
10.1.1. LEED of the Bare Surface	132
10.1.2. Quantitative Spot Profile Analysis	134
10.2. Au-Induced Wires on Ge(100)	138
10.2.1. LEED of the Au-Covered Surface	138
10.2.2. Extension of the Spot Profile Analysis to the Gold-Covered Surface	141
10.3. Conclusion of the Structural Analysis	145
11. Plasmonic Excitations in Ge(100)-Au	147
11.1. Electron Energy Loss Spectra	147
11.2. Dispersion of the Plasmonic Excitation	148
11.2.1. Description as Tomonaga-Luttinger Liquid Plasmon	149
11.2.2. Quasi-Free Electron Gas Description	151
11.3. Conclusion of the Plasmon Investigations	152
IV Conclusions	155
12. Summary of the Findings	157
12.1. Si(hhk)-Au	157
12.2. Ge(100)-Au	160
12.3. Conclusions Regarding Atomic Wires on Surfaces	160
12.4. Outlook	162
Appendix	165
Source Code of the Plasmon Calculations	167
Bibliography	173
Curriculum Vitae	191
List of Publications	193

List of Figures

1.1.	Examples for the realization of low-dimensional wire structures	23
2.1.	Simplified surface for electron diffraction and corresponding surface rods	29
2.2.	The two most dominant inelastic scattering processes in the dipole approximation . .	34
3.1.	Comparison of the plasmon dispersion relations in 1D, 2D, and 3D	38
3.2.	Parameter influences to the plasmon dispersion	41
3.3.	Calculated plasmon dispersion relations with corresponding wave functions	44
3.4.	Assumptions of the Tomonaga-Luttinger liquid model	46
4.1.	Sketch of vacuum chamber and sample handler	50
4.2.	Sketch of the SPA-LEED and the given scattering condition	51
4.3.	Sketch of the EELS-LEED	52
4.4.	Sketch of the Au evaporator used in this thesis	54
4.5.	Sketch of the hydrogen cracker	54
5.1.	Unreconstructed Si(111) surface	60
5.2.	Side view illustration of Si(hhk)	61
5.3.	Side views of structural models	62
5.4.	ARPES data for the four Si(hhk)-Au systems	63
5.5.	Brillouin zone and reduced $\times 2$ Brillouin zone for Si(hhk)-Au with denoted symmetry points.	64
5.6.	Simplified stick and ball models of Si(553)-Au HCW and Si(553)-Au LCW	65
5.7.	Sketch of the hybridization of the gold chain-induced electronic bands with the polarized step edge state of the honeycomb chain	68
6.1.	LEED patterns of the Au-adsorbed Si(553) and Si(775) surfaces	71

6.2.	LEED pattern of the low coverage phase of Si(553)-Au	72
6.3.	LEED patterns of Si(335)-Au and Si(557)-Au	73
6.4.	Energy dependent SPA-LEED scans for Si(553)-Au	75
6.5.	Variation of the Lorentzian background in direction perpendicular to the wires	76
6.6.	Line scans across the central spot in the direction parallel to the wires	77
7.1.	Electron energy loss spectra for Si(553)-Au and Si(775)-Au	80
7.2.	Electron energy loss spectra for Si(335)-Au and Si(557)-Au	81
7.3.	Dispersion relations of Si(553)-Au and Si(775)-Au	83
7.4.	Combined image of STM and STS on Si(553)-Au around E_F	85
7.5.	Dispersion relations of Si(335)-Au and Si(557)-Au	86
7.6.	Computation of the plasmon dispersion as taken from the numerically derived electronic band structure for Si(553)-Au	88
7.7.	Calculated upper boundary of the excitation spectrum for Si(553)-Au	91
7.8.	Calculated upper boundary ω_+ for Si(553)-Au in the low coverage phase	92
7.9.	Calculated ω_+ for Si(775)-Au for electron-like and hole-like behavior	94
7.10.	Calculated ω_+ for Si(557)-Au	96
7.11.	Calculated ω_+ for Si(335)-Au	98
7.12.	Peak intensities of the Gaussian fits for Si(553)-Au in HCW and LCW phase as extracted from the spectra	101
7.13.	Plasmon peak widths and corresponding lifetimes for Si(553)-Au in HCW and LCW phase as well as Si(335)-Au	102
7.14.	Plasmon peak widths and corresponding lifetimes for Si(775)-Au and Si(557)-Au	103
8.1.	Electron energy loss spectra before and after oxygen adsorption for Si(553)-Au, Si(775)-Au, and Si(557)-Au	108
8.2.	Shift of the plasmon energy as a function of the oxygen dose for the Si(775)-Au and Si(557)-Au surface	109
8.3.	LEED patterns of Si(553)-Au before and after adsorption of oxygen	110
8.4.	LEED patterns of Si(775)-Au before and after adsorption of oxygen	110
8.5.	LEED patterns of Si(557)-Au before and after adsorption of oxygen	111
8.6.	Electronic band structures after oxidation of various sites on the Si(557)-Au surface	113
8.7.	Dispersions and relative energy changes of the calculated plasmons after oxygen adsorption	114
8.8.	Electron energy loss spectrum before and after adsorption of atomic deuterium and relative change of the plasmon peak after hydrogen/deuterium treatment	116
8.9.	LEED patterns of Si(553)-Au before and after adsorption of deuterium	117

8.10.	Theoretical prediction of the changes in the electronic band structure after hydrogenation of a Si(553)-Au surface	117
9.1.	Surface reconstructions of the bare Ge(100) surface	124
9.2.	Side view of a buckled dimer	125
9.3.	Overview STM image of the Ge(100)-Au surface	126
9.4.	Internal structure of the induced wires	127
9.5.	Selection of proposed structural models	128
9.6.	Electronic band structure of Ge(100)-Au	129
10.1.	LEED patterns of Ge(100) before and after sputtering/annealing treatment	133
10.2.	False color energy dependent scan across the (00) spot in $[01\bar{1}]$ direction of a pure Ge(100) sample after one sputtering/annealing cycle	134
10.3.	In-phase and out-of-phase Voigt fits after 2 and 8 sputtering/annealing cycles	135
10.4.	$H(S)$ curves of pristine Ge(100)	136
10.5.	$G(S)$ curves of pristine Ge(100)	136
10.6.	Influence of sputtering/annealing to the terrace width and RMS roughness	137
10.7.	LEED pattern of Au reconstructed Ge(100) surface and the evolution of the Au induced reconstruction as a function of Au coverage	139
10.8.	False color SEM image of the cluster formation due to excess Au on a sample with a coverage of 2 ML	140
10.9.	$H(S)$ (a) and $G(S)$ (b) curves of a Ge(100) after various adsorptions of Au	141
10.10.	Terrace width and roughness development after the adsorption of Au on Ge(100)	142
10.11.	Roughness properties of the Au covered surface	143
10.12.	Simplified GMR model for a qualitative $G(S)$ analysis	144
11.1.	Electron energy loss spectra of Ge(100)-Au for increasing momentum with used fitting routine	148
11.2.	Data extracted from loss measurements with possible descriptive models for the plasmon dispersion relation	150
11.3.	Wave functions of varying widths for the description of the Ge(100)-Au plasmon	151
12.1.	Relation between electronic band structure and electron-hole excitation spectrum	158

Abbreviations, variables, and constants

Abbreviations

1D	One-dimensional
2D	Two-dimensional
2DEG	Two-dimensional electron gas
2PPE	Two-photon photoelectron spectroscopy
3D	Three-dimensional
ARPES	Angle-resolved photoemission spectroscopy
ATSGR	Au-trimer stabilized Germanium ridge (structural model for Ge(100)-Au)
DC	Direct current
DFT	Density functional theory
DOS	Density of states
EDC	Energy distribution curve
EELS	Electron energy loss spectroscopy
FWHM	Full width at half maximum
GMR	Giant missing row (structural model for Ge(100)-Au)
HCW	High coverage wires on Si(553)-Au
HD/AD	Heterodimer/Au-Homodimer (structural model for Ge(100)-Au)
HSE	Heyd-Scuseria-Ernzerhof hybrid functionals for DFT
HWHM	Half width at half maximum
IV-LEED	Intensity and Voltage dependent LEED measurements
L	Langmuir (unit) = 1.33×10^{-6} mbar s ⁻¹
LCW	Low coverage wires on Si(553)-Au
LEED	Low energy electron diffraction
LT	Low temperature (< 120 K if not defined otherwise)

RMS	Root mean square
PBE	Perdew-Burke-Ernzerhof approximation in DFT
RPA	Random phase approximation
RT	Room temperature ($\approx 20^\circ\text{C}$)
SPE	Electron-hole single particle excitation spectrum
STLS	Mean-field approximation by Singwi, Tosi, Land, and Sjölander
STM	Scanning tunneling microscopy
STS	Scanning tunneling spectroscopy
SXRD	Surface X-ray diffraction
UHV	Ultra-high vacuum (pressure $< 1 \times 10^{-9}$ mbar)

Used variables

a	Width of square-well potential
b	Ground state width of harmonic potential
a_0^*	Effective bohr radius
a_0	Surface lattice constant
a_c	Low- k plasmon normalization constant
a_x, a_y	Surface lattice vectors
C_n	Height correlation
χ_0	Electron gas polarizability
d_z	Step height of surface
E	Energy
E_F	Fermi energy
ϵ	Relative permittivity of the surrounding medium, to be multiplied with ϵ_0
f_n	Structure factor of atom f
\vec{G}_{\parallel}	Reciprocal surface lattice vector
$G_{\text{corr}}(k)$	Local field correction factor
g_s	Spin degeneracy factor
h_n, h	Height factor (multiplies with d_z)
I	Intensity
\Im	Imaginary part
k	Wave vector
$\vec{K}, \vec{K}_{\parallel}$	Scattering vector, its part parallel to the surface
$\vec{k}_f, \vec{k}_{\parallel,f}$	Final wave vector, its part parallel to the surface

k_F	Fermi wave vector
$\vec{k}_i, \vec{k}_{\parallel,i}$	Incoming wave vector, its part parallel to the surface
K_ρ	Luttinger electron interaction parameter
λ	Wavelength
m^*	Effective mass of electrons in a Fermi-fluid given in multiples of m_e
n	Electron density (if not index)
ω	Angular frequency ($= E/\hbar$)
ω_\pm	Upper and lower boundary of the electron-hole excitation continuum
Φ, Ψ	Electron wave functions
\vec{r}_n	Position of atom n in lattice
r_s^*	Dimensionless electron density parameter
\Re	Real part of an imaginary number
ρ	Charge density distribution
S	Scattering phase
v_c	Coulomb interaction matrix element
v_F	Fermi velocity

Constants¹

c	Speed of light	$= 299\,792\,458\text{ m s}^{-1}$
e	Elementary charge	$= 1.602\,176\,620\,8(98) \times 10^{-19}\text{ C}$
ϵ_0	Electric constant	$= 8.854\,187\,817 \times 10^{-12}\text{ F/m} = 1/(\mu_0 c^2)$
h	Planck constant	$= 6.626\,070\,040(81) \times 10^{-34}\text{ Js}$ $= 4.135\,667\,662(25) \times 10^{-15}\text{ eVs}$
\hbar	Reduced Planck constant	$= h/2\pi$
m_e	Electron mass	$= 9.109\,383\,56(11) \times 10^{-31}\text{ kg}$
μ_0	Magnetic constant	$= 4\pi \times 10^{-7}\text{ NA}^{-2}$
u	Atomic mass constant	$= 1.660\,539\,040(20) \times 10^{-27}\text{ kg}$

¹All data have been taken from the NIST Physical Reference Data available at <http://physics.nist.gov/cuu>

Part I:

Physical Principles and Theory

1

Motivation and Introduction

In the most recent past, low-dimensional systems have attracted an increasing amount of attention. On the one hand, the ongoing miniaturization of semiconductor electronics led to the limits of classical physics. Nowadays, modern electronics must at least consider quantum size effects for their description. On the other hand, one-dimensional systems are particularly interesting because of their strong electronic correlations [1]. This character leads to new physical phenomena such as charge or spin density waves [2, 3, 4] that may result in a Peierls-instability [5, 6, 7]. This effect drives the system from a metallic to an insulating state upon cooling and results in the competing energy reductions of the lattice versus the electronic states. Another effect is the so-called Tomonaga-Luttinger liquid behavior that leads to a separation of spins and charges [8, 9, 10] within a bosonic reformulation of the single-particle spectrum.

Whether or not some of these characteristics are beneficial for future incorporation into more and more miniaturized electronics, the fundamental grasp of such phenomena must show. However, first realizations of real 1D systems started in the 1970's with polymers and organic compounds [1]. As atomic metal chains are the smallest possible conductors, they can be suitable for the implementation into electronic circuits.

Apart from such fundamental characteristics, collective excitations of electrons called plasmons are of particular interest. Surface plasmon resonances of metallic nanoparticles have already been used by the ancient Romans for colorful cups [11] or in stained-glass windows of medieval churches [12] as they allow to very selectively sieve wavelengths out of the incident light. Of course, these people were not aware of any quantum effects when they mixed in gold to their molten glasses. It was not until

the beginning of the 20th century that Robert W. Williams indirectly observed a surface plasmon [13]. Nowadays, plasmons play a significant role in, e.g., sensor technology by a change of resonance after chemical adsorption [14], improvement of quantum efficiency in photovoltaic devices [15], and even in medicine as a sensor for molecular conformation [16] or cancer research as photothermal transducers [17].

Plasmons in low-dimensional systems, called sheet plasmons [18, 19, 20], came into focus because of their wavelengths that are typically two orders of magnitude shorter than those of photons at the same energy. Thus, THz plasmonics and waveguiding on the scale of a few nanometers becomes feasible. Moreover, theory predicts quasi-one-dimensional metallic channels to feature a plasmonic dispersion relation that is almost linear, see also Chapter 3. This property makes them perfectly suitable for the transport of information since their wave-packets do not delocalize over distance.

However, truly one-dimensional systems exhibit an inherent instability. To this date, the experimental realization of free-standing chains is only possible up to several atoms in length [21, 22]. Therefore, such structures must be modified by some stabilizing surrounding. One possibility is the construction on a crystal surface. As this approach is only possible due to the coupling of the wire to the substrate, the understanding of the crosstalk is of particular importance. Additionally, in arrays of wires, the interwire coupling has a significant impact on the plasmon properties. Although fundamental theories were taking into account these effects for many years [23, 24, 25], their predictions are still rather unsatisfactory. It is one aim of this work to shed some light into the discrepancies between the observed experimental data and the underlying theory.

1.1 Realization of Low-Dimensional Wires on Surfaces

Within the approach of constraining the wires on a surface, there are several possibilities to obtain quasi-one-dimensional structures, see also Fig. 1.1 for a sketch of typical examples.

One of these is to start with a two-dimensional system and then restrain it in one of its directions. Such a two-dimensional system is the Si(111)-($\sqrt{3} \times \sqrt{3}$)Ag surface [26]. Its metallicity can be tuned by excess Ag. However, when growing the same system on a Si(557) wafer, i.e. a Si(111) surface with an intentional miscut of 9.2°, Ag-covered (111) terraces of the $\sqrt{3}$ -reconstruction will form. Those terraces are separated by steps of (112) orientation leading to a structure with an expansion in only one dimension. The resulting metallic Ag stripes have a width of 3.6 nm [27, 28]. In this way, a two-dimensional system was confined to a strongly anisotropic behavior. Investigations of collective excitations showed a dispersing plasmon along these stripes and standing waves in the perpendicular direction. Therefore, the transport of information in the form of energy is only possible in one direction, and one may say the system behaves in a quasi-one-dimensional manner. Still, a tuning of the metallicity is possible for this system of reduced dimensionality [29, 30]. A similar mechanism also governs the growth of dysprosium wires on the same Si(557) surface [31]. These examples show the capability to transform 2D

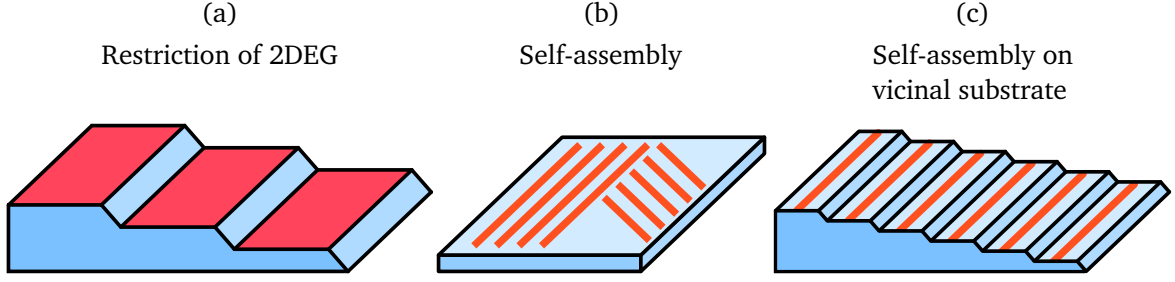


Figure 1.1: Examples for the realization of low-dimensional wire structures: (a) Lateral restriction of a two-dimensional electron gas (red) by a vicinal surface like for Si(557)-Ag. (b) Growth of wire structures (orange) by self-assembly like for Ge(100)-Au. This mode will typically result in multiple domains with different wire directions. (c) Wire growth (orange) by self-assembly on the terraces of a vicinal surface like for Si(hhk)-Au.

into confined 2D with 1D properties by the adequate preparation of the substrate.

Another 2D system is graphene [32]. It has the advantage of being a completely decoupled two-dimensional system of carbon atoms in a honeycomb lattice. It hosts a relativistic electron gas with high carrier mobilities [33] also leading to long-living plasmons [34]. By growing the system on a SiC mesa structure, quasi-one-dimensional sidewall nanoribbons can be produced that feature ballistic transport on length scales larger than $16\mu\text{m}$ [35].

A different possibility is to directly use the preferred growth mode of various surface reconstructions, i.e. growth by self-organization, to obtain systems of predefined extent. They form wire-like structures because of the natural reduction of surface free energy on the surface resulting in a lateral extent of only several Å. Such systems are, e.g. the Si(111)-Au 5×2 reconstruction [36], the Si(111)-In system [37, 38], and Ge(100)-Pt [39] as well as Ge(100)-Au [40]. Within those structures, plasmon investigations supported the development of models for the metal-insulator transition temperature in Si(111)-In [41] and the exact coverage of the Si(111)-Au system [42].

The wire-like structure of Ge(100) has been chosen in this work because of its proposed Luttinger-liquid character and its particularly interesting electron pocket band structure, see Part III. However, due to the geometric distribution of the surface orientations of the domains of the Ge(100) substrates, there will always be two domains of those wires present. This unwanted behavior can be overcome by the growth on surfaces that are slightly miscut ($\leq 4^\circ$) in the respective direction [43].

A similar class of quasi-one-dimensional wires is the growth of rare-earth silicide nanowires [44]. In contrast to the systems mentioned above, here, the wire growth is guided by surface strain due to the lattice mismatch.

Another kind of system only exists on vicinal surfaces that have large miscuts $\gtrsim 10^\circ$. Within this group, there is Si(557)-Pb [45, 46, 47] which is acutely sensitive to the coverage and can be tuned from 2D to 1D behavior. Moreover, one part of this thesis will focus on such a vicinal-only system: Si(hhk)-Au. When providing the corresponding submonolayer of gold to the Si(hhk) surface, wires of either single

or double atomic width will form on the (111) terraces of the substrate. This system is well-suited for systematic investigation because it allows for changes in the distance and the width of the wires.

The comparison of the systems to each other and with theory can help understanding the correlations of these intriguing low-dimensional structures. By this means, it is possible to change the situation from a by-chance-preparation to a controlled construction on demand. A promising potential application of low-dimensional plasmonic devices is waveguiding with very short wavelengths, leading to much smaller devices. Within this field, a plasmonic modulator could play a certain role [48]. Further plasmon based ideas, though mainly focusing on graphene, are given in Ref. [49].

1.2 Structure of This Thesis

This thesis will first give a short introduction to the physical principles of the measurement methods necessary for the investigations in Part I. That is why the dissertation starts with a summary of the elastic and inelastic scattering of low energetic electrons in Chapter 2. Thereafter, Chapter 3 introduces the low-dimensional plasmon theory known from the literature and also extends it for this work. Further recapitulation of the textbook theory is skipped. Some standard books in the literature are referenced here for the curious reader and the sake of completeness [50, 51, 52, 53, 54, 55]. Concluding this part, Chapter 4 gives a short explanation of the vacuum chamber and its primary tools.

In the experimental portion, this work portrays two examples of systems that host quasi-one-dimensional wire structures. Part II will deal with the various Si(hhk)-Au systems and use the inherent nature of vicinal silicon to form terraces of tunable width. These terraces host spatially restricted electronic states. For these systems, Chapter 5 shortly summarizes the current state of research. In Chapter 6 the structural properties are discussed with an estimation of the attained quality. Finally, Chapter 7 deals with the plasmonic excitations in Si(hhk)-Au. First, a general description is given. Then, the plasmon theory introduced in Chapter 3 is extended to implement numerically calculated electronic band structures. The chapter ends with a discussion about the obtained peak widths and height and their correlation to plasmon properties, such as lifetimes. Finally, Chapter 8 leads a discussion about the modifications to the electronic structure of Si(hhk)-Au by the adsorption of oxygen and hydrogen of the surfaces using the models derived in the previous chapter.

Part III deals with the Ge(100)-Au system that hosts a quasi-one-dimensional system by a self-organized surface reconstruction upon gold adsorption. Also here, a summary of the state of knowledge in the literature is given in Chapter 9. Since obtaining high-quality samples of germanium is not as easy as for silicon, a spot profile analysis in LEED is carried out for the system. It systematically investigates the change of roughness and terrace sizes after several sputtering and annealing cycles of the surface. This spot profile analysis is also extended to the gold covered surface. Chapter 11 deals with the collective excitations in this system that are visible from peaks with very low intensities in the loss spectra. Two attempts to describe this system with one-dimensional plasmon models are presented: a Tomonaga-

Luttinger liquid approach as well as a quasi-free one-dimensional model.

In the end, Part IV of this thesis summarizes the findings, evaluates the results, and gives an outlook for future investigations.

Low Energy Electron Diffraction

One of the standard methods for the crystallographic investigations of surfaces is the diffraction of low energetic electrons. It is also the key method during this thesis. Their wavelengths calculate by

$$\lambda(\text{\AA}) = \sqrt{\frac{150.4}{E(\text{eV})}} \quad (2.1)$$

to values between 1.23 Å to 2.24 Å for energies in the range from 30 eV to 100 eV and are, thus, in the dimension of the inner atomic distances in crystal lattices. Due to a high electron-electron interaction, the enhanced cross-section of the electrons with the solid leads to a penetration depth as low as 1 Å to 8 Å in that energetic region [56]. Conclusively, signals obtained by scattering only originate from the first atomic layers.

In the simplest case of purely elastic scattering, constructive interference has the following condition:

$$\vec{K}_{\parallel} = \vec{k}_{\parallel,f} - \vec{k}_{\parallel,i} = \vec{G}_{\parallel} \quad (2.2)$$

Accordingly, a so-called Bragg-peak will occur when the part of the scattering vector parallel to the surface \vec{K}_{\parallel} coincides with a reciprocal surface lattice vector \vec{G}_{\parallel} . Here, $\vec{k}_{\parallel,i}$ is the initial or incident and $\vec{k}_{\parallel,f}$ is the final vector of the scattered electrons. Perpendicular to the surface, the periodicities are undefined. Assuming an infinite distance to the next neighbor, then, in reciprocal space, the distance is infinitely small. The inverse of infinity leads to Ewald-rods standing perpendicular on the two-dimensional surface in k space, see also Fig. 2.1.

2.1 Kinematic Approximation

A way to describe diffraction is to coherently sum up the phases of electron wave functions. Also in that case, the scattering is described as already pointed out in Eq. 2.2 by a scattering vector \vec{K} describing the difference between initial \vec{k}_i and final wave vector \vec{k}_f . The kinematic approximation assumes only a single scattering process on the surface. In contrast to X-ray diffraction with complete bulk sensitivity and He-diffraction with extreme surface sensitivity, electrons are elastically scattered within the first layers of a surface. This character justifies the approach of only single scattering. The depth-dependence is represented by a fade-out of the contrast in Fig. 2.1 (a). Without a precisely defined \vec{G}_\perp on a surface, constructive interference is possible for almost every vector in reciprocal space perpendicular to a defined surface diffraction condition leading to the formation of the already mentioned Ewald-rods with only a slight modulation, as depicted in Fig. 2.1 (b).

With surface atom positions at \vec{r}_n , the amplitude of the resulting wave function is given by [57]

$$\Psi(\vec{K}, \vec{k}_i) = \sum_n f_n(\vec{K}, \vec{k}_i) \times \exp(i\vec{K}\vec{r}_n). \quad (2.3)$$

In this context, f_n is the structure factor of the n -th atom that contains information about the scattering properties such as amplitude and phase. Those f_n might vary over the whole surface even for the same kind of atom depending on its neighborhood and altering bonding conditions. Unfortunately, instead of the amplitude Ψ , the intensity $I = |\Psi|^2$ is measured in an experiment. As a consequence, all information about the phase is lost and a direct information about the texture of the surface cannot be obtained. The diffracted intensity is given by

$$I(\vec{K}, \vec{k}_i) = |\Psi(\vec{K}, \vec{k}_i)|^2 = \sum_{n,m} f_n(\vec{K}, \vec{k}_i) f_m^*(\vec{K}, \vec{k}_i) \times \exp(i\vec{K}(\vec{r}_n - \vec{r}_m)) \quad (2.4)$$

and mainly determined by the surface lattice.

When all atoms sit on perfect lattice sites, the surface lattice can be described by:

$$\vec{r}_n = \vec{r}(n_x + n_y) = \vec{a}_x n_x + \vec{a}_y n_y + \vec{d}_z h_n \quad (2.5)$$

$$= a_0 \vec{n} + \vec{d}_z h_n \quad (\text{square lattice}) \quad (2.6)$$

Integer multiples of the surface lattice vectors \vec{a}_x and \vec{a}_y define the lateral positions of atoms, the surface morphology for its part is described by $\vec{d}_z h_n$ with a height factor h_n for the unit cell at position n and the step height vector \vec{d}_z .

In the given parametrization and with an averaging $\langle \dots \rangle_m$ over all m the intensity results as

$$I(\vec{K}, \vec{k}_i) = \sum_n \langle f(\vec{n} + \vec{m}, \vec{K}, \vec{k}_i) f^*(\vec{m}, \vec{K}, \vec{k}_i) \times \exp(i\vec{d}_z K_\perp (h_{(n+m)} - h_m)) \rangle_m \times \exp(i a_0 \vec{K}_\parallel \vec{n}). \quad (2.7)$$

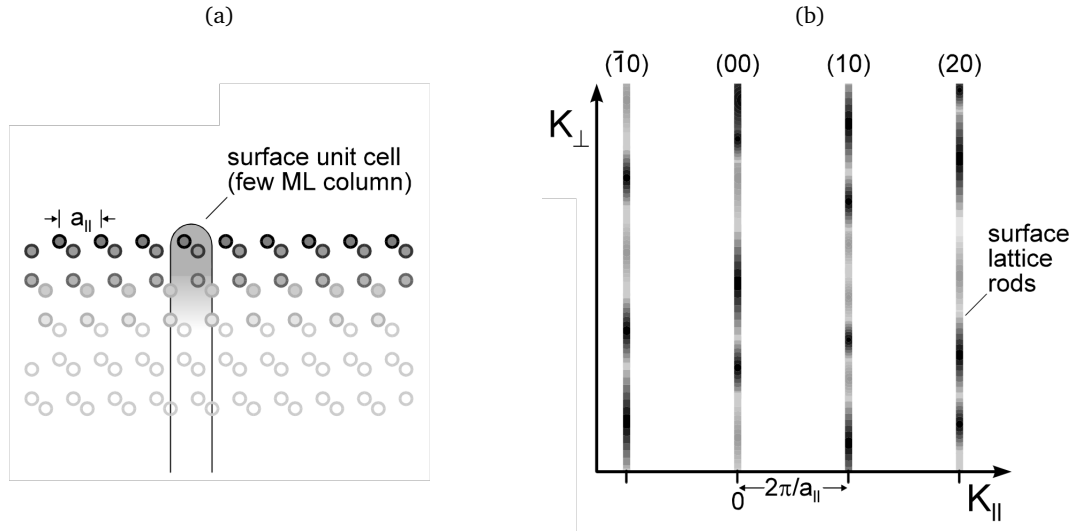


Figure 2.1: Simplified surface for electron diffraction (a) with the most contributing electrons and resulting surface rods (b) with only a slight intensity modulation due to the small penetration depths. Images taken from Ref. [57]

Here it becomes visible that both morphological as well as structural information influence the intensity. Within the kinematic approximation, K_{\perp} is a complex number in order to take into account the residual depth-dependence. To obtain details about the atomic structure in the unit cell, the diffraction spots have to be investigated as a function of electron energy and incident angles in combination with a theory that also includes multiple scattering. This can be achieved by intensity and energy dependent scans for smooth surfaces as it is put into practice by IV-LEED.

2.2 Spot Profile Analysis

The spot profile analysis carried out in this thesis relies on the kinematic approximation of only single scattering with some additional approximations. A discussion of multiple scattering effects on disordered surfaces is available in Refs. [58, 59]. One of these simplifications is the replacement of all structure factors by an average value $f = \langle f(\vec{n}, \vec{K}, \vec{k}_i) \rangle$. Indeed, this simple picture is only valid for flat surfaces with atoms of one kind. Additionally, merely small deviations are expected for different bonding conditions that occur on step edges. However, a variance is expected for differing atom species. Despite the fact of having a metal-semiconductor intermixed new surface unit cell consisting of two entirely different atoms in diverse binding varieties for the given systems, this approximation is applied in Chapters 6 and 10 for a rough approximation to the surface properties. A further approximation then must be that the different scattering factors f_{Au} only lead to a slight phase shift in contrast to scattering on atoms with f_{Si} or f_{Ge} . This phase shift will then behave like a virtual change in the height h_n . It will

be shown that it is even possible to qualitatively derive reasonable results.

For these given approximations, the intensity splits up into a dynamical form factor and the lattice factor given as

$$I(\vec{K}, \vec{k}_i) = F(\vec{K}, \vec{k}_i) \times G(\vec{K}). \quad (2.8)$$

Here, the dynamical form factor is simply the absolute square of the structure factor. The lattice factor is only depending on \vec{K} as

$$G(\vec{K}) = \frac{1}{2\pi} \left| \sum_n \exp(i a_0 \vec{K}_{\parallel} \vec{n}) \times \exp(i d \vec{K}_{\perp} h_n) \right|^2. \quad (2.9)$$

As the lattice factor does not change the integral intensity of the spots, the total intensity is conserved and normalized to unity. Therefore, it is independent on surface morphology and incident momentum $\approx \vec{K}_{\perp}$. Experimentally the lattice factor can be obtained by the assumption of $F(\vec{K}, \vec{k}_i)$ having only slight variation compared to the structure factor as described in Ref. [57] by

$$G(\vec{K}) \approx \frac{I_{ij}(\vec{K})}{\int_{\text{BZ}} d\vec{K}_{\parallel} I_{ij}(\vec{K}_{\parallel})}. \quad (2.10)$$

Despite these substantial simplifications made, the morphology of a sample with various steps can be explained besides the general description of diffraction patterns. The access to the morphology is possible by the Lorentzian and Gaussian parts of the shape of the refraction spots, and it can be used to get further insight into the lateral and vertical roughness of a system.

For these investigations the scattering phase S is introduced due to reasons of simplicity: Its integer numbers directly denote the energies of constructive interference, half-integers correspond to destructive interference. The definition directly refers to the Bragg condition

$$n\lambda = 2d_z \sin \theta \quad (2.11)$$

for simple reflection of a scattered wave front with incident angle θ . Substituting the wavelength λ by the momentum $k = 2\pi/\lambda$, this correlation can be reformulated for a perpendicularly incoming beam to

$$S = \frac{K_{\perp} d_z}{\pi}. \quad (2.12)$$

2.2.1 Lateral Roughness

When approximating a system simply as a two-level system in one dimension, a geometric terrace width distribution of mean terrace size $\langle \Gamma \rangle$ results in Lorentzian profile [57]. This average size can be derived

directly from the diffuse Lorentzian background of the profile for any scattering condition via

$$\langle \Gamma \rangle = \frac{4}{\text{FWHM}}. \quad (2.13)$$

However, for a surface with a multi-level roughness [57] and only steps of single atomic height, the normalized shape of an uprising diffuse part of the scattered intensity $I(K_{\parallel})$ varies with the scattering phase S [60, 61]. For any scattering condition except integer S , there are destructive interferences, with an intensity minimum at half-integer S . This broadening is of Lorentzian shape and convolved into the Gaussian distribution that describes the diffraction spot. In this case, the FWHM of the Lorentzian distribution $H(S)$ is directly proportional to the mean terrace width $\langle \Gamma \rangle$ as a function of the scattering phase S via the expression

$$H(S) = \frac{1}{\pi \langle \Gamma \rangle} [1 - \cos(2\pi S)]. \quad (2.14)$$

This result describes an approximation for a simple one-dimensional case and is the main method in this thesis to quantify the surface morphology. It is often referred to as $H(S)$ analysis. The formula but only describes the case of a domination of steps of single atomic height. A more generalized form for multiple step heights is

$$H(S) = \sum_{h \geq 1} \frac{\sigma_h}{\pi \langle \Gamma \rangle} [1 - \cos(2\pi Sh)]. \quad (2.15)$$

In this equation, σ_h are the probabilities of the occurrence of a step height $h \times d_g$. Whenever there are multiple steps (> 2) involved, the situation becomes imprecise, albeit, their values are directly accessible.

For a domination of only one step height, a particular and straightforward form results for the out-of-phase condition for half-integer values of the according S . Here, the terrace width directly estimates from the FWHM via

$$\text{FWHM}_{S=n+1/2} = \frac{2}{\pi \langle \Gamma \rangle}. \quad (2.16)$$

A slightly better estimation is possible when taking the difference between the in-phase and out-of-phase values to reduce systematic errors from the measurement. The device adds an offset to the recorded data as there is an intrinsic widening due to an always imperfect beam focus.

Further special cases for various surface simplifications are described in Section 2.2.1 of Ref. [57].

2.2.2 Vertical Roughness

The normalized central peak, i.e. the fraction of the central spike of the integrated peak intensity, can be used to obtain information about the vertical roughness [57] because it determines the variation of the central spike with K_{\perp} as given in Eq. 2.9. This so-called $G(S)$ -analysis depends on the distribution

of surface atoms at different height levels via

$$G(K_{\parallel} = 0, S) = \sum_h C_h \cos(2\pi Sh) = 1 - \sum_{h \geq 1} C_h [1 - \cos(2\pi Sh)]. \quad (2.17)$$

Here, all C_h denote the height correlations depending on the fraction of visible surface atoms $p_h = \theta_h - \theta_{h+1}$ that in turn depend on the specific coverages θ_h of layer h . The sum of all C_h is unity. Their relationship is given by

$$C_h = \sum_l p_l p_{h+l} = \frac{1}{2\pi} \int_{-\pi}^{+\pi} dS G(S) \cos(2\pi Sh). \quad (2.18)$$

The height correlations and, subsequently, the height distribution can be experimentally determined by either a Fourier transform of the $G(S)$ curve or an appropriate fit to its data with Eq. 2.17.

Another quite simple approach is the characterization of a surface's RMS-width Δ_{RMS} . When considering only scattering phases close to the in-phase conditions, $G(S)$ can be approximated by

$$G(S) \approx \exp[-\Delta_{\text{RMS}}^2 (2\pi \delta S)^2] \quad (2.19)$$

around the variation of the central peak δS as proposed by Wollschläger et al. [62, 63]. In this equation, the RMS value of the available level heights given calculate after Ref. [61] as

$$\Delta_{\text{RMS}}^2 = \langle h^2 \rangle - \langle h \rangle^2 = \sum_h C_h h^2. \quad (2.20)$$

These given formalisms allow to determine and optimize the surface quality of the germanium samples and to obtain further insight into the formation of the gold-induced wire structure in Chapter 10.

2.3 Inelastic Scattering of Electrons

Apart from the structural properties that are accessible by elastic scattering, inelastic scattering can be used to obtain information about excitations in a system. Such excitations could be, e.g., plasmons or phonons. The description of the energy loss of an electron needs further insight into the interaction between the incoming electron and the surface itself. Due to the high correlations in the solid, this issue may become very complicated. Therefore, any simple approach only leads to a very limited picture. However, two limiting cases shall be discussed in this section: In the long-range interaction regime, dipole scattering is an adequate description. In contrast, short-range interactions are characterized best by the so-called impact scattering. Nevertheless, it should be mentioned that there is no sharp boundary between them.

2.3.1 Small-Angle Inelastic Scattering by Dipole Fields

Strong scattering at small angles can be caused by long-range dipolar fields that are generated by molecular vibration. Indeed, any elementary excitation of a sample can lead to dipolar scattering when simultaneously a fluctuation in charge density is induced.

Within these considerations, the ground state charge density in a semi-infinite crystal $\rho_0(\vec{x})$ is disturbed [64]. It then becomes $\rho_0(\vec{x}) + \rho_1(\vec{x}, t)$ while keeping the whole system neutral. Therefore, the condition

$$\int d^3x \rho_1(\vec{x}, t) = 0 \quad (2.21)$$

has to be fulfilled. These fluctuations only rearrange charges already present. An electron with its charge e traveling to the surface for a scattering process will see the electrostatic potential

$$\varphi(\vec{x}, t) = \frac{1}{4\pi\epsilon_0} \int_{z' < 0} \frac{d^3x' \rho_1(\vec{x}', t)}{|\vec{x} - \vec{x}'|}. \quad (2.22)$$

Here, the sample with its induced density fluctuation is extended only in the negative z -direction. Retardation effects are ignored, any information about these fluctuations is transmitted instantly. After a reformulation using the scattering vector \vec{K}_{\parallel} of Eq. 2.2 this potential as seen from the electrons outside of the crystal reads

$$\varphi(\vec{x}, t) = \frac{1}{2\epsilon_0} \int \frac{d^2K_{\parallel}}{K_{\parallel}} \exp(i\vec{K}_{\parallel}\vec{x}_{\parallel}) \times \exp(-K_{\parallel}z) \int_{z' < 0} dz' \rho_1(\vec{K}, z', t) \exp(+K_{\parallel}z') \quad (2.23)$$

with a partial Fourier transform of the charge density fluctuation $\rho_1(\vec{K}, z', t)$. A contribution to the potential with spatial variation $\exp(i\vec{K}_{\parallel}\vec{x}_{\parallel})$ must necessarily decay when moving away from the sample as $\exp(-K_{\parallel}z)$. In the given relationship, the right integral is responsible for the scattering event of an incident electron with wave vector \vec{k}_i via the part of the scattering vector parallel to the surface \vec{K}_{\parallel} . In this description, the components of the scattering vector parallel to the surface \vec{K}_{\parallel} are conserved. However, there is no conservation of the perpendicular part of the wave vector. Therefore, a loss of energy ΔE for a given \vec{K} during the scattering process will define the direction of the outgoing electron. Additionally, the potential's extent into the vacuum can be approximated by K_{\parallel}^{-1} . Therefore, the excitation probability will be higher for longer wavelengths, and, in conclusion, also the interaction time will be longer.

Furthermore, for the observation of inelastic scattering, an additional momentum transfer to the electron is necessary to invert the direction of $\vec{k}_{\perp,i}$. This momentum will be provided by an elastic scattering on the crystal itself. As various additional multiple scattering paths are still possible, most of the electrons will penetrate into the bulk. Only some of the incident electrons experience elastic scattering, i.e. diffraction on the crystal lattice, of which merely a fraction scatters inelastically.

The calculation of the given formal description is possible by inserting Eq. 2.23 into the Schrödinger equation. Its solution is possible by perturbation theory in Born approximation [65, 66]. While there are

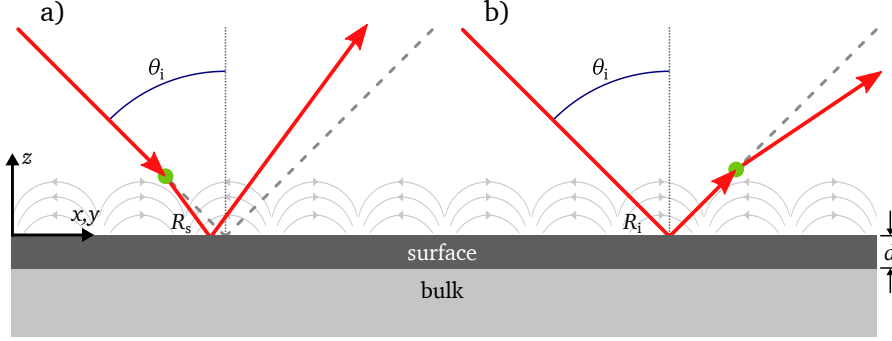


Figure 2.2: The two most dominant inelastic scattering processes in the dipole approximation: The inelastic scattering depicted by the green circle may take place before (a) or after (b) an elastic scattering on the surface. The elastic scattering amplitudes R_s and R_i are not necessarily the same. Depicted by the dashed grey lines is the elastic scattering path. The sketch was inspired by Ref. [64].

also possible scattering events involving a large momentum transfer, the cases depicted in Fig. 2.2 (a) and (b) only involve small angle scattering. These processes, where the difference $|k_{\perp,i}| - |k_{\perp,f}|$ is only a small fraction of $k_{\perp,i}$, result to be the dominant contribution to the cross section. Nevertheless, a distinction between these two cases has to be done because the probability amplitudes of specular reflection for the incident electron R_i and the already scattered one R_s are not necessarily the same. However, when the angular deflection that the electrons experience is small, it is reasonable to approximate $R_i \approx R_s$. The scattering efficiency is then described by [64]

$$\frac{d^2S}{d\Omega(\vec{k}_f)d\omega} = \frac{2m_e^2 e^2 v_{\perp}^4}{\pi^2 \hbar^4 \cos \theta_i} \times \left(\frac{k_f}{k_i} \right) \times \frac{|R_i|^2 P(\vec{K}_{\parallel}, \omega)}{\left[v_{\perp}^2 K_{\parallel}^2 + (\omega - \vec{v}_{\parallel} \vec{K}_{\parallel})^2 \right]^2}. \quad (2.24)$$

Here, θ_i is the angle of incidence with respect to the surface normal, see Fig. 2.2, v_{\parallel} and v_{\perp} are the parallel and perpendicular parts of the velocity of the incoming electron with mass m_e and charge e . Concluding from this relationship, the inelastic intensity increases with higher angles θ_i due to the extended interaction time with the surface. Please note, that at low energies very fine scale resonances can appear in $|R_i|^2$ under certain conditions due to the image potential of the incoming electron [67]. In this case, the approximation is no longer valid.

In the Eq. 2.24, $P(\vec{K}_{\parallel}, \omega)$ describes the response or probability of the system to a particular excitation. The simple case for a two-dimensional electron gas on a dielectric substrate [68] can be expressed by

$$P(\vec{K}_{\parallel}, \omega) = \frac{2 \hbar K_{\parallel}}{\pi} [1 + n_{\text{BE}}(\omega)] \times \Im \left[-\frac{1}{\tilde{\epsilon}(\vec{K}_{\parallel}, \omega) + 1} \right]. \quad (2.25)$$

In this relation, \Im denotes an imaginary part, where $\tilde{\epsilon}$ is an effective wave-vector dependent dielectric

function as seen by the incoming electron. Far away from the surface it is determined by the dielectric function of the bulk ϵ_b , in the vicinity of the surface by the one of the surface ϵ_s . The dependence on the Bose-Einstein statistics

$$n_{\text{BE}}(\omega) = \left[\exp\left(\frac{\hbar\omega}{k_B T}\right) - 1 \right]^{-1} \quad (2.26)$$

directly shows a strong dependence on the transferred energy during the scattering process.

2.3.2 Impact Scattering Regime

The physical picture of impact scattering events differs qualitatively from the small-angle dipole as described in the last section. Interaction only takes places within a region of a maximum distance of typically 1 \AA from the surface. Therefore, one can say that these inelastic events happen inside the structure and a microscopic theory is necessary.

A description is possible by scattering on short-range crystal potentials. Because of the interaction very close to the surface, no influence by mirror dipoles is present. Considering a macroscopic but finite solid with nuclei at positions \vec{R}_i and its collection denoted as $\{R\}$, the amplitude of the solution of the Schrödinger equation results in a function $f(\vec{k}_i, \vec{k}_f, \{R\})$. For fixed atomic positions on a lattice, the result is the solution of low energy electron diffraction as given by Eq. 2.2. But the nuclei are not fixed in their equilibrium positions at each point in time. Thermal vibrations lead to displacements u_i for each position according to

$$\vec{R}_i(t) = \vec{R}_{i,0} + \vec{u}_i(t). \quad (2.27)$$

As a consequence, the solid is disordered and not all electrons behave as predicted from the Bragg condition. A certain fraction is scattered away to form a thermal diffuse background.

In Ref. [64] an expansion of the scattering amplitude in powers of u_i has been carried out to quantize the vibrational motion. The cross section for inelastic scattering from the surface with the creation of a vibrational quantum $\vec{K}_{\parallel}\alpha$, i.e. a phonon, results in

$$\frac{dS_{\alpha}(\vec{k}_i, \vec{k}_f)}{d\Omega} = \frac{m_e E_i \cos^2 \theta_f}{2\pi^2 \hbar^2 \cos \theta_i} \times A |M(\vec{k}_i, \vec{k}_f, \vec{K}_{\parallel}\alpha)|^2. \quad (2.28)$$

Here, additionally to the same notation as in Eq. 2.24, E_i is the incident energy of the electron, and θ_f the angle of the scattered or final electron. A is the surface area of the crystal. M is the matrix element describing the creation of a vibrational quantum and is expressed in terms of the derivative of the scattering amplitude to nuclear displacement $\partial f / \partial R$. For an exact calculation, however, the vibrational modes have to be known leading to a defined structure in the energy variation of the loss intensity. As it was explicitly calculated for phonons in this case, the matrix element M may also express other excitations, such as plasmons.

Furthermore, the decrease of the elastically scattered intensity and the associated increase of this

diffuse background is calculated by the same ansatz of Eq. 2.27. As described in Ref. [52], it results in

$$I = I_0 \exp\left(-\frac{1}{3} \langle u^2(t) \rangle\right) = I_0 \exp\left(-\frac{k_B T}{m_a \omega^2} G^2\right). \quad (2.29)$$

This correlation is called the Debye-Waller factor [69, 70], where $\langle u^2(t) \rangle$ is the mean thermal displacement square of all nuclei, m_a is the mass of these atoms, $\omega = \sqrt{k_{\text{spring}}/m_a}$ results in the spring constant k_{spring} of the interaction between the atoms with mass m_a . Please note, that not only the elastic intensity, but also the inelastic intensity will be reduced by this factor.

3

Plasmons in Low Dimensions

Plasmons are the quantized longitudinal collective excitation of the electron density in a solid. Thus, a plasmon is the quasiparticle of the density fluctuation of the electrons in metal. Classically, one can think of a plasmon as an oscillation of the electrons with respect to the fixed positive ions in the background, in a very simple way comparable to a water wave. For the approximation at long wavelengths in a typical three-dimensional quasi-free electron gas case a plasmon will have the following energy [71]:

$$E_p = \hbar\omega_p = \hbar\sqrt{\frac{ne^2}{\epsilon\epsilon_0m^*}} \quad (3.1)$$

This is called the plasma energy. Consistently, ω_p is referred to as the plasma frequency. This relationship shows a basic characteristic: the ability to change the energy of a plasmon by the adjustment of the electron density in the corresponding system. This square root dependence seems to survive even down to the smallest systems as measurements on low-dimensional systems showed [30].

The dispersion relation of a plasmon can look quite different depending on the choice of dimensionality, as shown in Fig. 3.1 for a same electron density parameter r_s^* , cf. Eq. 3.15. As the plasmon energy is constant for a 3D system, at a critical wave vector k_{crit} the plasmon mode enters the blueish electron-hole pair continuum. The plasmon then decays by emitting electron-hole pair excitations damping it steadily. This effect is called Landau damping. Among other possible damping mechanisms like disorder or any momentum transfer, this is the most effective one. The upper boundary of this Landau regime is always the same for systems of all dimensions. Just the lower boundary changes due to the additional

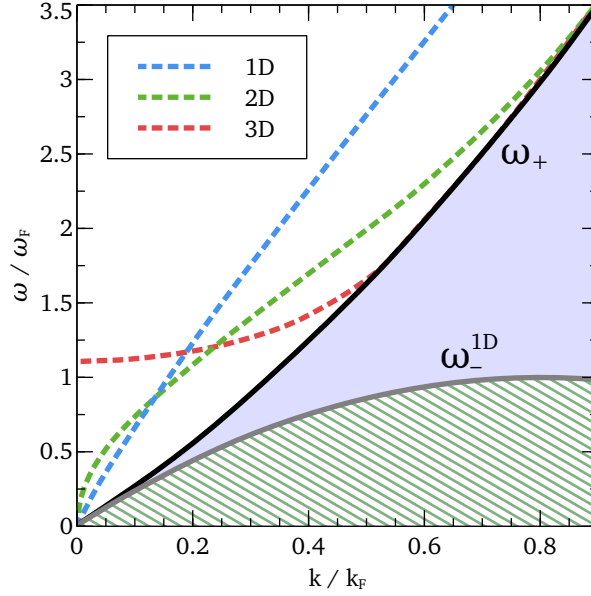


Figure 3.1: Comparison of the plasmon dispersion relations in 1D, 2D, and 3D: Given by the blueish region is the electron-hole pair excitation spectrum with upper boundary ω_+ and lower boundary ω_-^{1D} for one dimension. Here, Landau damping hinders plasmon propagation. For 2D and 3D, the green hatched region can be allowed depending on the band structure. The curves have been taken from Ref. [72].

excitation channels. Fig. 3.1 only shows the lower boundary for the one-dimensional case. The region in hatched green can, therefore, still provide possible single-particle excitations for 1D and 2D.

The dispersions of the lowest order in 1D and 2D start similarly at zero energy. The 2D case tends to converge strongly to the upper boundary of the single particle excitation, while the pure 1D dispersion has weak curvature, and is almost linear like the situation for light. A similarity of all plasmons is that their dispersions are energetically always located above the upper boundary ω_+ . In combination with wavelengths of around three orders of magnitude shorter compared to an electromagnetic wave in free space of the same energy, low-dimensional plasmons provide promising features. Understanding the various influences on the plasmon properties is one the aims of this chapter.

3.1 Theoretical Determination of Plasmons in Quasi-Free Electron Gases

For the calculation of the properties of a plasmon, one primarily needs to know the dynamical structure factor $S(k, \omega)$ of a system that contains information about inter-particle correlations and their evolution in time. It is proportional to the imaginary part of the inverse of the dynamical dielectric function $\Im[\epsilon(k, \omega)^{-1}]$. In the random phase approximation and for any kind of plasmon, the dielectric function

is always expressed by

$$\epsilon(k, \omega) = 1 - v_c(k)\chi_0(k, \omega), \quad (3.2)$$

where $v_c(k)$ is the Fourier transformed Coulomb interaction and $\chi_0(k, \omega)$ is the electron gas polarizability for the corresponding dimension [72].

The zeros of the real part \Re of the complex dielectric function define the dispersion:

$$\Re[\epsilon(k, z_p)] = 0 \quad (3.3)$$

In this case the frequency is complex, such that $z_p = \omega_p + i\alpha$, where ω_p defines to the dispersion and α the damping and, consequently, the lifetimes of the resulting plasmon. For the possibility of oscillations, the imaginary part of the dielectric function has to be low, i.e. only minor damping is allowed [73]. When using the dielectric formalism, the response of electrons to a weak space-time dependent external longitudinal electric potential is described by the density response function, also called Lindhard function:

$$\chi(k, \omega) = \frac{\chi_0(k, \omega)}{1 - v_c(k)[1 - G_{\text{corr}}(k)]\chi_0(k, \omega)} \quad (3.4)$$

Here, the plasmon excitation energy can be obtained by the poles of the equation. Thus, for the determination of the dispersion relation, the Coulomb interaction $v_c(k)$ needs to be well-known. G_{corr} describes a correction factor due to local fields extending the simple approach of the random phase approximation. Setting $G_{\text{corr}} = 0$ in Eq. 3.4 is one of the simplest approximations possible. The relation then becomes

$$\chi(k, \omega) = \frac{\chi_0(k, \omega)}{1 - v_c(k)\chi_0(k, \omega)} = \frac{\chi_0(k, \omega)}{\epsilon(k, \omega)}. \quad (3.5)$$

This description takes neither any damping nor field correlations into account and is identical to the pure RPA approach of Eq. 3.2.

3.2 Quasi-One-Dimensional Approach

One way to describe a one-dimensional system is to neglect the peculiarities that often originate from strong electronic correlations [1] in such systems and to use a quasi-free electronic approach. As also mentioned in Refs. [25, 72, 74], an approximation for the wave function of a wire along the x -direction is given by

$$\Psi(x, y, z) = \frac{e^{ik_{\parallel}x}}{\sqrt{L}} \phi(y, z). \quad (3.6)$$

The wave function $\phi(y, z)$ describes the system in the y and z -directions by considering the finite width in the directions perpendicular to the 1d wave vector k_{\parallel} along an idealized quantum wire of length L . These wave functions can be chosen from a particle-in-a-box confinement [75] or quantum harmonic

oscillator [76] for an expanded electron density in the given direction. For a stronger confinement in the z -direction, one can use a so-called Stern-Howard variational wave function [77] describing an exponential decay of the electron density or even a Dirac delta function to ignore this dimension entirely making the approximation truly two-dimensional. Ref. [74] compares the influences of various ground state wave functions:

I. Harmonic confinement in a tube with effective diameter b and $R = \sqrt{y^2 + z^2}$:

$$\phi(R) = \frac{1}{\sqrt{2\pi b^2}} \exp\left(-\frac{R^2}{4b^2}\right) \quad (3.7)$$

II. Infinite square-well confinement in y and z with the confinement size a :

$$\phi(y, z) = \frac{2}{a} \sin\left(\frac{\pi y}{a}\right) \sin\left(\frac{\pi z}{a}\right) \quad (3.8)$$

III. Infinite square-well in y direction and the variational wave function $\zeta(z)$ [77] in z :

$$\phi(y, z) = \sqrt{\frac{2}{a}} \sin\left(\frac{\pi y}{a}\right) \times \underbrace{\sqrt{\frac{\beta^3}{2} z \exp\left(-\frac{\beta z}{2}\right)}}_{\zeta(z)} \quad (3.9)$$

IV. Harmonic confinement in y like in eq. 3.7 and $\sqrt{\delta(z)}$ in z :

$$\phi(y) = \frac{1}{\sqrt[4]{2\pi b^2}} \exp\left(-\frac{y^2}{4b^2}\right) \quad (3.10)$$

V. Square-well confinement in y like in eq. 3.8 and $\sqrt{\delta(z)}$ in z :

$$\phi(y) = \sqrt{\frac{2}{a}} \sin\left(\frac{\pi y}{a}\right) \quad (3.11)$$

Within these formulations, a denotes the width of a square-well potential and b is the width of a harmonic potential at the ground state. Among other descriptions that might be physically correct, these five describe the limit cases. They mainly differ in their kind of extent in the form of a tube or a flat 2D channel and their edges of the potential. Hard walls result in a square-well, whereas harmonic confinement mimics softened edges of the channel. This approach considers only ground states in y and z , i.e. perpendicular to the conduction channel, as the confinement size is tiny and, therefore, sub-band excitations need extremely high energies.

Having defined the ground state wave function, the Coulomb interaction matrix element $v_c(k)$ that is necessary for the computation of the plasmon dispersion from 3.2 can be obtained by solving the

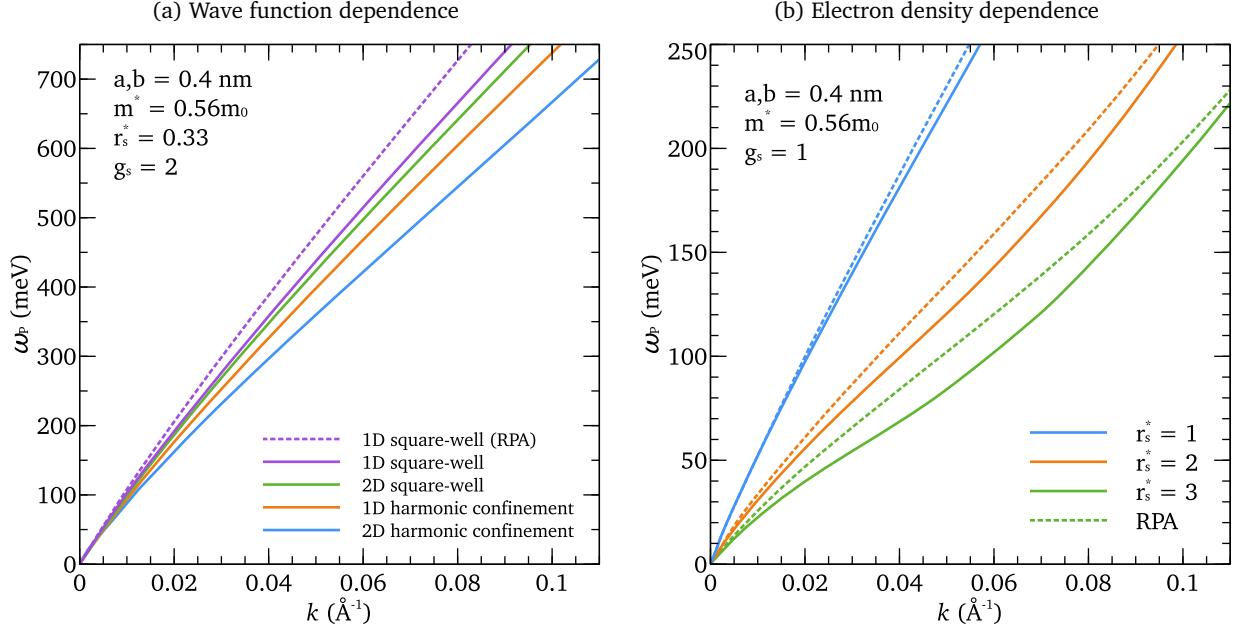


Figure 3.2: Parameter influences to the plasmon dispersion: (a) Influence of the ground state wave function. For a given set of system variables (top left), the resulting dispersion relations of square-well and harmonic potential are shown for both 1D and 2D confinement. The dotted curves are for RPA numerics showing the error of this method compared to STLS typically taken into account. (b) Influence of the electron density factor r_s^* (higher value means lower density). When lowering only the density in the 2D harmonic confinement, the STLS approximation suppresses the dispersion for higher momentum making it essential for such systems. All data have been taken from Ref. [74].

integral

$$v_c(k) = \frac{e^2}{2\bar{\epsilon}\epsilon_0} \int dy \int d\tilde{y} \int dz \int d\tilde{z} |\phi(y, z)|^2 |\phi(\tilde{y}, \tilde{z})|^2 \times K_0(k\mathbf{R}). \quad (3.12)$$

Here, $\bar{\epsilon}$ is the averaged permittivity of the environment, K_0 is a zeroth order modified Bessel function of second kind, $\mathbf{R} = \sqrt{(y - \tilde{y})^2 + (z - \tilde{z})^2}$. Please note that for the square-well potentials the integrals can only be obtained numerically, while an analytic solution is possible for harmonic confinement.

With the one-dimensional free electron density response function χ_0^{1D} , the poles of Eq. 3.4 define the dispersion relation of the corresponding plasmon via [74]

$$\omega_p(k) = \sqrt{\frac{\omega_+^2 e^{A(k)} - \omega_-^2}{e^{A(k)} - 1}} \quad (3.13)$$

with ω_{\pm} as the upper and lower boundary of the single electron-hole pair continuum. $A(k)$ is a function

of the Coulomb matrix element $v_c(k)$. Both are defined as:

$$\omega_{\pm} = \frac{\hbar(k^2/2 \pm kk_F)}{m^*}, \quad A(k) = \frac{\hbar^2 2\pi k}{m^* g_s v_c(k)} \times \frac{1}{1 - G_{\text{corr}}(k)} \quad (3.14)$$

Here, g_s is the spin degeneracy factor that can be either 2 or 1. For the calculations of this work, the local field correction factor $G_{\text{corr}}(k)$ originates in a self consistent mean-field approximation developed by Singwi, Tosi, Land and Sjölander [24] to consider electronic correlations – it is often abbreviated as STLS.

Ref. [74] carries out numerical calculations for the models listed above and data from the Si(557)-Au system with width $a, b = 0.4 \text{ nm}$, $m^* = 0.56m_e$, $k_F = 4.1 \text{ nm}^{-1}$, $g_s = 2$, and $\bar{\epsilon}_{\text{Si-surface}} = (11.5 + 1)/2$. Accordingly, the density parameter computes to $r_s^* = 0.33$, see Eq. 3.15. The results are shown in Fig. 3.2(a). The curves show a substantial difference depending on the confinement model. Harmonic confinement leads to a redshift in the plasmon energy compared to a square-well potential, as well as 2D confinement does compared to 1D confinement models. There is also a redshift when using the STLS approximation compared to pure RPA. The highest difference between those two in the given data is also shown by the dotted purple line for the 1D square-well model, all other dispersions have lower difference.

The STLS correction factor increases with higher k and has a higher value for all k for more densely packed electrons. It tends to redshift the plasmon energy compared to RPA. As shown in Fig. 3.2 (b), it is stronger for lower electron densities, i.e. higher r_s^* . Particularly, it has to be taken into account for systems $a/r_s^* < 1 \text{ nm}$ [74] where a is the confinement width and r_s^* is the dimensionless electron coupling or density parameter. This parameter can also help to compare electron systems of various parameters and dimensions [78] and for 1D is given by

$$r_s^* = \frac{1}{2na_0^*}, \quad a_0^* = \frac{4\pi\bar{\epsilon}\epsilon_0\hbar^2}{m^*e^2} \quad (3.15)$$

with a_0^* as the effective Bohr radius in a dielectric. Instead of $1/2$ a prefactor of $8/\pi^2$ may be implemented to refer to the residual extent to 2D of quasi-one-dimensional systems [72]. This inconsistency may sometimes lead to confusions.

However, the error between pure RPA and its enhancement with STLS is typically only $\leq 10\%$ [74, 79] for the systems investigated. Therefore, the STLS approximation could be neglected or strongly simplified. As for the computations carried out in this thesis, an empirical STLS simplification from the data of Ref. [74] was implemented that helped to minimize the mentioned error. Approximating with

$$G_{\text{corr}}(k) = 0.3g_s \sqrt[4]{k(\text{\AA}^{-1})} + 0.8k(\text{\AA}^{-1}) \quad (3.16)$$

can be justified by the fact that for all used systems the density factor is of the comparable value $r_s^* \approx 0.3$

when setting $g_s = 2$.

3.3 Arrays of Quasi-One-Dimensional Wires

As most of the one-dimensional wires grow via self-assembly on a surface, they arrange themselves into arrays. Now, in the vicinity of an isolated wire, there are infinite additional electronic channels with distance d . In a simple approach, this will add a term to the Coulomb matrix element describing the influence of the additional electron density [79]:

$$v_c^{\text{eff}}(k) = \underbrace{v_c(k)}_{\text{intrawire}} + \underbrace{v_c^{\text{array}}(k)}_{\text{interwire}} \quad (3.17)$$

This additional Coulomb interaction can be described by the following integral [25]:

$$v_c(k)^{\text{array}} = \frac{e^2}{\bar{\epsilon}\epsilon_0} \int dy \int d\tilde{y} \int dz \int d\tilde{z} |\phi(y, z)|^2 |\phi^{\text{array}}(\tilde{y}, \tilde{z})|^2 \times K_0(kR) \quad (3.18)$$

It calculates the interaction strength between the central wire $\phi(y, z)$ and electron density around it $\phi^{\text{array}}(\tilde{y}, \tilde{z})$. The surrounding density results in regularly aligned wave functions with distance d without the central wire wave function:

$$\phi^{\text{array}}(y, z) = \sum_{l \neq 0} \phi(y - ld, z) \quad (3.19)$$

Other approximations also take feedback or k -angle dependence into account as it has, e.g., been done by Inaoka [79] or Das Sarma et al. [25]. In this thesis the low- k blueshift is just modeled by an electron density surrounding and wave function overlaps giving already quite sophisticated results for systematic investigations. The source code for the numerical determinations of v_c is available in the appendix of this work.

Fig. 3.3 (a) shows the calculated data for two cases: the harmonic and the square-well potential ground state wave functions, corresponding to models number IV and V. For the determination of the dispersion relations the same variables as for the calculations from Moudgil et al. [74] have been used, cf. bottom right of (a). $G(k)$ was approximated with the STLS simplification suggested in Eq. 3.16. Comparing the two dispersion relations, the harmonic model tends to converge faster to the upper boundary of the single particle excitation spectrum (top black curve). For a single wire (dotted curves) both dispersions are very flat with a difference of around $100 \text{ meV} \approx 10\%$ at $k = 0.15 \text{ \AA}^{-1} = 0.37k_F$. The periodic arrangement leads then to an expected blueshift (solid curves) for lower momentum as the Coulomb interaction strength for long wavelengths is highly increased by the surrounding additional electron density. In the given data, the wire array was simulated by five wires on both sides of the original channel, leading to a total value of 11. Please note that the initial inclination of the slopes is

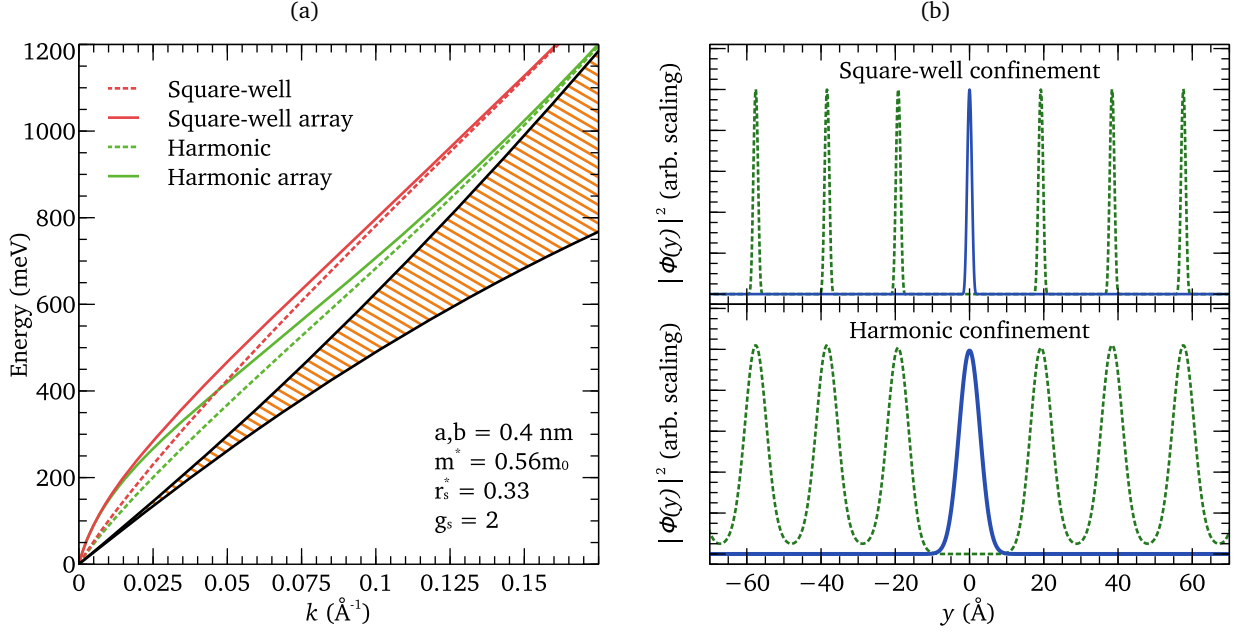


Figure 3.3: Calculated plasmon dispersion relations with corresponding wave functions: (a) Resulting dispersion relation for 1D confinement in a square-well (red) and harmonic potential (green) for a single wire (dotted) as well as in an array of altogether 11 wires (solid). The dispersion for a multiple wire setup is blueshifted for lower k for both states, for harmonic confinement the slope converges to the upper boundary of the single excitation faster. For the calculation the STLS simplification was used, cf. Eq. 3.16. (b) Squares of the absolute value of the used wave functions for the calculations. The single wire is given in blue, the surrounding array structure in dotted green. Both widths are the same, but due to the softer margin the wave function for the harmonic confinement is stretched out leading also to an overlap.

in each case the same for harmonic and square-well confinement. Here, only the total electron density of the system, the effective mass, and the long-wavelength Coulomb interaction are important. A low- k approximation describes this initial slope by [25]

$$E(k) = \hbar\omega_0 ka \times \sqrt{K_0(ka) + 2 \sum_{l=1}^n K_0(kld)} \quad (3.20)$$

when using the long-wavelength limit of $v_c(k)$ in Eq. 3.2. Here, ω_0 is a system specific constant given as

$$\omega_0 = \sqrt{\frac{2ne^2}{4\pi\bar{\epsilon}\epsilon_0 m^* a^2}}. \quad (3.21)$$

Fig. 3.3 (b) shows the densities of the used wave functions for both square-well (top) as well as harmonic confinement (bottom). Depicted in blue is the single channel wave function, in dotted green the

surrounding array's wave function.

Although both systems share the same width ($a, b = 4\text{\AA}$), the probability's density $|\Phi(y)|^2$ is much wider for the harmonic case as here the margins are not hard and therefore the wave function can spill out. The effective width seen in, e.g., scanning tunneling spectroscopy maps is therefore much wider for the harmonic potential. These observable widths of the square-well and the harmonic case are

$$w_{\text{sqw}} = \frac{1}{2}a, \quad w_{\text{harm}} = 2\sqrt{2\ln 2}b. \quad (3.22)$$

The spill-out of the wave function also has a significant influence on the surrounding array. As can be seen in the bottom of Fig. 3.3(b), the wave functions overlap, leading to a non-vanishing probability between the wires. For the square-well potential case, the probability here is 0. This overlap can also explain the more 2D-like behavior of the green curve in Fig. 3.3(a) when comparing it to the general slopes of Fig. 3.1. A plasmonic excitation in an array of wires on atomic scales, therefore, is on the margin between 1D and 2D making it a crossover of dimensions.

Nevertheless, when setting the given observable widths to the same value $w_{\text{harm}} = w_{\text{sqw}}$ while still having only small overlaps in the harmonic case, i.e. $w_{\text{harm}} \lesssim 0.5d$, the same plasmon dispersion builds up. That means that for systems with electronically quasi-separated wires only the lateral distribution of the electrons on the surface is important.

3.4 Plasmons in Tomonaga-Luttinger Liquids

Within the framework of highly correlated electrons in one dimension, a description of a 1D system is the Tomonaga-Luttinger liquid (TLL) model [9, 8]. In contrast to a 2DEG confinement of the quasi-one-dimensional case above, this model represents a strictly one-dimensional case with the approximation of electron-hole excitation spectrum being of purely linear shape. This kind of slope introduces two species of fermions: right and left movers, cf. Fig. 3.4. Density fluctuations $\rho(k)$ in such a system are only a superposition of particle-hole excitations with their operators c and c^\dagger [1]. They have a defined energy for a given momentum, and a spinless model is provided by

$$\rho^\dagger(k) = \sum_n c_{n+k}^\dagger c_n. \quad (3.23)$$

Being a combination of two fermionic operators, $\rho^\dagger(k)$ is of bosonic nature. One result of this bosonization is that for excitations in only one species (called g_4 processes, cf. Fig. 3.4) a renormalization of the velocity

$$u = v_F \left(1 + \frac{g_4(v_c)}{\pi v_F} \right) \quad (3.24)$$

takes place with a renormalization constant g_4 . For long-range interactions, this constant is given by the Coulomb potential $v_c(k)$. In that case, also the renormalization has to be calculated k -dependent

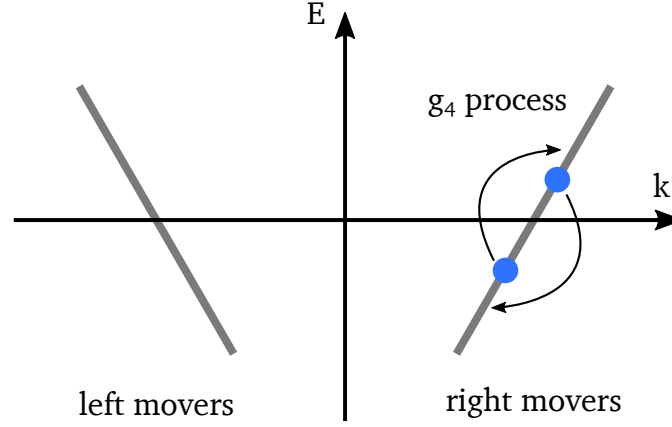


Figure 3.4: Assumptions of the Tomonaga-Luttinger liquid model: The electronic states are linearized leading to two species of electrons: left movers and right movers for negative and positive inclination. A density fluctuation as a superposition of single particle excitations can be described by using only one of these species, a so-called g_4 process.

and results in

$$u_\rho(k)K_\rho(k) = v_F \quad \text{and} \quad \frac{u_\rho(k)}{K_\rho(k)} = v_F \left(1 + \frac{2v_c(k)}{\hbar\pi v_F} \right) \quad (3.25)$$

with K_ρ as the Luttinger electron interaction parameter used in the power laws and u_ρ as the renormalized velocity of electron density excitations. From these equations, the plasmon dispersion relation can be derived to

$$\omega_p(k) = ku_\rho(k) = kv_F \underbrace{\sqrt{1 + \frac{2v_c(k)}{\hbar\pi v_F}}}_{1/K_\rho(k)}. \quad (3.26)$$

This result is the same as the results of the quasi-free electron gas theory for 1D when ignoring higher order terms $\mathcal{O}(k^3)$ [72]. However, in contrast to the RPA approach, the Coulomb interaction v_c is only given due to the screening by external electrons. When taking a quantum wire with diameter a in an isotropic medium of electrons, a phenomenological form [80] of the potential in real space is

$$v_c(r) = \frac{e^2}{4\pi\bar{\epsilon}\epsilon_0\sqrt{r^2 + a^2}}. \quad (3.27)$$

Taking into account the cut-off behavior and, therefore, the long-range interaction ($q \rightarrow 0$) of the potential, a Fourier transformed representation is given by

$$v_c(k) = 2\frac{e^2}{4\pi\bar{\epsilon}\epsilon_0}K_0(ka) + C(a). \quad (3.28)$$

Here, $C(a)$ is a constant with a logarithmic dependence in a , K_0 is again the modified Bessel function of zeroth order and second kind. Taking the dependence on $K_0(ka)$ as the dominating term for low k , a long wavelength solution for the plasmon with long-range interactions of this kind is then given by

$$\omega_p(k) = ku_\rho(k) = \sqrt{\frac{v_F e^2}{\hbar \pi^2 \bar{\epsilon} \epsilon_0}} \times k \sqrt{K_0(ka)}. \quad (3.29)$$

This result is also very similar to the low- k -approximation of Eq. 3.20 with the difference of a description via v_F instead of m^* and n , directly pointing at the closeness of low-dimensional approximations.

In the case of a renormalization of the charge oscillations due to the Coulomb interactions, an occurring spin density wave will, however, still have a linear dispersion $\omega_\sigma = ku_\sigma$ unless additional potentials affect their behavior. Indeed, such a feature has already been observed. In a work of Goñi et al. [81] two excitations are visible in a Raman scattering experiment: They explain one as a plasmonic excitation that is shifted upwards in energy due to Coulomb interactions. The other excitation is assigned to a spin density excitation describing a linear curve to the origin of the energy-momentum coordinate system.

4

The Vacuum Chamber Setup

This chapter will shortly summarize the experimental setup used for the investigations of this thesis. First, the main chamber will be explained, followed by a detailed description of the devices.

Due to the sensitivity to contamination of the systems used, all experiments were carried out in an ultra-high vacuum of around 5×10^{-11} mbar. The vacuum chamber is divided into two parts: the main chamber for the experiments and the load lock chamber providing a fast and clean introduction of samples into the main vacuum. To achieve such low pressures a variety of pumps is necessary. The main chamber is pre-pumped by a membrane pump followed by a turbo pump. Additionally, the chamber contains an active ion-getter pump and a titanium sublimation pump. For further reduction of residual hydrogen, an additional non-evaporable getter pump is used that contains a porous ZrVFe alloy. The load lock is pumped by a combination of a membrane pump and a turbo pump. Like every UHV system, the chamber needs a bake-out to reach low pressures, in this case at a particular temperature of 175 °C.

A sketch of the chamber is given as top view in Fig. 4.1 (a). An older but more detailed description can also be found in Ref. [29]. Samples can be introduced by the help of the load lock. Here, also a preheating is possible. The transfer into vacuum is possible via an in-house self-built arm mechanism that can hold the sample holder. This sample holder is then transferred into the main chambers sample handler that can be turned and laterally moved for the alignment to the various components. It holds the sample by clamping the sample holder, see Fig. 4.1 (b). The clamps are also used for direct current heating. The holder is made of copper and can be cooled from outside with liquid nitrogen or helium, though the heat transfer is not optimal due to the clamps' small contact. Cooling temperatures are measured by a Si diode inside the cooling flow line, and by an additional Pt1000 resistance put on the

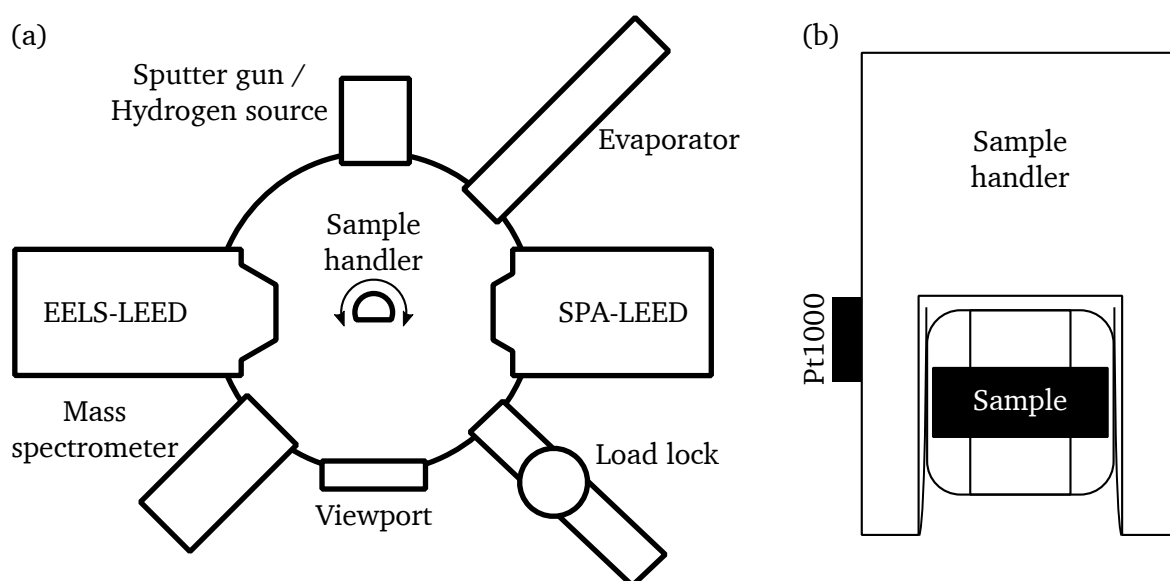


Figure 4.1: Sketch of vacuum chamber and sample handler: (a) Top view illustration of the positions of the various devices used in the investigations. In the center is the sample handler (b) that holds the self-built sample holder with durotherm (CoNiCrMo) clamps and align it to the different positions. Temperatures for LT measurements are taken from the side of one leg of the handler, relatively far away from the sample.

side of the handler. A slight temperature difference to the sample itself will, however, still be present. Through the viewport that is also known as window, the temperature of the sample can be measured optically by an IR pyrometer when heating it for preparation. The emissivity will constantly be changed during measurement according to the material by a computer software. Analysis of the residual gas is possible by a quadrupole mass spectrometer from Pfeiffer.

The preparation of the Au-induced superstructures is done with the a self-built evaporator and the surface properties are investigated by SPA-LEED. Electronic information about the system is available via EELS. The flange equipped with a hydrogen source in the Si(hhk) measurements is swapped for a sputter gun during the preparation of the Ge(100) surface. In the following the two main measurement methods are explained in detail. Also, short descriptions of the self-built evaporator as well as the hydrogen source are given.

4.1 SPA-LEED

The spot profile analysis low energy electron diffraction, short SPA-LEED, is a derivative from a conventional LEED with the advantage of gaining insight into the exact profile of diffraction spots. Using this technique, the information of Section 2.2 is experimentally accessible. Fig. 4.2 (a) shows a sketch of this device that was originally developed in the Henzler group in Hannover in the 1980s [82, 83, 84].

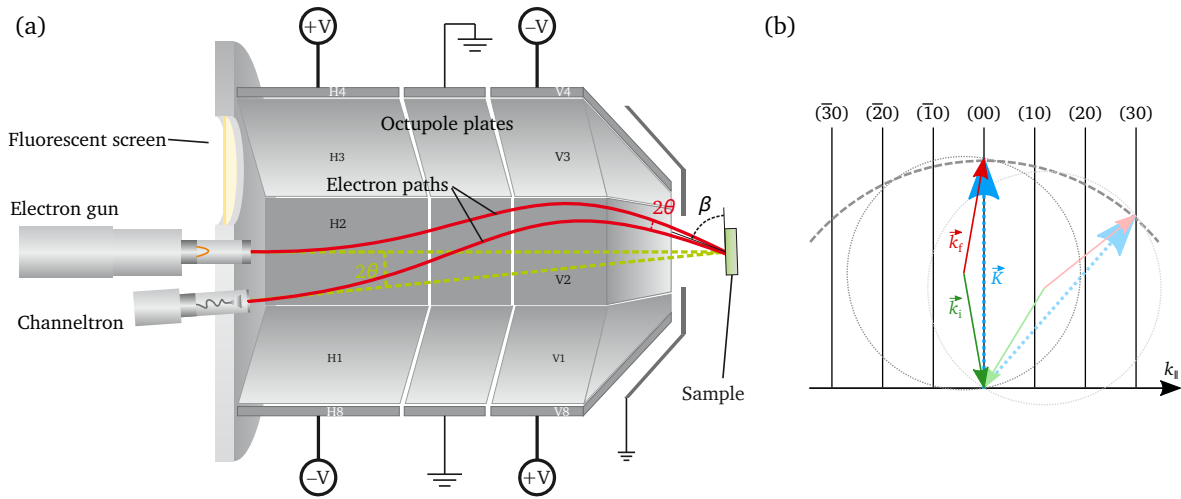


Figure 4.2: Sketch of the SPA-LEED (a) and the given scattering condition (b): (a) The free electrons generated and accelerated by the electron gun follow the paths that are determined by an octupole plate deflection unit, the detection is realized by a channeltron. The angle between incident and final wave vector is constant. The sketch was taken and modified from Ref. [85]. (b) Surface rods of the reciprocal space. The incident \vec{k}_i and final wave vector \vec{k}_f are always kept at the same relative orientation. The voltage regulation in the deflection unit leads to a change of the scattering vector \vec{K} granting access to the reciprocal space. The native Ewald spheres are given by the dotted grey circles, the new SPA-LEED sphere by the dashed partial circle.

A similarity is of course an electron gun that accelerates the electrons to the sample. In contrast to a conventional LEED, the image is not obtained on a fluorescent screen. Instead, the reflected intensity is analyzed by a channel electron multiplier, short channeltron. Only a distinct scattering path is pointing in the direction of this channeltron. Therefore, the system features a system of doubled eight concentric electrostatic plates to set the angle of the beam with respect to the surface, called octupole plates. The polarity of these plates is inverted between the two pairs (H and V) to force the electron onto an S-shaped path. Two of these paths are given in Fig. 4.2 (a). The angle between incident and diffracted beam is constant. Accordingly, the scattering condition is slightly changed compared to a conventional LEED. Instead of scanning the margin of the well-known Ewald sphere, a new sphere is generated that will be rolled out while changing the octupole voltages, see Fig. 4.2 (b). This new modified half-sphere has approximately double the radius. Consequently, using a SPA-LEED results in scans with a larger access to the reciprocal space.

However, during the acquisition of an image, the device has to scan over all scattering conditions. One could say that a SPA-LEED is a scanning electron microscope for the reciprocal space. The device used in this thesis also allows scanning while changing the acceleration voltages [86]. This mode directly maps the reciprocal space perpendicular to the surface. This mode denotes the energy dependent plots in this work. The control of the SPA-LEED is done by a computer software called WinSPA. To overcome

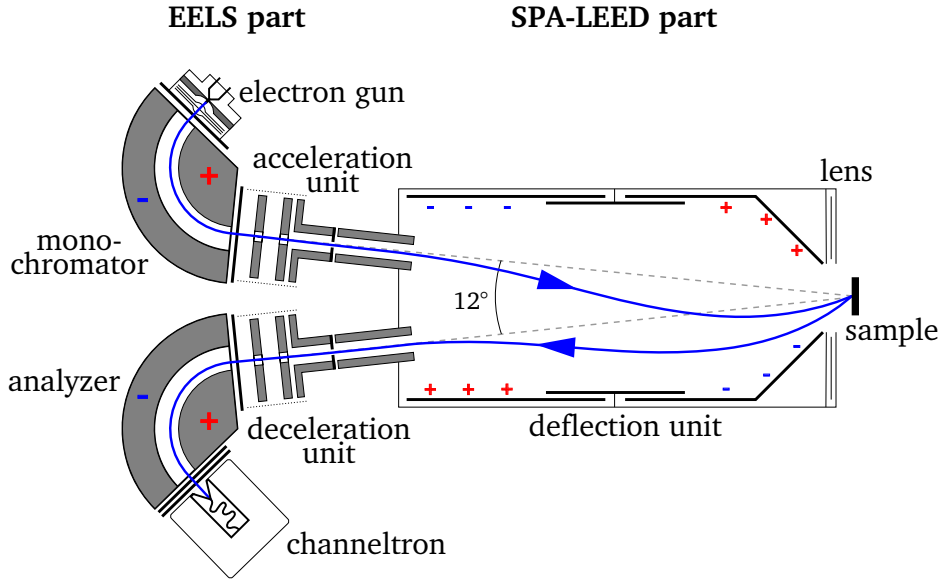


Figure 4.3: Sketch of the EELS-LEED: Compared to a SPA-LEED, this device features an additional lens system (left) with additional monochromator and analyzer to allow the measurement of inelastically scattered electrons. The image has been taken and slightly modified from Ref. [88]

the disadvantage of the slow measurement speed, the SPA-LEED features a small fluorescent screen for conventional LEED usage.

4.2 EELS-LEED

The other main device for investigations is the electron energy loss spectrometer in low energy electron diffraction with short form EELS-LEED, also given in Fig. 4.3. This device allows the investigation of inelastically scattered electrons for a given scattering condition by adding an energy resolving part to the typical setup of a SPA-LEED. The device was also developed in the Henzler group at the University of Hannover [87] with both a high energy and momentum resolution.

The excitation of the electrons is done by a tungsten filament. During this thesis the tungsten filament was exchanged to a LaB₆-cathode enhancing the electron yield for every given energy resolution. The generated free electrons are now accelerated by a lens system that focuses the resulting beam into the electron monochromator. This apparatus is a well-known 127.8° cylinder capacitor whose resolution is approximately given by the pass energy E_{pass} via [64]

$$\frac{\Delta E}{E_{\text{pass}}} = \frac{s}{r_0} + 0.4\alpha^2, \quad E_{\text{pass}} = \frac{\Delta U e}{2 \ln(R/r)}. \quad (4.1)$$

In these correlations $s = 0.3 \text{ mm}$ is the slit width, $r_0 = 35 \text{ mm}$ is the radius of the center path, R and r

are the radii of the outer and inner capacitor plates with $R/r \approx 1.4$, α is the maximum angle between the central path and the outmost electron trajectory, and ΔU is the difference in voltage between the two plates.

After the monochromator the electrons are accelerated to U_{acc} . In contrast to the SPA-LEED where the electrons are accelerated from a negative potential to ground, the whole octupole unit and also the sample are lifted on U_{acc} . The definition of the momentum k is possible by taking a LEED pattern, as described in the section above. The LEED part has a resolution of 0.01 \AA^{-1} .

The backscattered electrons will be decelerated symmetrically to the acceleration unit to allow the same energy resolution in the analyzer. This analyzer is the same type as the monochromator using the same parameters for ΔU . During most of the measurements ΔU was set to 0.7V giving an energy resolution of around 8 meV with the above parameters. However, the elastic peak resulted in a widths of around 20 meV most likely due to the electronic surface states of the investigated systems [87, 89]. Finally, the detection of electrons is realized by a channeltron analogously to the SPA-LEED setup.

To obtain information of the inelastically scattered electrons, the complete deceleration unit's voltage is tuned down to allow the slower electrons to pass this stage. This implementation will lead to a loss energy scan of a given point in reciprocal space. The EELS-LEED is controlled via an in-house computer software.

The usage with only low voltages of around 20V to 40V makes it susceptible to magnetic and electric fields. As a consequence, the whole device is put into a shielding of mu-metal that leads to a residual magnetic flux density below $7 \mu\text{T}$ [90].

4.3 Gold Evaporator

The evaporator of this work is one of the simplest versions possible, see also Fig. 4.4 It consists of a gold pearl of approximately 2 mm diameter that has been melted onto a tungsten wire. Applying direct current to this wire will results in a heat transfer to the pearl. It is possible to tune the evaporation rates in the range of ML/min with an uncertainty of $< 10\%$. As the total amount of gold is small, it cannot be used to grow thick layers.

The whole device is put into a cylindrically symmetrical water cooled copper base to prevent the resulting heat to deteriorate the vacuum. It is hosted on a CF-35 flange delimiting its lateral dimensions. By the opening and closing of a shutter, the exact time of evaporation is controlled. To know the amount of Au evaporated, two redundant quartz crystal oscillators are installed on the top plate. The relation

$$\Delta f = \frac{\rho_{\square} \times f_Q^2}{\rho_Q \times N_Q} \quad (4.2)$$

derived from the calculations for quartz microbalances of Ref. [91] allows the exact determination of the coverage by an oscillator at sample position. In this equation, ρ_{\square} is the additional density per area,

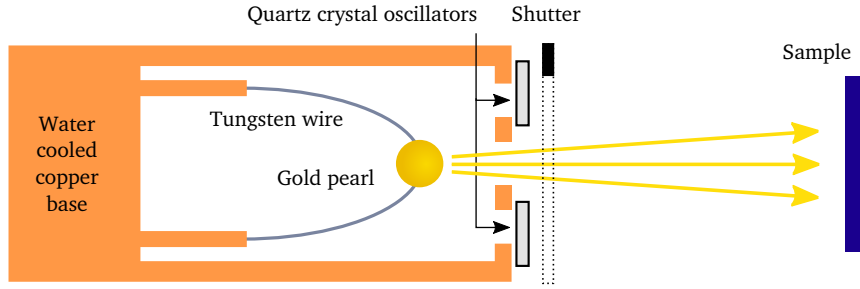


Figure 4.4: Sketch of the Au evaporator used in this thesis: Evaporation is done via direct current heating of a tungsten wire hosting a melted gold pearl. The amount is monitored by quartz crystal oscillators acting as microbalances. Exact timing of exposure is made possible by a shutter in front of the aperture.

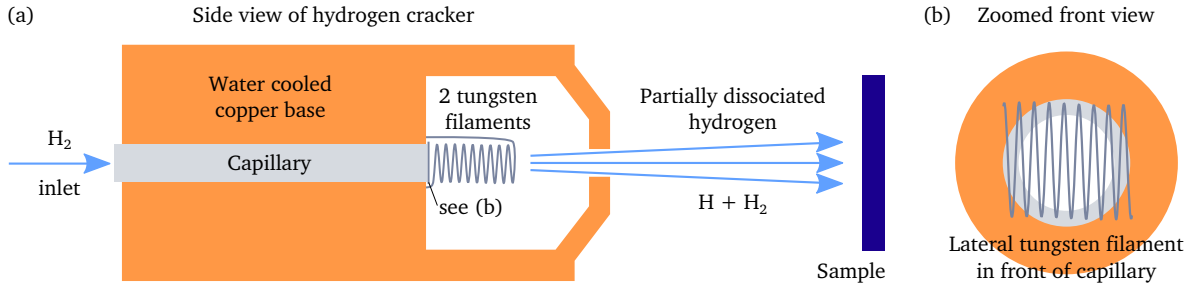


Figure 4.5: Sketch of the hydrogen cracker: (a) The side view shows the general setup of a capillary hosted on a water cooled copper base. The hydrogen is let in on the left side and will be partially dissociated by two filaments in front of the nozzle of the capillary. (b) The front view shows the alignment of the additional lateral tungsten filament.

$\rho_Q = 2.65 \text{ g/cm}^3$ the density of the quartz, $f_Q = 10 \text{ MHz}$ the ground frequency of the oscillator, and $N_Q = 1670 \text{ kHz mm}$ the eigenfrequency of the thickness shear mode for an AT-cut [92]. The sticking coefficient was estimated to unity as after an initial deposition the oscillator will be covered by a thin layer of Au, leading to a good adherence.

With according coverage densities for 1 ML of Au on Si(111) $\rho_{\square}^{\text{Si}} = 1.71 \times 10^{-7} \text{ g/cm}^2$ and on Ge(100) $\rho_{\square}^{\text{Ge}} = 2.04 \times 10^{-7} \text{ g/cm}^2$, the frequency changes at the sample position calculate to

$$\Delta f_{\text{Si}(111)} = 38.6 \text{ Hz} \quad (4.3)$$

$$\Delta f_{\text{Ge}(100)} = 46.1 \text{ Hz} \quad (4.4)$$

Calibrating the microbalances in the evaporator against the quartzes at sample position allowed an exact evaporation of Au onto the given samples.

4.4 Hydrogen Source

For the chemical desorption experiments of Chapter 8 atomic hydrogen was desired. Therefore, a simple dissociation source was built, inspired by the suggestions of Ref. [93]. A sketch is given in Fig. 4.5 (a) and (b). Also, this device is hosted on a CF-35 flange.

This so-called hydrogen cracker is mainly a tungsten capillary of 3 mm inner diameter that is placed inside of a water cooled copper base. A hydrogen minican is connected to the inlet via a fine control valve. At the nozzle of the capillary two tungsten filaments are placed. One is coiled in direction of the hydrogen flow, the other one is aligned along the cross section of the capillary as illustrated in Fig. 4.5 (b). These filaments are enclosed into the copper base to prevent the heat of the filaments to deteriorate the vacuum conditions during the adsorption of hydrogen. The partially dissociated hydrogen can only exit through a small aperture in the very front of the device.

The efficiency was not exactly determined, but can be approximated to 5-10% for 2000 °C as derived for a similar setup in Ref. [94].

Part II:

Gold-Induced Wires on Si(hhk)

5

A Golden Playground on Vicinal Silicon Surfaces

This chapter will give a short overview of the four surface orientations of silicon with their appropriate gold coverages as used in this work. The first section provides information about the structure of the bare Si and its surface, whereas the second part summarizes the surface reconstructions that appear when adding gold. The last section of this chapter outlines the discrepancies in the electronic structure of various publications.

5.1 The System Si(hhk)

This part of the thesis were carried out on silicon substrates. Their bulk orders in a diamond lattice with a lattice constant of $a_{\text{Si}} = 5.43 \text{ \AA}$. Due to its importance for the industry, the Si crystal itself is one the best-known structures, supported by its relative standard uncertainty of only 1.6×10^{-8} of the lattice constant¹. The indirect band gap of silicon is 1.1 eV, the direct one is larger with 3.5 eV.

As the experiments were carried out on surfaces, their structure is of importance. Miller-indices describe the cutting direction of the surface. Well-known is the Si(111)-surface. It shows a non-planar hexagonal unit cell with a surface lattice vector of 3.84 \AA , see also Fig. 5.1. The bare Si(111) surface features a 7×7 reconstruction at room temperature that has long been debated [95].

¹<http://physics.nist.gov/cuu>

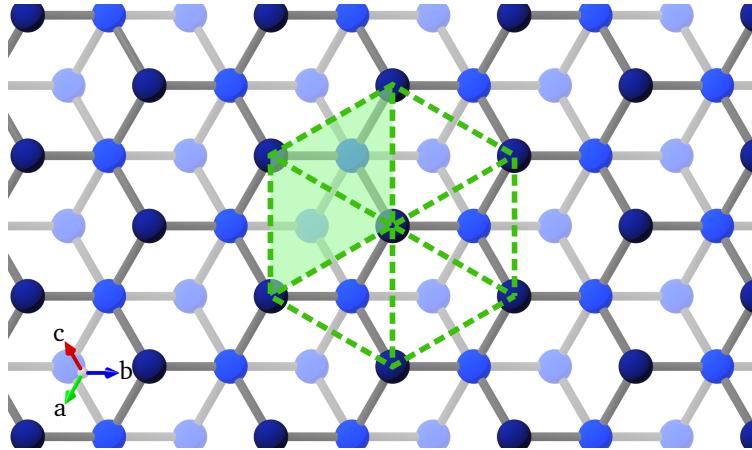


Figure 5.1: Unreconstructed Si(111) surface with surface unit cell in light green. The blue silicon atoms fade in color with increasing depth and show a hexagonal arrangement depicted in dashed green.

When cutting a bulk crystal not exactly to a $[111]$ surface but slightly changing the angle towards the (001) or (110) plane, then, for certain orientations, a regular arrangement of (111) terraces with separation by steps of single atomic height is possible. This arrangement is a direct result of the fact that it is only possible to remove integer values of atoms.

Fig. 5.2 illustrates the four directions used in this thesis showing a side view of the simplest resulting terrace distribution for these so-called vicinal surfaces. An angle toward the (001) plane will be referred to as positive inclination in this thesis, and an angle toward the (110) orientation will be called negative inclination. Their angles will, therefore, have the corresponding algebraic sign. The values are listed in Tab. 5.1.

However, a bare vicinal silicon surface not necessarily arranges in this depicted way. Surfaces also decay into terraces of other orientations that have a lower free surface energy. Terraces of (111) orientation are rather stable. Therefore, the surface will try to maximize their size. As a consequence, step-bunching will occur. These bunched steps will then refacet into other stable orientations. This

System	Angle	Terrace width	Au coverage
Si(335)	+14.4°	$(3 + 2/3)a_{\perp}$	0.27 ML
Si(557)	+9.5°	$(5 + 2/3)a_{\perp}$	0.18 ML
Si(553)	-12.5°	$(4 + 1/3)a_{\perp}$	0.48 ML
Si(775)	-8.5°	$(6 + 1/3)a_{\perp}$	0.32 ML

Table 5.1: Miscut angles and resulting terrace widths in multiples of the Si-row distance in $[11\bar{2}]$ -direction $a_{\perp} = 3.32\text{\AA}$ for the ideal reconstruction of vicinal silicon surfaces as depicted in Fig. 5.2. The Au coverage is the amount necessary for the growth of a gold-induced wire superstructure on the terraces, see Section 5.2. The background coloring scheme of the system will be used throughout the Si(hhk)-Au chapters for enhanced presentation.

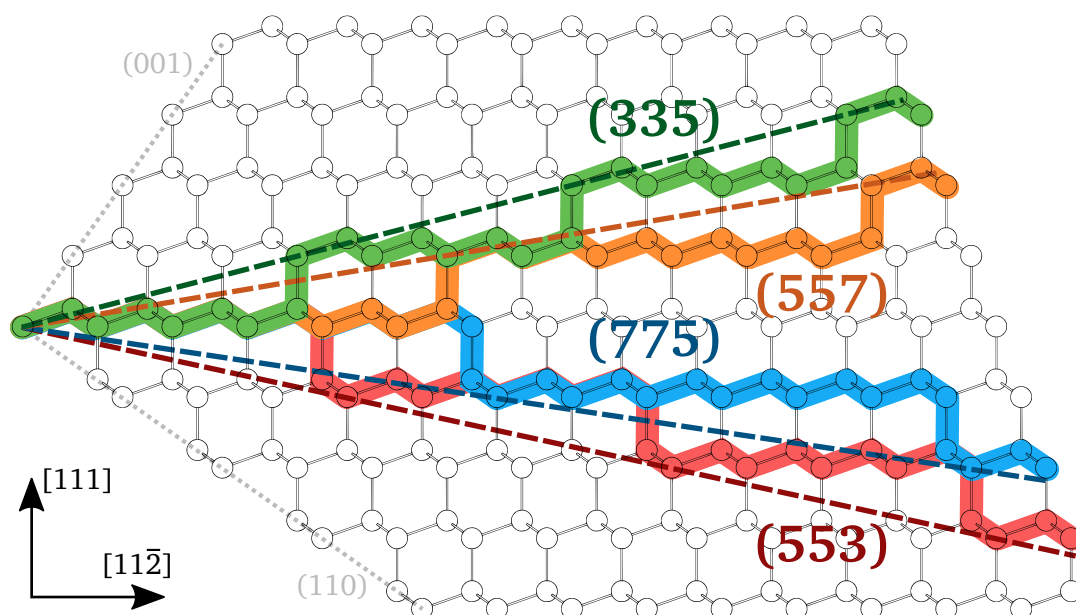


Figure 5.2: Side view illustration of Si(hhk): The systems used in this thesis are marked by the colored lines. The cutting angles with respect to the Si(111) surface are described by the dashed lines of the same color.

stability is, e.g., given for the $(\bar{1}12)$ orientation as it is the preferred step height boundary for epitaxial growth [96]. Investigations on the bare Si(557) found the separation of large (111) terraces of 5.7 nm by either a triple step of (112) [97, 98, 99] or (113) orientation [100]. The bare Si(553) surface, in contrast, facets into (111) terraces of 2.8 nm width, separated by simple double steps [101]. A work of Baski et al. [102] covering all angles from (111) to (001) discovered a growth of 7×7 reconstructed (111) terraces up to the (223) direction, i.e. $+11.4^\circ$ within the given notation, that are mainly separated by triple and single steps. Above this region and below 24.2° , 7×7 reconstructed unit-cell-wide nanofacets alternate with (5 5 12) planes.

It turned out during this thesis that the quality of the bare substrate was not crucial for the preparation. Conclusively, the Au adsorption process decreases the surface energy strongly enough such that it leads to a healing effect on the surface. The main issue was to avoid a refaceting into extended 7×7 reconstructed terraces for optimized initial growth conditions.

5.2 Structural Resemblances in Si(hhk)-Au

After the discovery of the Au surface reconstruction on the most stable Si(557) surface [36], soon other vicinal Si(hhk) surfaces with similar structures were found after the adsorption of the corresponding amount of gold, as listed in Tab. 5.1. In these cases and for all the investigated systems, they form

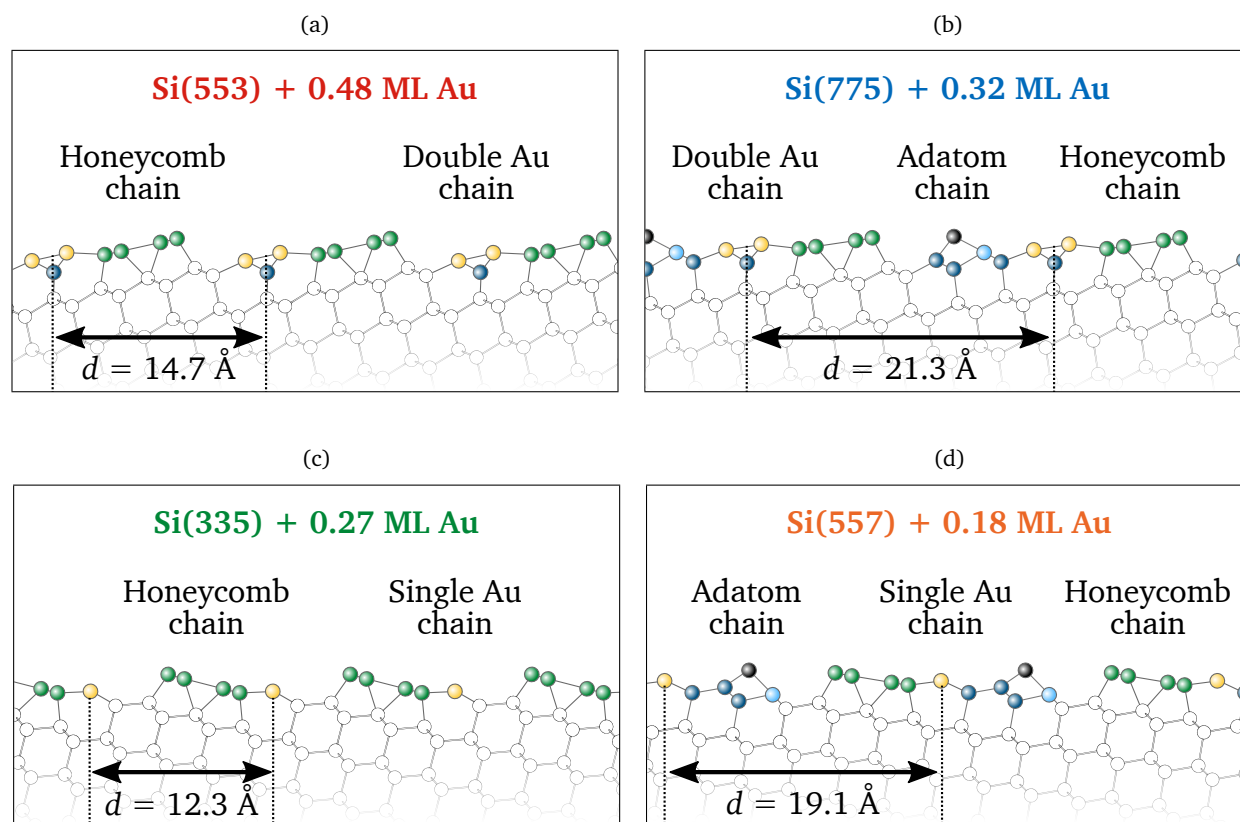


Figure 5.3: Side views of structural models: (a) Si(553)-Au with a double gold chain (yellow balls), (b) Si(775)-Au with a double gold chain and an adatom chain, (black balls) (c) Si(335)-Au with a single gold gold chain, (d) Si(557)-Au with a single gold chain and an adatom chain. All systems feature a honeycomb step edge (green balls).

the narrowest possible (111) oriented terrace separated by single steps, as one would assume from the sketch in Fig. 5.2. The terrace itself rearranges to a structure that now contains a gold wire. The step edge reorganizes into a silicon honeycomb or silicene chain. This was already suggested in early structural models [103], see also Fig. 5.6 for the Si(553)-Au models [104]. These reconstructions are depicted for all surfaces in a side view in Fig. 5.3. In the following, the structures of each system will be discussed in more detail.

5.2.1 Si(553)-Au – Double Gold Chain

For the Si(553)-Au surface, a coverage of 0.48ML is needed. The control of such small coverages is not easy, and STM does not resolve atoms but electronic states in combination with topography. As a consequence the coverage was first underestimated and, therefore, a chain of single atomic width on the mini (111) terrace was assumed [105, 106, 107, 103, 108, 109]. An exact experimental determination of the coverage, X-ray investigations [110], and ab-initio studies led to the now established model of a

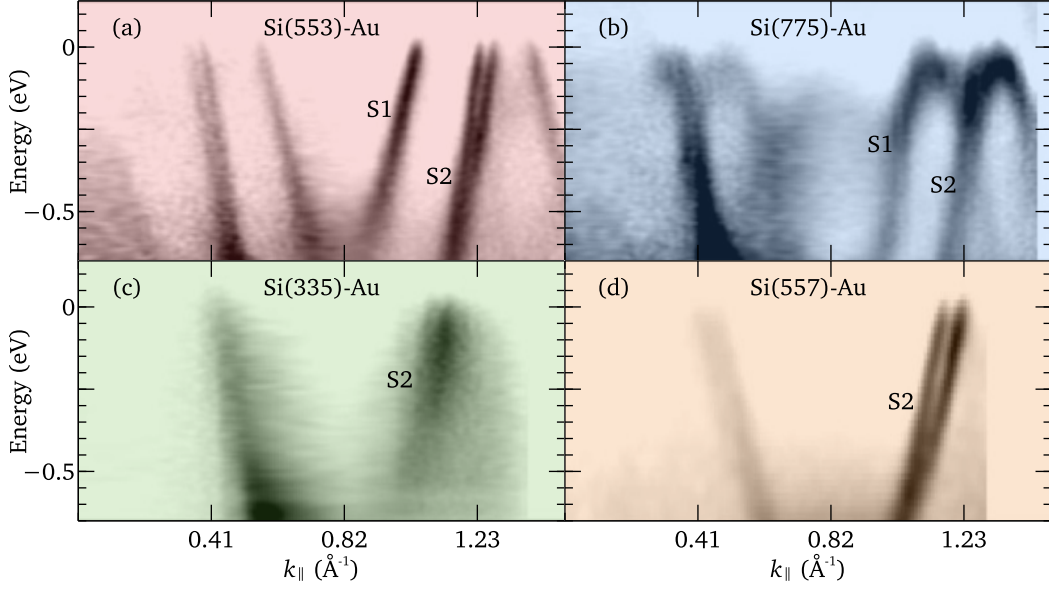


Figure 5.4: ARPES data for the four Si(hhk)-Au systems from Ref. [103] tinted in the coloring scheme of Tab. 5.1: The Si(553)-Au (a) and Si(775)-Au (b) systems show two dispersing bands (S1 and S2), whereas the Si(335)-Au (c) and the Si(557)-Au (d) only feature one (S2). The S2 states are Rashba-split. Numerical electronic band structure calculations yield further hybridization with bands of the honeycomb chain at the step edge that is not visible in ARPES, see Section 5.3 and Chapter 7. The direction of k_{\parallel} is given in Fig. 5.5.

double atomic row [111, 112], as depicted by the yellow gold atoms in Fig. 5.3 (a). This double row is an effect of the reduction of strain on the surface due to the bonding situation of the silicene chain in contrast to the other cutting direction. The Si honeycomb chain itself is sketched by the green balls. A $\times 2$ superstructure along the gold wire is present due to a dimerization along the chain as depicted in Fig. 5.6. The periodicity and also the interwire distance are specified by the terrace width of $4\frac{1}{3}a_{\perp}$ with $a_{\perp} = 3.32\text{\AA}$ as the Si-row distance in $[11\bar{2}]$ -direction and the inclination of -12.5° , and result to 14.7\AA .

This double atomic gold row is able to qualitatively explain the existence of two Au-induced bands S1 and S2, as observed in angle-resolved photoemission spectroscopy (ARPES) [113, 103, 114] and shown in Fig. 5.4 (a). Due to the $\times 2$ periodicity ($\Gamma' = 0.82\text{\AA}^{-1}$) the filling level of S1 is around $1/3$, of S2 around $1/2$. Those bands are the bonding and antibonding state of the two gold chains involved. Their effective masses are $m_{S1}^* = 0.3m_e$ and $m_{S2}^* = 0.6m_e$. An additional splitting of the S2 band is attributed to a one-dimensional Rashba-splitting [115].

For temperatures below $\approx 100\text{ K}$ a phase transition to a $\times 3$ superstructure takes place. Spin-dependent numerics resulted in a model of spin-polarized electronic states at the step edge atoms [111, 116] and were able to explain the $\times 3$ superstructure observed in STM measurements at 77 K [117]. This $\times 3$ ordering is not a Peierls distortion that changes the distances between atoms. It only leads to an increased

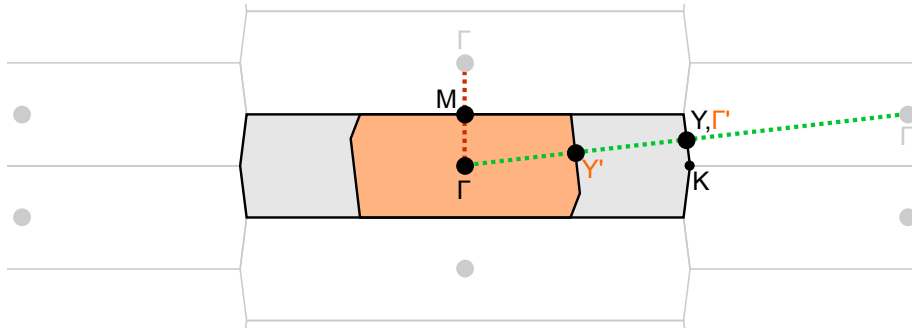


Figure 5.5: Brillouin zone (gray) and reduced $\times 2$ Brillouin zone (orange) for all Si(hhk)-Au with denoted symmetry points. The distance Γ -M- Γ (red dotted line) corresponds to the step train spacing $2\pi/d$. ARPES measurements as well as the numerically derived band structures used in Chapter 7 were carried out along Γ -Y- Γ direction (dotted green lines). Y is the new zone boundary for the $\times 2$ reconstructed surface.

density of unoccupied states on every third step edge atom. Furthermore, this ordering of the empty states is highly sensitive to the current during an STM investigation [118]. A more careful investigation of the order of these states by LEED [119] suggests the system to be a spin-liquid. This result means that there are no magnetic ordering and also no $\times 6$ superstructure present in the system as it was suggested before [111, 117]. Above the phase transition temperature these spins fluctuate and only a $\times 2$ reconstruction will be seen. Moreover a transition from $\times 2$ to $\times 1$ is predicted in the Au-chain².

Calculated band structures for the Si(553)-Au system show strong hybridization of states from the Si honeycomb chain with those from the gold chain [111, 120, 121]. This behavior cannot be seen easily in photoemission [113, 103, 115, 104] and will be discussed in more detail in section 5.3.

As a sample cannot be perfect, defects will be present on the surface. Intrinsically, cut-offs in the wire structure are present leading to a limited length of the quasi-one-dimensional wires. Additionally, the dissociation of water into OH and H on the silicon surface leads dominantly to an insulating defect that appears dark in STM [122, 109]. Defects also have an influence on the temperature of the phase transition. Furthermore, defects lead to pinning of the low temperature $\times 2$ and $\times 3$ reconstructions [123, 124], increasing the overall transition temperature.

Excess gold on the surface gives the possibility of doping the system by leading to a downshift of the S1 band [125]. A proposal for the protection from degradation to make it accessible outside UHV conditions is to coat it by a layer of graphene [126].

Apart from the structure described, on Si(553) it is possible to grow a structure with only 40% of the gold amount adsorbed before, i.e. 0.19 ML [104]. This procedure then results in the so-called low coverage phase or low coverage wires (LCW), as depicted in Fig. 5.6 (b). In this phase, only every second terrace is built up like the terraces of the high-coverage phase or high-coverage wires (HCW), separated by an intermitting empty terrace of $5\frac{1}{3}a_{\perp}$ width. It features a $\times 5$ superstructure along the terrace

²Current work of Frederik Edler et al.

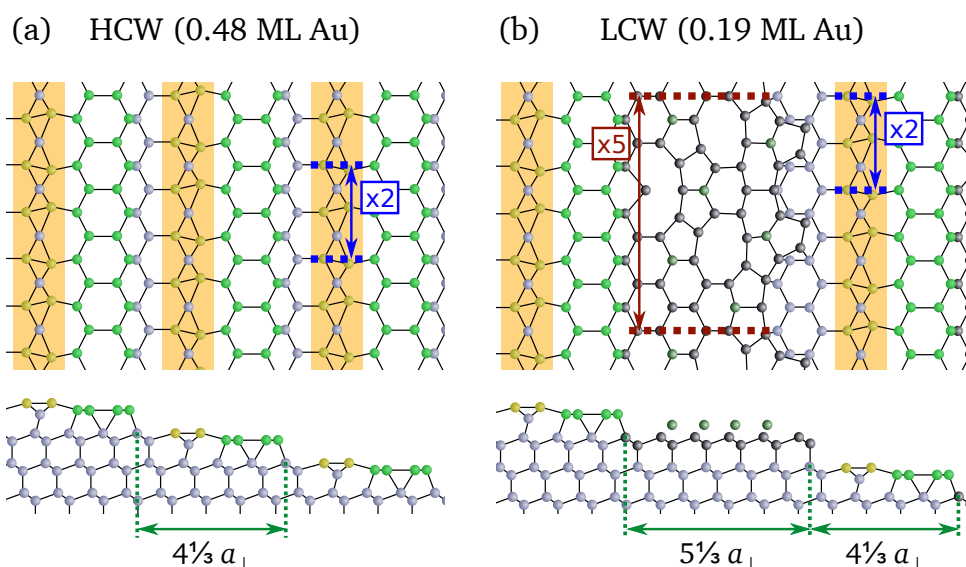


Figure 5.6: Simplified stick and ball models of Si(553)-Au HCW (left) and Si(553)-Au LCW (right). The HCW phase hosts $4\frac{1}{3}a_{\perp}$ terraces with a double atomic gold chain (yellow balls) with slight tilting that leads to a $\times 2$ reconstruction and a hexagonally arranged Si edge atom row (green balls). On the LCW phase, there is an additional $5\frac{1}{3}a_{\perp}$ terrace hosting a $\times 5$ superstructure (dark steel blue) with some atoms sticking out (dark green) as proposed by Song et al. [104]. The side view only indicates the lateral positions of these prominent atoms. Unreconstructed atoms are depicted in steel blue. The $\times 2$ and $\times 5$ reconstructions are also observed in LEED, see Chapter 6.

and is not margined by a honeycomb chain but rather by protrusions as a result of its superstructure. The periodicity perpendicular to the terraces is given by the sum of the two terraces that also lead to another angle of -11° as the correct miscut direction is (11 11 7). The resulting interwire distance is 32.7 \AA . Although the structure features an additional terrace, photoemission shows almost no difference in the electronic bands. Solely, the S1 band shifts down by 200 meV. This resemblance makes the two systems a perfect couple for the investigation of effects that are strongly depending on the interwire distance, such as plasmons.

5.2.2 Si(775)-Au – Double Gold Chain and Adatom Chain

The formation of the Si(775)-Au system is possible by the adsorption of 0.32 ML of Au. It was already found to be a stable facet on miscut (111) samples and therefore assumed to form a low energy reconstruction [127, 128]. The coverage was first considered to be 0.25 ML [103], corresponding to 1.5 atoms per unit cell. Coverage dependent investigations of a Bachelor's thesis [129] running at the same time as this work found superior LEED patterns for a coverage of 0.32 ML, accompanied by plasmon signals that turned out to be more robust over time. These results were attributed to a lower concentration of

vacancy type defects on the whole surface leading to smaller reactivity with residual gas molecules.

In contrast to the Si(553)-Au system, the surface features an additional adatom chain between the step edge and the double gold chain, as depicted by the blue and black atoms in Fig. 5.3 (b). This adatom chain also exhibits a period doubling along the terrace. The black adatom is protruding only at every second unit cell, whereas the light blue restatom is lowered at every second unit cell. Apart from this additional structural element, from a structural point of view, Si(775)-Au is very similar to the Si(553)-Au. Its period along the steps is given by the terrace width of $6\frac{1}{3}a_{\perp}$ and its inclination of -8.5° result in a periodicity of $d = 21.3 \text{ \AA}$. However, though sharing almost the same structure, neither an ordered nor an unordered spin polarization at the step edge was found so far [130].

In addition, ARPES measurements also observe similarities, see Fig. 5.4 (b). In comparison to the Si(553)-Au system, the bands of Si(775)-Au are shifted downward in energy by roughly 250 meV with an apparent back-folding below the Fermi level. The resulting full bands mean an insulating behavior that plasmon spectroscopy does not confirm, see Chapter 7 or Ref. [131]. Band structure calculations carried out in Ref. [132] were not able to reproduce this behavior, but show hybridizations of the states induced by the structural elements present on the surface.

5.2.3 Si(335)-Au – Single Gold Chain

Upon adsorption of 0.27 ML of Au on the Si(335) surface, the Si(335)-Au system emerges. It is the simplest of the systems with a gold chain of just single atomic width next to the Si honeycomb ribbon on every terrace, as shown by the yellow balls in Fig. 5.3 (c). Its terrace width of $3\frac{2}{3}a_{\perp}$ and angle of 14.4° lead to a periodicity of 12.3 \AA . Due to only a single atomic chain, only one almost completely filled band is visible in photoemission [103, 133] with an effective mass of $m_{S_2}^* = 0.4m_e$, see Fig. 5.4 (c). Numerical calculations also predict a spin-orbit splitting in this band [134]. However, these calculations also give a strong hybridization that photoemission does not show.

Investigations about the mobility of atoms on top of this structure predict a substantial anisotropic movement with its easy direction along the terraces [135]. The material transport is of importance for the annealing step during the sample preparation. As the hopping barriers along the steps are much higher than for the Si(553)-Au system, in comparison, a lower overall quality is expected.

5.2.4 Si(557)-Au – Single Gold Chain and Adatom Chain

The Si(557)-Au forms after adsorption of 0.18 ML of Au on Si(557). Similar to the systematics of the systems with negative inclination, the Si(557)-Au adds an adatom chain to the terrace positioned between the step and the gold chain [136, 137] as depicted by the black and blue balls in Fig. 5.3 (d). Due to its structure with an angle of 9.5° and terrace width of $5\frac{2}{3}a_{\perp}$ a periodicity of 19.1 \AA arises.

Having simply one Au chain like Si(335)-Au, only one band with spin-orbit splitting is seen for Si(557)-Au with an effective mass of $m_{S_2}^* = 0.6m_e$. It is almost entirely filled as for the other sys-

tems [103, 133]. Also in Si(557)-Au, electronic band structure calculations predict a hybridization with the Si honeycomb chain as well as the adatom chain states [137, 138, 121]. Electron energy loss spectroscopy has already been carried out [139]. Its dispersion is described by a quasi-free electron gas behavior when taking into account exchange-correlation effects, see Eq. 3.13.

Temperature dependent STM and STS investigations showed a metal-insulator transition in the honeycomb chain that is explained by a freezing of an up-down buckling along the step edge [140, 141]. This thermally activated state leads to a change of the band edge positions for elevated temperatures.

Defects play a significant role in the Si(557)-Au system. There are various adsorption and defect sites on the surface: Dissociated water will bond to the step-edge dangling bonds with high probability [109]. A major defect is also the dislocation or a stacking fault on the adatom chain. Oxygen adsorption experiments showed a change in the electronic anisotropy in transport revealing two favorable adsorption sites: The step edge and the adatom chain. Furthermore, coverage dependent investigations found a refacetting to superstructures of gold covered Si(111), Si(112), and Si(335) parts when not providing the correct amount of Au [142].

5.3 Discrepancy between Photoemission Data and Electronic Band Structure Calculations

As pointed out before, there is a strong discrepancy between the electronic band structure measured in ARPES when compared to the numerical band calculations. On the one hand, the general slope of the gold-induced bands is often shifted in k or E , see, e.g., Fig. 7.7 when comparing the experimental data from Ref. [103] with the calculations of Ref.[121]. However, this just needs some careful inspection of the structural model used and the preparation conditions given.

On the other hand, there are band gaps involved that are not seen in photoemission. When computing strictly in $\times 2$ geometry, a band gap is seen at the Fermi level in the Si(553)-Au system. As the plasmon measurements are carried out at RT, there must be a difference to the 0K band structure. A metal-insulator phase transition is in this case inevitable.

Furthermore, there is always a hybridization of the gold-induced states with those of the step edges in the calculations. A sketch of this effect is given in Fig. 5.7. However, such behavior is not seen in photoemission, though an attempt to see those states for the low coverage phase of Si(553)-Au has been carried out in Ref. [104] by a careful analysis of the ARPES intensities. A possible explanation is given in Ref. [111] as follows: There is a polarized and an unpolarized state of this step edge band. Due to thermal fluctuations, the system constantly flips between those two states making it impossible to resolve them. On the other hand, this should not be the case for the low temperatures used in most of the photoemission experiments [103, 104].

Another explanation is the bad energy resolution of the experiments of Ref. [103], cf. Fig. 5.4. In contrast, in the data of Barke et al. [115], small energy gaps in the electronic states around the Fermi-

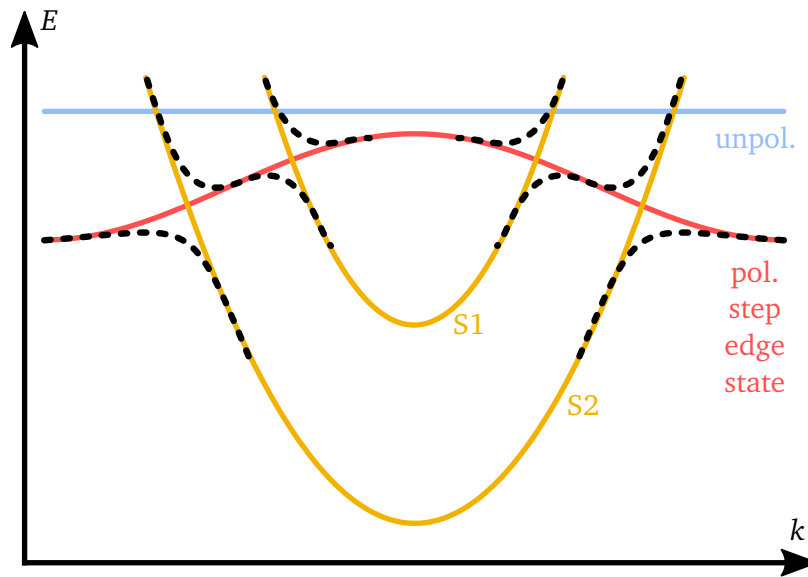


Figure 5.7: Sketch of the hybridization of the gold chain-induced electronic bands (yellow) with the polarized step edge state of the honeycomb chain (red): The resulting dispersion is given by the dashed lines. The polarized state can thermally be excited into an unpolarized more localized edge state (blue). In the real systems, the Fermi level is located in the vicinity of the red and blue bands.

level are resolvable with synchrotron radiation at a photon energy of 34 eV. In their publication, they mention a resolution of 15 meV for photons and 20 meV for electrons. This may be sufficient for the resolution of the unseen band-gaps mentioned above.

In addition, taking into account matrix element effects, the step edge bands may become invisible for ARPES. However, with a further fine-tuning of the excitation conditions as it must have been carried out in Ref. [115], it might be possible to see those states. Therefore, it is highly recommended to carry out new APRES measurements for all Si(hhk)-Au. Anyway, it must be remarked that this problem of not seeing the whole band structure in ARPES is existent. Hence, a careful usage of such data is advised.

All these considerations do not take into account an influence of the uncertainty in momentum by these photoemission excitations. Here, an important parameter is the local excitation that leads to a short informational exchange range. In other words, on the surface only leads to a coherent excitation of an outgoing electron wave within a radius of several atoms. Therefore, also the definition of the momentum is poor. Accordingly, for a steep dispersion, an additionally deteriorated energy resolution occurs that, finally, leads to a blurred information about the electronic band structure.

As will be seen in Chapter 7, the hybridization of the gold-induced states with the step edge states is necessary for a reasonable description of the collective excitations in all the systems.

6

Structural Properties of Si(hhk)-Au

This chapter gives an overview of the preparation of the desired wire structures and their resulting LEED patterns. The end of this paragraph estimates the quality of the samples by an energy dependent spot profile analysis.

6.1 Sample Preparation

Both LEED and EELS are methods averaging information from the entire surface irradiated by the electron beam spot. Therefore, in contrast to local methods like STM, care has to be taken to obtain homogeneous surface structures. Fortunately, the removal of the oxide layer [143, 144], preparation of pristine Si surfaces [102, 145, 97, 146, 147], as well as the formation of Au-reconstructed superstructures¹ [103] are well-known.

There are two standard methods to clean a Si surface: etching with chemicals as it also seems necessary for germanium, cf. Chapter 10, and thermal desorption of the native oxide by subsequent rapid annealing to a temperature slightly below the melting point at 1410 °C. In this thesis, the second option was chosen.

The experiments are carried out on Czochralski-grown wafers from Crystek in Berlin. They have an n-doping with phosphorus, leading to a resistance of around 0.1 Ω cm at RT. From a circular 2 in (≈ 5 cm) geometry they were cut to rectangular samples of 15 mm × 5 mm size with an in-house diamond saw.

¹Every article about any Si(hhk)-Au system contains a similar recipe for the growth of the Au-induced wire structure.

The vicinal steps were aligned along the longer side of the wafer allowing the electric current to flow parallel to these steps for DC heating. This layout circumvents possible step bunching due to surface electromigration.

Before the loading to vacuum, the samples were cleaned in ultrasonic baths of petroleum-benzene, acetone, and isopropanol for 10 min each for the removal of water and grease from previous processing. In-situ, the samples were degassed by steadily increasing the temperature up to 600 °C, a region moderate enough to keep the oxide layer unharmed. This oxide layer acts as a shield to protect the topmost layers from contamination. When reaching a pressure below 5×10^{-11} mbar, rapid annealing of only a few seconds to ≈ 1250 °C was carried out while keeping the pressure below 5×10^{-9} mbar. Immediately after this, a rapid cool-down period followed by turning off the heating current. This procedure leads to the desorption of the oxide layer as well as several top layers of the silicon substrate resulting in a clean and flat pristine surface.

The Au-induced superstructure was grown by evaporation of the corresponding submonolayer amount for each system at a rate of 0.15 ML/min and with the sample at 630 °C. This temperature is high enough to strongly decrease the oxidation, hydroxylation and hydrogenation probabilities and to increase the mobility of Au on the surface while still being too low for its desorption. Tab. 5.1 shows the amounts of Au needed. After a cool-down time of around 10 min, the sample was rapidly annealed at 930 °C for < 1 s. This so-called post-annealing step removes a slight overshoot in coverage and also improves the order in the superstructure. However, for the low coverage phase on Si(553), the LEED image deteriorates after post-annealing, resulting in a less sharp step train. Therefore, this last step was left out for the Si(553)-Au LCW system.

6.2 Surface Properties Probed by Electron Diffraction

After the described preparation steps, all samples showed a LEED image with a reconstruction consisting of a so-called step train. This row of dense spots in reciprocal space originates from the sequence of equally spaced step edges and, therefore, the formation of terraces. All LEED images are taken at room temperature (RT).

To begin with, Fig. 6.1 shows the resulting LEED patterns for Si(553)-Au for the high coverage phase as well as for Si(775)-Au. These two surface orientations have a negative inclination with respect to the $[11\bar{2}]$ -direction as defined in the last chapter. The two images demonstrate the close structural similarities between the systems. as already mentioned in Chapter 5. Fig. 6.1(a) and (b) are characteristic for regularly stepped Si(553) and (775) surfaces consisting of (111)-oriented terraces. These terraces are separated by steps of double atomic height $h_{\text{Si-step}} = 3.14 \text{ \AA}$, as also shown in the simple sketch in Fig. 5.6. The spot splitting of 22 % surface Brillouin zone (100 % SBZ = $b_{\text{Si}(111)} = 1.89 \text{ \AA}^{-1}$) along the step train for Si(553) computes to the periodicity arising from a tilted array of terraces with a distance

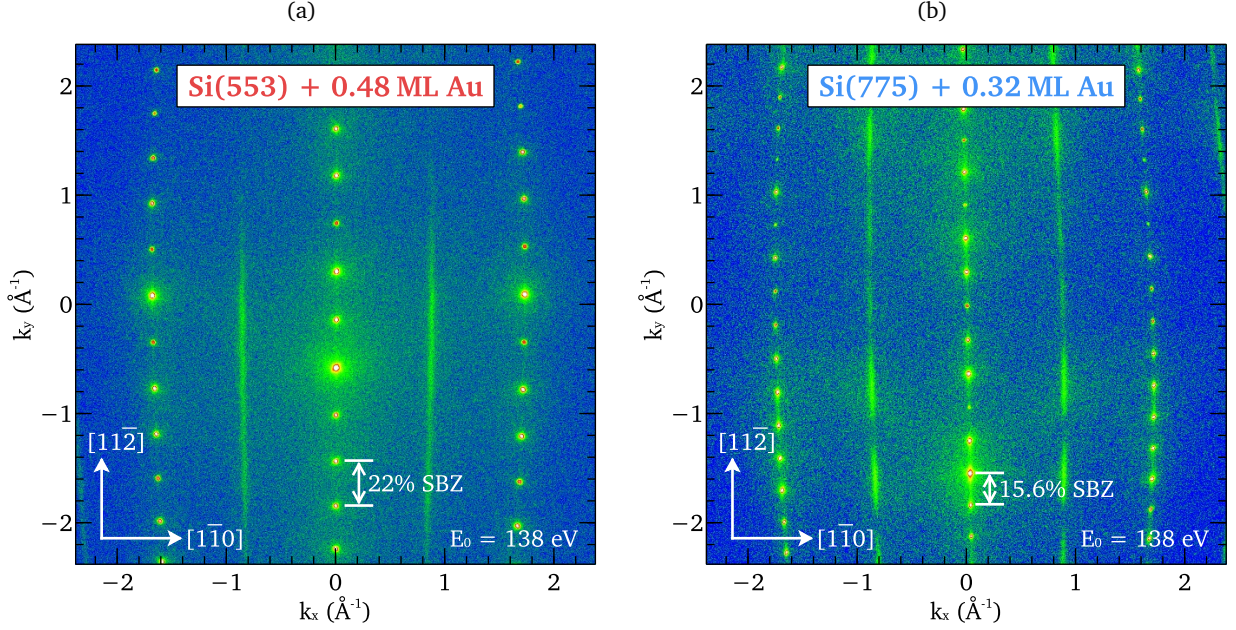


Figure 6.1: LEED patterns of the Au-adsorbed Si(553) (a) and Si(775) (b) surfaces: (a) Si(553)-Au: The distance of step train spots leads to a periodicity of 14.7 \AA , the $\times 2$ -streak can be attributed to a double chain of Au atoms with a period doubling along their extent. (b) Si(775)-Au: Step train distances give a periodicity of 21.3 \AA , a modulation in $\times 2$ streaks gives an indication of the existence of a Si-atom chain.

of

$$4\frac{1}{3}a_{\perp} / \cos 12.5^{\circ} = 14.7 \text{ \AA}. \quad (6.1)$$

Here, $a_{\perp} = 3.32 \text{ \AA}$ is the Si-row distance in $[11\bar{2}]$ -direction. Equivalently, the splitting of 15.6% in the diffraction of Si(775) results in terraces with a width of

$$6\frac{1}{3}a_{\perp} / \cos 8.5^{\circ} = 21.3 \text{ \AA}. \quad (6.2)$$

From these numbers it is evident that the adsorption of the corresponding amount of Au leaves the ideal periodic arrangement untouched. This is also in accordance with STM measurements [117, 130].

The appearance of $\times 2$ streaks between the step-trains has its origin in the induced double Au-chains on each terrace with a period doubling along its direction. Along the terraces these streaks are sharp, indicating a good order. As there is no modulation in this streaks in the direction perpendicular to the wires, presumably only short-range correlations between the double periodicity on each terrace are present. For the Si(775)-Au system, the $\times 2$ is additionally resulting from a period doubled Si-atom chain. The reason for a slight modulation is a better correlation between these Si chains.

An exceptional case is the low coverage phase on Si(553). When only 40% of Au compared to the

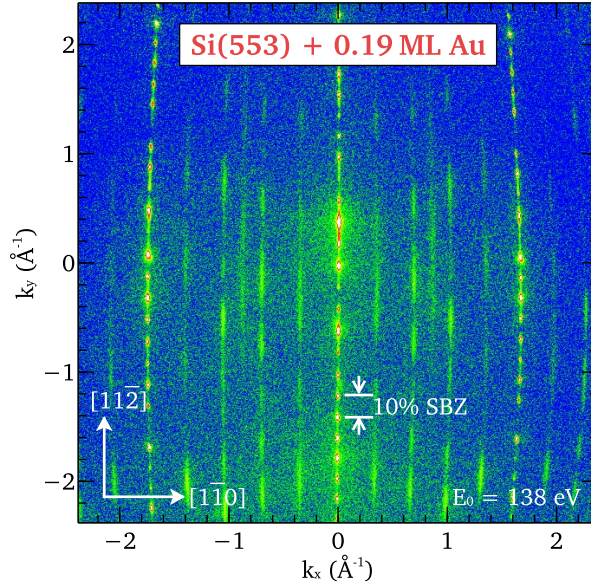


Figure 6.2: LEED pattern of the low coverage phase of Si(553)-Au: The step train distance leads to a periodicity of 32.7Å . The appearing $\times 5$ streaks originate in an additional terrace made of only Si. These terraces alternate with the standard Au-Si terraces of the high coverage phase that give the still present $\times 2$ streaks.

conventional preparation is adsorbed, the surface undergoes a surface reconstruction with additional LEED spots as shown in Fig. 6.2. Now a spot-splitting of 10% surface Brillouin zone is found. This periodicity is generated by the formation of a more complex structure composed of two terraces: One strongly resembles the terrace of the high coverage phase with a width of $4\frac{1}{3}$ surface units. The second terrace forms without any Au-induced reconstruction and a width of $5\frac{1}{3}a_{\perp}$. Summing up these two terraces, the 10% splitting has its roots in a much bigger reconstruction with a periodicity of

$$9\frac{2}{3}a_{\perp}/\cos 11.3^{\circ} = 32.7\text{Å}. \quad (6.3)$$

The second type of terrace also leads to the formation of a $\times 5$ modulation along its extension coming from the proposed reconstruction of Si atoms on an empty terrace of this kind. An additionally observable faint $\times 2$ streak originates from the Au chain that still features a period doubling. In conclusion, the recorded LEED pattern is in agreement with the structural model proposed by Song et al. [104]. Please note that this low coverage phase no longer fits perfectly on a (553)-cut Si substrate, as from their terrace widths it corresponds to a Si(11 11 7) having a smaller inclination by 1.2° . Therefore, this difference in miscut will be compensated by inevitably appearing step bunches. Concluding from these LEED data, there is a long-range periodic ordering of two alternating terrace types that leads to a large unit cell. Not only aligning locally but rather on the entire surface, this kind of self-assembly indicates a high terrace-terrace interaction.

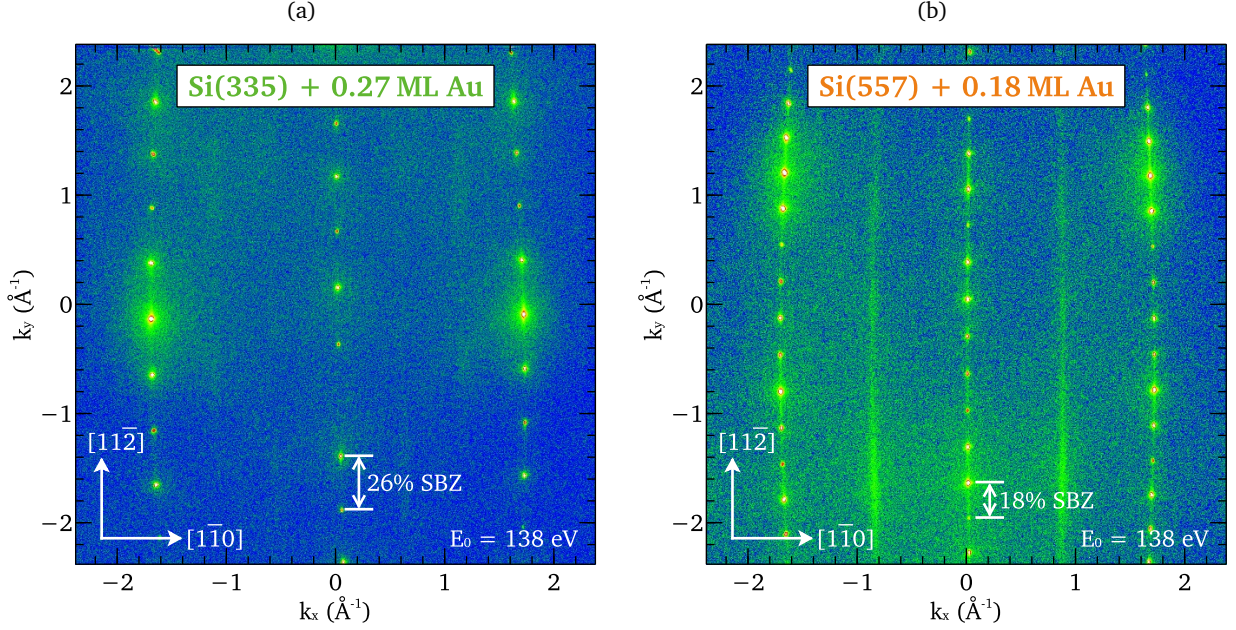


Figure 6.3: LEED patterns of Si(335)-Au (a) and Si(557)-Au (b): (a) Si(335)-Au: The step train gives a periodicity of 12.6 \AA , no period doubling can be seen. (b) Si(557)-Au: Here, a modulation of 19.1 \AA is obtained, the present $\times 2$ streaks give an indication of a period doubling in the adatom chain.

LEED patterns from samples of Si(335)-Au and Si(557)-Au are shown in Fig. 6.3. These systems have a positive inclination with respect to the $[11\bar{2}]$ -direction. The image from the Si(335)-Au system in (a) shows a splitting of 26 % surface Brillouin zone that arises from a periodicity which is

$$3\frac{2}{3}a_{\perp} / \cos 14.4^{\circ} = 12.6 \text{ \AA}. \quad (6.4)$$

Although the terrace size is similar to the Si(553)-Au system, the coverage needed for the formation is much lower. Only $0.27 \text{ ML} / 0.48 \text{ ML} = 56\%$ of the Au is needed here. When taking into account the inclination and exact terrace size, these numbers indicate the formation of a gold chain of only single atomic width. The lack of $\times 2$ streaks reveals that along the terraces none of the structural elements features a period doubling.

Another possibility for this absence is also a bad sample quality compared to the other systems. In Ref. [135] it is reported that diffusion of excess atoms on Si(335)-Au proceeds mainly along the chains. The calculated diffusion barriers for interchain hopping are higher than for Si(553)-Au. Therefore, using the same preparation parameters, the sample results less ordered. An increasing of the annealing temperature should improve the ordering. However, then already Au desorption sets in.

Fig. 6.3 (b) shows the structural character of the Si(557)-Au surface. The spot splitting here is 18 %

SBZ coming from

$$5\frac{2}{3}a_{\perp}/\cos 9.5^{\circ} = 19.1 \text{ \AA}. \quad (6.5)$$

Normalized to the terrace width and within the accuracy of $\approx 10\%$ the evaporator, only half the amount of gold of the Si(775)-Au system is necessary for the formation of the wire reconstruction. This half coverage is indicative of a single atomic Au chain on the terrace. Nevertheless, a $\times 2$ streak is visible here again, originating from a once more present Si adatom chain. Also in this case, the individual terraces do not show a correlation as seen by an only mild and washed-out modulation of the streak along the terraces. The sharpness of the streak in wire direction, however, indicates a strong order.

Finally, it is possible to draw some conclusions from the extracted information giving some systematics among this family of five investigated systems: On the wafers with positive inclination, i.e. towards (001), and after the adsorption of one gold atoms per unit cell, the formation of a gold chain of single atomic width takes place on a terrace with a width of $(n + \frac{2}{3})a_{\perp}$. A period doubling is seen for the Si(557)-Au system. For negative inclinations, i.e. toward (110) orientation, terraces are of width $(n + \frac{1}{3})a_{\perp}$. The induced Au chain is of double atomic width and features a period doubling. A long-range ordering is only present along the wires. Perpendicular to the wires, the streaks reveal no ordering. For the bigger terraces of Si(557)-Au and Si(775)-Au an adatom chain of Si occurs next to the Au chain. A slightly special case is the low coverage phase on Si(553)-Au which refacets into a Si(11 11 7) periodicity consisting of two different terraces. One of these terraces still behaves like the terrace seen on Si(553)-Au with high coverage and is always interlaced by an additional part of only Si. It allows for investigations in wire distance influences.

However, no direct information about the origin of the periodicities is available via LEED. It can only be obtained by comparison with STM and theoretical models.

6.3 Spot Profile Analysis of Si(553)-Au

For an estimation of the chain lengths and overall sample quality, an energy dependent LEED scan was carried out exemplarily for the Si(553)-Au sample. The quality of the bare Si(553) substrate was investigated in a Master's thesis [148] using a step and kink correlation derived in Ref. [149] after careful preparation as described above. The resulting variance of the terrace width $\sigma/\langle\Gamma\rangle = 0.5$ reveals a surface where approximately every second terrace is of different size. However, it turned out that the quality of the substrate itself was dispensable. Various preparations during this work showed that the adsorption of Au has a strong healing effect, i.e. also samples of even lower quality resulted in reconstructed surfaces that showed perfect LEED patterns. Though the substrate itself was of minor importance, an extremely careful preparation of the substrate was always carried out anyway.

These energy-dependent measurements of the Au reconstructed surface are given in Fig. 6.4. As the sample is highly anisotropic, those scans were carried out perpendicular to the wires to demonstrate

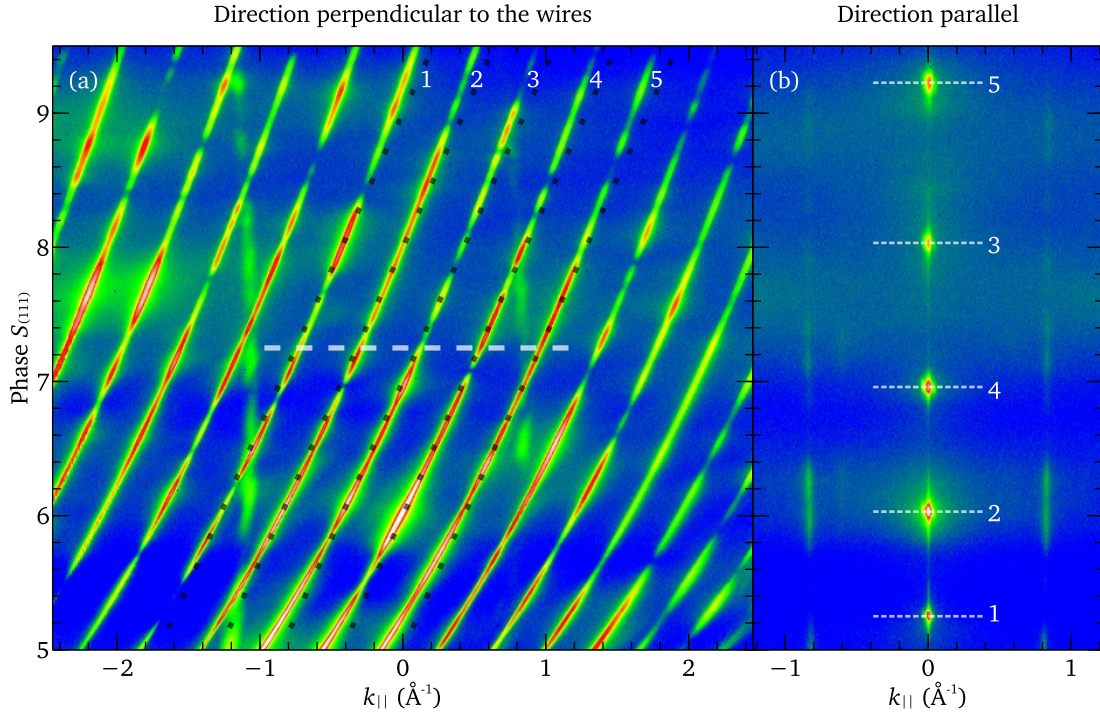


Figure 6.4: Energy dependent SPA-LEED scans for Si(553)-Au: (a) The direction perpendicular to the wires shows inclined Ewald rods, since the SPA-LEED was set to a (111) surface setup. The black dots indicate the slope expected for ideal conditions. The dashed white line indicates the direction of the extracted line scans. (b) Energy dependent scan in the direction parallel to the wires. Dashed lines indicate conducted line scans.

the quality of the array. Measurements parallel to the wires resulted in information about the length of these wires. All scans have been aligned to the (111) surface. Therefore, the (553) Ewald rods in (a) are inclined with respect to their real space inclination of 12.5° . Those rods do not completely match with their theoretical expectations given by the black dotted lines. The reason is an imperfect correction of the electron beam shift over a large energy scale, in this case 95 eV to 345 eV, in combination with the typical pillow distortion of a SPA-LEED.

As clearly evident, the reciprocal space map is covered with rods that only show minor modulation, indicating a very good sample condition. Additionally, faint rods aligned upright at around -1.1 \AA^{-1} and 0.9 \AA^{-1} are the (111) 1×1 spots of the surface, indicating also the formation of such facets, possibly due to the compensation of an imperfect cutting direction. However, as there are no additional superstructure spots visible for these facets, they must be of very small size.

Line scans perpendicular to the formed wires were extracted for the five denoted rods to obtain quantitative information about the surface. The line scan direction is denoted by the white dashed line. These data were then fit with Voigt functions. This fit procedure is exemplarily shown in Fig. 6.5 (a) for

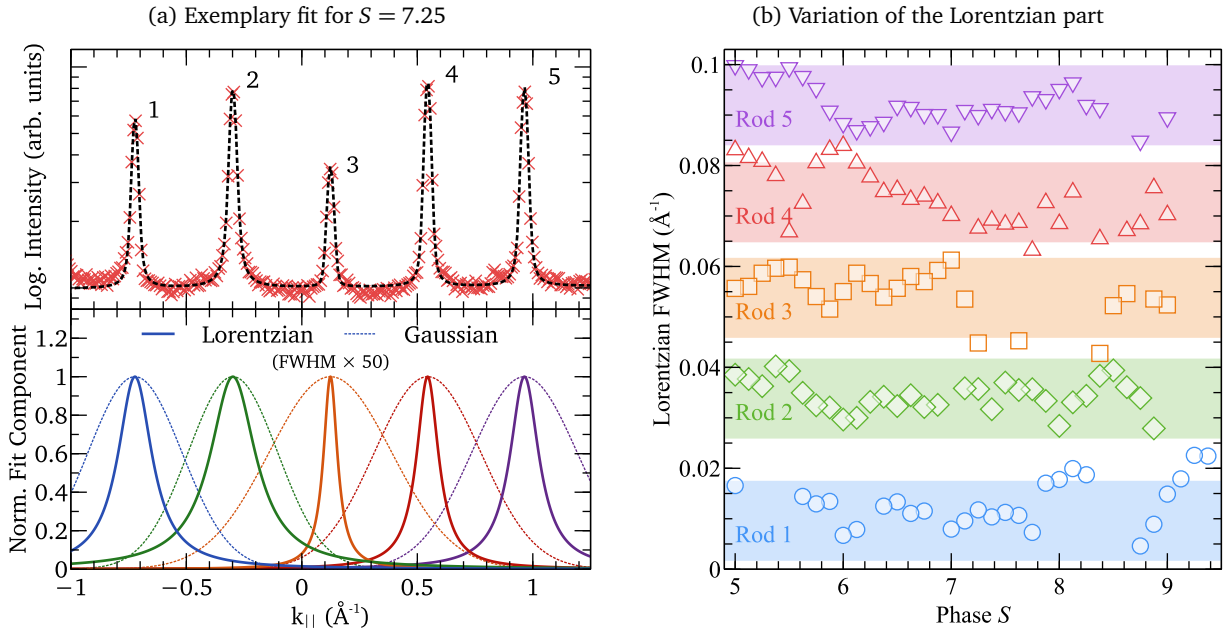


Figure 6.5: Variation of the Lorentzian underground in direction perpendicular to the wires for the rods denoted in Fig. 6.4: (a) shows a exemplary multiple Voigt fits for $S = 7.25$ with the deconvolved Lorentzian and Gaussian parts in the lower panel. For better visibility the widths have been multiplied by 50. In (b) the variation of the Lorentzians widths is depicted as a function of the Phase S . The data of each rod were shifted by 0.02 \AA^{-1} for better visibility. The pale bars in the background indicate a rough approximation of the variation of the data.

$S = 7.25$. From these fits, the width of the Lorentzian part was extracted and plotted in Fig. 6.5 (b). None of the peaks shows a trend of parabolic or sine behavior, but they are rather randomly distributed around a constant. Their variation around the mean value is approximately 0.015 \AA^{-1} , indicated by the colored bars in the background. An instrumental part is in this case already taken care of by an offset. Using the approximation of Eq. 2.13 results in a lower limit for the lateral ordering of $\geq 250 \text{ \AA}$, i.e. at least 17 wires.

Furthermore, Fig. 6.4 (b) shows an energy dependent scan on the same sample for the direction parallel to the wires. As the rods cut this direction only for an in-phase condition, the intensity is only given there. The streaks in the graph correspond to the $\times 2$ reconstruction of the surface. The widths of the Lorentzian part were obtained at the positions depicted by the white dashed lines in analogy to the perpendicular part, see Fig. 6.6. Assuming a geometric distribution of wires that are only separated by defects, the width of the Lorentzian background function can be considered constant for all scattering phases S . Thus, also the width of the in-phase condition yields a mean wire length via the same approximation of Eq. 2.13. An average value of $0.045(9) \text{ \AA}^{-1}$ computes from all given fits. After subtracting an instrumental broadening offset of $\approx 0.01 \text{ \AA}^{-1}$ as seen during the $H(S)$ analysis of Chapter 10, a lower

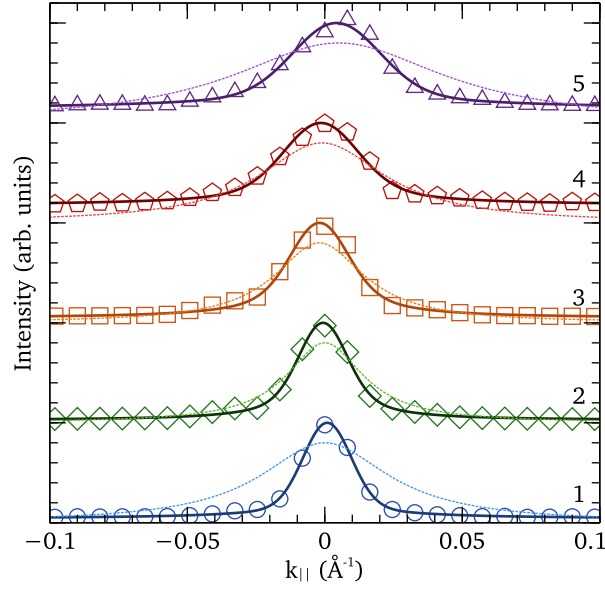


Figure 6.6: Line scans across the central spot in the direction parallel to the wires: The curves correspond to the dashed lines in Fig. 6.4 (b). The data were fit with a Voigt function by the solid lines. The deconvolved Lorentzian part is depicted by the dashed lines.

boundary for the chain length results in $l > 115 \text{ \AA}$. The $\times 2$ streaks at $S = 6$ have a width of 0.03 \AA^{-1} . Carrying out the same calculation, wire lengths of $l > 200 \text{ \AA}$ are obtained.

These values are compatible with chain lengths reported for plasmon measurements carried out with IR resonance [150] observing chains of several 100 \AA length or with wires investigated by STM [123, 117]. Moreover, these lengths allow investigating the system with the EELS-LEED as the longest wavelength possible is $\lambda = 2l \approx 400 \text{ \AA}$ corresponding to momenta of $< 0.015 \text{ \AA}^{-1}$. With the wires being statistically distributed, also slightly longer chains are available to excite plasmons with even longer wavelengths.

Knowing the structure and having estimated the quality of the wires, the substrates allowed to carry out electron energy loss spectroscopy measurements in the following chapter.

Plasmonic Excitations in Si(hhk)-Au

This chapter covers the properties of the collective excitations of electrons known as plasmons on the vicinal silicon systems. First, the general shapes of the excitation spectra from EELS are discussed. The following part tries to explain the slope of the plasmonic dispersion relation both by empiric comparison as well as by a modification of the single particle excitations for the plasmon model of one-dimensional quasi-free electrons. Finally, an analysis of the widths of the excitation peaks in the spectra is carried out for the discussion of further properties as, e.g., lifetime. Parts of this chapter were already published in Refs. [131] and [151].

7.1 Electron Energy Loss Spectra

As introduced in the previous two chapters, on all of the Si(hhk)-Au systems electron energy loss spectroscopy measurements were performed. Fig. 7.1 and Fig. 7.2 shows sequences of loss spectra on a semi-log scale as a function of increasing k . The left part of these graphs show spectra for increasing k_{\perp} in $[11\bar{2}]$ direction, i.e. perpendicular to the wires. The spectra along the wires for k_{\parallel} in $[1\bar{1}0]$ direction are shown from center to the right. The data are plotted normalized to the intensity of the elastic peak. Additionally, the curves are shifted upwards with increasing k_{\parallel} . The integration time of the curves was ≈ 5 s per data point measured with a resolution of 7 meV. As the signal from the Si(335)-measurement was weak due to a presumably far from perfect sample preparation, for Fig. 7.2 (a) the curves were smoothed by a local linear regression in every point to the surrounding next neighbors.

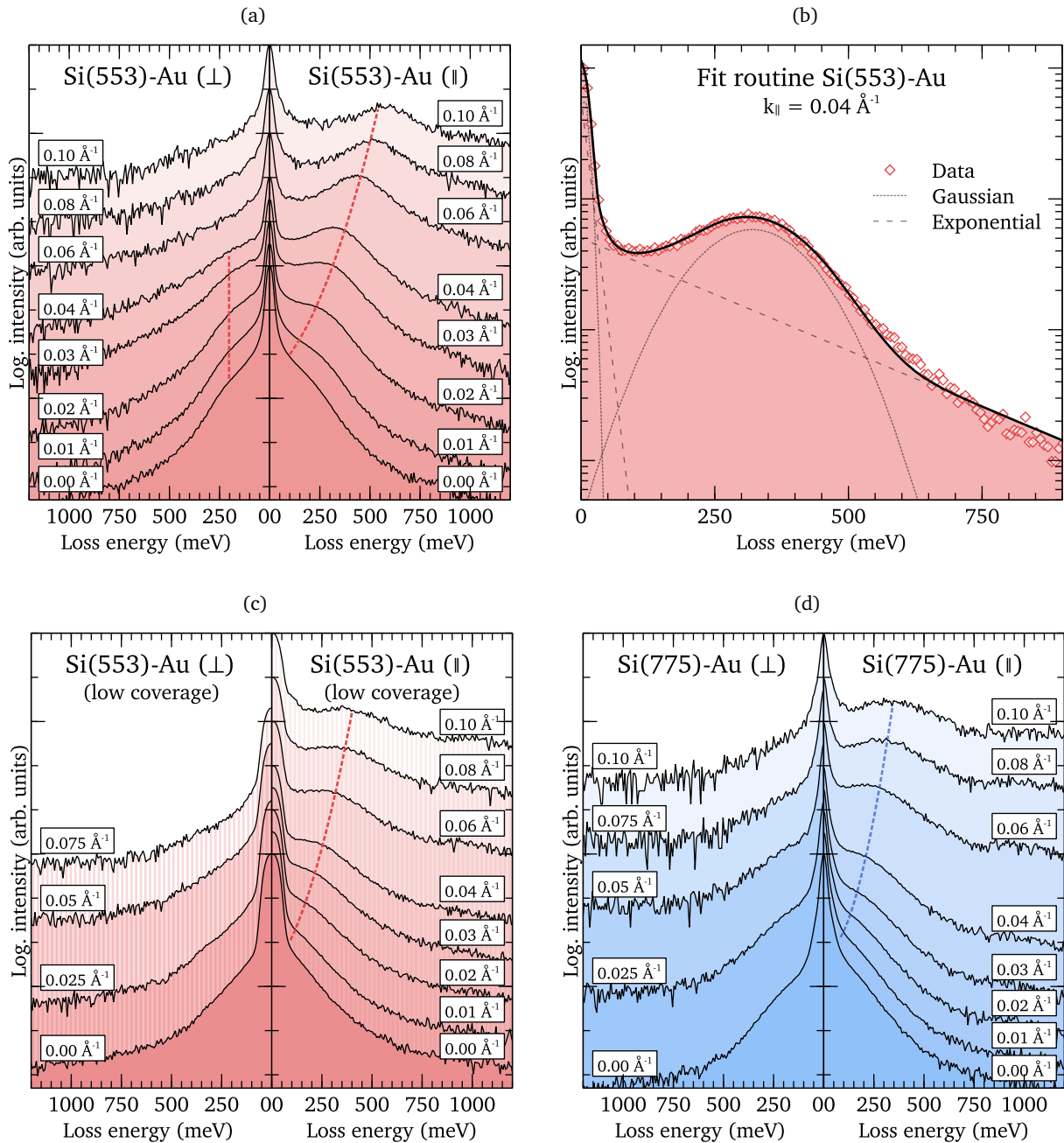


Figure 7.1: Electron energy loss spectra for Si(553)-Au and Si(775)-Au: (a) Raw spectra for the Si(553)-Au high coverage phase with k perpendicular (center to left) and parallel (center to right) to the extent of the terraces. A dispersing excitation can be seen only for the parallel direction. (b) Component functions and resulting fit that was used for all spectra of the systems investigated in this chapter. (c) Raw spectra for the low coverage phase of the Si(553)-Au system in parallel and perpendicular direction: A dispersing feature only parallel different to the high coverage phase is visible. (d) Raw spectra in perpendicular and parallel wire direction: Also here, a dispersing feature in parallel direction is present. The spectra are shifted in intensity for increasing k for better visibility.

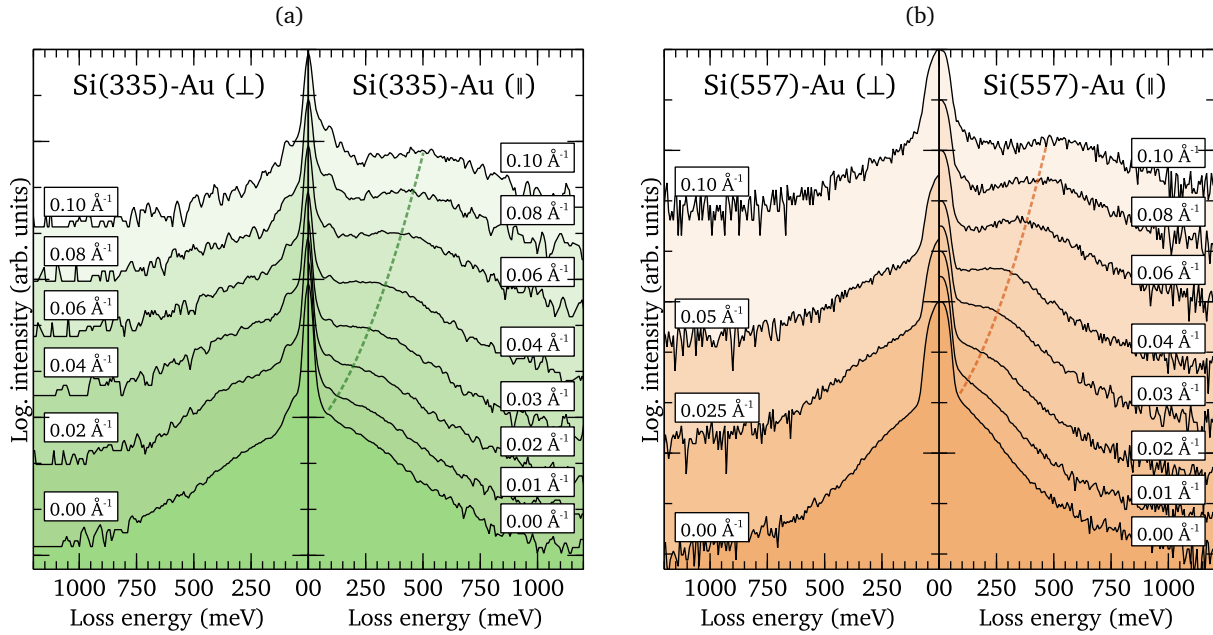


Figure 7.2: Electron energy loss spectra for Si(335)-Au (a) and Si(557)-Au (b): Both systems show a dispersing excitation only in the k -direction parallel to extent of the terraces. Like in Fig. 7.1 the spectra have been shifted upwards in intensity for increasing k for better visibility. The raw data of Si(335)-Au is filtered by a moving average to the next neighbor due to a poor reflected intensity.

Close to $k = 0$ the spectra do not show any excitation peaks apart from the peak originating in the elastically scattered electrons at $E = 0$. One might argue that there is a slight excitation visible, strongest in Fig. 7.1 (a) for Si(553)-Au, indicated by the dashed line. There are two possible explanations for this effect. However, an attribution to a quantum-well state can be ruled out. Investigations by Fourier transformed IR spectroscopy with the same preparation method reveal wires of $\gg 100 \text{ \AA}$ length [150], an estimation of the wire length in the last chapter resulted in lengths $\gg 200 \text{ \AA}$. Their appropriate energies are almost zero and can additionally be ruled out by the resolution mentioned before. On the other hand, eigenenergies of a quantum-well with a width of only several \AA perpendicular to the wires will be much higher than observed. Moreover, the peak could have its origin in the k resolution of the loss spectrometer. Therefore, even at $k = 0$ a small signal from $k \neq 0$ in wire direction is present. This suspicion is strengthened by the fact that this peak remains at the same loss energy for increasing k_{\perp} . However, it dies out less quickly than expected for the resolutions of the spectrometer of $\approx 0.01 \text{ \AA}^{-1}$. Nevertheless, a residual parallel momentum for all k_{\perp} due to the resolution as well as is the most probable influence.

Another influence is the shape of the inelastic intensity next to the elastic peak. All spectra show this to first order exponentially decaying loss intensity next to the elastic peak, known as the Drude tail

[152, 89]. This background is also seen in other quasi-one-dimensional systems [31, 28, 29] that is a typical signature of the low-energy single particle excitation continuum in metallic systems. Therefore, all the investigated systems seem to be metallic, in agreement with ARPES, [113, 103, 115, 104], and for Si(553)-Au and Si(775)-Au with STM data [117, 130]. However, this exponential decay is just the first approximation. Slight variations from this behavior are possible, as the internal electronic structure of the system also influences the Drude tail. A combination of the resolution and this Drude tail variation are most probably the reason for the deviations and also the explanation for the faint, but pronounced shoulder in the curve for Si(553)-Au.

In the direction along the wires, the spectra show clear loss features that shift to higher energies with increasing scattering angles, i.e. increasing k_{\parallel} . In the k_{\perp} direction across the wires, the data exhibit no dispersing modes.

When comparing the dispersing features of all spectra, a definite difference in the size of the shift is directly visible, as depicted by the dashed lines through the loss maxima. This result is to some extent surprising as all systems seem to have similar k_F and effective mass m^* . Therefore, a similar dispersion relation is expected according to Eqs. 3.20 and 3.13. Even for the Si(553)-Au low coverage phase a clear difference can be identified, although, according to ARPES [104], the two systems share the same electronic band structure within only a few % variation.

Any additional small features visible near the elastic peak are attributed to small residual gas adsorption. It was tried to reduce this effect by taking special care about the pressure and its composition. Anyhow, the small feature at ≈ 100 meV, mainly pronounced on the Si(335)-Au surface, is most likely due to a Si-OH bending mode [153].

All spectra with an apparent loss peak were accurately fit by the following parametrization: Gaussian type functions describe the elastically scattered peak and the loss peak, whereas exponential functions approximate the Drude background. A linear offset is used for the background intensity. The appropriate parts as well as the resulting curve exemplarily overlay the experimental data for Si(553)-Au at $k_{\parallel} = 0.04 \text{ \AA}^{-1}$ in Fig. 7.1 (b). The same routine was applied to all spectra and, thus, led to the experimental dispersion relations of the plasmons.

7.2 Two-Dimensional Crossover of One-Dimensional Electron Density

The plots in Fig. 7.3 and Fig. 7.5 show the extracted data from all measurements on the Si(hhk)-Au systems with negative inclination in $[11\bar{2}]$ direction, in particular Si(553)-Au in both high as well the low coverage phases, and the Si(775)-Au system.

Measurements were carried out at an incident energy of the electron beam of 20 eV and 36 eV. Additionally, the temperature of the system was changed from room temperature (RT) to low temperature (LT) < 120 K by the use of liquid nitrogen. A more exact determination of the temperature cannot be given due to the sample holder setup, see Chapter 4 for further information.

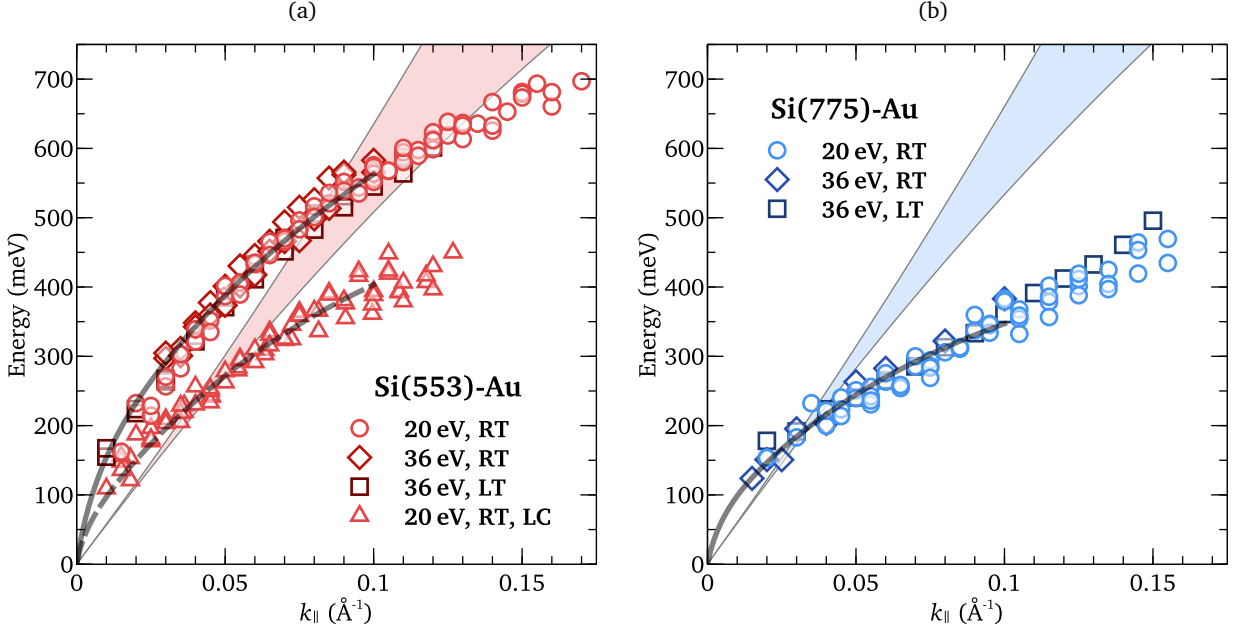


Figure 7.3: Dispersion relation of Si(553)-Au and Si(775)-Au: (a) The dispersion of Si(553)-Au is not changing by change from room temperature (RT) down to < 120 K (LT) nor by the change of the initial excitation energy from 20 eV to 36 eV. It is but depending on the coverage when only evaporating 40%, i.e. 0.19 ML, as given by the triangle data. (b) The same independence holds true for Si(775)-Au, a low coverage phase was not observed. The fits correspond to the modified quasi-one-dimensional low- k approximation originally introduced by Das Sarma et al. [25] as explained in Eq. 7.1. The shaded area in the background indicates the extrapolated electron-hole excitation spectrum of a parabolic band fit to ARPES.

Within the accuracy of the measurements, no changes could be resolved although at least the Si(553)-Au systems undergo an electronic phase transition for lower temperatures [111, 117]. Though a transition to a partial $\times 3$ superstructure was observed, a change in the energy of the plasmon for even lower temperatures cannot be ruled out altogether. In the present case, most likely the majority of the wires did not yet feature the low- T phase, as it is the case for an observed defect pinning in Ref. [123]. Defects are also responsible for a varying transition temperature that is inversely proportional to the density of defects along the step edge [124, 154]. They are not characterized in detail and, thus, could be of any kind, such as a missing atom or OH bond to the step edge. In addition to a Peierls distortion, it provides a mechanism that can lower the total energy for 1D chains.

In this picture just described, the main signal is generated by the RT phase and, therefore, it explains that no change was seen. However, this is in contrast to recent results of Hötzel et al. [155], where a temperature dependent shift of the plasmon energy was seen. As this shift was on the scale of several meV, the resolution of the EELS is not sufficient for its detection.

When preparing the Si(553) substrate to a state where only every second terrace is covered with gold wires, i.e. the low coverage phase, a change in plasmon dispersion is visible. As all systems seem to be of a one-dimensional character, they should be compared to 1D plasmon theory, cf. chapter 3. The theoretical approach there is to use a confined quasi-free electron gas with near-field STLS corrections. With this background, the shift can be explained by wires that are further apart and, therefore, the blueshift induced by the change of the wire spacing d is lower, cf. Fig. 3.3.

Nevertheless, in comparison with the Si(775)-Au dispersion, there is a shift to lower energies similar to the one observed for the low-coverage phase of Si(553)-Au. From ARPES data [103] a higher electron density with the same effective mass of the band lower in energy in combination with a denser spacing than for the low coverage phase should lead to a dispersion with a slope that is placed between the two already discussed curves.

These results already show that the use of a quasi-free electron gas model leads to massive difficulties regarding the systematics acquired by the theory of chapter 3. When additionally depicting the extrapolated single-particle excitation spectrum in Fig. 7.3 in light red for Si(553)-Au (a) and light blue for Si(775)-Au (b), one can see that the experimental dispersions cross this regime. This behavior is highly unlikely due to the strongly increased probability of the decay into electron-hole pairs. Correspondingly, a plasmon described by theory should always be above the upper boundary ω_+ of this Landau regime, in contrast to the experimental findings.

A quantitative fit was only possible by an empirically modified low- k approximation of coupled wires in a periodic array of square-well potentials, as earlier described in Eq. 3.20, and also carried out in [131, 151], given as

$$E(k) = \hbar k \omega_0 a_c \times \sqrt{K_0(ka) + 2 \sum_{l=1}^n K_0(kld)} \quad (7.1)$$

The modification is the introduction of a_c as an arbitrarily chosen normalization constant with dimension

System	d (Å)	t (Å)	n (cm ⁻¹)	m^*/m_e	a (Å)	a/t
Si(553)-Au HCW	14.7	14.7	2.9×10^7	0.6	7.9	0.54
Si(553)-Au LCW	32.7	16.4	2.9×10^7	0.6	9.8	0.59
Si(775)-Au	21.3	21.3	3.0×10^7	0.6	11.0	0.52
Si(335)-Au	12.6	12.6	2.0×10^7	0.4	5.4	0.43
Si(557)-Au	19.2	19.2	2.4×10^7	0.6	4.6	0.24

Table 7.1: Input values on the left taken from Ref. [103] and the resulting effective widths a from fitting the given data with the modified model given in Eq.7.1. The resulting width was normalized to the width t of the terraces that host the Au chain. Respectively, $t = d$ except for the low coverage Au phase on Si(553).

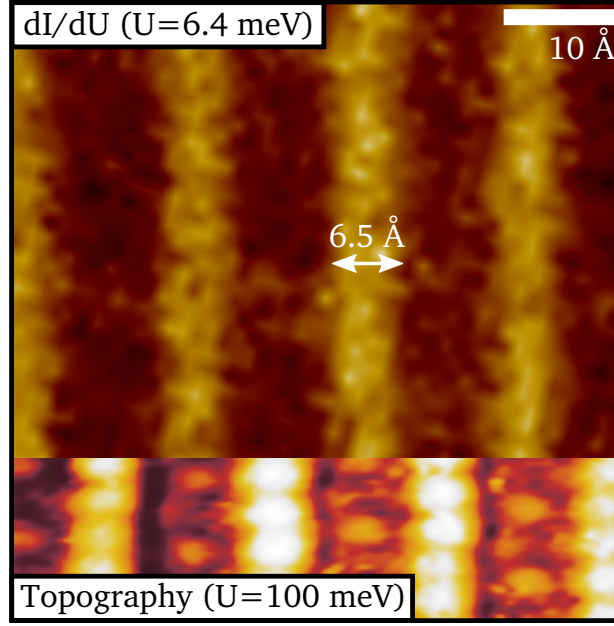


Figure 7.4: Combined image of STM and STS on Si(553)-Au around E_F . Bottom: Topography image ($U = 0.1\text{ V}$, $I = 50\text{ pA}$) showing the bright Si honeycomb chain at the step edge and the period doubled Au chains in between. Top: dI/dU map recorded with lock-in technique ($U_{\text{mod}} = 10\text{ mV}$) close to the Fermi energy ($U_{\text{DC}} = +6.4\text{ meV}$). The DOS is significantly enhanced at the Au chains with a FWHM of 6.5 \AA . The image was captured by Julian Aulbach and already published in a collaborate publication of Ref. [131].

length. Still, the frequency constant remains

$$\omega_0 = \sqrt{\frac{2ne^2}{4\pi\bar{\epsilon}\epsilon_0 m^* a^2}}. \quad (7.2)$$

With these changes, the equation is strongly depending on the first part defining the general inclination of the dispersion by a distribution of the electron density to the wire width a . The two terms under the second square root account for the self-interaction of a single wire and the interaction between different wires at multiples of the interwire spacing d . The one-dimensional electron density $n = 2k_F/\pi$ as well as the effective mass m^* have been taken from the energetically lower band S2 observed in ARPES [103] assuming a quasi-free electron character, cf. Fig. 5.4. The experimentally derived ratios n/m^* are identical within 8% for both bands in all systems leading to two degenerate plasmons within the given theory.

Fig. 7.3 shows the fits as an overlay to the extracted data with $a_c = 6.64\text{ \AA}$ set to twice the Si-Si distance for the lateral extent of a double chain. During fitting a was the only free parameter, the input values are shown in Tab. 7.1, the surrounding $\bar{\epsilon} = (11.5 + 1)/2$ was taken as the mean value of silicon and vacuum. This value was used because of its usage in other plasmon papers [79, 74] originally

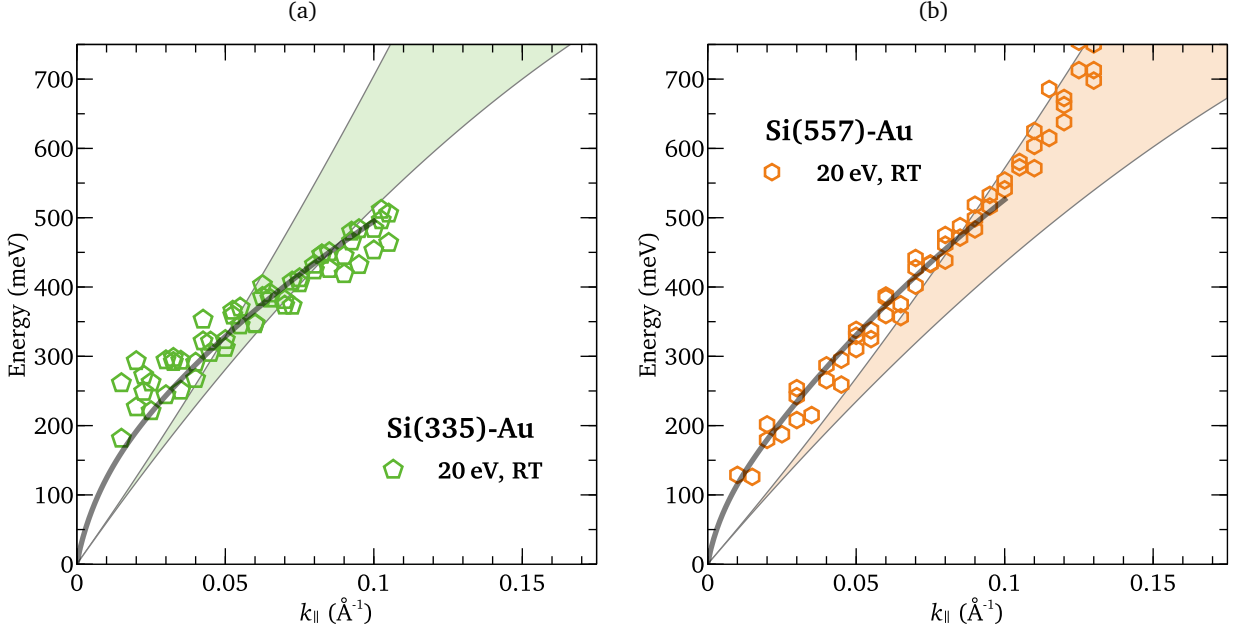


Figure 7.5: Dispersion relations of Si(335)-Au (a) and Si(557)-Au (b): All data have been extracted from loss measurements with $E_0 = 20$ eV at room temperature. The fits correspond to the modified quasi-one-dimensional low- k approximation as given in Eq. 7.1. Again, the shaded area in the background indicates the electron-hole excitation spectrum for the bands from photoemission data.

referring to Ref. [156]. The terrace width t is identical to the periodicity for Si(553)-Au in the high coverage phase and Si(775)-Au. For Si(553)-Au with low coverage, a closer look has to be drawn to the structural model in chapter 5 proposed by Song et al. [104]. The $\times 5$ terraces not covered by gold are under tension with the consequence of atomically rough edges. This roughness gives the electronic system on the gold covered surface the possibility to spill out into the uncovered neighboring terraces by approximately $0.5a_{\perp} = 1.7 \text{ \AA}$, leading to a slightly wider terrace of $t = 16.4 \text{ \AA}$.

The resulting effective widths obtained by this routine are given in Tab. 7.1, slightly optimized with respect to Refs. [131, 151]. The wider the terrace is, the wider also the widths of the wires seem to be. When normalizing them to the terrace width t , the same factor $\gamma \approx 0.55(4)$ is obtained for Si(553)-Au HCW, LCW, and Si(775)-Au. These findings can be summarized by

$$\omega_p \propto \sqrt{\frac{n}{m^* a^2}} \quad (7.3)$$

with $a = \gamma t$ meaning strong lateral distribution of the electrons within each wire. This factor is strongly extending the standard 1D plasmon properties.

Comparing the data with an actual STS map as given in Fig. 7.4, the values obtained seem to be a

reasonable result. The image shows a high contrast in the DOS around the Fermi-level at the position of the gold chain. The width of this intensity is also very close to twice the Si-Si distance = 6.64 \AA in the direction perpendicular to the wires yielding another possible interpretation.

Playing this empiric trick further with the data for the two other surface orientations as shown in Fig. 7.5, it will work for the Si(557)-Au system when normalizing to $a_c = 3.32 \text{ \AA}$. This width has been chosen as there is a single Au chain in this system. The normalized $a/t = \gamma = 0.24$ is then approximately half the value of that one derived from the systems with negative inclination, i.e. Si(553)-Au and Si(775)-Au. The game changes for the last system in the family, Si(335)-Au, leading to a wider effective width though having a narrower terrace. It also behaves differently in ARPES already, as here the effective mass is only $m^* = 0.4m_e$. Additionally, why the same atomic assembly of Au on a different system leads to a different electronic band structure, remains to be clarified. A much lower electron density would be needed here for the proportionality to work.

Summarizing the results of this section, a dependence of the slope of the plasmonic dispersion on the terrace width t was observed for negative inclination, i.e. the Si(hhk)-Au systems with $h > k$. In particular, the electrons on the Si(553) and Si(775) surface distributed over the full terrace. This picture does not hold true entirely for the positive inclination, i.e. Si(335) and Si(557). Consequentially, the electronic band structure seems to be of a more complex composition than just extrapolated parabola as observed in photoemission spectroscopy. Anyhow, the starting slopes depicted for the dispersions shown still resemble the overall slope coming from this simple theoretical approach. This result shows that the essentials to understand the mechanisms of those quasi-one-dimensional systems might only need a slightly changed ansatz in plasmon theory. An approach of this kind is made in the next section.

7.3 Deviations from the Quasi-Free Electron Character

Although giving already some insight into the systematic behavior of the changes in the electronic structure, the description via an empirical modification is unsatisfactory. It explicitly shows that the band structure is not given by a simple parabola, as the plasmon dispersion enters into the electron-hole pair continuum that unavoidably would lead to a strong damping. Therefore, this approach is rather unphysical. Additionally, there is a strong correlation between the electron-hole excitation boundaries and the plasmonic dispersion, as given by Eq. 3.13. It defines the slope by the difference of the upper and the lower edge weighted by a factor $e^{A(k)}$ that takes the Coulomb interaction between all electrons into account. Thus, changes of the Landau regime are required for a description of the plasmon.

Albeit the derivations of Chapter 3 are explicitly carried out for a parabolic dispersion of a quasi-free electron gas, this derivation should also work for any kind of dispersion and, therefore, for any given electronic band structure. In order to be able to describe the plasmon with such an approach, the single particle excitations of the system must obey various rules, i.e. the electronic band structure of the system must deviate from that of a quasi-free electron gas and allow a distinct definition of electronic

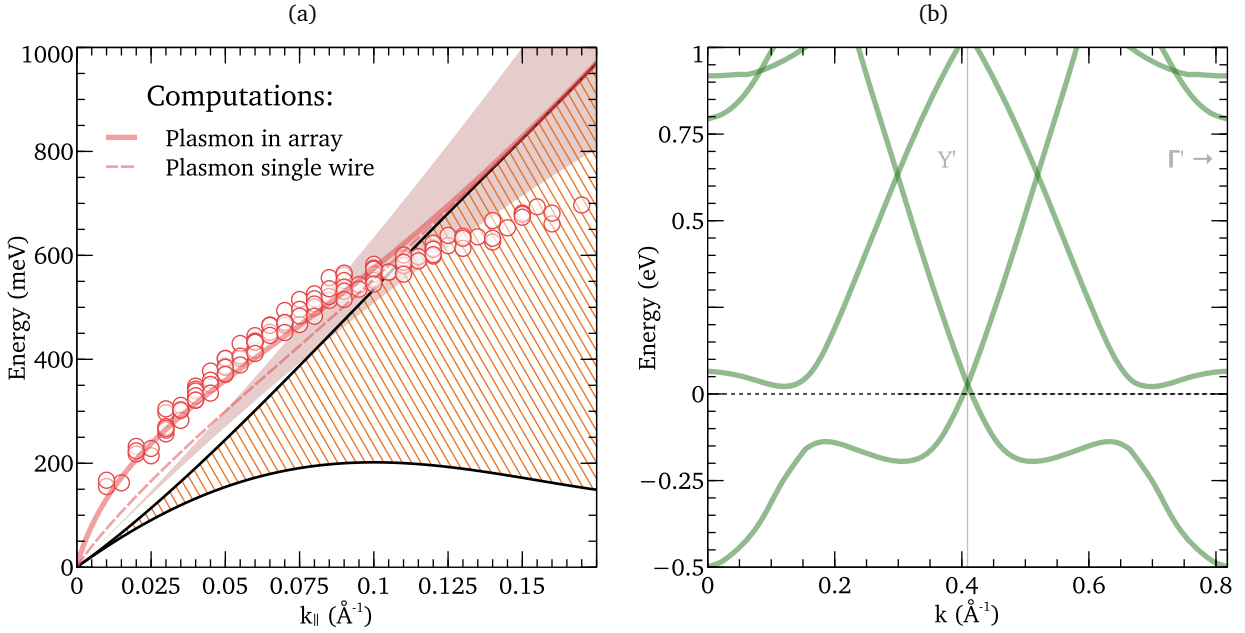


Figure 7.6: Computation of the plasmon dispersion (a) as taken from the numerically derived electronic band structure of Ref. [121] for Si(553)-Au (b): The electron-hole pair continuum is given by the orange striped region, limited by the limits ω_+ and ω_- originating in the shape of the electron bands. The thick red line corresponds to the case of coupled wires. The dashed line denotes the single wire case. A good agreement is found up to $\approx 0.1 \text{\AA}^{-1}$. As a comparison, the electron-hole continuum for the system without hybridization is shown as the shaded red area.

states. Recent band calculations for the systems were carried out by the Paderborn group around W.G. Schmidt, S. Sanna, et al. and were published in Ref. [121], the Korean group in Pohang of H.W. Yeom et al. [104], as well as the Polish group in Lublin of M. Krawiec et al. [134]. Indeed, the electrons show a noticeable deviation from a quasi-free character. In contrast to the experimental data, they do not show pronounced parabolic Au-induced bands. Instead, they predict a hybridization of all surface bands arising from the step edge as well as eventually occurring bands from the Si-atom/restatom chain with the states that originate in the presence of the Au chain, as already discussed in Section 5.3.

However, the states that have the highest probability density around the Au chain, indeed have a parabolic shape in reciprocal space. Anyway, their curvature, Fermi wave vector k_F , as well as their energetic minimum slightly deviate from the bands observed in ARPES. Moreover, it remains unclear why photoemission is that selective to only the states that have the highest probability density around the Au atoms.

The numerically derived band structure of the high coverage phase of Si(553)-Au of Ref. [121], given by the green lines in Fig. 7.6 (b) was now taken to extract the single particle excitations ω_{\pm} . In this

case, ω_+ was the band structure above the Fermi-energy, and ω_- the states below. These data were then used to calculate the plasmon dispersion via Eq. 3.13

$$\omega_p(k) = \sqrt{\frac{\omega_+^2 e^{A(k)} - \omega_-^2}{e^{A(k)} - 1}} \quad (7.4)$$

when taking the Fermi wave vector k_F as a new reference for $k = 0$. Here, the effective mass necessary for $A(k)$ was chosen to be the one at k_F . For the present band structure it calculates to $m^* = 0.23m_e$. The Coulomb matrix element $v_c(k)$ was calculated for a Gaussian periodic distribution of electrons with $d = 14.7 \text{ \AA}$ and $w = 6.6 \text{ \AA}$, i.e. the experimentally observed shape in Fig. 7.4 corresponding to twice the Si-Si distance. As already pointed out in Section 3.3, there is no difference in the Coulomb element $v_c(k)$ between square-well or harmonic confinement when the width w is small enough ($\lesssim 0.5d$).

The results are shown in Fig. 7.6. Represented by the red line is the resulting plasmon dispersion for the case of coupled wires, the single wire case is depicted in dashed red. Up to $k_{\parallel} = 0.1 \text{ \AA}^{-1}$ there is a good description of the data. As already concluded in the last section, the overall shape for these low k values favors coupled wires over isolated ones.

The striped area is the electron-hole continuum as derived from the band structure. It is delimited by the black lines that correspond to ω_+ and ω_- . The shaded area in the graph shows the electron-hole continuum when taking the bands observed in photoemission [103]. Here, the plasmon even completely crosses this regime, making it a highly unfavorable situation. Although the difference in ω_+ between the calculated and the experimentally obtained band structure is not severe, the change of ω_- is highly different. This variation of the lower boundary is highly responsible for the starting slope of the dispersion relation.

As these results take into account the hybridization of the bands of the Au chain with the Si honeycomb states below the Fermi level, it also concludes that the hybridization is a necessary condition to describe the behavior of the plasmon dispersion. Therefore, it also strongly supports the general result of a hybridization in the numerical calculations.

Anyhow, the dispersion relation cannot yet be explained for higher k with this approach. Because of the dispersion relation but still entering the single-particle continuum, further modifications to theory or variations of the numerically derived band structure are necessary. The plasmon is still expected to converge to ω_+ for higher k .

7.4 Computation of the Electron-Hole Pair Continuum Boundary

The question now is: How should the shape of the upper boundary of the electron-hole pair continuum look like to describe the plasmon dispersion that was observed? To answer this question, the calculations are turned around. Instead of calculating the dispersion of the plasmon, the measured data is used to derive this boundary ω_+ assuming the simplifications made in the last section. By a simple algebraic

conversion, the relation of Eq. 3.13 was changed to

$$\omega_+(k) = \sqrt{\frac{\omega_p^2(k)(e^{A(k)} - 1) + \omega_-^2(k)}{e^{A(k)}}}. \quad (7.5)$$

Here, as with increasing k the values of $A(k)$ increase, the convergence of $\omega_+ = \omega_p$ for high momentum is still present.

7.4.1 Si(553)-Au in High and Low Coverage Phase

Now, as the low- k data was already a good description, the calculated electronic band structure up to E_F was taken for ω_- . Its influence is only of importance for values around k_F , i.e. $k = 0$ for the plasmon dispersion, as the difference between ω_+ and ω_- sharply defines the starting slope of the plasmon, the fine tuning is done by $v_c(k)$. The effective mass and the Coulomb matrix element remained as before. The resulting ω_+ data points shifted by k_F are plotted over the numerically derived bands along the chain direction in Fig. 7.7.

Of course, the correspondence is good for lower energies up to 500 meV as this part was already nicely describing the plasmon in Fig. 7.6. But now a deviance from the electronic band structure is directly visible. Interestingly, the starting point of this variation is near a crossing point of two bands. This unavoided crossing results in calculations for only $\times 1$ periodicity in chain direction with subsequent back-folding at the new Brillouin-zone boundary. For an explicit $\times 2$ calculation one would expect a band-gap to open there. Other band structure calculations explicitly take a dimerization of the Au chain into account [112, 157]. Indeed, in those calculations a band gap opens at the crossing. Recent results also predict the width of the band gap to depend on the dimerization of the Au chain¹. Please note that the band structure calculations are for $T = 0$ K, whereas the plasmon measurements have been carried out at room temperature.

For further guidance, additional information has been added to the figure. The thick red line demonstrates the honeycomb chain-induced band that hybridizes with the two Au chain bands. The Au bands as observed in ARPES measurements [103] are depicted as the thick yellow curves. Here, albeit a similar inclination, a high difference can be observed. This mismatch can either be an energetic offset with an origin of an altered or aged surface during the experimental setup, or also an underestimation of the energetic distance between occupied and unoccupied states in the numerical calculations with subsequent misalignment of the Fermi energy. The difference might but also be in momentum due to misaligned angles during the photoemission.

Experimental STS data at 77 K from Aulbach et al. [117] at various sites on the surface has been added to the right side of the band structure sketch, aligning the bias axis to the energy axis of the band structure. Non-ordered local spin-polarized electron densities at the step edge are theoretically

¹Private communication Simone Sanna

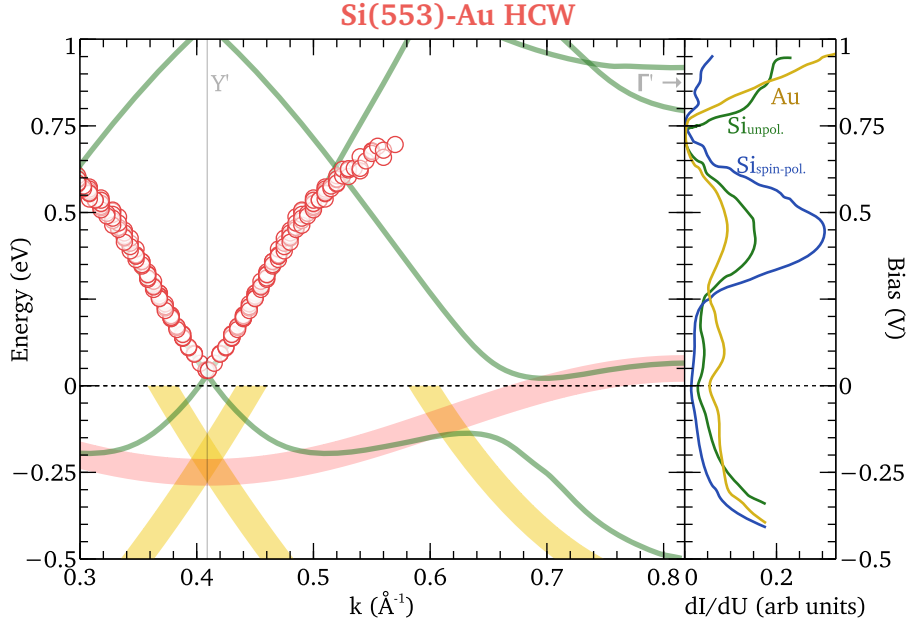


Figure 7.7: Calculated upper boundary of the excitation spectrum for Si(553)-Au: The graph features ω_+ shifted to k_F as derived from the plasmon excitation given as red circle in respect to the electronic band structure given by the green lines taken from Ref. [121]. The red dotted curve represents a speculative extrapolation of ω_+ . The red line is a sketch of an unhybridized band from the Si honeycomb step edge. Yellow lines show a parabolic fit to the data from Crain et al. [103]. To the right side, STS data from Aulbach et al. [117] is scaled according to the Energy axis of the band structure. These data indicate a missing state at around 0.45 eV.

predicted in this temperature range. Therefore, denoted as spin-polarized, the blue curve stands for the high density in STM at the Si honeycomb chain step edge, whereas the green curve is for the lower density there. The yellow curve is the measurement on the Au chain. The overall behavior of the dI/dU data resembles more or less the band structure given, except in the region around 500 meV and above. STS sees no states below 0.75 V, predicting a higher energetic region for the band gap. Additionally, according to all STS curves a high DOS should be visible slightly below 0.5 V. As STS is more sensitive to states around Γ , the pronounced peak in the data suggests a high density at the Brillouin-zone center. As the STS data has but been carried out at 77 K, this strong DOS will be related to a $\times 3$ superstructure that features a band gap in this energy [120].

Fortunately, also band calculations were available for the low coverage phase [104]. Unfortunately, they lack a complete description of the unoccupied states. Therefore, a direct computation of the plasmon as carried out for the high coverage phase in Fig. 7.6 was not possible. As a consequence, only the same procedure of deriving ω_+ for the occupied states was possible as depicted in Fig. 7.8. In this case, the band in green as extracted from Ref. [104] has a Fermi-level that is 0.12 eV higher in energy.

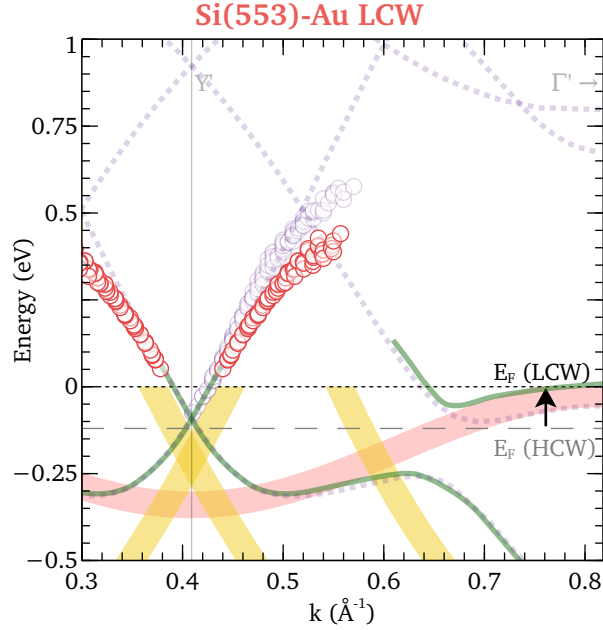


Figure 7.8: Calculated upper boundary ω_+ for Si(553)-Au in the low coverage phase: The plot shows ω_+ as derived from the plasmon dispersion shifted by k_F . The calculated band structure in green is taken from Song et al. [104]. Sketched in red is the Si honeycomb state, yellow line represent the parabolic fit of the photoemission data. The red dotted curve is a presumed extrapolation of ω_+ . In pale purple dotted lines the electronic band structure of the high coverage phase has been added by shifting the Fermi level to fit to the unoccupied states from Song et al., also indicated by the two Fermi level lines.

The green band up to E_F was used to calculate back to ω_+ . The Coulomb matrix element $v_c(k)$ was computed with $d = 32.7 \text{ \AA}$ and $w = 6.6 \text{ \AA}$. The effective mass was chosen to $m^* = 0.3m_e$ resulting from the band at k_F .

A similar slope can be observed as for the high coverage phase. A deviation of ω_+ occurs again around the crossing point, where a band gap is supposed to open, though, being slightly stronger curved. For comparison, the bands of the high coverage phase were aligned to the part of the band structure and plotted in dotted pale purple. Interestingly, the bands could be aligned completely on top of each other for the occupied states when shifted downwards in energy by 0.12 eV. Additionally, the derived upper boundary from the high coverage phase was added in pale purple circles, also shifted by the same value of 0.12 eV, i.e. the Fermi-level difference of the two systems. Here, a slight difference in overall inclination to the low coverage's ω_+ is directly visible.

In conclusion, there is a close electronic similarity between the HCW and LCW phase: They both seem to share a resembled band structure shifted and compressed in energy. This energy difference might be due to the difference in terrace size of $0.5a_{\perp}$ mentioned before, leading to a shift of the eigenenergies of the potential perpendicular to the conduction channel. Depending on the shape of the

edge of this confinement, a compression is possible, i.e. the energetic distance of the eigenenergies does not necessarily stay the same. This compression then leads to the lower increase of ω_+ as a function of k for the low coverage phase. For the plasmon dispersion this means that the difference in the starting slope is, thus, not only caused by the damped blueshift due to a wider distance in the array, but also by an overall decrease of the band structure. Another possible influence is the possibility of slightly different dimerizations of the Au chain that change the width of the band gap in the unoccupied states.

Comparing the experimentally recorded band structure from photoemission from the same paper of Ref. [104], the calculations are in this case closer to one band, but have a stronger offset to the other one. Bands arising from the 5×5 terraces were neither visible in photoemission spectroscopy nor in calculations nor taken into account in this approach. Anyhow, this reconstruction type should only lead to non-dispersing states and, therefore, its bands would lie outside of this area of interest. Anyway, the deviation of ω_+ from the calculated states as well as the STS data highly enforce to reconsider the calculations made. Particularly in the unoccupied states, both systems show substantial deviations at the unavoided band crossing points.

Nevertheless, all electronic band structure calculations used are carried out at zero temperature. Most measurements, however, took place at room temperature, some at around 120K. Therefore, the electronic band structures in the experiments do not necessarily look like the ones from the calculations. Furthermore, the discussion about the $\times 2$ and $\times 3$ superstructure steers in the direction of a metal-insulator phase transition taking place below 100K [123].

7.4.2 Si(775)-Au

Due to an additional structural motif of a Si adatom chain, the system gets a bit more complex. A numerically derived electronic band structure from Christian Braun [132] is plotted in Fig. 7.9. The solid green lines correspond to the computation with Perdew-Burke-Ernzerhof (PBE) approximation [158]. This approximation is also the common method of quickly obtaining a structures electronic states. The highest difference to these bands results from Heyd-Scuseria-Ernzerhof (HSE) hybrid functionals [159], a more accurate but time consuming approach. This difference between the two approximations is shown to illustrate the possible variance that might occur when using different methods. It also shows that for consistency within a systematic investigation, it is essential to use the same approach for all systems.

However, this system features various band gaps, e.g. bands 1 and 2 are induced by the additional adatom/restatom chain. However, such a case is not covered by a simple one-band-approach that only deviates from a parabola. Whereas a definition of the lower boundary ω_- is still easily possible, a precise curvature of ω_+ cannot be extracted. Thus, one could simply assume that only the overall excitation spectrum for the plasmon is necessary for its excitation. Nevertheless, this approach overcomplicates the investigations and leads to huge uncertainties. Additionally, the question arises which bands are to be included into this method and which ones should be left out.

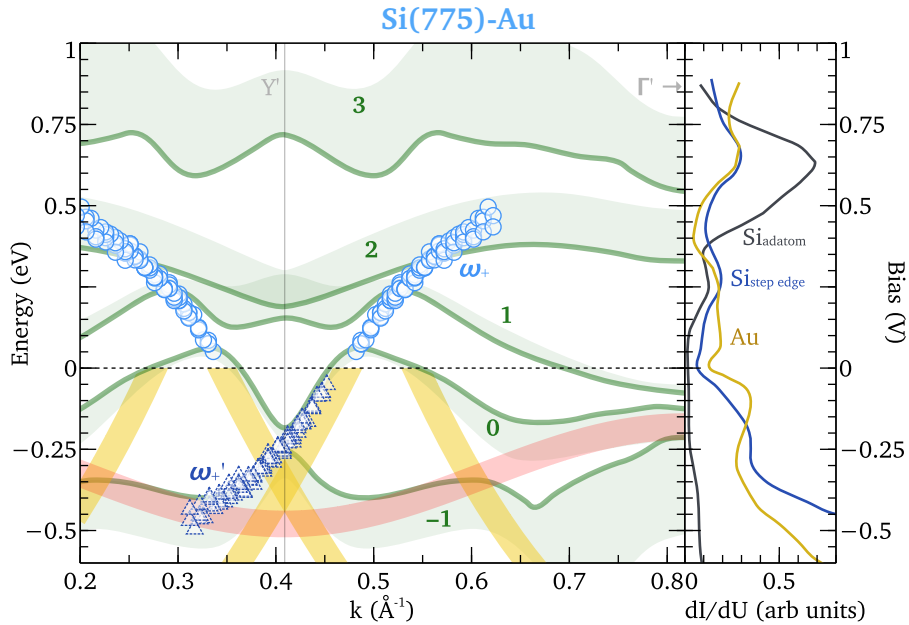


Figure 7.9: Calculated ω_+ for Si(775)-Au: The data have been derived by taking the lower boundary from the electronic band structure from Christian Braun [132] around k_F : blue circles show the result for electron-like behavior, dark blue dotted triangles for a hole-like plasmon. The band structure given by the green line was calculated by HSE functionals, the shaded area depicts the difference to PBE functionals. The bands are numbered arbitrarily around E_F . The Si honeycomb state is sketched in red, yellow lines depict the data as observed in ARPES [103]. To the right STS data from Aulbach et al. [130] is aligned to the energy axis of the band structure.

As the present electronic structure allows to estimate ω_- from the flat band around E_F at 0.351 \AA^{-1} , resp. 0.467 \AA^{-1} , the approach was used to directly start calculating the upper boundary from the plasmon dispersion and to compare it with the numerically derived electronic band structure afterward. These values are given by the blue dots. The effective mass at k_F was calculated to $m^* = 0.08m_e$, $v_c(k)$ was derived numerically with distribution width $w = 6.6 \text{ \AA}$ and periodicity $d = 21.7 \text{ \AA}$. Due to this very small effective mass and, hence, a larger correlation function $A(k)$, the curvature of ω_+ almost completely determines the plasmon dispersion. For an approach to the unoccupied states, ω_+ is running through two band gaps, touching only some states for the first band (1) over the Fermi-level only for the PBE calculations. It then tends to converge to the HSE state in band 2. However, those two bands from calculations with HSE functionals can be attributed quite well to the DOS probed by STS spectra on the right [130].

Another approach is to look at the hole character of the 0th band with only a minimal amount of charge carriers inside. The resulting ω_+' is then faced downwards and depicted by the dark blue dotted triangles in Fig. 7.9. The slope follows the states of band 0 straightly. After apparently ignoring the band

gap, the data follows the slope of band -1 , though favoring the calculated PBE states instead of HSE. Comparing the -1 st band with the measured DOS, a slight energetic upshift is plausible. This upshift would then hit the sketched red Si edge band.

Additionally, this plot also shows the parabola fitted ARPES data in the fat yellow curves. The calculated data as well as ω'_+ are compatible with their slope. Nevertheless, also in this system the hybridization of the Si edge band with the Au-induced states leads to a strong deviation that cannot be seen in photoemission. The back-folding of the electronic band structure, on the contrary, is reproduced by the numerical calculations but it cannot be seen by plasmon spectroscopy.

Furthermore, the question arises if this one-band approach is still valid. And if so, why is the plasmon spectroscopy ignoring band gaps? This issue cannot be overcome without changing the band structure. From the current point of view it seems likely that there is a selection rule defining the wave functions that contain the electrons for the excitation of the plasmon. Anyway, a one-band approximation must be the correct approach since there is only one plasmon visible in the loss spectra.

Besides, the numerical calculation only show those electronic states with a very low imaginary part that have a considering lifetime. However, there are possibly also electronic states with a relatively high imaginary part in the band gaps that participate in the formation of a plasmon.

In conclusion, the plasmon observed in Si(775) is most likely of hole-like character. The much wider terrace acting as confinement potential shifts the bands down in energy. In combination with the hybridization of the Si adatom states and the subsequent opening of band gaps, it leads to this almost entirely filled conduction band. This metallic behavior could also be confirmed by a pronounced Drude tail in the raw spectra of Fig. 7.1 (d) and, therefore, at least one band has to cut the Fermi level. These results, however, only favor the hole behavior, but they do not confirm it. By slight changes in the band structure for the unoccupied states featuring parts with an inclination comparable to those of ω_+ and smaller band gaps, the plasmon can also have its roots in those states. It is possibly correlated to a temperature dependent effect, such as a structural or electronic phase transitions. Therefore, special care has to be taken about the resulting band structures. Please add in mind that the photoemission data by Crain et al. [103] were recorded at ≈ 100 K. Their measurements should also be re-checked as their samples might have aged leading to the adsorption of OH at the step edges altering the electronic band structure of the system.

7.4.3 Si(557)-Au

The electronic structure of Si(557)-Au also features a rich variety of bands with corresponding gaps, also shown in Fig. 7.10 by the green curves. Here, the same behavior as for the Si(775)-Au system is present. The states from the Si adatom chain (band 2 at Γ), Si restatom chain (band 1 at Γ), as well as the Si edge band (band 0 at Γ) hybridize with the now single band from the Au chain. The Si honeycomb chain band is sketched in red. Only one band from the Au chain is present as the chain is only of single atomic width. Therefore, the bonding-antibonding splitting does not take place.

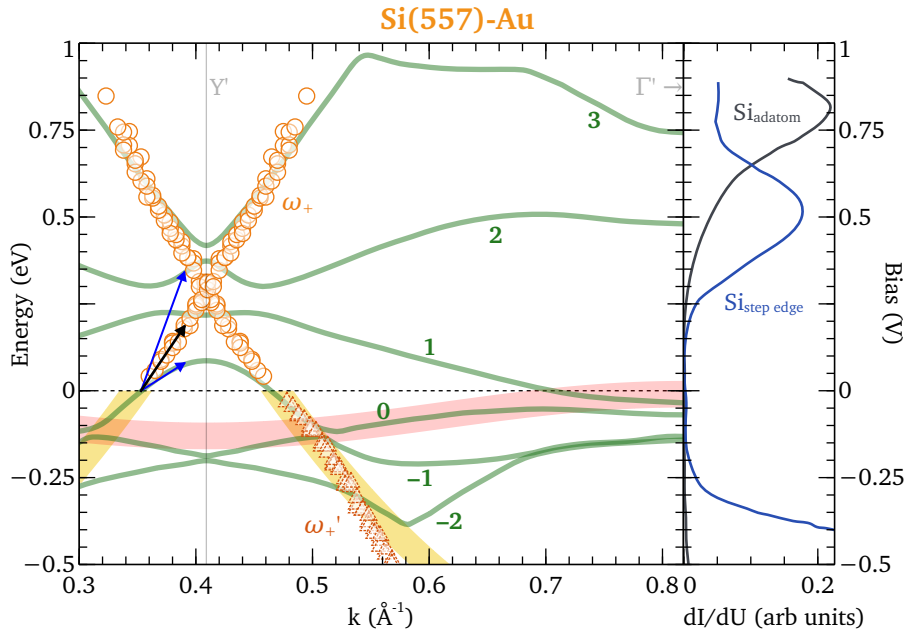


Figure 7.10: Calculated ω_+ for Si(557)-Au: The band structure was taken from Edler et al. [121] and the resulting upper boundary of electron-hole excitation was derived for the electron-like (orange circles) and hole-like (dark orange dotted triangles) case. The red line approximates the pure Si honeycomb state, yellow line shows a parabolic fit to the ARPES data [103]. To the right STS data of Aulbach et al. has been added [130] aligning the bias voltage to the energy axis.

Here, again, one runs into troubles similar to Si(775)-Au: What defines ω_+ having all these band gaps? Therefore, also the two approaches as for Si(775)-Au have been carried out. First, as a quasi-free electron situation, band 0 has been taken up to E_F for the definition of ω_- . In this case, the system features an effective mass of $m^* = 0.23m_e$, the lower boundary of the system is given by the occupied states of band 0. The Coulomb matrix element $v_c(k)$ was now calculated with a periodicity of $d = 19.2\text{\AA}$ and $w = 3.3\text{\AA}$ according to a chain of single atomic width. The resulting data for ω_+ is then given by the orange circles, resulting in a slope that reasonably agrees with the states of band 3. However, three band gaps had to be ignored for this approach.

The other case is a hole approach taking the negative curvature of band 0 into account. Here, the effective mass results to $m^* = 0.5m_e$, $v_c(k)$ is the same as for the other case. The result ω_+' is given by the dark orange dotted triangles. The data deviate from the given band structure rapidly and also ignore the present gaps.

These results are somewhat unsatisfactory, also given the fact that the band calculations seem to be fine according to the peaks in the STS spectra on the right [130]. However, if one only takes the overall excitation spectrum itself into account, the spectrum of the occupied states approximately fills the band gaps in the unoccupied region and vice versa. Therefore, the system switches between electron and

hole plasmon excitations. When reaching band 3, it is purely electron-like again.

Another possibility of ignoring the band gaps is an uncertainty of ω_+ in these band gaps. With the example for a momentum of 0.04 \AA^{-1} , indicated by the black arrow, there is no state with the same group velocity for the measured energy. It is, however, possible to make single particle excitations for that k , as shown by the two blue arrows. The black arrow is then approximately the mean vector of those other two. For this behavior, a strong increase of the peak widths is expected around this momentum.

There are also two findings in the literature that are compatible with this hypothesis. One is that the widths of the plasmon peaks in the loss spectra first increase up to 0.05 \AA^{-1} and then start to decrease again [139]. This behavior could explain the presence of the band gaps mentioned above. It was also observed in this work and will be discussed in the last section of this chapter. Furthermore, it is possible to describe the plasmon completely by quasi-free electron theory. This finding indicates the necessity for only small band gaps, which leads to an approximately-quasi-free excitation spectrum. Si(557)-Au even has the best accordance with the photoemission data from Crain et al. [103], as depicted by the yellow lines, that helped to describe the plasmon within a quasi-free electron theory [79]. Nevertheless, this single-band approach is a more satisfying explanation for the plasmon dispersion. In Ref. [139] only half of the electron density was used within a free-electron gas plasmon model. This value was motivated by spin-orbit splitting in S2. In contrast, within this work a description is possible taking all electrons into account.

Concluding these investigations on Si(557)-Au, the plasmon is described within an approach of the overall excitation spectrum that ignores the band gaps. Unfortunately, the more hybridization with different states is present, the more tricky it is to obtain the correct excitation spectrum. These multi-band structures like Si(557)-Au and Si(775)-Au also show the limits of simple modified quasi-free electron theories, as also the definition of m^* in the correlation function $A(k)$ does not have a definite reference anymore. Unambiguous predictions about the positions of electronic states cannot be given in this context.

7.4.4 Si(335)-Au

The insights gained in the previous sections are now used to apply this to the electronic band structure of Si(335)-Au [134]. This is shown in Fig. 7.11.

The green curves are the band structure as calculated for a case without spin-orbit splitting. Although LEED did not reveal a $\times 2$ streak, the system shows period doubling inside its band structure by a symmetry around Y' at 0.41 \AA^{-1} . The yellow curves represent the data as they have been extracted from photoemission [103]. Additionally, the band arising from the Si honeycomb step edge is sketched by the red line. The data up to E_F was taken for ω_- obtaining an effective mass of $m^* = 0.3m_e$. The Coulomb interaction $v_c(k)$ was computed numerically for a width of $w = 3.3 \text{ \AA}$ and a periodicity of $d = 12.6 \text{ \AA}$. The excitation spectrum ω_+ results as plotted by the green circles.

These data finally end on states for the highest depicted band and also here the approach ignores the

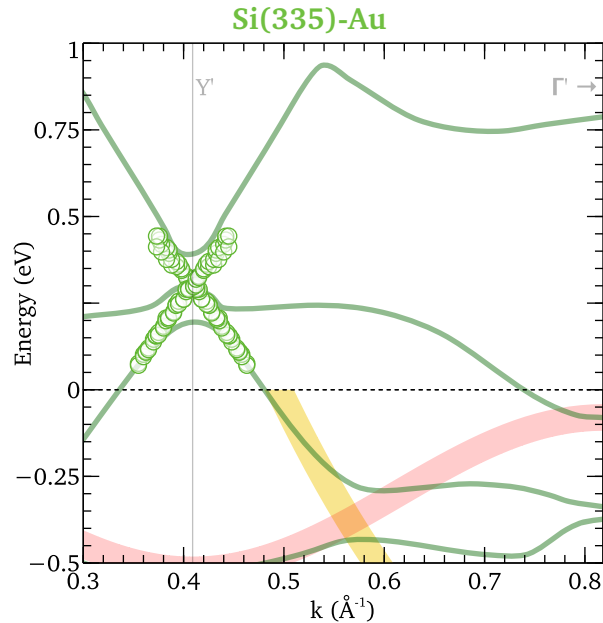


Figure 7.11: Calculated ω_+ for Si(335)-Au: The band structure in green has been taken from Krawiec et al. [134] and the lower boundary ω_- chosen to be the electronic states up to the Fermi energy. The green circles depict the calculated upper boundary ω_+ . The ARPES data of Crain et al. [103] is shown in yellow and slope of the Si honeycomb states is sketched by the red line.

presence of a band gap that results in the presence of the step-edge bands and its hybridization with the Au-induced states.

Taking a closer look at the Si step edge band in red, a much stronger curvature is observed compared to the other systems. Its shape indicates that the modularization of the structure by simply putting together all their electronic states is not as simple as suggested. The strong curvature in reciprocal space also means that the electronic states are rather delocalized leading to an additional or widened conducting channel. This different electronic landscape is a possible explanation for the nonconformity with the systematics of Tab. 7.1 that result in a bigger effective wire width.

7.4.5 Conclusions from the Excitation Spectrum Calculations

The investigated systems show various systematics: All system have in common that they at least feature a Si honeycomb edge state that was sketched by the red band. This state hybridizes with the gold bands, either the single band for the single Au chain or the two bands arising in bonding-antibonding splitting for the double atomic Au chain. This hybridization changes the lower boundary for the plasmonic excitation quite drastically so that it can no longer be described by the Au bands alone.

Additionally, the systems with a Si-adatom/restatom chain add two further bands into the structure

that also hybridize and open extra band gaps. If those gaps are small enough, the plasmon seems to ignore them and only the overall excitation spectrum is necessary for the plasmon to establish. Simultaneously the lifetime of the plasmon should increase strongly in this region. Nonetheless, the widths of the peaks in the loss spectra widen, indicating a decrease of lifetime. It is unclear why the plasmon can exist in a band gap with a finite lifetime. Therefore, a discussion of the widths is carried out in the next section. Furthermore, the plasmons can not only be described by an electronic character, especially for the systems hosting an adatom chain, i.e. Si(557)-Au and Si(775)-Au, the plasmon can also behave hole-like.

But despite all these systematics, there is still a lack of clarity about any selection rule that determines the band responsible for the plasmon dispersion. Therefore, it remains an open question which of the bands have to be taken into account for the upper boundary of the overall excitation spectrum. On the other hand, ω_- can always quite easily be found.

However, most of the parts of this single-band approach are still universally valid. Especially, the calculation of $v_c(k)$ is true for any band structure as it only takes the lateral distribution of the electrons into account. Only beginning from Eq. 3.13, the density response function χ_0 defines the system quasi-free one-dimensional. Certainly, its solution is simplistic because it only needs the upper and lower boundary of the single-particle excitation spectrum. Nevertheless, a more general choice of χ_0 is a possible way to improve the presented calculations.

Altogether, the presented systems explicitly show the possible influences in the form of dimensional crossover from 2D and 3D to the one-dimensional wire system after the assembly on a surface. The initial parabolic band structure of the Au chain is highly affected by the additional structural elements on the terrace. Hybridizations lead to a completely new electronic band structure that features also additional band gaps. These changes strongly feed back to the plasmonic dispersion. Intra- and inter-wire correlations as predicted by simple plasmon theory [25] lead to an additional blue shift in energy depending on the distance. This was explicitly shown by the HCW and LCW phase of the Si(553)-Au surface. Further screening by the bulk was treated by the choice of permittivity $\epsilon = (11.5 + 1)/2$. Due to a complicated electronic landscape, it is questionable if this is a sufficient approximation. Here, another possible step is the implementation of a k -dependent dielectric function.

7.5 Further Insight – Excitation Probabilities and Lifetimes

Additionally, an investigation of the detailed information that can be obtained from the intensities and widths of the measured plasmonic excitations is carried out. As already shown, the lateral distribution of the electrons in the wire array influences the curvature. Furthermore, the shape of the electronic band structure is an important factor for the overall slope of the plasmon. Nonetheless, other important aspects of plasmons are the excitation probability as well as the lifetime. These properties are particularly attractive for the eventual realization of future devices.

Concerning the Si(553)-Au system in both the high and low coverage phase, Fig. 7.12 shows the peak intensities of the plasmon losses with respect to the elastically scattered intensity for no energy losses at $k_{\parallel} = 0$. Two assumptions are made for this value to be the direct measure of the excitation probability:

- Inelastic scattering of electron only happens once, cf. Fig. 2.2, and the inelastic intensity is withdrawn from the elastically scattered current with $I(\Delta k = 0, \Delta E = 0) \gg I(\Delta k \neq 0, \Delta E \neq 0)$.
- Since all detectable electrons are backscattered, the elastically reflected intensity at $k = 0$ is a good reference because the probability for elastic scattering at other k_{\parallel} is only a weak function of angle.

The extracted plasmon intensities are below 1 ‰ of the elastic intensity for both systems by the red markers and decay rapidly with increasing k_{\parallel} until they can no longer be distinguished from the background noise. The excitation is around 20 % less probable for the low coverage phase, most likely due to the lower wire density on the surface. All data are fit as depicted in red lines by an empirical function given by

$$I(k) = k \times [C_1 k + (C_2 - C_3 k)^2]^{-2} \quad (7.6)$$

with arbitrary constants C_n . This fit reflects the behavior expected for a dipole scattering process of electrons with a two-dimensional electron gas on a surface as derived in Eq. 2.24 that, in a rough approximation, is also valid for a surface covered by a wire structure. Quasi-one-dimensional plasmon theory predicts similar slopes in literature [72]. Although the decaying part of the intensity for low- k cannot be resolved in the spectra, the short wavelength regime is described perfectly by this function, giving a strong indication of multipole scattering being the main process taking place during the excitation of the plasmons.

The excitation probabilities are slightly susceptible to disorder induced by the adsorption of residual gas. As given by the purple data and curves, after 12h in a vacuum of 5×10^{-11} mbar the excitation probability decreases by roughly only 30 %. This stability against deterioration even under the influence of an electron beam grants enough time to conduct the measurements.

When comparing the curves with theory [25, 72, 73], the maxima are predicted at relatively large k_{\parallel} , an outright difference to the observations. Nevertheless taking the description of Eq. 2.24, the scattering process itself also has a strong effect in the overall excitation probability. This influence is then possibly responsible for the observed behavior. Consequently and in contrast to the theoretical prediction, one can see that the given excitation probabilities do not simply measure the dynamical structure factor for plasmonic excitations. However, an energy dependent analysis is needed to subtract the impact of the scattering geometry. To this date, however, this thesis settles for the result of a lower boundary of around 1 ‰ excitation probability. A similar analysis of the intensities of the other systems is skipped.

The discussion will now focus of the measured peak broadening of the plasmon peaks. Fig. 7.13 (a), (b), and (c) as well as Fig. 7.14 (a) and (b) show the measured full widths at half maximum for all systems as extracted from the fits of the spectra in Section 7.1. All data start at large initial width for

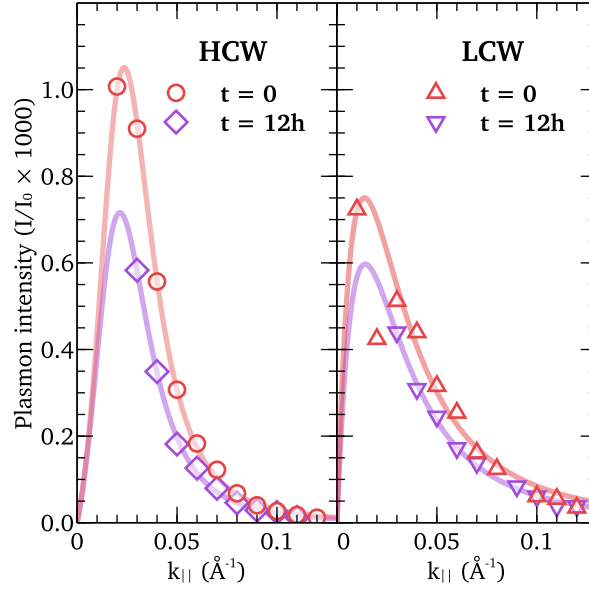


Figure 7.12: Peak intensities of the Gaussian fits for Si(553)-Au in HCW (left) and LCW (right) phase as extracted from the spectra of Fig. 7.1 (a) and (c): The data are given directly after preparation as well as after 12 h in a vacuum of 5×10^{-11} mbar and have been normalized to the corresponding elastically scattered intensity I_0 at $k = 0$ to give an estimate of the excitation probability. The fit curves are motivated by the scattering cross section of dipole scattering of chapter 2.

$k_{\parallel} = 0$ which exceeds by far the instrumental resolution of around $\Delta E = 20$ meV. The width then increases for higher k_{\parallel} . In a very simple picture, this broadening denotes a decrease of the lifetime.

Starting with the Si(553)-Au systems in Fig. 7.13 (a) and (b) and concentrating on the FWHMs in the limit of $k_{\parallel} \rightarrow 0$, it is obvious that these widths cannot be attributed to a lifetime, since in this limit the plasmonic excitation energies also converge to zero, and, therefore, they will live infinitely long. Taking these widths as lifetime would mean a highly over-damped plasmon, which is in sharp contrast to plasmons at 125 meV in comparable systems, where the mean free paths also exceed several 100 Å [160, 150].

The widths start at a slightly higher value for the HCW phase than for the LCW. As the resolution in k is only around 0.01 \AA^{-1} , this offset can be attributed to a consequential uncertainty in energy. Consequently, due to its energetically lower slope of the dispersion relation, the starting widths of the LCW system are lower. Starting from this socket as depicted by the dotted gray line, the plasmon width increases by around 40 meV in the HCW and 120 meV for the LCW phase. There are various possible reasons for this broadening. It is either related to a reduced lifetime or due to the existence of nearly degenerate excitations, such as two plasmons, as, e.g., proposed earlier in Ref. [151]. After the findings of the last section, the latter can be excluded as all electronic bands undergo a hybridization affecting the properties of only one plasmon.

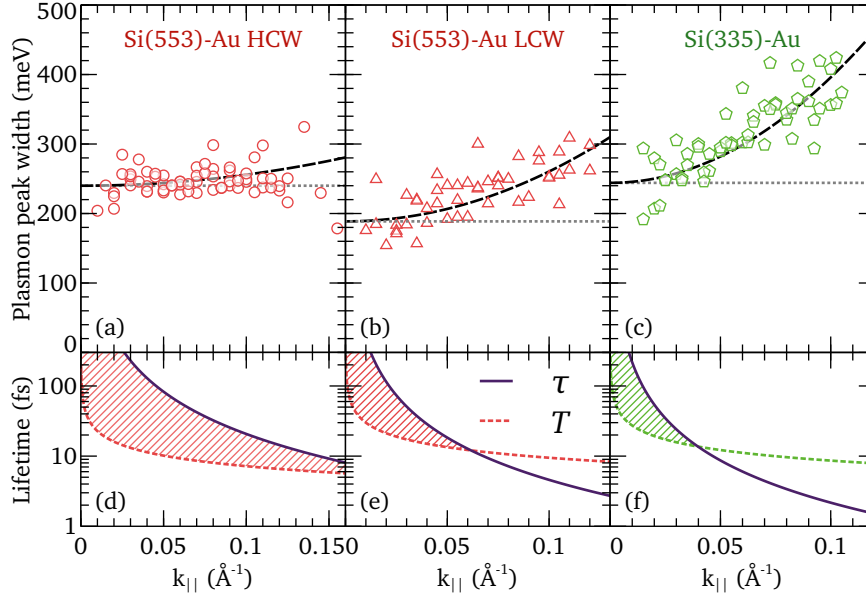


Figure 7.13: Plasmon peak widths (top) and corresponding lifetimes (bottom) for Si(553)-Au in HCW and LCW phase as well as Si(335)-Au: The linewidths in (a), (b), and (c) have been fit with a polynomial of second order. The lifetimes τ are estimated after the subtraction of the dotted offset in comparison with the oscillation period T derived directly from the dispersion relations.

Therefore, lifetime broadening alone should be a reasonable explanation for all systems. An explanation can be given by collisional damping describing short range electron-electron scattering [161] with a subsequent decrease of the lifetime for higher $k_{||}$. This approach is ignored in RPA. For two-dimensional systems, these collisions lead to a linear increase in width [162, 163]. However, there is no such approach for a quasi-one-dimensional case. The best empirical description was possible by polynomials of second order as given by the black dashed lines. Albeit the two system being of nearly the same character, the observed increase of the broadening is stronger for the LCW phase. This can only be explained by a less perfect ordering, cf. chapter 6, that increases the number of additional short-range Coulomb scattering centers and, accordingly, additionally the peak width due to lifetime broadening.

From all these data, plasmon lifetimes were estimated by assuming only Lorentzian convolution, i.e. the socket was subtracted and the resulting broadening was put into Heisenberg's uncertainty principle $\Delta E \Delta t \geq \hbar/2$ to obtain a lower limit. These estimated τ are plotted by the purple lines in Fig. 7.13 (d), (e), and (f) below the graphs showing the widths of the peaks. Additionally, the graphs contain the minimum amount of time necessary for a plasmon to emerge given by one period of the oscillation calculated via $T = \hbar/E(k_{||})$ with E taken from the dispersion relation fits.

For Si(553)-Au HCW, the estimation is above this minimum time T . The other two system start above and cut the minimum line. If the broadening is only given by the lifetime, plasmons only exist in the hatched regions. Therefore, the observed widths of the peaks must be caused by additional broadening

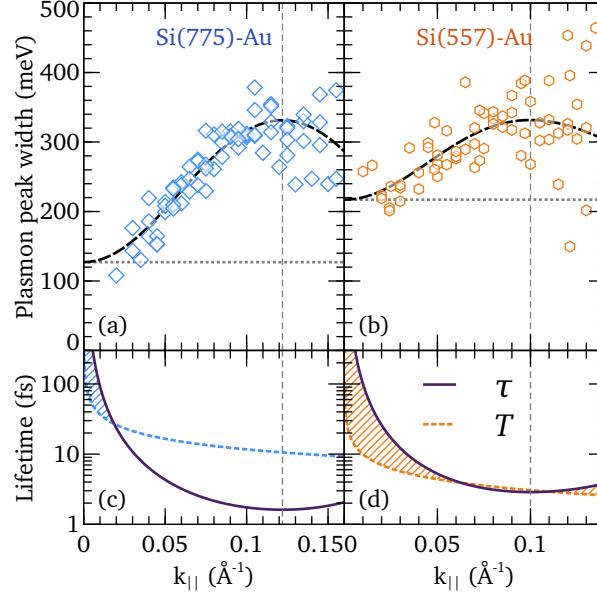


Figure 7.14: Plasmon peak widths (top) and corresponding lifetimes (bottom) for Si(775)-Au and Si(557)-Au: The line widths show a maximum and have been fit with an exponentially decay times a polynomial of second order. The lifetime estimation is the same as in Fig. 7.13.

mechanisms. The offset in width by the spectrometer was already subtracted and can, therefore, be ruled out. Furthermore, a phonon-induced effect is also excluded assuming the same mechanism in all systems as the data for Si(553)-Au HCW contain measurements for both RT and LT, cf. Fig. 7.3. A similarly strong broadening was already observed in a two-dimensional system and attributed to a damping via multiple electron-hole pair excitations induced by electron-electron scattering [162]. For a broadening beyond lifetimes, an explanation can be given by a defect-induced charge doping to the wires [113, 103]. With a geometric distribution of wires, also a geometric distribution of doping is available for the wires, leading to a geometric distribution of dispersion relations. Their difference then increases for higher k and the observed peaks will undergo an additional broadening.

A further possible influence to the widening of the plasmonic peak is the scattering geometry itself. It originates in the scattering distance and, as the distance from the atom decreases with increasing transfer of k , the scattering process becomes more and more localized. Accordingly, the uncertainty in k and, thus, also in E will increase.

Another influence is the order of the system: As estimated in the last chapter, the wires are not of infinite length. However, the definition of electronic states is highly depending on the order. The less ordered the system gets, the more softened is the definition of an electronic states for a higher $k_{||}$. This mechanism is, therefore, most likely the dominating part and explains why the broadening is that sensitive to structural disorder.

In slight contrast is the behavior of the linewidths of the plasmons for the Si(775)-Au and Si(557)-Au

system as depicted in Fig. 7.14 (a) and (b). Their slope also starts on a socket indicated by the vertical gray dashed line that is attributed to a broadening due to the resolution of the spectrometer depending on the starting slope of the dispersion relation. The width first increases up to a critical k and then decreases again. This slope is illustrated by the black dashed line. Although the scatter in the data is relatively high, this behavior was already seen in another publication, cf. Fig. 4 of Ref. [139].

A simple lifetime broadening must also be excluded here as, similar to above, the lower limit is below one period of the oscillation for various k , see Fig. 7.14 (a) and (b).

Comparing the maximum width of the curves with the calculated bands and the corresponding upper boundary of the electron-hole excitation spectrum derived from the plasmon dispersion in Figs. 7.9 and 7.10, the widths increase as long as there are no dispersing states and start to decrease when the appropriate k hits a dispersing part of the electronic band structure. This connection might be a coincidence, but in case it is real, this behavior points at another strong correlation of the single particle excitations with the collective ones apart from the upper and lower boundary being the margins for the dispersion itself. A possible explanation is a feedback of the energetic uncertainty in the band gaps. For multiple bands there are also multiple single particle excitation energies defined, as also already illustrated in Fig. 7.10 by the blue arrows.

7.6 Conclusions from the Plasmon Investigations

This chapter analyzed the plasmon peaks in the electron energy loss spectra of the various Si(hhk)-Au systems.

After a careful fit procedure, the energetic positions of the Gaussian distributions yielded the experimental dispersion relations. However, a description by simple theory was not possible. Using a free-electron gas model placed the plasmon inside the Landau regime. An empiric adjustment of a low- k approximation in Eq. 7.1 was able to describe the data and resulted in a terrace width dependence at least for the Si(553)-Au HCW and LCW, the Si(775)-Au system, and the Si(557)-Au system.

In the next part, single-band approximations of electronic band structure calculations were used to define the upper and lower boundary of the electron-hole excitation continuum. Using this band for the plasmon theory of Chapter 3, a fairly good description of the Si(553)-Au system is possible for long wavelengths. Turning around these calculations and using the experimental plasmon data together with the lower boundary of the single-particle continuum allows an experimental determination of the unoccupied electronic states and a comparison with the calculated bands of other groups. As long as the electronic band structure does not get too complicated, i.e. for Si(553)-Au and Si(335)-Au, this derivation leads to a decent overlap with DFT. Eventually occurring band gaps will, however, be ignored. For the systems with additional adatom chain, there are induced additional band gaps. In this case, the description is unsatisfactory as there are no dispersing bands where the experimentally determined upper boundary suggests electronic states.

Anyhow, this results showed the strong correlation between single particle and collective excitations. Furthermore, the differentiation between a plasmon and an electron-hole excitation is no longer possible in the picture for high momenta $k_{\parallel} > 0.15 \text{ \AA}^{-1}$, i.e. for very short wavelengths of $< 40 \text{ \AA} = 2\pi/k_{\parallel}$, although both are still different kinds of excitations. Though using this fairly simple approach, the results yield a good description of the band structure. Additionally, the finite temperature during the measurements must be considered as all calculations are for a structure at zero temperature. Therefore, possible transitions of insulating states to a metallic behavior for higher temperatures can annihilate the numerically derived band gaps.

The two approaches of this chapter both allowed an explanation for the deviation from quasi-free electron gas behavior. Though the ansatz was different, all information about the rather complex hybridizations of the electronic band structure are combined in the effective wire width. As the empiric model was only the modification of a low- k approximation, it is still only valid for this region. In contrast, the electron-hole continuum approach of Section 7.3 has its highest uncertainty in the region for small k , as it is highly susceptible to the slope of the band structure around k_F .

In the last part of this chapter, the shape of the plasmon peaks was investigated in more detail. The excitation probabilities obtained from the peak heights were shown to be 1 % of the elastic intensity at the maximum. A discussion of the widths revealed an effect beyond lifetime broadening that depended most likely on the defect density and the band gaps of the electronic states.

8

Chemisorption-Induced Modification of the Electronic Structure

This chapter deals with the possibility of changing the electronic character of the systems by adsorption of oxygen and hydrogen onto the surfaces. It is motivated by the fact of spontaneous dissociation of water molecules on the surface, forming Si-OH with the dangling bonds of the honeycomb chain [109].

8.1 Adsorption of Molecular Oxygen

A lot of dangling bonds on the surface allow for the saturation with oxygen, e.g. at the honeycomb chain or on the eventually occurring adatom/restatom chain, cf. Fig. 5.3. Due to its higher electronegativity compared to silicon, a strong localization of the electronic states involved in the adsorption process and, therefore, a modification of the electronic landscape is expected.

The procedure for these measurements was as follows: First, a sample was prepared as described in Chapter 6 with a following structural confirmation via SPA-LEED. Then, a loss spectrum was taken with the EELS-LEED for a given k at RT. It was taken care to keep this procedure as quick as possible. After this first step, the ion getter pump was turned off, and the chamber was flooded with an oxygen atmosphere of $\approx 2 \times 10^{-9}$ mbar. While keeping the chamber at this pressure, loss spectra were taken continuously with an integration time of around 20 min per scan. After several hours, when it was no longer possible to resolve any loss peak attributed to a plasmon, the measurement was stopped.

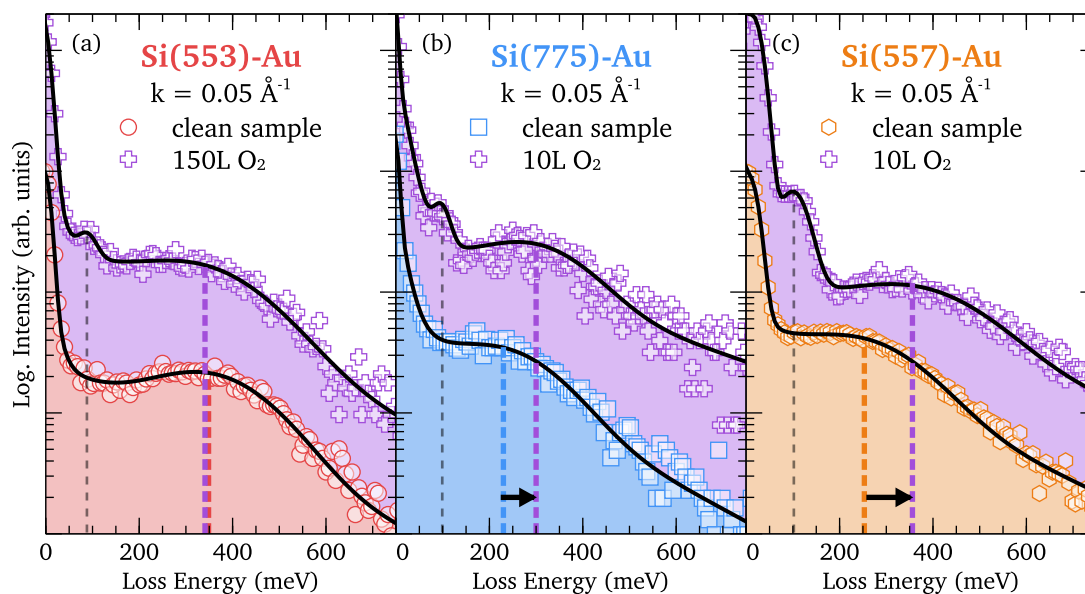


Figure 8.1: Electron energy loss spectra before and after oxygen adsorption for (a) Si(553)-Au, (b) Si(775)-Au, and (c) Si(557)-Au: A shift of the plasmon peak to higher energies is observed for the Au reconstructed surfaces of Si(775) and Si(557), no change apart from lifetime broadening is seen on Si(553)-Au. On all systems, Si-OH stretch modes appear marked by the gray dashed lines demonstrating oxygen adsorption.

The resulting spectra before the adsorption as well as after a defined amount of oxygen are depicted in Fig. 8.1. For the Si(553)-Au system in (a), there is no visible change of the position of the loss peak of the plasmon after the adsorption of 150L of O_2 . However, there is a drop in intensity and an increase in width that is most likely attributed to the induced disorder on the surface by the adsorbates. Additionally, a peak around 100 meV emerges. This peak is attributed to a Si-O stretch mode that has approximately the same energy as the Si-OH mode [153]. Thus, this behavior is an indicator that the system underwent an oxidation and built up -O onto the silicon. The generation of Si-OH bonds cannot be ruled out completely as hydrogen or water are inevitably present in the residual gas of the vacuum chamber. In any case, hydrogen is always the dominating peak in all mass spectra taken from the system.

This Si-O peak is also visible on the oxidized Si(775)-Au (b) and Si(557)-Au surface (c) indicating that similar processes are taking place. However, only a small amount of 10L is necessary to already show energetic shifts of the plasmon peaks to higher energies: From ≈ 220 meV to ≈ 300 meV for Si(775)-Au and from ≈ 250 meV to ≈ 350 meV. This is to some extent surprising, as an oxidation would typically localize an amount of electrons to the Si-O bonds reducing the electron density of the system close to E_F . From a classical point of view, cf. Eq. 3.1, a decrease in the plasmon energy is expected. A possible explanation is a change in the electronic band structure, as will be discussed in Sec. 8.2.

The change of the plasmon energy as a function of the oxygen dose is shown for the two reactive systems in Fig. 8.2 (a) and (b). The increase of the energy was normalized to the energy of the plasmon

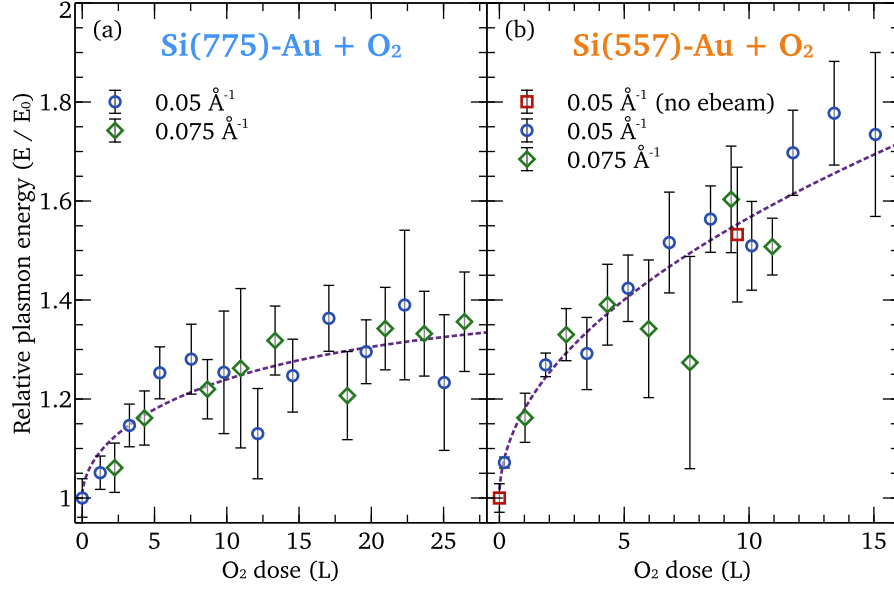


Figure 8.2: Shift of the plasmon energy as a function of the oxygen dose for the (a) Si(775)-Au and (b) Si(557)-Au surface: The energy change has a saturating square root dependence and increases up to 30 % on Si(775) after a dose of 25 L, resp. 70 % on Si(557) after 15 L.

energy without any oxygen and, thus, values for $k_{\parallel} = 0.05 \text{ \AA}^{-1}$ and $k_{\parallel} = 0.075 \text{ \AA}^{-1}$ were plotted in the same graph. The uncertainties of each data point are the direct value obtained by the fit routine within Fityk [164]. The increase of the energy can be described by a modified square root function given by

$$E/E_0 = 1 + C_1 \sqrt{1 - \exp(-C_2 \times D)} \quad (8.1)$$

with C_n as fitting constants and D the provided dose. This behavior is expected for an electron density dependence $E \propto \sqrt{n}$ and when the oxidation process donates a certain amount of electrons. The exponential part takes into account a decrease of the sticking coefficient, as it is the case for a more and more covered surface. For Si(775)-Au, the energy increases by approximately 30 % for 25 L. Visible from the fit, its shift reaches almost saturation. The Si(557)-Au system shows an energy that is 70 % higher than without oxygen already after the adsorption of 15 L. In good approximation, the fit of these data is a root function, i.e. $C_1 \gg 1$ and $C_2 \ll 1/D$, indicating a situation far from saturation.

Although only a rough approximation, data for both k values measured behave the same within the limits of their uncertainties, also the general curvature of the plasmon dispersion does not change within these limits.

Still, the question remains why only the plasmons of Si(775)-Au and Si(557)-Au change, but the plasmon of the Si(553)-Au system keep their initial energy. The main difference between the mentioned systems is the lack of a reactive adatom chain on the Si(553)-Au surface. As this adatom chain induces a $\times 2$ superstructure to the system, its intensity is expected to drop after oxygen adsorption.

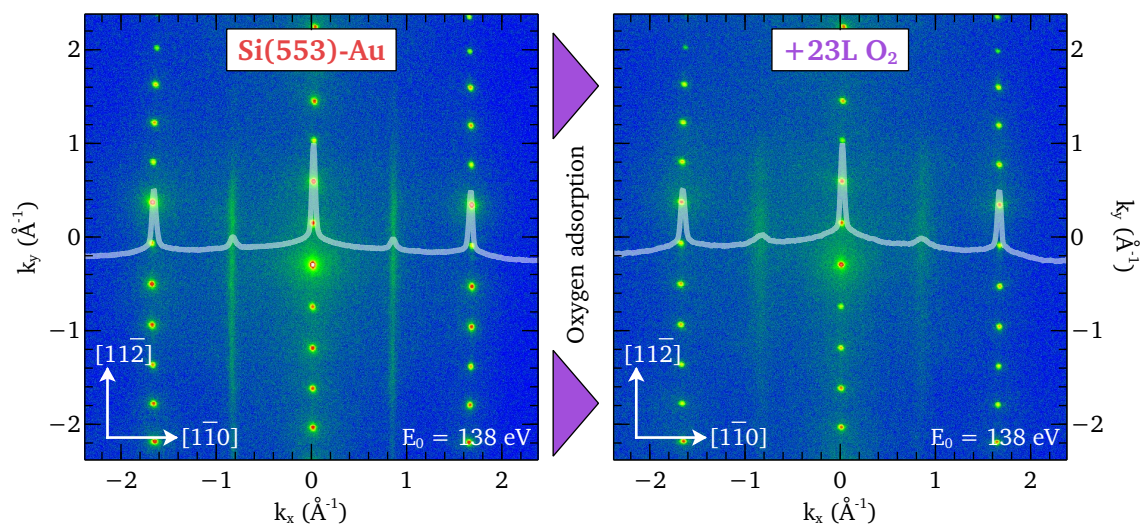


Figure 8.3: LEED patterns of Si(553)-Au before (left) and after (right) adsorption of 23 L oxygen: As line scan a sum of all k_y normalized to the central spike intensity is given in transparent white for both patterns. Apart from disorder-induced broadening, no change in the overall intensity of the $\times 2$ streak is visible.

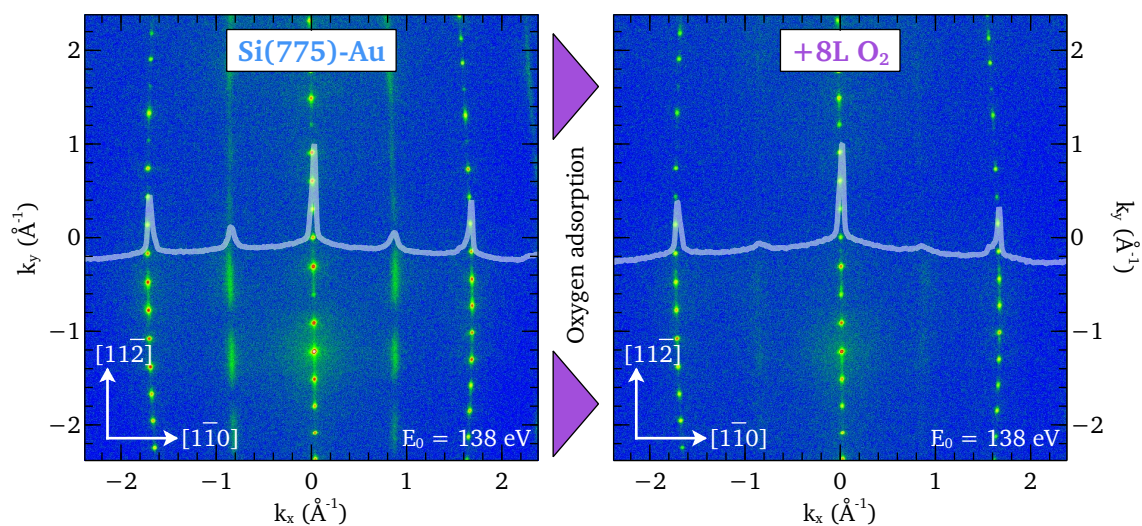


Figure 8.4: LEED patterns of Si(775)-Au before (left) and after (right) adsorption of 8 L oxygen: The line scan in transparent white on both images is the sum of all k_y normalized to the central intensity. After adsorption, this linescan sum shows a strong decrease of the $\times 2$. In the LEED image itself the streak is barely visible.

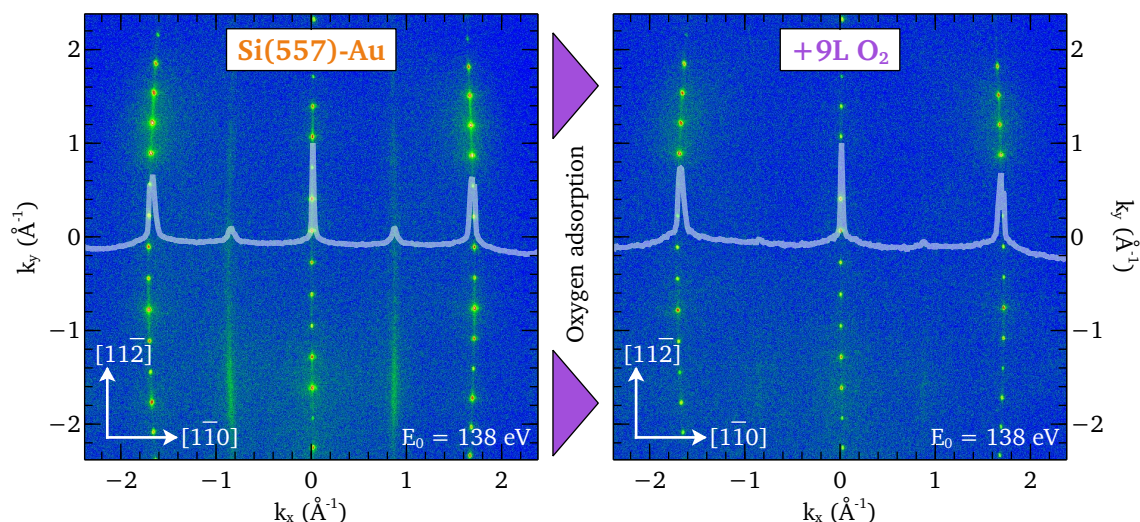


Figure 8.5: LEED patterns of Si(557)-Au before (left) and after (right) adsorption of 9 L oxygen: All k_y are summed up and then normalized to the central intensity. The corresponding line scan is shown in transparent white. The $\times 2$ intensity of the oxygen adsorbed surface almost vanishes. In the LEED image itself the streak can also no longer be made out clearly.

Therefore, the structural behavior was investigated. LEED images on freshly prepared samples were taken before and after an oxidation in an atmosphere of $\approx 1 \times 10^{-7}$ mbar and are shown in Fig. 8.3 for Si(553)-Au, in Fig. 8.4 for Si(775)-Au, and in Fig. 8.5 for the Si(557)-Au system. Additionally, an average of all line scans across the whole pattern is placed over the false color plot to enhance the visibility of occurring changes.

As can be seen for Si(553)-Au, the $\times 2$ streak, invoked by only the double Au chain is still existent after the adsorption of 23 L. Nonetheless, because of the adsorption of oxygen and the subsequent disorder on the surface, it is albeit washed out, i.e. an increased width and a decreased intensity of the central spike. For all k_y line scans have been extracted and normalized to its central spike intensity. They are plotted as an overlay to the LEED images. Here, the effect just described is visible more clearly. In combination with no energetic shift of the loss peak, it can be concluded that the structure as well as the electronic states responsible for the plasmon remain unchanged.

LEED images for the Si(775)-Au and Si(557)-Au surfaces before and after oxidation with 8 L, respectively 9 L oxygen dose show a decrease of the overall intensity of this $\times 2$ streaks. This effect is even better visible for the sum of all k_y in the white overlay. Where for the Si(775)-Au system still a very faint intensity of $\approx 10\%$ can be seen, it is barely there for the Si(557)-Au system. This is possibly attributed to the fact, that for Si(775)-Au the $\times 2$ streaks are not only generated by the step edge, but also by Au chain periodicities. These results give a strong indication that the reactive adatom chain is responsible for a modification of the electronic surface structure. It has also already been shown by DFT calculations that the adatom site is more favorable for adsorption than the honeycomb chain by 250 meV [121]. Still,

the adatom chain on Si(557)-Au is most likely more reactive than the Si(775)-Au system as both the plasmon energy as well as the LEED intensity changes are stronger for the same amount of oxygen.

8.2 Oxygen-Induced Modifications of the Electronic Band Structure

As already pointed out above, an increase of the energy of a plasmon for a given k can be correlated to an increase in electron density for a quasi-free-electron gas character. Therefore, one approach is to look at the deviations from this simple model in the form of a single-band approach, as already carried out in Chapter 7. Electronic band structure calculations for Si(557)-Au surfaces that were oxidized on various sites are available from the Paderborn group, cf. Ref. [121]. Unfortunately, no such calculations exist for the Si(775)-Au surface so far.

These data are shown in Fig. 8.6 (a), (b), and (c) for a region from Γ over the Brillouin zone boundary Y' at 0.41 \AA^{-1} to Γ' . The unoxidized band structure is plotted for all graphs by the green dotted lines. The calculations are carried out with an explicit $\times 2$ superstructure in the adatom/restatom chain as described in Chapter 5. In (a) the blue lines display the case of the oxidation of the adatoms of the system, i.e. only the dangling bonds of the black balls in Fig. 5.3 (d). In comparison to the single-band approach of the clean surface in dashed grey, the slope of an idealized single-band slope (in dotted black) is decreased slightly. The Fermi wave vector changes from 0.35 \AA^{-1} to 0.37 \AA^{-1} and an one-band extrapolated effective mass at the Fermi energy changes from $0.13m_e$ to $0.23m_e$.

When additionally oxidizing the restatoms, cf. bright blue balls in Fig. 5.3 (d), the electronic band structure is described by the red lines of Fig. 8.6 (b). In this case, the slope of the single-band approximation given in dotted black has the same slope as for the unoxidized state. The extrapolated Fermi vector changes drastically to 0.4 \AA^{-1} leading to a filled state with a band-gap in the band structure. The effective mass of the idealized one-band-approximation is now $0.5m_e$.

A third case is given by the adsorption of oxygen at the honeycomb chain site next to the Au chain. These data have been obtained via private communication with Simone Sanna from Paderborn and are shown by the purple lines in Fig. 8.6 (c). In this case, the system has a lower k_F of only 0.27 \AA^{-1} . This means a reduction of conducting electrons compared to the other cases with an increased electron density. A single-band approximation again has a similar slope compared to the unoxidized state, with an effective mass of $0.37m_e$ at the Fermi level.

These single-band-approximations of the derived numerical data have been used to calculate a single-particle excitation spectrum with its margins ω_{\pm} . Together with the effective mass at the Fermi level, an approximation of the plasmonic dispersion relation was carried out as given by Eq. 3.13 and as already done in Chapter 7. The resulting dispersions are depicted by the colored lines for each system and by the gray dotted line for the bare Si(557)-Au in Fig. 8.7 (a). Although the single band approximations differ strongly in their lower boundary ω_- that is given by the part of the band below E_F in these cases, its feedback is of minor influence. The key ingredient to the plasmon dispersion is the slope of ω_+ as

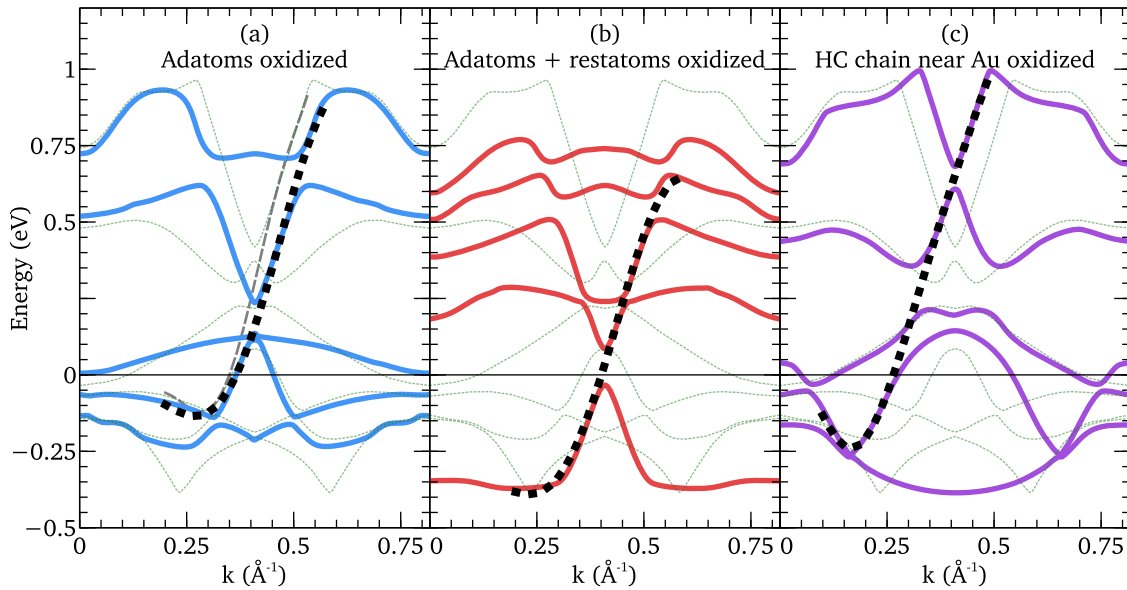


Figure 8.6: Electronic band structures after oxidation of various sites on the Si(557)-Au surface: Calculations have been carried out by Simone Sanna et al. [121] for oxygen on (a) the adatom of the adatom chain, (b) both the adatoms and the restatoms, and (c) the honeycomb chain near the Au. The original bands are given by the green dotted lines. The single band approximations for the plasmon computations are marked by the black dotted lines. In (a) also the single-band approximation for the bare Si(557)-Au surface is given by the gray dashed curve.

already realized and explained in the last chapter.

Compared to the original plasmon, the dispersions after the oxidation of the adatoms and restatom or the honeycomb chain lead to a plasmon that is only slightly increased in energy for a given k_{\parallel} and has its highest differences around 0.05 \AA^{-1} . The blueshift is only 11 % for the oxidation of both adatoms and restatoms as illustrated in Fig. 8.7 (b). The blueshift for honeycomb chain oxidation is even of only 6 %. A difference to the observed 80 % is too high to be attributed to uncertainties of the various methods. Also, the oxidation of merely the adatoms leads to a redshift of the plasmonic energy of -14% compared to the bare Au reconstructed surface within this single-band approximation. Moreover, this adatom oxidation is proposed to happen first. A first decrease of the plasmon energies cannot be observed though. A possible explanation for the findings of Fig. 8.2 (b) is a surface that is already oxidized directly after preparation due to a little amount of oxygen and water available in the chamber during the evaporation process. The difference between merely adatom oxidation and the oxidation of both adatoms and restatoms is as high as 30 % and is, then, only an underestimation of what is happening. Due to the special care that has been taken to avoid such contaminations, this origin can calmly be ruled out.

However, DFT calculations usually make an error in energy for states far away from the Fermi level.

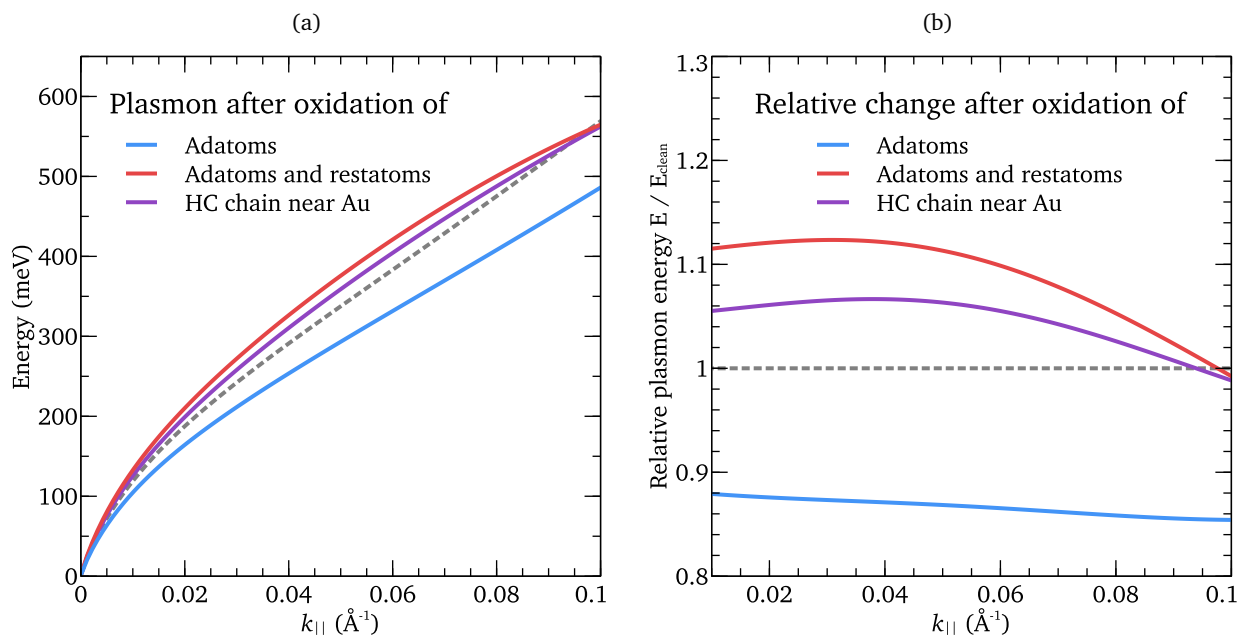


Figure 8.7: Dispersions (a) and relative energy changes (b) of the calculated plasmons after oxygen adsorption: For the adatom and restatom or honeycomb chain oxidation, a small increase in energy results for the plasmon. In case of only an oxidation of the adatom atoms a decrease of the plasmon energy will result.

This result is due to the nature of DFT itself only taking into account the electron density leading to an incorrect description of intermolecular interactions, e.g. charge transfer processes. Therefore, the uncertainty of the calculations made in Fig. 8.6 is not necessarily the same for all depicted electronic band structures. Moreover, the bands in the given form can be an incorrect description of the oxidation process. In these cases, the bands are not suited to describe the variation of the plasmon after oxygen adsorption.

Additionally, DFT does not take into account anything related to kinetics on the surface. Although such oxidation probabilities arise from different bonding energies, the impact site probability of every impinging oxygen molecule is normally distributed on the whole surface. Therefore, if the encountered position allows for oxidation, it also will take place. However, the description of electronic transport in an oxygen atmosphere was explained by a preferred bonding location [121]. Nevertheless, there must be a big overlap of the two analogous processes. Furthermore, other sites that allow for oxidation must also be oxidized during the time in an oxygen atmosphere.

Therefore, calculations of an electronic band structure that has all possible sites in an oxidized form could prove very useful. In particular, that means an oxidized adatom, restatom, and honeycomb chain. If the systematics of an increase of the Fermi level, as depicted in Fig. 8.6 (b), remain the same for (c) with additional adatom/restatom oxidation, a strong shift of k_F is expected because of the flat band

around E_F . Such a shift in combination with only a weak change of the upper bands can then explain the very strong increase of the plasmon energy.

Certainly, all these considerations are just rough approximations. There are certain other knobs that can be adjusted during an oxidation of the surface that feeds back to the plasmon dispersion via $A(k)$, cf. Eq. 3.13. The blueshift for low k values strongly depends on the effective wire width, cf. Sec. 7.2. Therefore, a possible confinement of the conducting channel induced by the oxidation of the adatom/restatom chain will influence the energy of the plasmon. The use of the empirical approach of Sec. 7.2, e.g., results in an effective width of 58 % of the original conduction channel for the Si(557)-Au+O₂ surface (76 % for Si(775)-Au+O₂).

Additionally, by the saturation of bonds on the surface the dielectric function in the vicinity of the wires changes such that an approximation with $\bar{\epsilon} = (11.5 + 1)/2$ is not necessarily a good approach anymore.

Anyway, the agreement with simulations is unsatisfying up to now. Albeit a rough systematic understanding of the influences on the electronic band structure to the plasmon dispersion, the present theoretical data cannot describe the strong changes in plasmon energy observed in the experiment and, therefore, need further refinement. The discussion revealed possible critical steps that must be clarified before a clear explanation can be given. However, as the bands can describe the transport properties seen in another experiment [121], they must already represent a good starting point for further theoretical investigations.

Experimentally, the determination of a complete plasmonic dispersion for a given amount of oxygen can help to identify its influence to a high degree. Additionally, a numerical DFT analysis for the Si(775)-Au would be highly useful to see the similarities during oxidation. Their electronic band structures can then help understanding the systematics in those two related systems.

8.3 Adsorption of Atomic Hydrogen on Si(553)-Au

Apart from oxidizing the surface, also a hydrogenation of the Si(553)-Au system was carried out. Instead of only keeping the sample in H₂ atmosphere, a self-build hydrogen cracker was used to increase the reactivity with the surface by the use of atomic hydrogen. See also Chapter 4 for a description of that hydrogen cracker.

The procedure was similar to the oxygen adsorption: After the preparation of the sample and its structural determination in LEED, an electron energy loss spectrum was acquired for a finite k . The sample was then turned to face the hydrogen cracker. After turning off the ion-getter pump, hydrogen was let into the chamber via a small capillary with its outlet directly at the filament of the cracker, see Fig. 4.5. While holding the chamber at 2×10^{-8} mbar, the pumping speed and accordingly the throughput of hydrogen was determined to around $\approx 1 \times 10^{-9}$ mbar/s. This hydrogenation was carried out at RT.

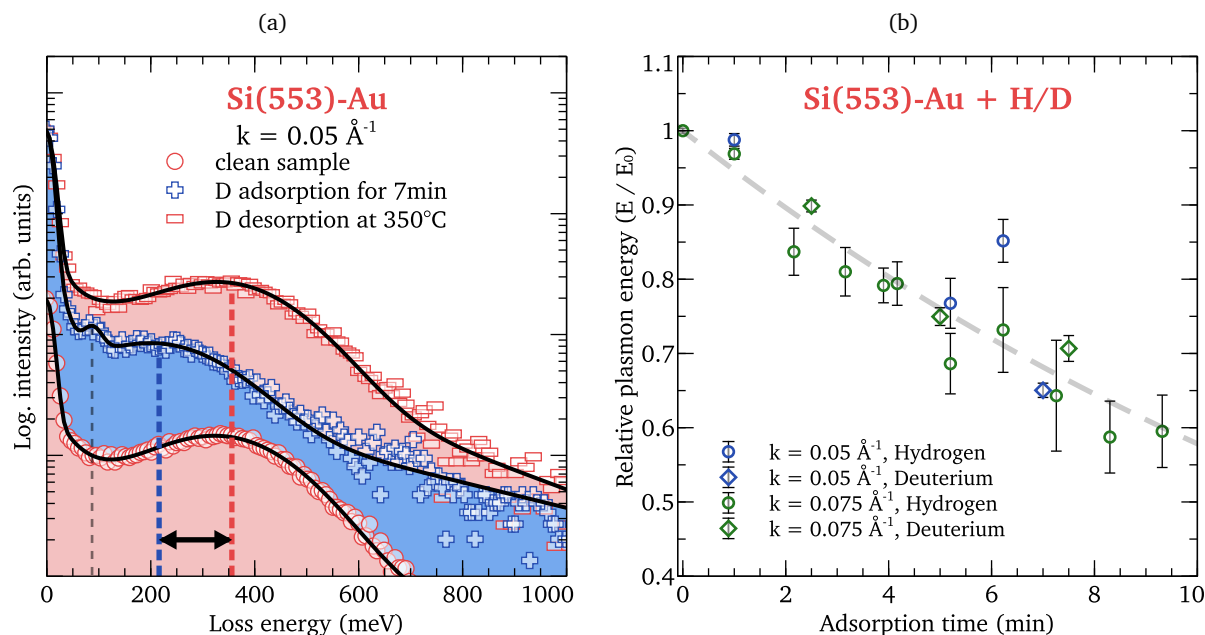


Figure 8.8: Electron energy loss spectrum at $k = 0.05 \text{ \AA}^{-1}$ before and after adsorption of atomic deuterium as well as desorption (a) and relative change of the plasmon peak (b): In (a) a strong shift of the plasmon energy to lower energy can be observed after oxygen adsorption. This shift is reversible after heating to 350°C . After this process, a Si-OH stretch mode can be seen in the spectrum depicted by the gray dashed line. The behavior of hydrogen and deuterium doping for various k values over time is depicted in (b). After 10 min the plasmon peak could no longer be resolved in the spectrum.

A rough approximation of the flow of atomic hydrogen is possible as follows: Estimating the volume of the chamber with 50l and the dissociation efficiency of the simple hydrogen cracker with 5% [94], a flow of around $1 \times 10^{11} \text{ cm}^{-2} \text{ s}^{-1}$ of atomic hydrogen will hit the sample with its area of 0.75 cm^2 .

The filament was turned on for a defined amount of time. After this adsorption process the hydrogen flow was stopped and the ion getter pump turned back on. The sample was rotated to face the EELS for a new loss spectrum. To rule out effects of residual gasses, e.g. hydrogen, the measurements were additionally carried out with deuterium. The same procedure was also performed without a hydrogen flow leading to no results. Therefore, filament-induced effects can safely be ruled out.

The resulting spectra before and after 7 min of adsorption time are depicted in Fig. 8.8 (a). A shift of the plasmon peaks to a lower energy is directly visible. From a classical point of view, this result is to some extent surprising as the saturation of the dangling bonds leads to an increase of the electron density at k_F . A description will be given below that is again attributed to the electronic band structure. Beside this energy shift, an emerging peak around 100 meV is found that is again attributed to a Si-OH stretch mode [153]. The appearance of this mode indicates a simultaneously happening oxidation by

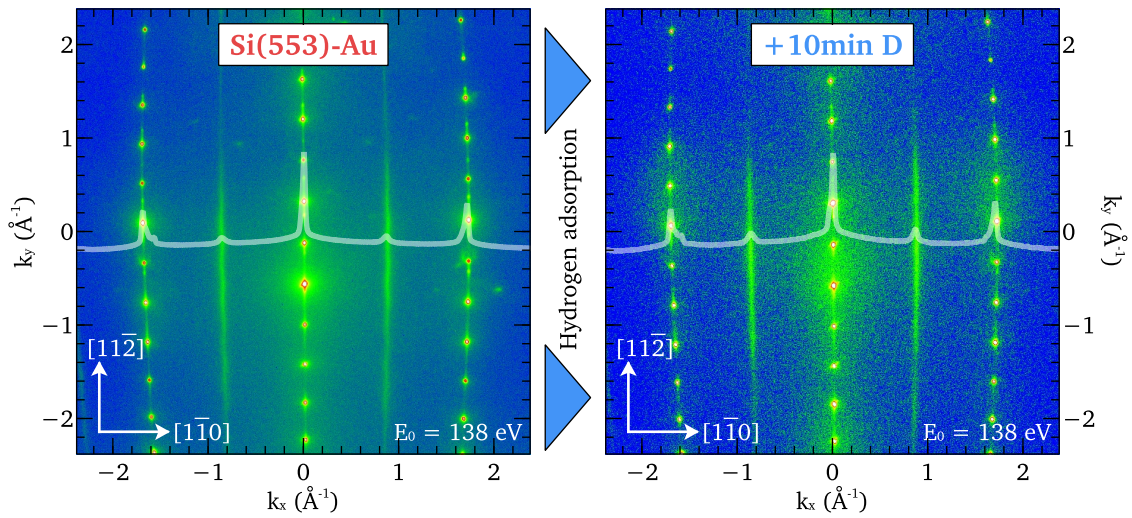


Figure 8.9: LEED patterns of Si(553)-Au before (left) and after adsorption (right) of deuterium: All k_y are summed up and then normalized to the central intensity. The $\times 2$ intensity of the oxygen adsorbed surface does not change.

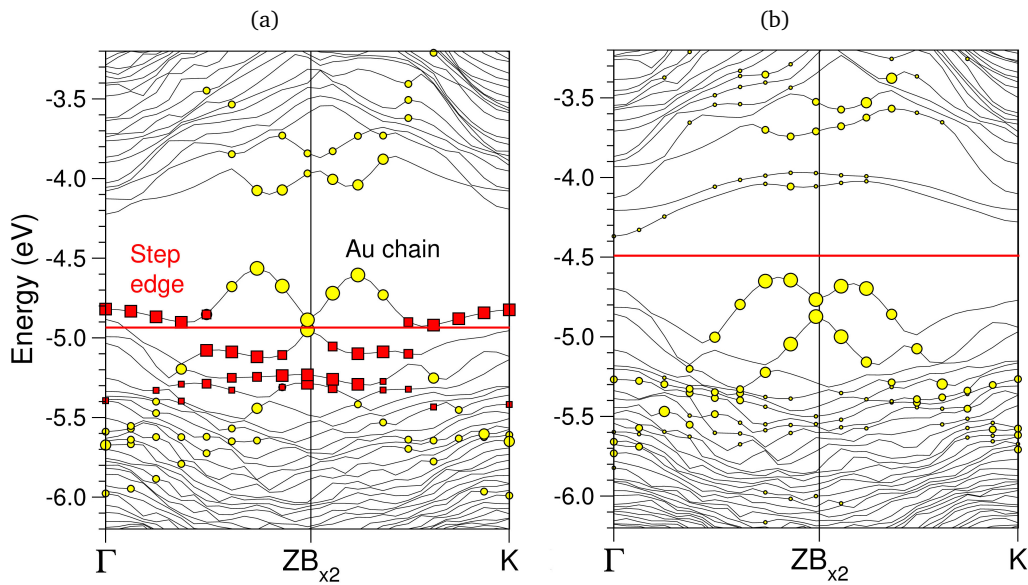


Figure 8.10: Theoretical prediction of the changes in the electronic band structure after hydrogenation of a Si(553)-Au surface. (a) Electronic band structure after preparation. (b) After hydrogenation the whole band structure is shifted downwards in energy. The image was provided by Conor Hogan [157].

residual oxygen in the vacuum as observed in Fig. 8.1 (a). However, the formation of Si-OH is without an effect to the plasmonic excitation according to the findings of section 8.1. Additionally, a spectrum after a short heat-up of the sample to 350 °C is plotted in this figure that leads to the primary plasmon excitation as for the as-prepared surface. It has the minor difference of a slightly higher width due to increased disorder. Nevertheless, this procedure shows the possibility of cleaning or refreshing a sample. Preparing the samples at 500 °C is, therefore, a temperature high enough to lead to a hydrogen-adsorbates-free surface.

Fig. 8.8 (b) shows the time dependence of the exposure shift of the plasmon energy for $k = 0.05 \text{ \AA}^{-1}$ and $k = 0.075 \text{ \AA}^{-1}$ as a function of both hydrogen and deuterium adsorption. For both momenta and adsorbates, the shift is the same within the uncertainty of the experiment and it decreases to 40 % below the plasmon energy for the clean surface after 10 min.

LEED images before and after the adsorption of atomic hydrogen on the surface are shown in Fig. 8.9. Within the resolution of LEED, there is no change visible. Summing up all k_y of the pattern, the resulting curves that are given in white as an overlay show no differences in the overall intensity of all peaks. Various additional spots on the pattern for both surfaces are due to refaceted areas. This is a typical result of a sample that has been used frequently.

An explanation of the plasmon shift is possible by an electronic band structure discussion: During the adsorption of hydrogen on the dangling bonds of the step edge, the Fermi level of the system shifts upward in energy [157], see also Fig. 8.10. Therefore, the curvature observed in Fig. 7.7 is reached earlier. These changes in ω_+ then lead to an overall decrease for the plasmon itself although the system's electron density increases. An increase in energy is expected after a certain amount of hydrogen, as here the system to swaps ω_+ and ω_- . This region could not be resolved.

For the case of 10 min adsorption time, a Fermi level shift of around 300 meV is necessary to modify the plasmon in the picture developed. Assuming a nearly linear dependence of this shift on the amount of hydrogen adsorbed on the step edges in the data provided by Hogan et al. [157] in Fig. 8.10, a step edge saturation of around $\theta = 50\%$ can be approximated. This value is compatible with the atomic hydrogen flow estimated above and a step edge density of $1 \times 10^{14} \text{ cm}^{-1}$. Those values result in a coverage of the step edge of 60 %.

These findings show the simple picture elaborated in Chapter 7 to hold true even for a changing Fermi level and, thus, qualitatively describe the observed behavior.

8.4 Conclusion from the Adsorption Experiments

This chapter showed the possibility of tuning the plasmon energy by chemisorption on the surface with both oxygen and hydrogen. After several Langmuir of oxygen adsorption, only the systems hosting a restatom/adatom chain showed a perceivable change in the plasmon energies. This was attributed to the high reactivity of this structural element. When bringing in the electronic band structure, the

system ends up in a drastic change of the electronic states. This is in stark contrast to simply changing the filling factor of the band structure. Therefore, although reducing the electron density, the plasmon dispersion relation increases in energy. The available numerically derived electronic band structure was not able to reproduce this behavior, though. This result suggests a calculation of bands for a surface with simultaneously oxidized adatom, restatom, and honeycomb chain.

Hydrogen adsorption, in contrast, resulted in an energetic decrease of the plasmon dispersion though an increase in the electronic density around k_F is expected. Numerical calculations of Hogan et al. [157] show the bands shifting downwards in energy. As there is a back bending in the bands, the slope feeds back to the plasmon reducing its energy.

The results of this chapter also show the vigorous influence of gasses that are also present inside the residual gas of most of the UHV vacuum chambers. Therefore, special care must be taken during measurements to obtain results from a pure Si(hhk)-Au surface.

Furthermore, the findings demonstrate the big differences in the presented adsorption processes: The description of hydrogen adsorption results in a rather simple picture. The Fermi level of the pure system is shifted up, leaving the band structure almost untouched. As the adsorption is only acting locally, this behavior illustrates a kind of proximity effect that makes it still comparable to a doping process. In contrast, the oxidation of a Si(hhk)-Au surface with adatom/restatom chain leads to electronic bands that are strongly disturbed, cf. oxidation of Si(557)-Au in Fig. 8.6. Therefore, here the original doping picture is no longer valid.

Part III:

Gold-Induced Wires on Ge(100)

Introduction to Ge(100)-Au

In the last part, the nanowires were grown on a vicinal silicon substrate. Their inclination was the boundary condition for the induced structure after Au adsorption. This part will show a different approach of forming a quantum wire system: the intrinsic surface structure of the Ge(100) surface will guide the growth. Therefore, this chapter will first cover the basic structural properties of the bare Ge(100) surface. Afterward, a summary of its Au covered reconstructions will be given together with the current knowledge about the electronic properties.

9.1 The Pristine Ge(100) Surface

Germanium is very similar to silicon. They share the same crystal structure, with the lattice constant for Germanium¹ being a slightly bigger with $a_{\text{Ge}} = 5.658 \text{ \AA}$. The germanium bulk has a direct band gap of 0.8 eV and an indirect one of 0.66 eV. The melting point, however, is at 937°C, significantly lower than for silicon (1410°C) [165].

Also, the surface properties are similar when cleaving a crystal along a defined lattice plane. When cutting along the [100] direction, the system results in a square lattice with a surface lattice constant of $a_{\text{Ge}}/\sqrt{2} = 4.001 \text{ \AA}$. It is tilted 45° to the bulk lattice, and in one direction an additional atom is sitting $1/4a_{\text{Ge}}$ above with two dangling bonds that are aligned upward to the left and right as illustrated by the gray balloons in Fig. 9.1 (a). As this unreconstructed surface is energetically unfavorable, a (2 × 1)

¹from Ioffe Institute: <http://www.ioffe.ru/SVA/NSM/Semicond/Ge/>

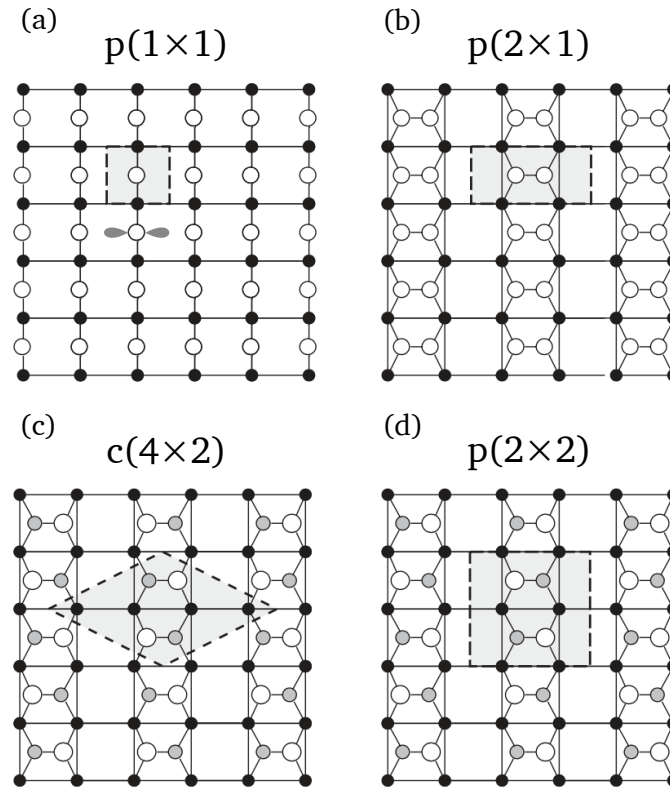


Figure 9.1: Surface reconstructions of the bare Ge(100) surface: (a) Unreconstructed surface with dangling bonds indicated by the gray balloons. (b) Dimerization to a $p(2 \times 1)$ reconstruction to reduce dangling bonds. Further reduction of the surface free energy by the formation of a buckled dimer is possible by arrangement into (c) $c(4 \times 2)$ reconstruction with alternating buckling perpendicular to the dimer rows or (d) $p(4 \times 2)$ reconstruction with oriented buckling. Image from Ref. [165].

reconstruction model was proposed where the number of dangling bonds is reduced [166] as depicted in (b). This (2×1) is confirmed by LEED. The dimers will buckle spontaneously to reduce the surface energy even further by the opening of a gap between occupied and unoccupied states [167], cf. Fig. 9.2. In this buckled case, a charge of $0.1e$ is transferred from the lower to the upper atom of the dimer [165]. These buckled dimers align in a $c(4 \times 2)$, alternating as depicted by Fig. 9.1 (c). The other possible $p(2 \times 2)$ superstructure has a similar surface free energy. It is, however, less favorable when thinking in a simple model of dipole-dipole interactions [165].

This discussed superstructure will now form dimer rows on a given substrate. However, as a sample is never completely flat, there will always be a distribution of two domains on the surface that are tilted by 90° and separated by steps of single atomic height $= 1/4a_0$.

Nevertheless, these calculations are carried out at zero temperature. The system will, therefore,

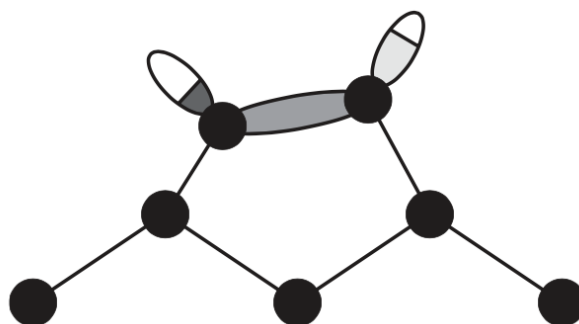


Figure 9.2: Side view of a buckled dimer: The buckling leads to a charge transfer from the lower atom to the upper atom increasing the gap between occupied and unoccupied states. Image from Ref. [165].

only exhibit the $c(4 \times 2)$ reconstruction for low temperatures and undergo a phase transition between 100 K and 250 K [168, 169, 170]. The room temperature phase consists of an admixture of $p(2 \times 1)$ and $c(4 \times 2)$ domains [171] that will align parallel in stripes on the surface [40]. The composition of this phase is due to anisotropy in the tensile stress component along the dimer bonds [172]. By the formation of an ordered domain pattern, the surface free energy is lowered although the generation of domain walls is energetically unfavorable. The $p(2 \times 1)$ part of such patches is then generated due to a fast thermal switching between both possible buckling orientations. Accordingly, the system will exhibit a large population of (2×1) at elevated temperatures and above $\gtrsim 320$ K the surface fully converts into these domains [40].

However, already small amounts of defects in the form of strongly bonding C-atoms have an influence on this ordered domain pattern as the surface stress is then reduced here, and the formation of the $c(4 \times 2)$ reconstruction is inhibited [168]. On the contrary, another kind of defect in the form of a missing dimer can lead to step pinning that is known to stabilize a reconstruction [173]. These effects can also influence and hinder the growth of metal-induced superstructures on top of the substrate.

9.2 Structure upon Adsorption of Au

First investigations with ML adsorption of gold on a Ge(100) surface were carried out in 1988 by Benson et al. [174]. However, they did not find a reconstruction, most likely due to an imperfect surface preparation. Later experiments of Wang et al. [175] showed the growth of a nanowire structure similar to the ones induced by Pt [176]. Deeper STM investigations revealed that the primary part, i.e. ≈ 0.1 ML of the adsorbed gold moves beneath the surface, resulting in islands with stabilized germanium dimer rows [177]. With increased adsorption, the Au-induced wire phase grows on the surface in islands.

An excellent ATM overview picture of the surface has been published by Mocking et al. [178], and is displayed in Fig. 9.3: The figure shows an STM image of $100 \text{ nm} \times 100 \text{ nm}$. A flat surface will have an

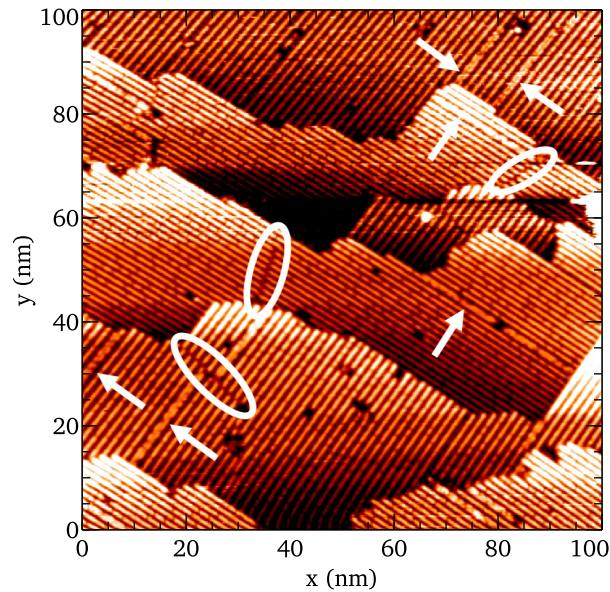


Figure 9.3: Overview STM image of the Ge(100)-Au surface: Wires will form on two evenly distributed domains. Arrows denote double wires, ellipses mark phase defects. The image has been taken from Ref. [178]. The sample bias is -1.5 V , the tunnel current is 0.5 nA .

equal distribution of wire domains that are perpendicular to each other. Their crystallographic directions are $[110]$ and $[\bar{1}\bar{1}0]$ and the direction changes with each monoatomic step. The wire spacing of 16 \AA is four times the surface lattice constant. In between, there are trenches whose depth cannot be clearly measured with STM. Schäfer et al. [179] propose a profile that matches best to a single atom with a height of around 1 \AA , whereas Van Houselt et al. [180] see a depth of 6 \AA , approximately four atomic layers of the Ge(100) substrate. This difference is possibly related to various tip shapes, e.g. blunt and sharp, and its real value might be even higher.

Additionally, Fig. 9.3 shows typical defects on the surface: the formation of a double wire as marked by the arrows, phase defects surrounded by the ellipses, and vacancies seen as dark interruptions of the wire structure. Further details can be found in the Ph.D. thesis of Tijs Mocking [181].

A schematic of the detailed alignment of these wires is given in Fig. 9.4 taken from Blumenstein et al. [182]. It shows the protruding wires with a $c(8 \times 2)$ reconstruction aligned in an additional zig-zag $p(4 \times 1)$ superstructure that might be either upward or downward depending on a stacking fault. This rather complicated superstructure explains the LEED pattern observed in Fig. 10.7 of Chapter 10. Note that the zig-zags are only visible in the occupied states. This additional superstructure leads to another kind of defect: Because of a break in the periodic extent of the VW-structure, flipflop dimers can occur that will change their orientation as observed during an STM scan [178]. Furthermore, the $p(4 \times 1)$ undergoes a second order phase transition around $300\text{ }^\circ\text{C}$.

Due to its growth behavior and the fact that the $c(8 \times 2)$ reconstruction is already visible in LEED for

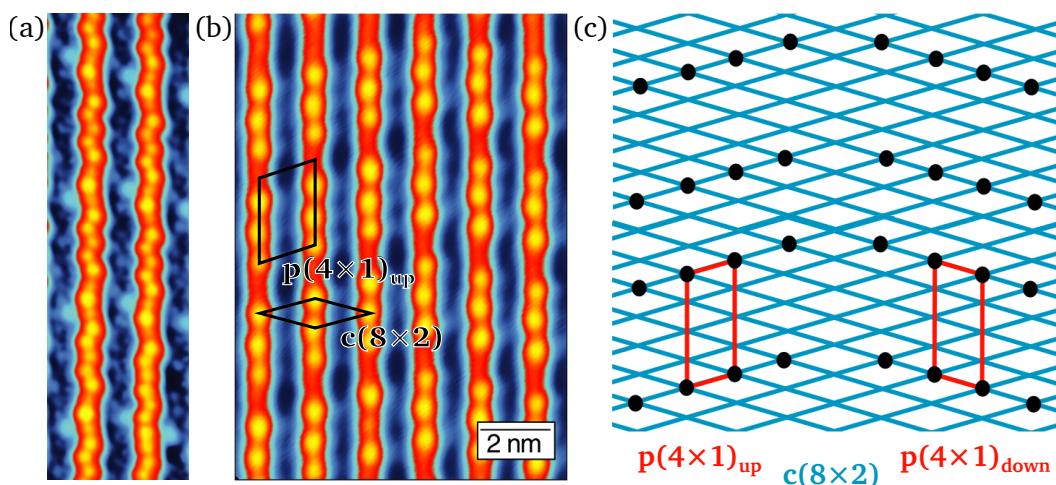


Figure 9.4: Internal structure of the induced wires: (a) Occupied states of the wires show a zig-zag-VW superstructure ($U = -0.8V$). (b) Unoccupied states only show an intensity triplet ($U = 1.6V$, $I = 0.4nA$). The wire reconstructions are aligned to each other in an additional $p(4 \times 1)$ superstructure. (c) Schematic of the wire alignment. The data have been taken from Ref. [182] and are all at 4.7K.

coverages as low as 0.3 ML, a considerable mass transport on the surface must be assumed [183]. After covering the sample to saturation, three-dimensional clusters will form [177, 180, 184].

However, the amounts of gold necessary for the saturation of this structure differ between the various publications available: Wang et al. [175] report a saturation of 1.5 ML, Schäfer et al. [179, 185] give a value between 0.5 ML and 1.0 ML, Van Houselt et al. [180] only evaporated a coverage of 0.2 to 0.3 ML, and Gallagher et al. [183] talk about a saturation coverage of 0.75 ML. Although giving their temperature during deposition, only Wang et al. [175] talk about their deposition rates. As gold is soluble in germanium up to a ratio of 2×10^{-5} [186] corresponding to around 100 ML on a sample of 1 mm thickness, diffusion of the gold into the bulk over time and moderated by the preparation temperature cannot be ruled out. Additionally, the calibration of an evaporator is delicate and can lead to false information, cf. Chapter 4. Nevertheless, a good approximation from all these data is a coverage of 0.8(4) ML necessary for the preparation of the structure.

This uncertainty in gold amount gave an ample scope for structural models, a selection is illustrated in Fig. 9.5: (a) shows the Heterodimer/Au-Homodimer (HD/AD) model from an SXRD analysis of Meyer et al. [187] in side and top view. It corresponds to 0.75 ML. On top of the top view is an overlay of the expected STM image in the occupied states. The model was originally derived from first principle calculations carried out by Sauer et al. [188]. The model is the result of the optimization of a Patterson map. However, it cannot describe the deep trenches between the wires observed in STM. The model in (b) shows the giant missing row reconstruction (GMR) with 1 ML Au coverage, proposed by Van Houselt et al. [180] motivated by a comparison with the Ge(111)-Au system. The sides of a wire correspond in

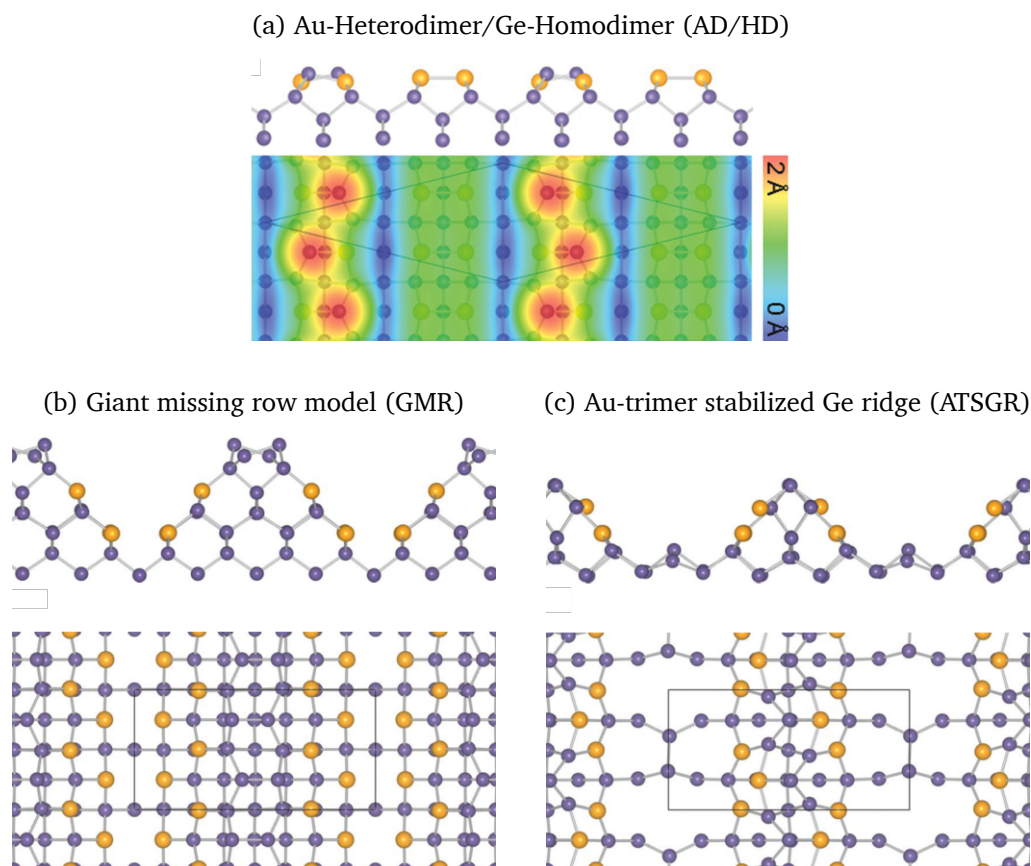


Figure 9.5: Selection of proposed structural models: (a) The Au-Heterodimer/Ge-Homodimer model (AD/HD) with 0.75 ML coverage was able to describe SXRD data in Ref. [187]. (b) The giant missing row model was proposed by Van Houselt et al. [180] to explain a groove between the wires. (c) The Au-trimer stabilized Ge ridge (ATSGR) is an energetically improved model of the GMR. The structural models of (b) and (c) are taken from Ref. [188].

this case to stabilized (111) facets. It can describe the deep grooves. However, DFT calculations [188] showed this system to be energetically unfavorable. Nevertheless, it is possible to modify this structure to improve the surface free energy. One of these results is the Au-trimer stabilized Ge ridge (ATSGR) model, depicted in (c), corresponding to 0.75 ML. Such structural optimizations have been carried out by Shioh-Fon Tsay [189] that suggest the (111) facets to be the precursor of a $(\sqrt{3} \times \sqrt{3})$ -Au reconstruction. Further models have been theoretically investigated also for a replacement of the Ge dimers by Au atoms [190]. Unfortunately, their investigations do not result in a $c(8 \times 2)$ reconstruction. A detailed study of Vanpoucke et al. [191] tries to explicitly match STM images to those patterns generated by various models. Beside, newer theoretical investigations also started to increase the Au coverage to even 1.25 and 1.75 ML [192], helping to stabilize a structure with deep trenches.

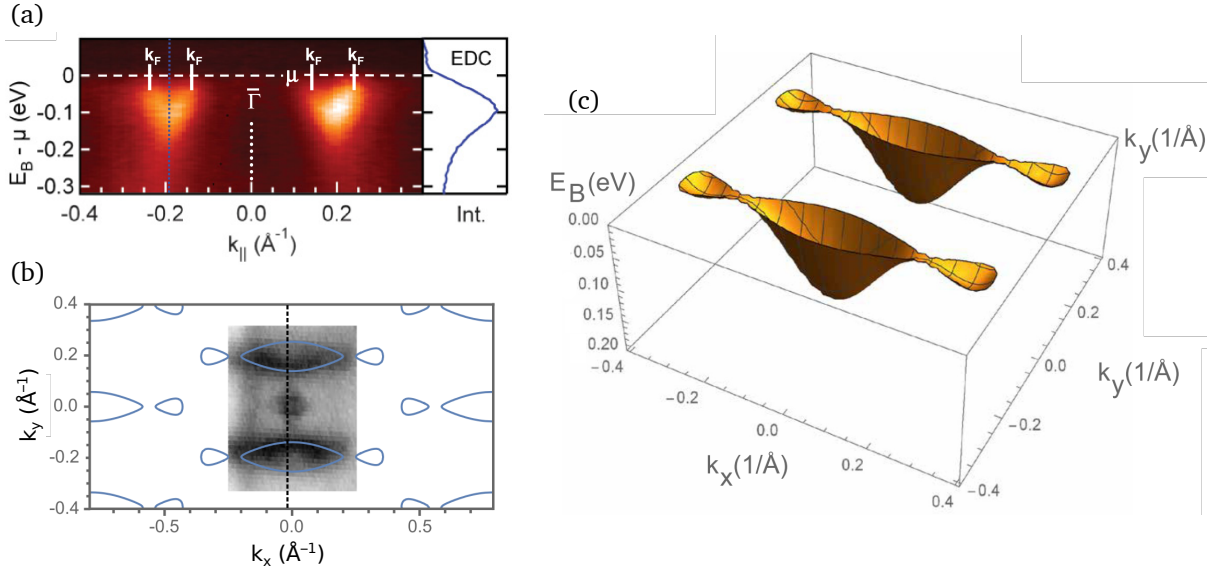


Figure 9.6: Electronic band structure of Ge(100)-Au: (a) Photoemission in wire direction shows two electron pockets located at the Brillouin zone boundary, taken from Ref. [193]. (b) shows the Fermi surface indicating a two-dimensional behavior with an overlay of a tight-binding fit, taken from Ref. [194]. (c) The two dimensional tight-binding fit for the ARPES data from Ref. [194].

9.3 Electronic Properties of Ge(100)-Au

As long as the theoretical models are only roughly approximating the complex structure of the Ge(100)-Au reconstruction, also their electronic properties are only a very uncertain description of the real world. Among others, such data are available in Refs. [188, 190].

Experimentally, angle-resolved photoemission reveals the existence of electron pockets at the Brillouin zone border along the wire direction [195, 193], as depicted in Fig. 9.6 (a). In a parabolic approximation it has an effective mass of $\approx 0.13m_e$ and a Fermi vector of $k_f = 0.058 \text{ \AA}^{-1}$. The zone boundary is depicted by the dashed blue line. To the side, an energy distribution curve (EDC) is plotted taken from a line scan at the zone boundary. Interestingly, these pockets strongly resemble the electronic structure of the Ge(111)- $(\sqrt{3} \times \sqrt{3})$ -Au surface [195], indicating a relation of the sidewalls being a precursor to the $\sqrt{3} \times \sqrt{3}$ -Au reconstruction mentioned above.

Due to a power-law behavior in the STS measurements taken on the wires for very low energies [196, 197] not seen in earlier measurements [198], this system was dealt with as a possible candidate for a Tomonaga-Luttinger liquid on a surface. An appropriate Luttinger density coefficient was extracted to $K_\rho = 0.26$, similar to other values from bulk TLLs [199]. However, there were some disproofs to this suggestions. Park et al. [200] showed that the power-law behavior only holds true for very low energies and De Jong et al. [194] showed the electronic band structure to even be of an anisotropic

two-dimensional character, see Fig. 9.6 (b). Here, a cut through the Fermi surface is shown with an overlay of a tight-binding fit. In their investigations they find a dispersing state also perpendicular to the wires. With this perpendicular dispersion, a shape of the overall electronic structure similar to that of a cowboy hat results. A surface plot of this shape up to -134 meV is given in Fig. 9.6 (c). As the dispersion perpendicular to the wires has a very high effective mass, it is barely visible in photoemission.

In conclusion, the system is most likely an anisotropic two-dimensional metal with a coincidental power-law behavior in the density of states around the Fermi level.

10

Structural Investigation of Ge(100)-Au

This paragraph describes the preparation of Ge(100) surfaces, including a detailed discussion about the influences of Ar⁺-sputtering to the sample properties. The determination of the surface quality is done by a LEED spot profile analysis as derived in section 2.2. Flat substrates with small roughness are obtained. In the second section, the same method will be expanded to approximate the growth properties of the Au-induced quantum wire structure.

Parts of this chapter were elaborated in the Master's Thesis of Heiko Teiken [148] and are already published in Ref. [201].

10.1 Pristine Ge(100)

Before the adsorption of gold and the growth of the quantum wire phase, it is important to know the quality of the bare Ge(100) surface. The available samples were Sb n-doped, Czochralski-grown 2 in wafers with a resistance of around 10 Ω cm. They were cut to rectangular samples of 15 mm × 5 mm size with an in-house diamond saw.

In contrast to SiO₂, GeO₂ is water soluble and forms a poor interface with Ge [202], i.e. a cracked and easy removable oxide layer. Respectively, it is not a good protection against contaminants that will accumulate in the first top layers of the germanium bulk. Therefore, the preparation of a clean surface requires a careful execution of the subsequent steps that are inspired by the variety of recipes in literature, e.g. Refs. [203, 204, 205]:

1. The wafers are cleaned primarily in an ultrasonic bath of Petroleum-benzene, acetone, and isopropanol to remove residuals of water and grease originating from the previous cutting processes.
2. The sample is dipped in piranha etch for 5 s. In this case, it is a solution of 7 parts 95 % sulfuric acid (H_2SO_4), 2 parts 30 % hydrogen peroxide (H_2O_2), and 1 part purified and deionized water. This mixture is a strong oxidizing agent. Thus, it removes most of the organic material. Furthermore, due to containing hydrogen peroxide, it will also hydroxylate the germanium surface, making it highly hydrophilic.
3. Directly after the dip, the surface is rinsed with purified water for one minute. As the hydroxylated surface will now dissolve in water [203], several top layers are ablated to flatten the surface and free it from contaminations. Afterward, residual water will be removed by dry blowing with N_2 .
4. To protect the substrate from degradation, a new thin oxide layer is grown by placing the wafer on a hot plate of 380°C for approximately 5 min.
5. After the transfer into UHV, the samples first degas at 380°C , a temperature below the desorption of the protective GeO_x [206, 144].
6. Having reached a pressure $< 1 \times 10^{-10}$ mbar, the sample is heated to 500°C for the removal of the oxide layer to obtain a pure Ge(100) surface for investigations. Keeping the pressure below 5×10^{-8} mbar, the sample is flash-annealed to 850°C . This temperature comes close to the melting point at 938°C and, thus, induces atomic mobility on the surface, helping to flatten the surface slightly, i.e. to improve the surface quality.
7. To get an even smoother surface, typically a sequence of several cycles of Ar^+ sputtering followed by flash-annealing to 850°C for ≈ 5 s is performed.

To investigate the effects of the last step, i.e. the improvement of the surface quality, a systematic investigation of this sputtering/annealing is carried out concerning the number of cycles and ion acceleration energy by a qualitative energy-dependent analysis of the diffraction spot profiles.

10.1.1 LEED of the Bare Surface

First of all, a glance will be taken at the LEED images and its meanings before the upcoming section takes a look into a quantitative investigation.

Fig. 10.1 shows two LEED patterns taken after the first flash annealing and after four cycles of the sputter/annealing treatment (electron energy at 169 eV, phase $S = k_{\perp}d/\pi = 3$, $d = 1.415 \text{ \AA}$, $T = 300 \text{ K}$). The dimerization of Ge atoms can be seen by the presence of a (2×1) reconstruction. A detailed description can be found in Chapter 9 as well as in Ref. [165]. The essence is that its uniaxial stress favors the formation of two domains separated by monoatomic steps of height $d = 5.66 \text{ \AA}/4 = 1.42 \text{ \AA}$. This behavior is similar to the Si(100) surface [167, 207].

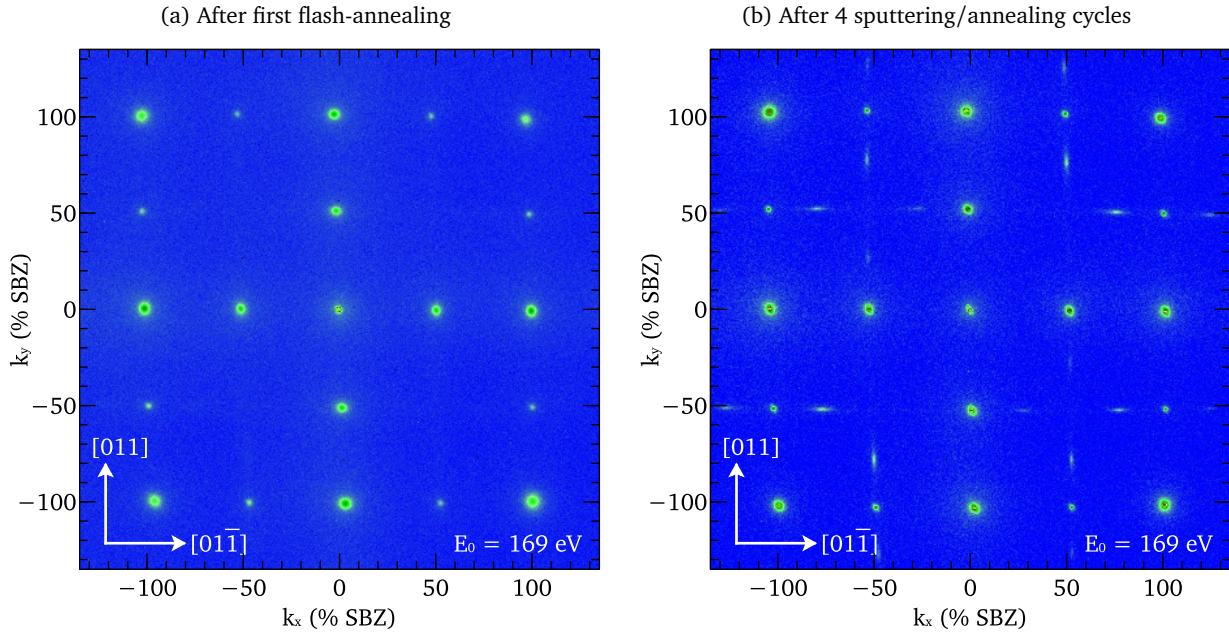


Figure 10.1: LEED patterns of a Ge(100) surface before (a) and after (b) four times Ar^+ sputtering with 800V ion acceleration voltage and annealing: The treatment results in sharper (2×1) superstructure spots with higher intensity. Additionally, faint (4×2) spots are visible. Both images share the same scaling and false colors and are taken at RT.

When directly comparing the two LEED patterns, one can instantly see an improvement in the sharpness of the (2×1) superstructure spots: Their widths are smaller, while their intensity has increased. This profile change is already an indication of an improved surface quality. Additionally, a (4×2) reconstruction emerged originating from buckled dimers. Well-known from the literature [171], defects like vacancies and impurities and the ensuing reduction of the surface energy can cause this reconstruction. Here, it is but an indication for nearly defect-free samples with large terraces as will be shown below by Fig. 10.4. In this case, the (4×2) superstructure is the result of the anisotropy of the surface stress tensor [171, 40]. Therefore, the LEED image shows high ordering within the buckled dimer rows.

For a more quantitative information about the surface quality, a line scan across the (00) -spot was taken for various electron energies E_0 [86]. This energy-dependent plot is shown in Fig. 10.2 for the left LEED pattern (a) in Fig. 10.1. Here, one can already see some basic information about the surface. Around the in-phase (integer of S) conditions a higher intensity is observed than for the out-of-phase (integer $\pm 1/2$ of S). This result matches the expectations for a surface with its step height d . Additional modulation of intensity and width cannot directly be attributed to surface properties as they originate from the more complex topography of the surface. For a deeper understanding, the (00) -spot of every line scan was fit with a Voigt function. This distribution consists of a convolution of a Gaussian part containing the vertical information of the surface and a Lorentzian part that is defined by the lateral

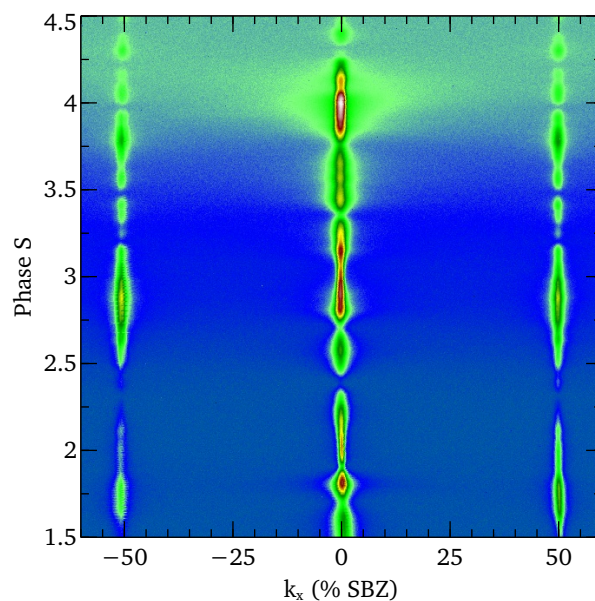


Figure 10.2: False color energy dependent scan across the (00) spot in $[01\bar{1}]$ direction of a pure Ge(100) sample after one sputtering/annealing cycle: the modulation of the width and the intensity gives insight to the roughness of the surface.

characteristics, e.g. the terrace sizes.

10.1.2 Quantitative Spot Profile Analysis

The following section presents the results of a quantitative treatment of the spot profiles: Measurement series were carried out for multiple cycles of sputtering at 800V, respectively 500V ion acceleration voltage with each time subsequent rapid annealing to 850°C. The sputtering was handled with the chamber in an Ar atmosphere of 3×10^{-5} mbar and an ion current on the sample of $0.5 \mu\text{A cm}^{-2}$. During the sputtering process, the samples remained at room temperature.

The energy plots gave access to line scans for all available phases and sputtering/annealing cycles. They were fit with a Voigt function and afterward deconvolved into a Gaussian function with a Lorentzian shoulder.

As an example, line scans for an in- and out-of-phase condition, in particular for phases 2 and 2.5, are shown in Fig. 10.3 after two and eight sputtering/annealing cycles with the corresponding fit and convolutional parts. From the change in width difference after eight cycles, it is directly apparent that the average terrace size has increased by at least a factor of 2. As the Voigt fits were carried out in a batch script with all parameters free, also the Gaussian parts varied slightly. These variations are directly visible, e.g., in Fig. 10.3 (c) and (d).

As obtained from the Voigt fits, Fig. 10.4 plots the evolution of the Lorentzian widths for two series with 800V and 500V sputtering voltages. The decrease of the modulation amplitude of the widths with

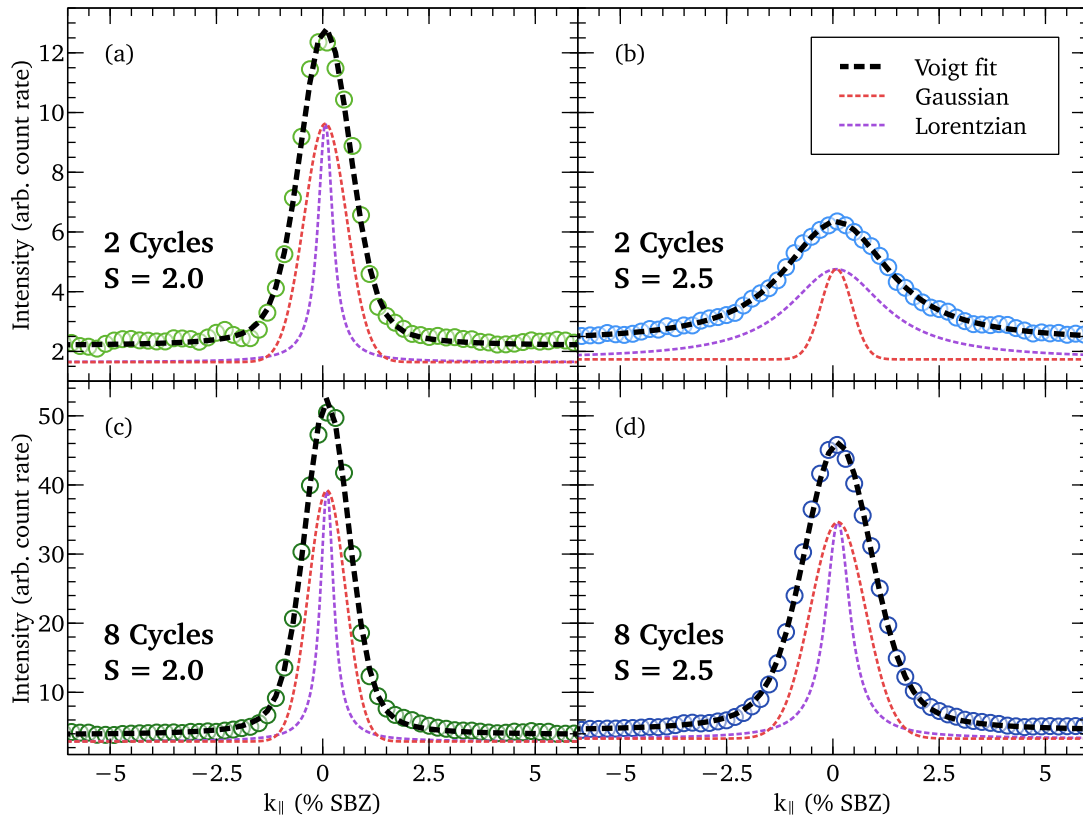


Figure 10.3: Voigt fit functions (black dashes) of the data (open circles) taken from the energy plots for in- and out-of-phase conditions after 2, respectively 8 cycles of the sputtering/annealing treatment at 800V (cf. Fig. 10.2): Deconvolved Lorentzian and Gaussian parts of the Voigt fit are given in red and purple and have been scaled to 75% for better visibility. Less intensity difference is observed in the lower graphs for the surface with more frequent treatment. Furthermore, the Lorentzian width difference is smaller, whereas neither a difference nor a change in the Gaussian widths can directly be seen.

increasing number of cycles is visible distinctly. The dashed lines are fits to the data with the following function:

$$H(S) = \frac{a_0}{\pi \langle \Gamma \rangle} \times (1 - \cos(2\pi S)) + P_2(S). \quad (10.1)$$

This equation was elaborated in section 2.2.1. Here, $a_0 = 4.002 \text{ \AA}$ is the surface lattice constant of Ge(100), $\langle \Gamma \rangle$ is the resulting mean terrace size and the free fit parameter. An instrumental broadening, a slight surface miscut, as well as suboptimal lens settings were considered by a second order polynomial offset $P_2(S)$.

Fig. 10.6 (a) shows the resulting mean terrace width as a function of sputtering/annealing cycles. It increases continuously and can become up to 600 \AA . For each of the measurement series, a new sample from the same wafer was used. Therefore, the results can directly be compared. Nevertheless, the

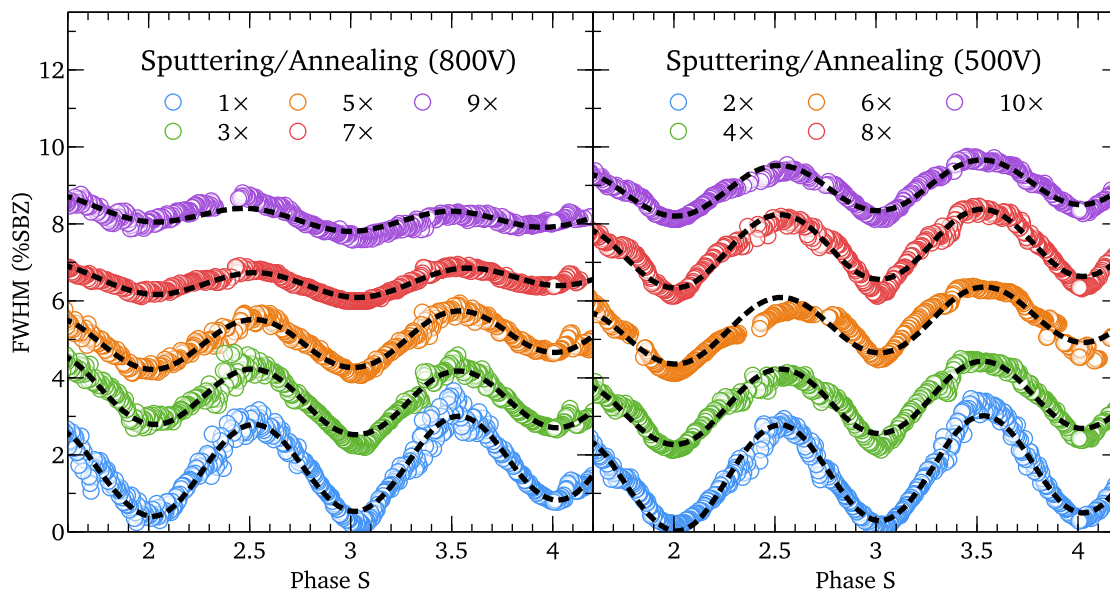


Figure 10.4: $H(S)$ curves of pristine Ge(100) samples after definite cycles of sputtering at 800V (left), resp. 500V (right) ion acceleration voltage and subsequent flash-annealing to 850 °C: For an increasing number of cycles the amplitude of the oscillation decreases, a sign for the growth of the terrace size. The data have been shifted for the sake of visibility.

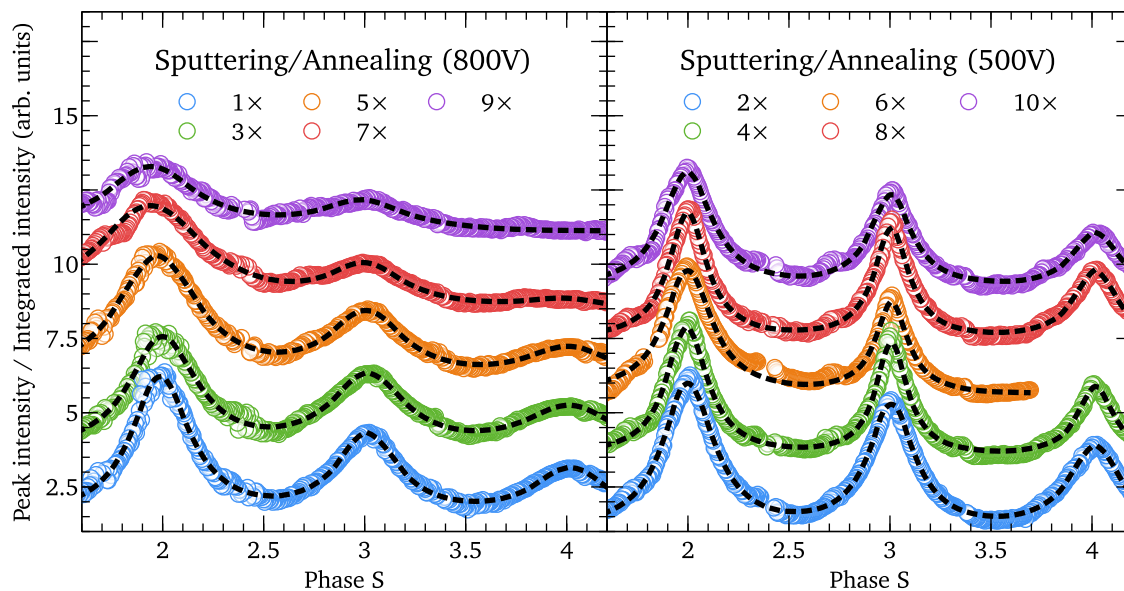


Figure 10.5: $G(S)$ curves of pristine Ge(100) samples after their sputtering and annealing cycles with 800V (left), resp. 500V (right) ion acceleration voltage: After several cycles a decrease of the width of the integer phase peaks can clearly be seen for the 800V data and denotes a decrease in surface roughness. The curves have been shifted for visibility reasons.

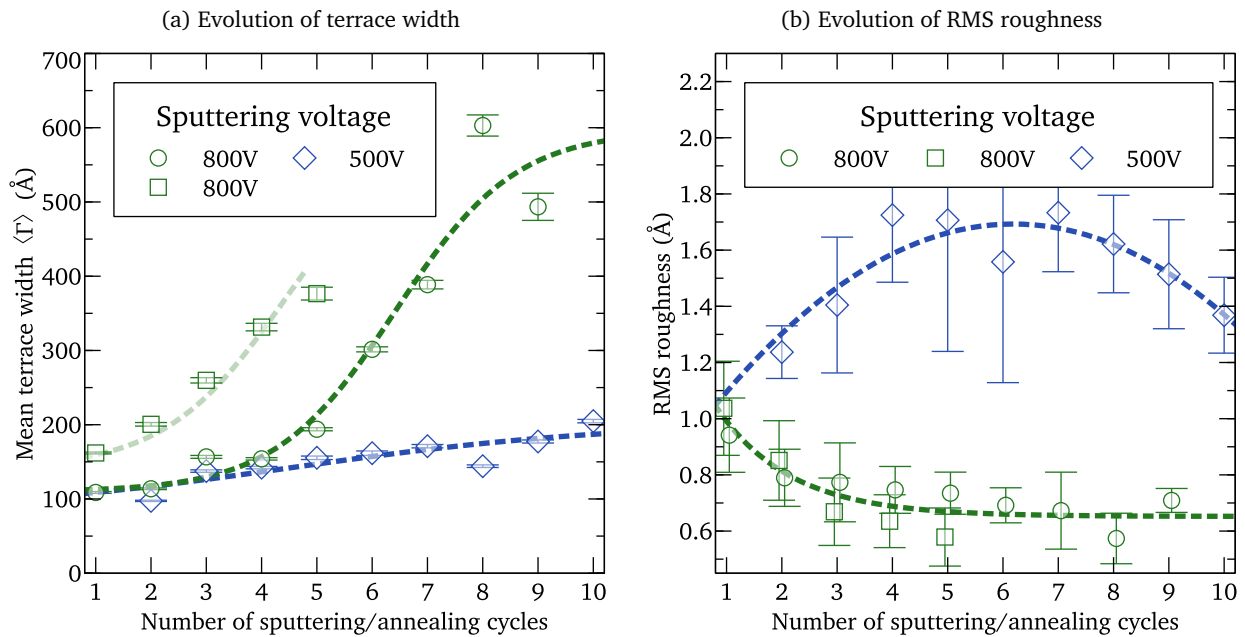


Figure 10.6: Influence of sputtering/annealing to the terrace width (a) and RMS roughness (b) for distinct sputtering voltages: (a) Sputtering at 800V results in larger terraces of around 600Å (green circles and squares) in comparison to 500V (blue diamonds). (b) 800V sputtering is also more effective in the reduction of the surface roughness.

quality of the samples depends strongly on the sputtering parameters: Big terraces were obtained when sputtering at 800V (green data). Two measurement series (squares and circles) show the same trend, albeit one of the samples started at a higher initial value. Using merely 500V (blue) for the acceleration of the Ar^+ ions, the average value increases only slowly and appears to saturate at a much lower value than for the higher voltage.

Although this ion-energy dependence was not carried out systematically for various voltages, a possible explanation is that a threshold energy is necessary to remove contamination from the surface or even the first subsurface layers. These defects otherwise may lead to step pinning during the annealing process.

The peak intensity normalized to the integrated intensity, i.e. the area of the Voigt profile, is plotted in Fig. 10.5 giving the $G(S)$ curves. The in-phase intensity decreases slightly for increasing phase S . This damping is most likely caused by the variation of the layer distance on the surface due to relaxation effects [208, 209].

The in-phase peaks widen with increasing treatment step for a sputtering voltage of 800V while the area under the curves remains the same. For 500V there is no effect directly visible. Following

Wollschläger's approximation [62, 63] around an in-phase condition S

$$G(S) \approx \exp[-\Delta_{\text{RMS}}^2 (2\pi\delta S)^2] \quad (10.2)$$

the variation of the central spike as a function of the variance δS may be described by a Gaussian distribution if also the levels are distributed normally, also named geometrically.

However, in the present case, the given data were fit best by multiple Lorentzian peaks. This behavior has its roots most likely in an almost-normal distribution with strong outliers. Then a Gaussian shape will shift to a Lorentzian one. From their full widths at half maximum the RMS-roughness Δ_{RMS} was determined corresponding to Eq. 10.2 as:

$$\Delta_{\text{RMS}} = \frac{\sqrt{\ln 2}}{\pi} \frac{1}{\text{FWHM}} \quad (10.3)$$

The resulting data are plotted in Fig. 10.6(b). For a sputtering with 800V ions extremely smooth Ge(100) surfaces with a value below 1\AA are obtained. When using 500V acceleration voltage, the roughness first increases to around 1.7\AA but then decreases after approximately five treatment cycles. Assuming a lower sputter yield for a lower impact energy supports the hypothesis mentioned above that step pinning at surface and subsurface defects also leads to a higher roughness. After the removal of these defect-prone layers, the surface may also evolve into a very smooth surface. This route but was not further investigated. To sum up, sputtering at 800V results far more efficient as it could also be directly reproduced by another series, cf. squares in Fig. 10.6.

10.2 Au-Induced Wires on Ge(100)

The same analysis was now extended to the Au-covered surface. The adsorption took place with the sample at room temperature with a deposition rate of approximately 0.15 ML/min. Thereafter, the sample was annealed at 500°C for nearly 10s. The coverage was increased systematically conducting the same deposition successively. After each desorption, an analysis of the spot profiles was carried out with an evaluation similar to the pristine germanium surface. Before new adsorption, the surface was sputtered according to the recipe given in the previous section. This cleaning ensures a germanium surface free of remaining gold coverage. Then, an evaluation similar to the pristine germanium surface was carried out.

10.2.1 LEED of the Au-Covered Surface

Once more, to begin with, depicted in Fig. 10.7 (a) is a LEED pattern that results after the adsorption of 1.25 ML of Au. A new superstructure can be seen that is identified as a $c(8 \times 2)$ reconstruction, exemplarily indicated by a red diamond. There is also an additional $p(4 \times 1)$ superstructure (yellow

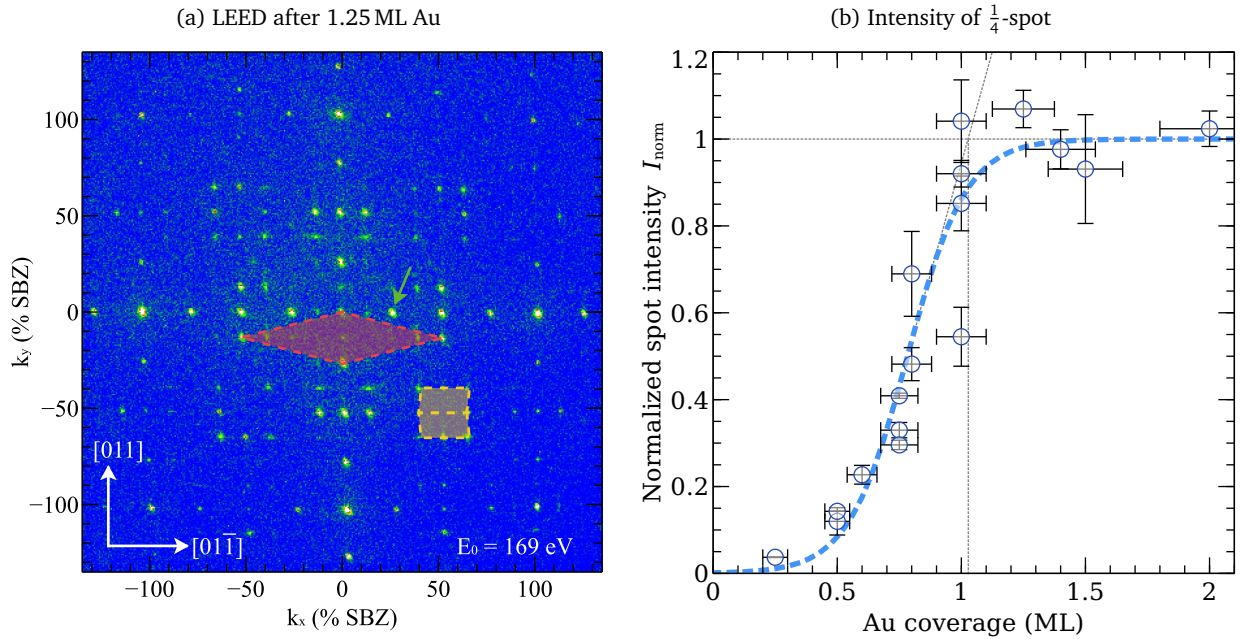


Figure 10.7: LEED pattern of the Au reconstructed Ge(100) surface and the evolution of the Au induced reconstruction as a function of Au coverage: (a) LEED shows a new $c(8 \times 2)$ reconstruction marked with a red diamond and an additional superstructure marked with a yellow rhomboid, both related to the induced wire structure on the surface. (b) Evolution of the $1/4$ -spot marked with a green arrow in the LEED for various coverages normalized to the mean value of the data points ≥ 1.25 ML: The blue fit is a dose-response relationship showing a saturation at around 1 ML after triangulation as shown by the dotted lines.

rhomboids) on top of this basic $c(8 \times 2)$: This reconstruction can either be 'up' or 'down' depending on the arrangement of the supercells, cf. Chapter 9 and Refs. [197, 182]. These superorder reflexes are attributed to a long-range interaction between adjacent wires. Consequently, the appearance of long-range order in combination with the very sharp structural spots already gives an indication of an extremely well-ordered sample.

This part also tries to clarify the controversially discussed coverage of the Ge(100)-Au wires ranging from 0.25 ML to 1.5 ML, cf. the various models given in Chapter 9. Thus, a first hint is given by the analysis of the integral intensities of the Au-induced reconstruction spots. For various coverages, the mean value of the $1/4$ -spots depicted in Fig. 10.7 by a green arrow was extracted from the LEED patterns and normalized to the according (00)-spot. Then the data was again normalized to the mean value of the data above 1.2 ML as the intensity might vary depending on the quality of the surface. The resulting data are plotted in Fig. 10.7 (b). One can see the clear trend of the data to saturate justifying the normalization approach. Fitting the intensity emersion with a dose-response relationship and triangulating the slope, a saturation coverage close to 1 ML is obtained. Excess coverage results in the

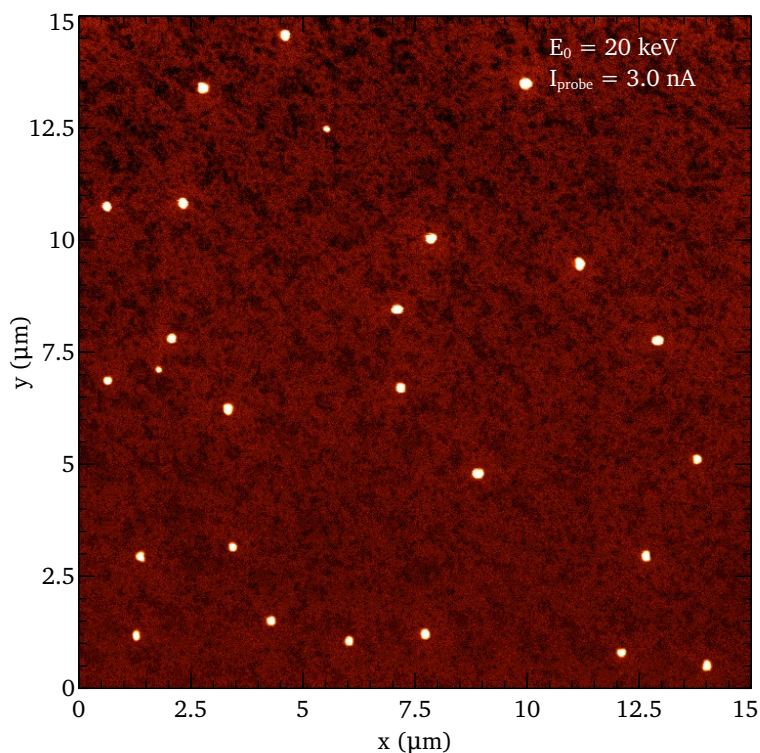


Figure 10.8: False color SEM image of the cluster formation due to excess Au on a sample with 2 ML coverage: The clusters appear as bright dots because of the higher work function compared to the oxidized surface. The scaling is linear from black and red over yellow to white. The contrast has been slightly increased to let the clusters become clearer.

growth of Au-clusters on the surface [184]. Due to the complete absence of any Au(111) diffraction spots their size and distribution must be low.

As a confirmation of cluster growth, a sample of 2 ML coverage was checked with a SEM. During the transfer to this device the sample had to be exposed to the atmosphere and, therefore, the highly reactive surface oxidizes except for the Au clusters. A false color plot of the SEM data in Fig. 10.8 shows them as bright dots, i.e. high intensity, most-likely due to an edge contrast of those small gold droplets on top of the slightly oxidized Ge-Au surface. However, Au is reported to always appear brighter on semiconductors [210]. There is a more or less random distribution with distances between $2\mu\text{m}$ and $5\mu\text{m}$. They are all approximately 150 nm in diameter.

These clusters also work as a reservoir. Gold travels from these 3d structures across the nanowire domains forming the desired structure. This behavior can explain a sometimes lower amount of gold needed when reusing a germanium sample [201]. In this case, the surface was most likely not completely purged from those clusters.

However, the need for 1 ML coverage is in contrast to most of the predicted coverages of ≤ 0.75 ML and suggests to recheck the proposed structures. Stabilizing subsurface gold positions are a possible

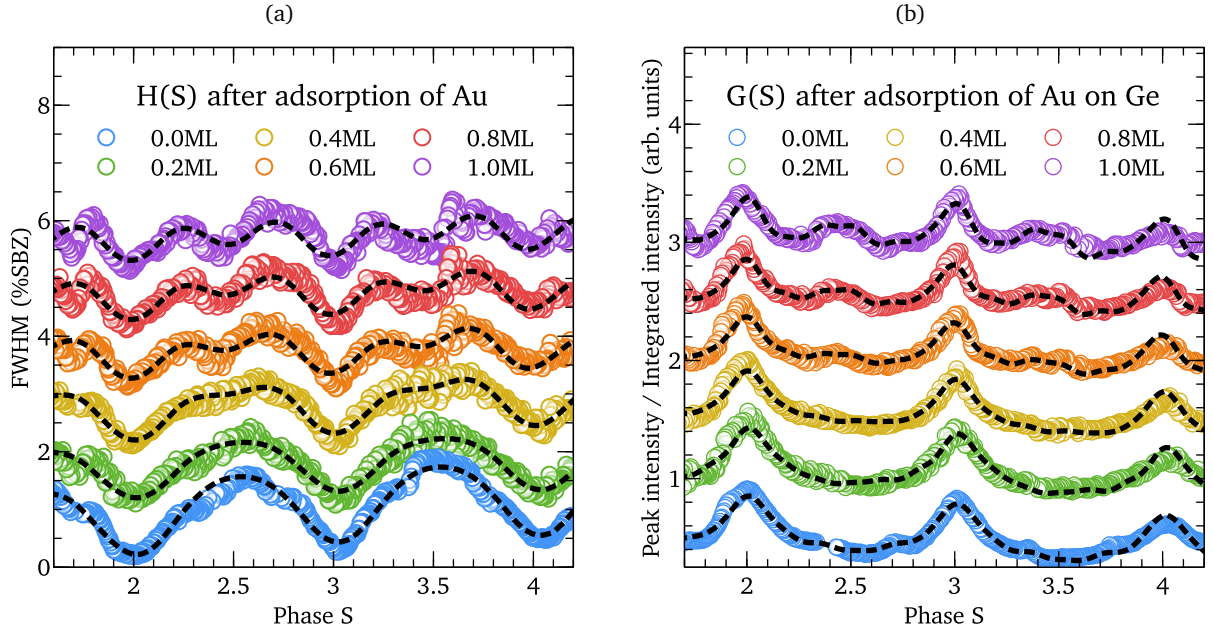


Figure 10.9: $H(S)$ (a) and $G(S)$ (b) curves of a Ge(100) after various adsorptions of Au: There is a strong change in the data for increasing coverage. (a) An additional minimum starts to evolve at half integer phases indicating the formation of domain boundaries of double atomic step height. (b)

origin. However, such a high coverage leans towards one of the more complex structural models.

10.2.2 Extension of the Spot Profile Analysis to the Gold-Covered Surface

For a more detailed characterization of the structure, $H(S)$ and $G(S)$ curves were extracted from the energy dependent plots after each evaporation step, although the surface now contains two kinds of atoms with different scattering factors f_{Au} and f_{Ge} . Anyhow, the relations elaborated in section 2.2 will now be extended to this more complex structure.

Fig. 10.9 (a) shows the variation of the widths of the Lorentzian part of the central peak. The data are plotted as a function of the scattering phase S with respect to the single atomic step height of a Ge(100) surface. There is a significant change in the overall oscillation period with increasing Au coverage. While for the pristine surface and low coverage $\leq 0.2\text{ML}$ the dominating step height is the single step, for higher coverages the probability of double steps increases strongly. With the entire surface being covered with the Au wire structure, double steps are the dominating interdomain separation. Following Eq. 2.15, the data were fit with

$$H(S) = \frac{a_0}{\pi(\Gamma)} \times \sigma_1 (1 - \cos(2\pi S)) \times (1 - \sigma_1) (1 - \cos(2\pi S h_2)) + P_2(S). \quad (10.4)$$

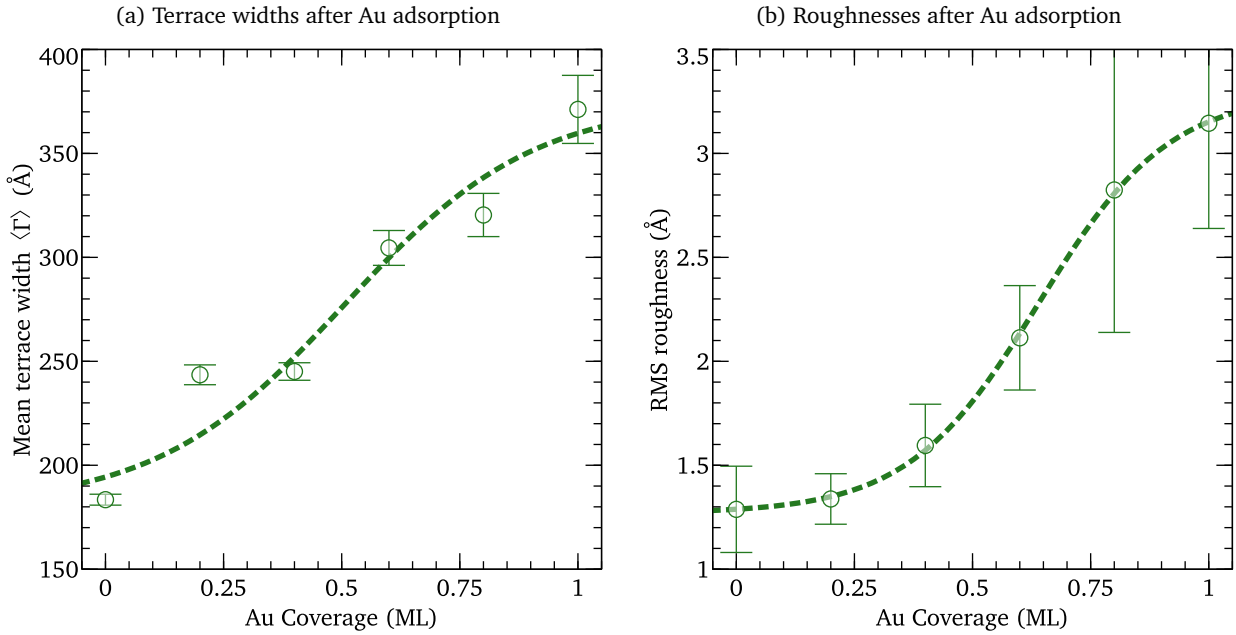


Figure 10.10: Terrace width (a) and roughness (b) development after the adsorption of Au on Ge(100): While the adsorption of Au triggers the growth of the terraces, the roughness is also increased. This results strongly supports a reconstruction with deep trenches.

In this equation σ_1 is the probability of a monoatomic step between domains, $1 - \sigma_1 = \sigma_2$ accordingly for twice this height. $\langle \Gamma \rangle$ is the mean terrace width, a_0 the lattice constant, and $P_2(S)$ is an offset, all in accordance with Eq. 10.1. As an approximation to phase changes that might occur due to different form factors of Au and Ge, the height of a double step h_2 was allowed to change slightly. The best fits were achieved with $h_2 = 2.04$ for coverages ≥ 0.4 ML, corresponding to a strain or phase shift of 8 % in the topmost layers.

Although there are more features hidden in the $H(S)$ curve, the used fit function already gives reasonable results. The mean terrace widths derived from the fits is shown in Fig. 10.10. Starting on a sample of 200 \AA , the adsorption of gold effectively increases the terraces to around twice this size. A domain growth and, therefore, an increase in quality of the sample is a typical behavior when growing metal-induced structures as the induced superstructure is energetically much more favorable due to the reduction of the surface energy.

The probability σ_1 of a single step domain boundary is given at the top of Fig. 10.11 (a) and drops from almost 1 to below 0.4 for a surface covered with 1 ML of Au. As a consequence, the share of double steps on the surface increases to values as high as 60 %.

The formation of steps with double atomic height upon Au adsorption is well known for vicinal Si(100) [211]. Also pristine vicinal Si(100) as well as Ge(100) show the formation of double steps when their miscut angle forces the system to exhibit strong domain imbalance [43]. On the given surface, however,

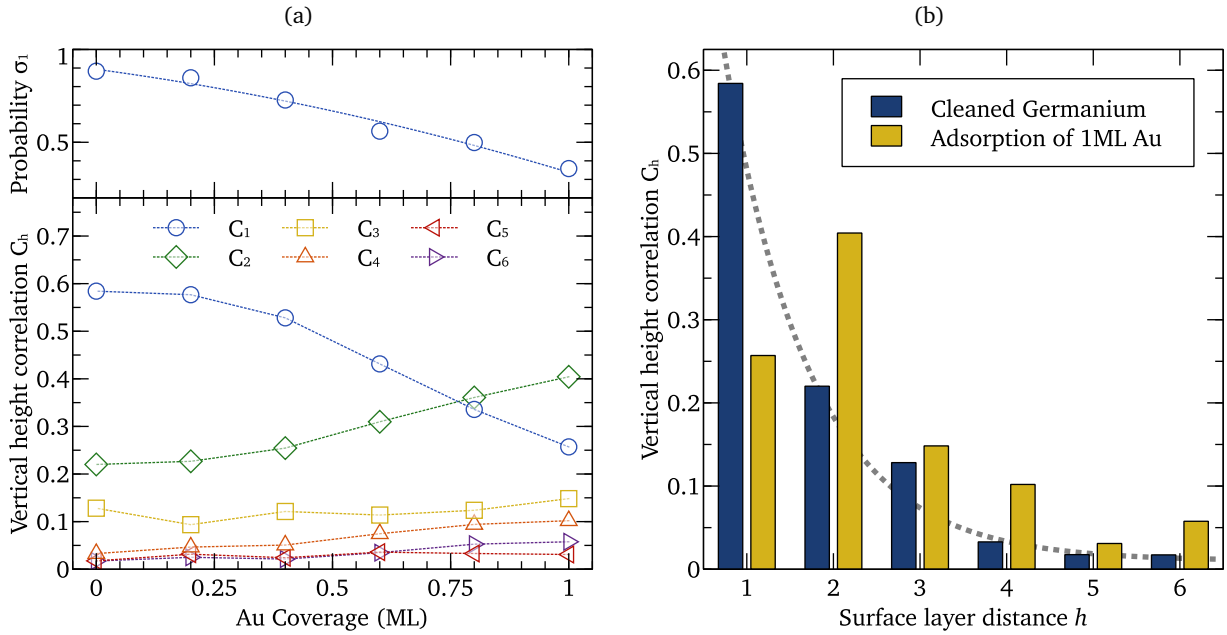


Figure 10.11: Roughness properties of the Au covered surface: (a) The probability of a single step from $H(S)$ (top) and the vertical height correlations C_h from $G(S)$. (b) A direct comparison between the pristine surface and one that is covered with 1 ML showing the surface roughness increase into higher amounts of double, quadruple, and sextuple steps.

despite the creation of double steps, there is no difference in the intensity ratio of reconstruction spots originating from different domains. When assuming a conservation of the initial miscut of the surface, steps of single atomic height are still needed to balance both domains.

A similar trend of roughening is seen from the $G(S)$ curves that are shown in Fig. 10.9 (b). Peaks start to develop for the gold covered surface and are clearly visible for coverages > 0.6 ML, in agreement to the $H(S)$ curves. Also in this data, there are features of higher order originating in the now more complicated alignment of the rearranged gold-induced structure. Like for the clean Ge(100) surface, a damping of the amplitudes can be explained by relaxation effects in the surface-near layers [208, 209].

The width of the integer phase peaks is decreasing meaning an increase of roughness. The data has again been fit with Eq. 10.2 and the extracted result is plotted in Fig. 10.10 (b). Albeit large error bars due to this very simple approximation, the roughness increases to $\approx 3 \text{ \AA}$ that is about three times its starting value. A trend to form larger terraces but with higher roughness is a behavior vice versa to the terrace growth after the cleaning process described before. This result gives an indication to a complex rearrangement of atoms in the Ge(100)-Au surface. This result tends to favor one of the corrugated models with deep grooves between the developing conducting channels.

For a more in-depth understanding, the $G(S)$ curves were analyzed in detail. The following expres-

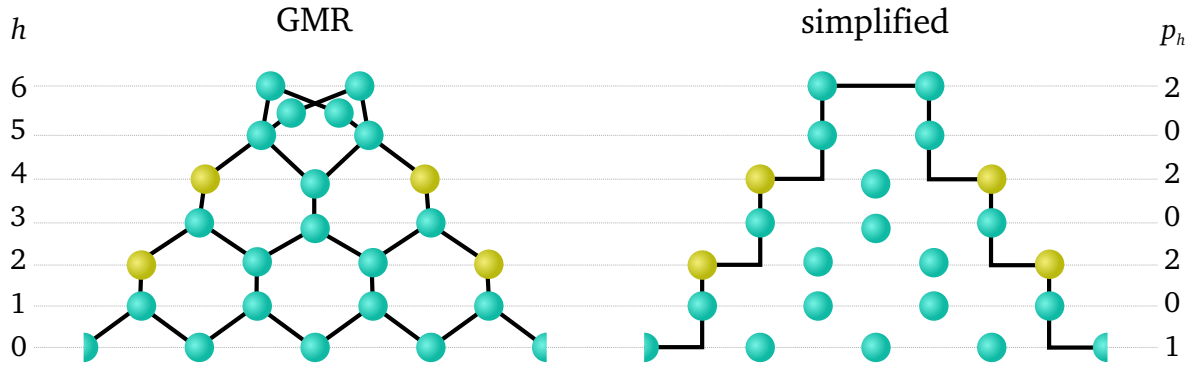


Figure 10.12: Simplified GMR model for a qualitative $G(S)$ analysis: The proposed GMR model [180] to the left was simplified by aligning the atoms in a rectangular shape in side view, cf. also Fig. 9.5 (b). Germanium atoms are depicted in cyan, gold atoms in yellow. For every even height h there is a finite layer distribution p_h , the odd heights are covered.

sion, cf. Eq. 2.17, was able to describe the data with the assumption that each layer is identical:

$$G(S) = P_2(S) - \sum_h^6 C_h \times [1 - \cos(2\pi Sh)] \quad (10.5)$$

Here, C_h are the correlation coefficients giving the presence probability for a height h . This height was again allowed to shift slightly as approximation for relaxation and different form factors. After the fit the correlation coefficients were normalized such that the sum of all C_h is 1.

The resulting C_h for every measured coverage are displayed in the bottom of Fig. 10.11 (a). One can see a clear trend that after the evaporation of around 0.25 ML C_1 is strongly falling whereas C_2 increases. A relative increase in C_4 and C_6 is also visible. A bar chart comparing the values before and after adsorption is given in Fig. 10.11 (b). Also these data support the corrugation upon Au adsorption.

Based on the GMR model shown to the left in Fig. 10.12 that has been suggested by van Houselt et al. [180] and calculated by Sauer et al. [188], a simple estimation can yield values for all C_h by the simplified model to its right side. Induced by Au adsorption on the side of this model only the second, fourth and sixth layers have a finite coverage p_h , the coverages of the odd-numbered layers are zero. Their values are assumed to $p_0 = 1$ and $p_2 = p_4 = p_6 = 2$. With the formula for height correlations of Eq. 2.18 the following normalized values are obtained:

$$C_0 = \frac{13}{31}, \quad C_2 = \frac{10}{31}, \quad C_4 = \frac{6}{31}, \quad C_6 = \frac{2}{31}, \quad C_1 = C_3 = C_5 = 0$$

Here, C_0 is a self-interference term. Qualitatively, these ratios were found by the $G(S)$ analysis. Therefore, a model closely related to the GMR is supported by the results of this chapter. It may need, however, some refinement to take the discrepancy between the theoretical and the experimental coverage into

account. A key to that might be hidden in subsurface regions. Recent calculations by the Seino et al. [192] already started into this direction.

10.3 Conclusion of the Structural Analysis

The results of this chapter show that the Ge(100) surface needs an extraordinary treatment to obtain a system with large terraces and free from defects. Additionally, multiple cycles of flashing with subsequent annealing are crucial within this recipe. The terraces obtained are as large as 600 Å with a roughness below one atomic height difference.

Although the formalism derived in Chapter 2 for the $H(S)$ and $G(S)$ analyses is only valid for the assumption that the scattering properties of all terraces are identical, the approach was extended to the gold covered surface. As it turned out, the resulting data described the rearrangement of atoms on the surface rather well, at least qualitatively. There is an increase in roughness in the form of double, quadruple and sextuple step heights with a simultaneous growth of the terrace size. This leads to the preference of one of the corrugated structural models introduced in Chapter 9 such as the GMR or the ATSGR. Furthermore, the reduction of free surface energy by the adsorption of Au leads to a healing effect on the surface seen by the terrace growth. This is the same driving force that also improves the Si(hhk)-Au systems of Part II or leads to a faceting of Si(100) surfaces with 4° miscut upon gold adsorption [212].

In addition, carrying out $G(S)$ and $H(S)$ analyses on a relatively complex structure showed that it is possible to obtain reasonable information from a spot profile analysis. Other approaches are the time consuming numerical fits of IV-LEED or the generation of Patterson maps in SXRD experiments. Of course, their results are far more accurate. Nevertheless, it is recommended to use energy dependent SPA-LEED more often for first hints about an uncertain topology of a surface.

11

Plasmonic Excitations in Ge(100)-Au

This chapter presents the excitations attributed to plasmons seen in electron energy loss spectroscopy. First, the overall shapes of the losses in the spectra are discussed. Then, attempts for the description of the losses are carried out within a Tomonaga-Luttinger liquid and quasi-free electron gas approach.

11.1 Electron Energy Loss Spectra

On the Ge(100)-Au systems, as introduced in the previous two chapters, electron energy loss spectra were recorded. Fig. 11.1 (a) shows sequences of these spectra on a semi-log scale as a function of increasing k for a sample with 1 ML Au coverage. The shown measurements have been carried out in $[01\bar{1}]$ direction. However, no difference was seen when measuring in $[011]$ direction. This behavior is expected as the surface exhibits two domains distributed equally on the surface. All data were plotted normalized to the intensity of the elastic peaks of each spectrum and shifted upward in intensity with increasing k for better visibility. The integration time of the curves was ≈ 10 s per data point with a resolution of 3 meV. These time-consuming settings were necessary due to the very low intensity of the plasmonic signal as also directly visible in the spectra given.

Fig. 11.1 (b) shows the fitting procedure to obtain the positions of the excitations. The spectra of Ge(100)-Au could be fit in the same way as the Si(hhk)-Au spectra, cf. Chapter 7. However, compared to the excitations of the Au wires on vicinal silicon the intensity of the plasmon is 100 times lower and at least three orders of magnitude below the elastic peak of a spectrum. These widths also result in a high uncertainty of the exact position of the Gaussian part during the fitting process. Additionally, the

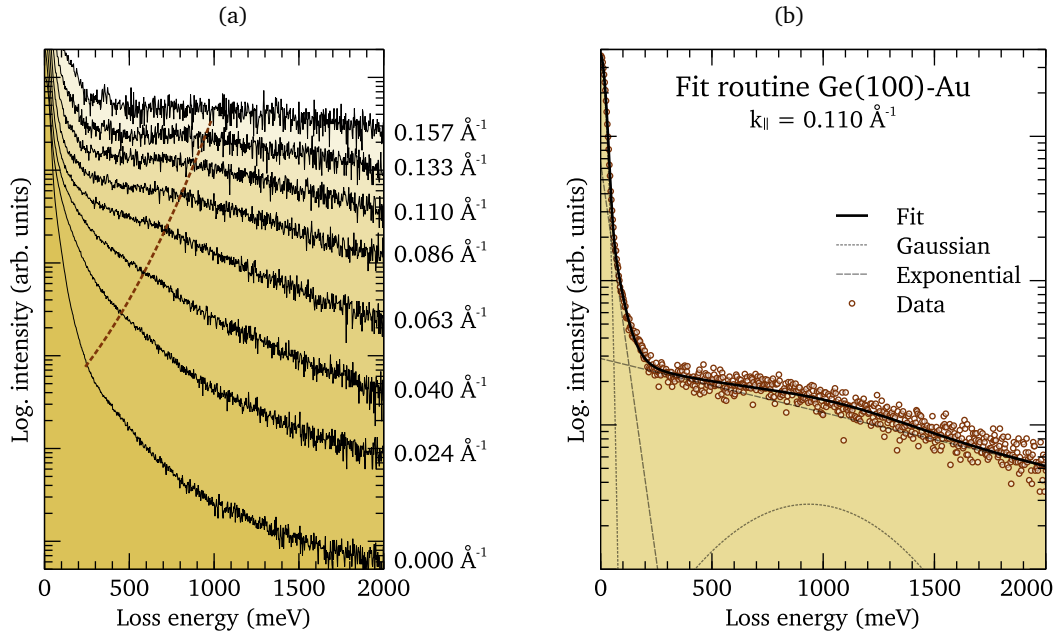


Figure 11.1: Electron energy loss spectra of Ge(100)-Au for increasing momentum with used fitting routine: (a) Though having a very low intensity, a dispersing feature can be seen for increasing momentum in the spectra given as black lines. Its shift is highlighted by the dashed dark yellow line. (b) Example of the fit routine for $k_{||} = 0.110 \text{ \AA}^{-1}$. The data was described with an empiric description of the background, fitting the plasmon peak with a Gaussian function. The individual components are depicted by the gray dashed lines, the resulting fit in solid black. The data is given by the dark yellow circles. The intensity of the plasmon loss is three orders of magnitude below the elastic intensity of the given spectrum.

exponential decay of the spectrum next to the elastic peak is much flatter having its origin most likely in the much lower electron density of this system of only $n = 7.4 \times 10^6 \text{ cm}^{-3}$. Such a small density also gives a possible explanation of the low excitation probability of the plasmon.

Nevertheless, a dispersing feature can be seen in the spectra of Fig. 11.1 (a) that shifts to higher energies with increasing k . Its trend is indicated by the dark yellow dashed line through the loss maxima.

11.2 Dispersion of the Plasmonic Excitation

All spectra were analyzed as described above and depicted in Fig. 11.1(b). The extracted data together with two possible descriptive models are plotted in Fig. 11.2.

Measurements were carried out for coverages from 0.5 ML to 2 ML, indicated by a different marker as defined in the key. The accuracy of the coverage was around 10%. Although there is a high scatter in the data, no difference or trend was found that shows an effect on coverage. This indifference is in

agreement with the fact that upon adsorption the gold covered superstructure grows in patches [177] with the subsequent formation of excess gold clusters [184], cf. the SEM image of Fig. 10.8 and Chapter 9. In conclusion, the plasmon occurs in a locally reconstructed part that is insensitive to an incorrect amount of Au. However, not all measurements showed a plasmon excitation peak although the LEED pattern and sample quality were excellent. The origin of the lack of a plasmon remains unclear. Albeit, a possible explanation is an excitation intensity too low to be visible in the background noise.

Unfortunately, due to their small intensities, the centers of the Gaussian part of the plasmon could only be determined for k values above 0.04 \AA^{-1} . The data seem to saturate for $k < 0.1 \text{ \AA}^{-1}$ and increase steadily above. A first approach is to assume a finite wire length that leads to a standing wave and, consequently, to no dispersion for low k . From the quasi-free electron dispersion relation

$$E = \frac{\hbar^2 k_n^2}{2m^*} = \frac{\hbar^2 \pi^2}{2m^* l^2} n^2 \quad (11.1)$$

with $n = 1$ and $m^* = 0.13m_e$, a length of $l = 20 \text{ \AA}$ results. Compared to the structural investigations in the previous chapter that showed minimum terrace sizes of 200 \AA , this value is extremely low and, respectively, there is no reason to assume a mean distribution of such short wires. As all measurements were carried out on dual-domain samples, standing waves perpendicular to the wires are also a possible source. The wire spacing itself is 16 \AA and, assuming an infinite square well of this size, results in an eigenenergy of 1.1 eV . Therefore, this origin can also be ruled out since the measured values are lower in energy.

Thus, two different approaches are carried out in Fig. 11.2: In (a) the data was fit with the model for a Tomonaga-Luttinger liquid of Eq. 3.26 and in (b) a quasi-free electron gas plasmon was numerically computed.

11.2.1 Description as Tomonaga-Luttinger Liquid Plasmon

Since a fit with an isotropically screened Coulomb potential, as suggested in Eq. 3.27, cannot describe the high curvature seen in the data, the fit of Fig. 11.2 (a) contains an arbitrary interaction potential perpendicular to the wire as also already introduced in context with a TLL elsewhere [213] and given by

$$v_c(k) = \alpha \pi \hbar v_F \exp(-k^2/k_{\text{crit}}^2). \quad (11.2)$$

The resulting dispersion to first order is then specified by

$$E(k) = \hbar v_F k (1 + \alpha \exp(-k^2/k_{\text{crit}}^2)). \quad (11.3)$$

The data can be described by setting $v_F = 1.08 \times 10^6 \text{ m/s}$, $\alpha = 2.0$, and $k_{\text{crit}} = 0.06 \text{ \AA}^{-1}$. In this case, Fourier transforming the Coulomb potential leads also to a Gaussian distribution with $r_{1/2} = 27.8 \text{ \AA}$, meaning a strong electronic screening by charges located at a distance of $r = 40 \text{ \AA}$, much larger than

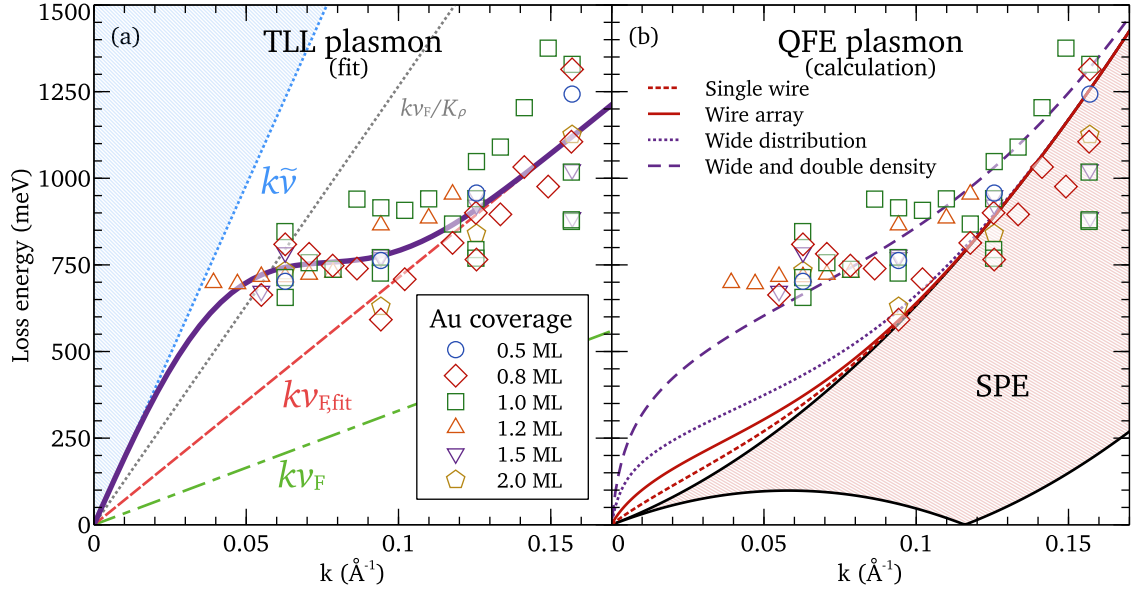


Figure 11.2: Data extracted from loss measurements with two possible descriptive models for the plasmon dispersion relation: No dependence of the data on coverage can be made out, cf. colored markers in the key. (a) The TLL model was used in combination with an arbitrary Gaussian distributed Coulomb interaction given by the purple line. Here, v_F for the fit does not result in the one from photoemission, cf. red and green line. K_ρ from STS data results in a renormalization lower than expected; it should be inside the blue region. (b) Calculations of a QFE plasmon with an extrapolated parabolic band from photoemission for a single wire (dashed red) and an array of wires (solid red) with $w = 5 \text{\AA}$ as well as an array of wires with $w = 20 \text{\AA}$ (dotted purple) and with additionally doubled electron density (dashed purple). The bright red area shows the electron-hole excitation continuum.

the interchain distance d .

Although the resulting parameters perfectly describe the data, their values are highly questionable. First of all, for high k the dispersion aligns to a v_F that is twice the value of a Fermi velocity acquired from photoemission [193] and a tight-binding calculation [194] for the direction parallel to the wires, indicated by the red dashed line for the fit and the green dash-dotted line for the experimental data in Fig. 11.2 (a). This value is still compatible when taking into account the constant C introduced in Eq. 3.28 lifting the interaction also for short wavelengths. However, it remains unlikely to be that strong. Additionally after the interpretation of the STS data [196], Luttinger theory yields $K_\rho = 0.26$. Thus, this value renormalizes the velocity to $u = v_F/K_\rho \approx 4v_F$, shown by the grey dotted line. In contrast, the fit results in a much higher renormalization, as depicted by the blue dotted line. Due to the lack of data points for low k , an upper boundary for this Luttinger constant arises to $K_\rho \leq 0.17$. The region filled in bright blue is the corresponding region for these values. All these contradicting results rule out the presence of a TLL behavior.

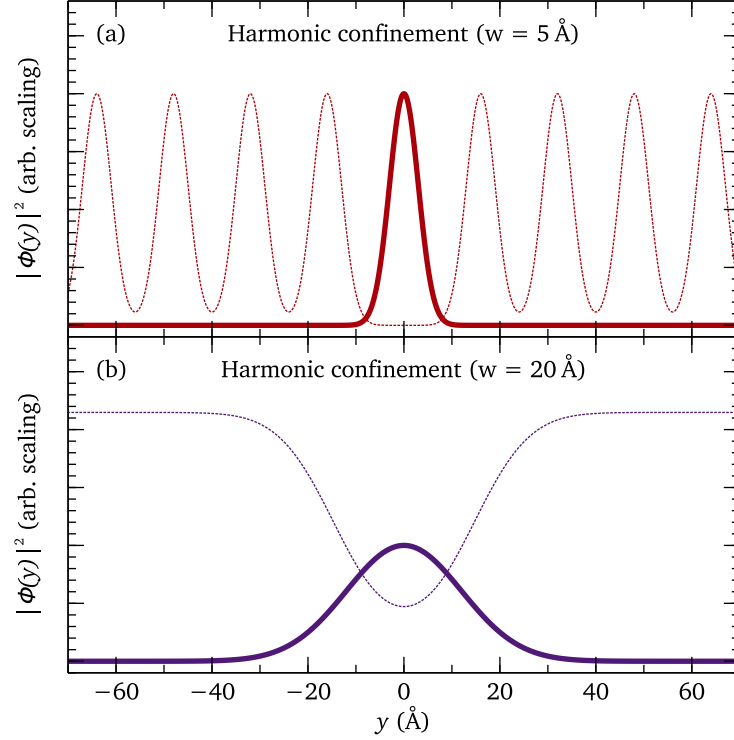


Figure 11.3: Wave functions of varying widths for the description of the Ge(100)-Au plasmon. Changing the width from 5 Å (a) to 20 Å (b) leads to a strong overlap in the surrounding wavefunction.

11.2.2 Quasi-Free Electron Gas Description

Another approach was the treatment as a 1D Fermi liquid, as conducted also for the Si(hhk)-Au systems in Chapter 7 and elaborated in Chapter 3 for numerical calculations. The electronic structure of this system was fit with a parabola to $m^* = 0.13m_e$ and $k_F = 0.058 \text{ \AA}^{-1}$ in direction parallel to the wires [196, 194]. Thus, simple theory was possible after the computation of $v_c(k)$.

The calculations were carried out with a wave function of Gaussian electron distribution with a width of $w = 5 \text{ \AA}$ and an interchain distance of $d = 16 \text{ \AA}$, cf. Fig. 11.3 (a). Choosing this width is reasonable when comparing with STM data [179, 184]. The system was modeled with five wires to the left and additional five to the right of the conduction channel. The dielectric constant was chosen as the mean value of germanium¹ and vacuum as $\bar{\epsilon} = (16.2 + 1)/2 = 8.6$.

The resulting plasmonic dispersion is plotted in Fig. 11.2 (b) by the dashed red line for a single wire and by the solid red line for one placed within an array of wires. For high $k > 0.09 \text{ \AA}^{-1}$, there is a good agreement between the data and the calculation. This conformity is mainly attributed to the behavior of the upper boundary of the electron-hole single-particle excitation spectrum (SPE). This agreement

¹From Ioffe Institute (<http://www.ioffe.ru/SVA/NSM/Semicond/Ge/>)

also gives an indication that the chosen dispersion of the electronic band is correct. For lower k -values the data is lying both above the array's plasmon as well as the single wire one. As the overlap of the wave functions increases the energy for long wavelengths, the extent of the Gaussian functions with FWHM of 5 \AA used in the model is not sufficient.

Therefore, the same calculation was carried out for wave functions with a width of $w = 20 \text{ \AA}$ of each wire to obtain an immense overlap as depicted in Fig. 11.3 (b). To include this overlap appropriately, the numerics were carried out in an array of 51 such wires. In total, the system now corresponds to a wider channel in a 2D environment. The resulting dispersion relation shows a trend toward the extracted data depicted by the dotted purple curve. Its induced blueshift but is still not sufficient.

Qualitatively, the data can only be described by a further increase in the electron density to twice the value compared to the one observed in ARPES, as given by the dashed purple line. One possible explanation for this doubled amount of electrons is the fact, that there are two electron pockets per unit cell. Another explanation is the elliptic two-dimensional Fermi surface as described by the work of De Jong et al. [194]. Their description of the electronic band structure has the shape of an upside-down hat, with a general slope of higher effective mass perpendicular to the wires compared to the parallel direction. Thus, in a two-dimensional case, the electron density is highly underestimated within this 1D theory.

While the difference in electronic structure also leads to anisotropic conduction properties, an additional perpendicular conduction channel leads to a substantial delocalization of electronic states. This crossover to two dimensions was modeled by the stretch-out of the wave function in the given case, justifying the approximation made. However, the lower boundary of the SPE must be neglected in a real 2D case.

11.3 Conclusion of the Plasmon Investigations

Both description trials with a TLL model and the free-electron gas plasmon are unsatisfactory as they need severe modification that cannot directly be attributed to the properties of the system. However, albeit the need for a higher electron density, the slope of the stretched-out electron system is most likely the best approach to the observed excitations. Anyway, the predictions of Fermi liquid and Luttinger liquid theory are qualitatively very similar. The primary influence is given by the Coulomb interaction in the form of $v_c(k)$, and there is no real reason to use the arbitrary Gaussian potential of Eq. 11.2.

In conclusion, these results in combination with newer ARPES investigations [194] suggest the Ge(100)-Au system to be a strongly anisotropic 2D metal. Accordingly, this finding indicates that not all wire structures necessarily have a one-dimensional electronic behavior. For a more quantitative investigation of this system, an angle-dependent measurement on a single-domain surface is necessary. Such a system can be realized on a vicinal Ge(100) wafer with only several degrees miscut as already reported

in Ref. [214]. For a quasi-one-dimensional plasmon, a dependence of

$$E(\vec{k}) = E(k_{\parallel}) \times \cos \theta \quad (11.4)$$

is expected [215, 216, 217], with k_{\parallel} as the part of \vec{k} aligned parallel to the wire direction and θ as the angle between \vec{k} and the wire. Investigations on such samples have been started already within this group. Although the LEED patterns mainly showed sharp spots of one domain, energy loss spectroscopy did not yield a visible plasmonic excitation.

Part IV:
Conclusions

Summary of the Findings

This chapter is meant to summarize and evaluate the findings of this work and to give some overall conclusions. It starts with the results from Si(hhk)-Au and Ge(100)-Au, draws some conclusions regarding atomic wires on surfaces, and provides an outlook in the end.

12.1 Si(hhk)-Au

First, this thesis investigated the Si(hhk)-Au system with LEED and EELS-LEED in Part II. Well-ordered structures of quantum wires consisting of either one or two atoms width were grown on wafers with the four cutting directions (335), (557), (553), and (775). In Chapter 6, an analysis of the structure was carried out. In particular, for the Si(553)-Au HCW system, the wire lengths were estimated to be $\gtrsim 200 \text{ \AA}$ with a similar perpendicular order.

In Chapter 7, electron energy loss spectroscopy revealed plasmon dispersions that deviated strongly from the expectations of the quasi-free electron gas behavior obtained in ARPES. By an empiric modification to quasi-1D plasmon theory, a description was possible. For the gold-induced wire phases on Si(553), Si(775), and to some extent also for Si(557), a direct proportionality to the terrace width was found.

For a more ingenious approach, the parabolic shape of the quasi-free electron gas model of Chapter 3 was replaced with the single-particle excitations resulting from numerical band structure calculations. Most of them were available by the Paderborn group [121, 132]. Those electronic state computations included additional bands induced by the present structural elements. These elements were, in particular,

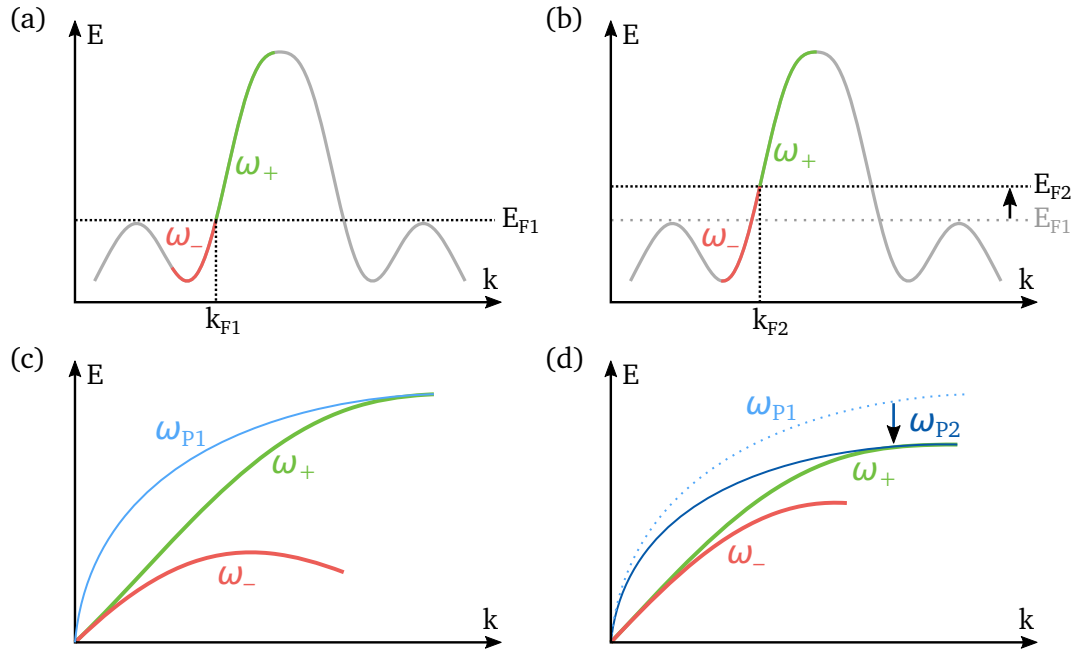


Figure 12.1: Relation between electronic band structure and electron-hole excitation spectrum: The arbitrary band structure of (a) defines the limits of the single particle excitation spectrum ω_{\pm} by the Fermi level E_{F1} and k_{F1} . With the definition of Eq. 3.13, ω_{p1} results with ω_+ as its lower limit. For the same band structure with a higher Fermi level E_{F1} in (b), the plasmon energy ω_{p2} in (d) will be lower due to the shape of the band.

the Si step edge and, where applicable, the adatom chain. By comparison with the plasmon dispersion, slight disagreements were found. Nevertheless, proposals for changes of the electronic structure were given by turning the calculations around and calculating the continuum from the given plasmon data. As finding of the lower boundary ω_- of the electron-hole excitations spectrum was quite easy, there are various issues that arise when calculating the upper boundary ω_+ for more complex band structures: Inside a band gap there is no distinct definition of ω_+ and for some systems it is unclear whether an electron or a hole-like character is dominating. For simple structures, however, it is relatively clear which band to take into account.

The findings can be summarized by Fig. 12.1 (a) and (c). For an arbitrary band structure of (a), ω_+ and ω_- are defined by the Fermi energy E_{F1} around k_{F1} . Taking these curvatures, the calculation of the plasmon dispersion ω_{p1} with Eq. 3.13 results in the blue curve in (c).

However, the empiric model as well as of the band structure dependent approach show the same physics. The terrace width dependence seen in the first model is simply caused by the additional structural elements that will occur on wider terraces. In the second model, these elements directly change the band structure, leading to a more sophisticated description.

Further information was obtained from the shape of the plasmon excitation peaks. The maximum

excitation probability was around 1/1000 of the elastically scattered intensity. Furthermore, the systems were quite stable with a loss peak decrease of around 30 % after 12 h in the present vacuum of 5×10^{-11} mbar. The investigation of the widths revealed a broadening beyond a lifetime effect. The primary influence is due to the k -space resolution of the spectrometer that feeds back to the energy resolution depending on the dispersion relation of a given system. Further discussion about the increase of the width is also carried out, mentioning among others the band structure, electron-electron scattering, and the scattering geometry itself as possible influences.

In Chapter 8, the influence of the adsorption of oxygen and hydrogen was investigated. Substantial changes in the plasmon energy were observed for the systems with an adatom chain, in particular the plasmon in Si(557)-Au increased its energy by 70 %, the plasmon in Si(775)-Au by 30 % for a dose of around 15 L. No changes were observed for the Si(553)-Au system. Thus, the origin was attributed to the adatom/restatom chain. Numerical calculations of the electronic band structure for various oxidation sites on Si(557)-Au were not able to indicate such behavior when using the procedure elaborated before. Calculations for Si(775)-Au were not available. Anyhow, a decrease of the electron density at E_F is expected for oxidation. As an increase in the plasmon energy is seen, the band structure must change in a way that the slope of ω_+ is much steeper for both systems. Within the empiric low- k model, this behavior is explained by an increase of the confinement.

Atomic hydrogen adsorption on Si(553)-Au led to a decrease of the plasmon energy by 40 % after saturation of approximately half of the step edge atoms. Though the electron density is increased, this behavior was explained by the shift of the Fermi level to a situation such that the slope of the upper boundary ω_+ was decreased, as also suggested by calculations of Hogan et al. [157].

This behavior is also illustrated in Fig. 12.1. In (b), the Fermi level E_{F2} is shifted upwards in respect to the same band structure as given in (a). Accordingly, ω_+ and ω_- change. As a consequence of the slope of the band itself, the resulting plasmon ω_{p2} will be lower in energy than the plasmon ω_{p1} of the original system, though the electron density has increased. However, this model only works as long as ω_+ is energetically higher than ω_- . For the case of $\omega_+ < \omega_-$ they would change their sign and the considerations become hole-like. In that case, the energy of the plasmon would increase again. None of the investigated systems of the chemisorption in Chapter 8 showed such a behavior, though. Such inversion of ω_{\pm} is expected for the hydrogenation of the Si(553)-Au surface. During those measurements the plasmon energy shifted downwards until the loss peak could no longer be resolved. However, the reduction of 40 % observed is still compatible with the region depicted in Fig. 12.1 (d).

Moreover, it is not verified if hole-like plasmons in the picture just developed exist at all. The description of the plasmon in Si(775)-Au was both possible by an electron-like or such a hole-like approach where ω_+ points into the occupied states. A possible experiment to a solution of this problem is a sample with a backgate. Due to the field effect, the Fermi level can be shifted while the shape of the band structure is untouched. In this manner, the correct model is directly seen by the increase or decrease of the plasmon energy for a particular voltage bias.

All in all, these investigations revealed what to include in the understanding of plasmonic excitations of atomic wires embedded into a rather complex environment. The dimensional crossover to 2D and 3D is significant. Its main parts are the dielectric background of the substrate, the interwire correlation of the adjacent conducting channels in the array, and most importantly additional structural elements next to the wires that modify the electronic band structure of the entire system by hybridization. This influencing crossover can also be used to tune the properties of a 1D plasmon.

12.2 Ge(100)-Au

The investigations on Ge(100)-Au were carried out in Part III. Special attention was put into the sample preparation due to the inherent lower quality of germanium substrates. In Chapter 10, a recipe of sequences of Ar⁺ sputtering with subsequent annealing was developed that allowed obtaining high-quality Ge(100) surfaces as seen by spot profile analysis techniques in LEED, i.e. $G(S)$ and $H(S)$ analyses. The following preparation of the Ge(100)-Au wire structure yielded a corrugation that highly supports a structure related to the giant mission row reconstruction that was proposed by Van Houselt et al. [180]. The coverage of the system was determined to 1 ML suggesting a modified structural model similar to GMR, potentially with subsurface Au positions.

In Chapter 11, EELS showed only very broad plasmon loss peaks of low intensity. This result was also one of the reasons to improve the quality of the samples. However, even for optimized growing conditions, the peaks remain the same. The origin of this behavior remains unclear.

The plasmon dispersion relation acquired from the loss spectra shows a behavior that neither a Tomonaga-Luttinger liquid model nor a quasi-free electron gas approach can explain. A rather qualitative description was possible with an increased electron density and a high overlap of the lateral distribution of electrons with the adjacent wires. As already indicated in the literature, this circumstance must be attributed to an anisotropic 2D nature of this system.

12.3 Conclusions Regarding Atomic Wires on Surfaces

The observed collective excitations of this thesis gave insight into the possible influences to the electronic properties when embedding atomic wires on a surface. Lateral structural elements have a strong feedback. Furthermore, especially the results of Chapter 7 revealed that the structural motifs are not a modular part of a construction kit, but strongly influence each other. As an example, the silicene band on Si(335)-Au has a much stronger curvature compared to all other systems, meaning a less localized state in real space. That electronic change is a possible indication why the simple systematics of the empirically modified low- k model no longer work for this surface. Furthermore, some motifs may act as potential barriers, e.g. a silicene step edge or, as proposed in Chapter 8, the oxidized adatom/restatom chain, leading to the modification of the quantum states. Coulomb screening for a decoupled substrate

in the form of an effective dielectric environment $\bar{\epsilon}$ as well as by adjacent wires in an array is an important aspect, especially for plasmons. This work showed that these predictions in the form of the numerically derived Coulomb matrix element $v_c(k)$ were compatible with the observations.

However, the influence of the bulk is not always that simple. It turned out that the Au-induced wires on germanium are most likely an anisotropic 2D metal. As the wires are not connected to each other, the substrate itself must induce a conducting channel perpendicular that short-circuits the wires. This result also shows that a wire-like looking structure is not necessarily one-dimensional in its electronic states.

Additionally, this work showed that it is important to be very careful with photoemission data. For both wire families, a carefree usage led to misinterpretations: In the case of the Si(hhk)-Au systems, invisible hybridizations were not taken into account until DFT calculations revealed their existence. As it turned out, they were a crucial aspect for the description of electronic excitations in these systems. In the case of Ge(100)-Au, the system was interpreted to be of one-dimensional metallic character because the insufficient resolution of the measurements did not uncover the elliptic Fermi surface of this anisotropic 2D system.

The specific modifications of the electronic states of such systems by, e.g., chemical adsorption can result in a rather complex issue. While the saturation of dangling bonds with hydrogen acted similar to macroscopic doping processes because of a kind of proximity effect, the oxidation of the Si(hhk)-Au adatom chains had a tremendous effect on the band structure. In conclusion, such attempts are a delicate approach when thinking about an on demand fabrication of atomic wires.

The insights into quasi-1D plasmons gained in this work allow to divide them into two parts: a low- k and a high- k regime. For low- k , the system is dominated by the inter- and intrawire correlations, by bulk screening, as well as by the feedback of the additional structural elements. All these properties are hidden in the empirically introduced effective wire width a when assuming a quasi-free electron gas behavior of the conducting chain. For the high- k region, only the electronic band structure is important and there it is no longer possible to distinguish between the upper boundary of the single-particle excitation spectrum ω_+ and the plasmon ω_p . Their energies are degenerate. Although there is no sharp boundary between those two regimes, for the systems investigated in this work, the low- k behavior dominates below 0.05 \AA^{-1} and the ambiguity of the high- k regime starts for momenta $> 0.1 \text{ \AA}^{-1}$.

How realistic is the application of such atomic wire systems in general? The world is far away from the embedding into real devices, as the formation up to now is only possible by self-assembly. A designed fabrication of atomic wire circuits is still impossible. The investigations of the widths of the plasmon peaks revealed a broadening beyond an effect of lifetime. The damping mechanisms are not fully understood, but the similar trend for all systems indicates the same driving force for such small wires. Unfortunately, this effect leads at least to an energetic uncertainty for higher k . On the contrary, lifetimes of $> 100 \text{ fs}$ can be estimated for $k < 0.02 \text{ \AA}^{-1}$. With a typical propagation speed of $1 \times 10^6 \text{ m s}^{-1}$, such plasmons travel distances of $> 100 \text{ nm}$. This is a sufficient range for an on-chip application.

Anyway, a defect in an atomic wire always means the end of metallic conduction. Therefore, a perfect fabrication would be necessary. As a consequence, a more promising approach for future applications of small plasmonic channels is the use of systems that condone defects. Such systems are, e.g., 2DEG ribbon structures like the wider Ag nanowires on vicinal silicon surfaces or graphene.

12.4 Outlook

In contrast to earlier investigations on, e.g., Si(557)-Ag [29] or DySi₂ wires [218], the applied modifications to plasmon theory showed that the simple model of using the approximation of a quasi-free electron gas would no longer hold true for atomic wires embedded into structural elements of the same scale. Obtaining the slope of a plasmon for such rather sophisticated systems always needed the knowledge of the complex dielectric function $\epsilon(k)$. However, the numerical calculation of this function requires additional orders of magnitude of processing power compared to the determination of merely the ground state, i.e. the computation of the electronic band structure.

This thesis showed a modification that can be done within the simple plasmon theories to obtain a plasmon dispersion directly out of the bandstructure, cf. Fig. 12.1. However, there is still a lack of clear instructions, as the effective masses m^* , e.g., were obtained rather empirically around k_F and it remains unclear how to cope with band gaps. Furthermore, the behavior for ω_+ in the occupied states is not thoroughly clear. A backgate experiment was already suggested above in order to systematically understand this issue.

Another good starting point beyond the approximations of this work might be the exchange of the density response function χ_0 in Eq. 3.4. Here, instead of the quasi-1D description, a more general form could be used, if possible. Anyway, it would be advantageous to see the discrepancies between a complete computation of one of the quasi-1D plasmons within the same framework of the calculated band structures and the approaches that have been done in this thesis. In this way, the quality of the modifications can be determined.

The bending of the calculated ω_+ for the Si(553)-Au systems was attributed to the band gap. A newer calculation shows that it originates from the dimerization of the Au chain. If this dimerization is temperature-dependent, a change in the plasmon for higher k should be visible. The scatter of the present data of the plasmon dispersion of this thesis is rather high. This uncertainty might be the reason why this feature was not seen for LT. Another potential explanation is that the temperature was not low enough to see an effect. Therefore, special care must be taken to observe this possible behavior. With the new and brighter LaB₆ filament in the EELS-LEED the resolution can be improved while keeping the same backscattered intensity. This property can help such observations.

Talking about the doping experiments of Chapter 8, data were only recorded at selected k . For further insight into the changes in the band structure, complete dispersions for a defined adsorbed amount of both oxygen and hydrogen would be highly useful. Furthermore, numerical calculations for the oxidized

Si(775)-Au are crucial for the understanding of the oxidation processes.

During this work, the spot profile analysis of the Ge(100) and its Au-induced wire construction helped improve the growing conditions. Nevertheless, it is still unclear which structural model is right. As the results highly support a structure with a deep groove, further improvements were already carried out for a family of wires with coverage > 1 ML in Ref. [192]. However, the discrepancy between the coverages in the literature might be one of the big uncertainties, possibly because gold has a higher solubility in germanium compared to, e.g., silicon [219]. Therefore, the attention should be directed to the optimization of the surface free energy and the accordance with experimental data. As the plasmon data showed that the system is unlikely one-dimensional, also the electronic band structure of those models must not be 1D.

An angle-dependent plasmon investigation can also help clarify the nature of the anisotropy in the electronic states. Such a measurement is possible for a sample with most of the surface domains featuring the same wire direction. This growth mode is possible on a vicinal Ge(100) sample with only minor miscut of $\approx 4^\circ$. Such investigations already started within our group but led to no visible loss peaks in the spectra although the samples were of superior quality.

Apart from additional studies on the same systems, the insights gained in this work can also be used to clarify the situation in other structures. As a particular example, the elaborated systematics of Fig. 12.1 might lead to a better explanation for the plasmonic excitation in Si(111)-In [41], where also hybridizations change the electronic band structure [220]. In a wider sense, as the result on Si(hhk)-Au indicated, the values for higher k will give a good approximation for the slope of the unoccupied states and, thus, can be a simpler and quick experimental approach compared to the typical two-photon photoelectron spectroscopy (2PPE) experiments.

In addition, the influences of structural elements as well as the chemisorption-induced changes showed various ways that change plasmon properties. This information will give a good starting point for the future engineering of plasmonic structures on the atomic scale.

Appendix

Source Code of the Plasmon Calculations

The calculations for the plasmon dispersion were carried out with a short script for Python, called “Dispcalc_harm.py” see Lst. 1. This software will load constants from “constants.py” and a defined wavefunction, in the given case the one according to harmonic confinement as defined in “wfl dharm.py”. Alternatively, it is possible to use square-well confinement by replacing the file to “wfl dsq.py”. Their source code is given below. The variables are set to the values used for the Si(553)-Au system when taking the data from ARPES. The given wavefunction is used in the integrals defined by the functions in lines 45 and 49 to obtain the Coulomb interaction as defined in Eqs. 3.12 and 3.18. All values will be calculated in SI-units, only the energies in the output of the file “data.asc” will be in eV.

Listing 1: Dispcalc_harm.py

```
1 #General import
2 import numpy as np
3 import scipy as sp
4 import scipy.integrate as integrate
5 import scipy.special as special
6 from math import pi as pi
7 from math import exp as exp
8 import matplotlib.pyplot as plt
9
10 #Import constants
11 from constants import *
12
13 #Import of wavefunction
14 from wfl dharm import *
15
16 #Variables
```

```
17 #mstar
18 m = 0.59*me
19 #gs dimensionless
20 gs = 2
21 #kF in inverse meters
22 kF = 0.448e10
23 #E_F in J and eV
24 Ef = hbar*hbar*kF*kF/(2*m)
25 Efev = hbar*hbarev*kF*kF/(2*m)
26 #Confinement width in meters
27 a = 2.76e-10
28 # 2.76 is FWHM = 6.6 (twice Si-Si)
29 #Wire spacing
30 d = 14.8e-10
31 #Number of wires to the left and right
32 n = 5
33 #Epsilon dimensionless
34 epsilon = (11.5+1)/2
35
36 #Resolution in inverse meters for dispersion relation
37 rng = 0.2e10
38 res = rng/200
39 k = sp.arange(rng/1000,rng,res)
40
41 #Prefactor of Coulomb interaction v_c
42 vfvc = (2*e**2)/(4*pi*epsilon0*epsilon)
43
44 #Definition of integrating function to obtain v_c without prefactors
45 def vcsim(k,a):
46     return integrate.dblquad(lambda y,ys: special.kn(0,np.abs(k*(y-ys
47         )+1e-100))*(wf(y-a/2,a)**2)*(wf(ys-a/2,a)**2), -10*a, 10*a,
48         lambda y:-5*a, lambda y:5*a)
49
50 #Definition of Coulomb interaction to the adjacent wires
51 def vcsimmultiple(k,a,d,n):
52     return integrate.dblquad(lambda y,ys: special.kn(0,np.abs(k*(y-ys
53         )+1e-100))*(wf(y-a/2,a)**2)*(wfmultiple(ys-a/2,a,d,n)**2), -n*
```

```

    d-10*a, n*d+10*a, lambda y:-n*d-10*a, lambda y:n*d+10*a)
51
52 #Simplification of STLS approximation
53 def gkorr(k_inp,gs_inp):
54     return 0.3*gs_inp*(k_inp*1e-10)**(1/4)+0.8*k_inp*1e-10
55
56 #omega+ and omega-
57 def omegaplus(k_inp, kF_inp):
58     return (hbar/m)*((k_inp**2)/2 + k_inp*kF_inp)
59 def omegaminus(k_inp, kF_inp):
60     return (hbar/m)*((k_inp**2)/2 - k_inp*kF_inp)
61
62 #Empty arrays
63 vc = np.zeros(len(k))
64 vcmultiple = np.zeros(len(k))
65 avonk = np.zeros(len(k))
66 avonkmultiple = np.zeros(len(k))
67 omega = np.zeros(len(k))
68 omegamultiple = np.zeros(len(k))
69 omegaplus_values = np.zeros(len(k))
70 omegaminus_values = np.zeros(len(k))
71
72 #For loop for calculation, prints step
73 for i in range(0,len(k)):
74     print(i)
75     temp = vcsim(k[i],a)
76     tempmultiple = vcsimmultiple(k[i],a,d,n)
77     vc[i] = vfvc*temp[0]
78     vcmultiple[i] = vfvc*(temp[0]+tempmultiple[0])
79     avonk[i] = hbar**2 * 2 * pi* k[i] / (m * gs * vc[i] *(1-gkorr(k[i]
80         ],gs)))
81     avonkmultiple[i] = hbar**2 * 2 * pi * k[i] / (m * gs * vcmultiple
82         [i] *(1-gkorr(k[i],gs)))
83
84     omegaplus_values[i] = omegaplus(k[i],kF)
85     if k[i]<2*kF:
86         omegaminus_values[i] = np.abs(omegaminus(k[i],kF))

```

```
85     else :
86         omegaminus_values[i] = 0
87
88     omega[i] = np.sqrt((omegaminus(k[i],kF)**2 - omegaplus(k[i],kF)
89         **2 * np.exp(avonk[i])) / ( 1 - np.exp(avonk[i])) )
90
91     omegamultiple[i] = np.sqrt((omegaminus(k[i],kF)**2 - omegaplus(k[
92         i],kF)**2 * np.exp(avonkmultiple[i])) / ( 1 - np.exp(
93         avonkmultiple[i])) )
94
95     #Write to file
96     file = open('data.asc', 'w')
97     file.write("k\tvc\tvcmultiple\tomega\tomegamultiple\tomega+\tomega-\n
98         ")
99     for i in range(0, len(k)):
100         file.write(str(k[i]))
101         file.write("\t")
102         file.write(str(vc[i]))
103         file.write("\t")
104         file.write(str(vcmultiple[i]))
105         file.write("\t")
106         file.write(str(hbarev*omega[i]))
107         file.write("\t")
108         file.write(str(hbarev*omegamultiple[i]))
109         file.write("\t")
110         file.write(str(hbarev*omegaplus_values[i]))
111         file.write("\t")
112         file.write(str(hbarev*omegaminus_values[i]))
113         file.write("\n")
114     file.close()
```

The following file “constants.py” inputs necessary constants into the scripts as the measurements have been carried out in SI-units with energies in eV.

Listing 2: constants.py

```
1 #hbar in Js
2 hbar = 1.05457148e-34
3 #hbar in eVs
4 hbarev = 6.582119514e-16
5 #e in C
6 e = 1.6021766208e-19
7 #me in kg
8 me = 9.10938356e-31
9 #epsilon0 in F/m
10 epsilon0 = 8.854187817e-12
```

The input wavefunction for all calculations is given by a harmonic potential resulting in a Gaussian distribution of electrons. The function is defined in the following file “wf1dharm.py”.

Listing 3: wf1dharm.py

```
1 #Harmonic wavefunction
2 def wf(y,a):
3     return (1/(2*pi*a**2))**(1/4)*np.exp(-y**2/(4*a**2))
4
5 #Wavefunction of the harmonic array
6 def wfmultiple(y,a,d,n):
7     wfsum = 0
8     for i in range(-n,n+1):
9         if i != 0:
10            wfsum = wfsum + wf(y-i*d,a)
11        else:
12            wfsum = wfsum
13    return wfsum
```

Another possibility of a wavefunction is the result for a square-well potential, resulting in a sine. It is defined as described in “wf1dsq.py” and was only used in the plasmon theory of Chapter 3.

Listing 4: wf1dsq.py

```
1 #Square-well wavefunction
2 def wf(y,a):
3     if y<0:
4         return 0
5     elif y>a:
6         return 0
7     else:
8         return np.sqrt(2/a)*np.sin(pi*y/a)
9
10 #Wavefunction of the square-well array
11 def wfmultiple(y,a,d,n):
12     wfsum = 0
13     for i in range(-n,n+1):
14         if i != 0:
15             wfsum = wfsum + wf(y-i*d,a)
16         else:
17             wfsum
18     return wfsum
```

Bibliography

- [1] T. GIAMARCHI, *Quantum Physics in One Dimension*, Clarendon Press, Oxford, 2003.
- [2] S. KAGOSHIMA, H. NAGASAWA, T. SAMBONGI, *One-Dimensional Conductors*, volume 72 of *Springer Series in Solid-State Sciences*, Springer Berlin Heidelberg, Berlin, Heidelberg, 1988, doi:10.1007/978-3-642-83179-9.
- [3] G. GRÜNER, *The dynamics of charge-density waves*, Rev. Mod. Phys. **60**, 4:1129, 1988, doi:10.1103/RevModPhys.60.1129.
- [4] G. GRÜNER, *The dynamics of spin-density waves*, Rev. Mod. Phys. **66**, 1:1, 1994, doi:10.1103/RevModPhys.66.1.
- [5] R. PEIERLS, *Zur Theorie der elektrischen und thermischen Leitfähigkeit von Metallen*, Ann. Phys. **396**, 2:121, 1930, doi:10.1002/andp.19303960202.
- [6] H. W. YEOM, S. TAKEDA, E. ROTENBERG, I. MATSUDA, K. HORIKOSHI, J. SCHAEFER, C. M. LEE, S. D. KEVAN, T. OHTA, T. NAGAO, S. HASEGAWA, *Instability and Charge Density Wave of Metallic Quantum Chains on a Silicon Surface*, Phys. Rev. Lett. **82**, 24:4898, 1999, doi:10.1103/PhysRevLett.82.4898.
- [7] S. WIPPERMANN, W. G. SCHMIDT, *Entropy Explains Metal-Insulator Transition of the Si(111)-In Nanowire Array*, Phys. Rev. Lett. **105**, 12:126102, 2010, doi:10.1103/PhysRevLett.105.126102.
- [8] J. M. LUTTINGER, *An Exactly Soluble Model of a Many-Fermion System*, J. Math. Phys. **4**, 9:1154, 1963, doi:10.1063/1.1704046.
- [9] S.-I. TOMONAGA, *Remarks on Bloch's Method of Sound Waves applied to Many-Fermion Problems*, Prog. Theor. Phys. **5**, 4:544, 1950, doi:10.1143/ptp/5.4.544.

- [10] K. SCHÖNHAMMER, *Luttinger liquids: the basic concepts*, in *Strong Interact. low Dimens.*, volume 25, chapter 4, 93–136, Springer Netherlands, Dordrecht, 2004, doi:10.1007/978-1-4020-3463-3_4, arXiv:cond-mat/0305035v2.
- [11] I. FREESTONE, N. MEEKS, M. SAX, C. HIGGITT, *The Lycurgus Cup — A Roman nanotechnology*, *Gold Bull.* **40**, 4:270, 2007, doi:10.1007/BF03215599.
- [12] K. BAMMEL, *Oberflächliche Farbenpracht*, *Phys. J.* **5**, 12:52, 2006.
- [13] R. W. WOOD, *On a Remarkable Case of Uneven Distribution of Light in a Diffraction Grating Spectrum*, *Proc. Phys. Soc. London* **18**, 1:269, 1902, doi:10.1088/1478-7814/18/1/325.
- [14] B. SCHWARZ, P. REININGER, D. RISTANIĆ, H. DETZ, A. M. ANDREWS, W. SCHRENK, G. STRASSER, *Monolithically integrated mid-infrared lab-on-a-chip using plasmonics and quantum cascade structures.*, *Nat. Commun.* **5**, May:4085, 2014, doi:10.1038/ncomms5085.
- [15] H. A. ATWATER, A. POLMAN, *Plasmonics for improved photovoltaic devices.*, *Nat. Mater.* **9**, 3:205, 2010, doi:10.1038/nmat2866.
- [16] J. N. ANKER, W. P. HALL, O. LYANDRES, N. C. SHAH, J. ZHAO, R. P. VAN DUYN, *Biosensing with plasmonic nanosensors.*, *Nat. Mater.* **7**, 6:442, 2008, doi:10.1038/nmat2162.
- [17] C. AYALA-OROZCO, C. URBAN, M. W. KNIGHT, A. S. URBAN, O. NEUMANN, S. W. BISHNOI, S. MUKHERJEE, A. M. GOODMAN, H. CHARRON, T. MITCHELL, M. SHEA, R. ROY, S. NANDA, R. SCHIFFE, N. J. HALAS, A. JOSHI, *Au nanomatryoshkas as efficient near-infrared photothermal transducers for cancer treatment: Benchmarking against nanoshells*, *ACS Nano* **8**, 6:6372, 2014, doi:10.1021/nn501871d.
- [18] T. NAGAO, G. HAN, C. HOANG, J.-S. WI, A. PUCCI, D. WEBER, F. NEUBRECH, V. M. SILKIN, D. ENDERS, O. SAITO, M. RANA, *Plasmons in nanoscale and atomic-scale systems*, *Sci. Technol. Adv. Mater.* **11**, 5:054506, 2011, doi:10.1088/1468-6996/11/5/054506.
- [19] L. VATTUONE, M. SMERIERI, T. LANGER, C. TEGENKAMP, H. PFNÜR, V. M. SILKIN, E. V. CHULKOV, P. M. ECHENIQUE, M. ROCCA, *Correlated Motion of Electrons on the Au(111) Surface: Anomalous Acoustic Surface-Plasmon Dispersion and Single-Particle Excitations*, *Phys. Rev. Lett.* **110**, 12:127405, 2013, doi:10.1103/PhysRevLett.110.127405.
- [20] H. PFNÜR, C. TEGENKAMP, L. VATTUONE, *Plasmons in one and two dimensions*, *Springer Handb. Surf. Sci.* 2017, arXiv:1701.05049.
- [21] V. RODRIGUES, J. BETTINI, A. R. ROCHA, L. G. C. REGO, D. UGARTE, *Quantum conductance in silver nanowires: Correlation between atomic structure and transport properties*, *Phys. Rev. B* **65**, 15:153402, 2002, doi:10.1103/PhysRevB.65.153402, arXiv:cond-mat/0201156.

-
- [22] J. BETTINI, F. SATO, P. Z. COURA, S. O. DANTAS, D. S. GALVÃO, D. UGARTE, *Experimental realization of suspended atomic chains composed of different atomic species*, Nat. Nanotechnol. **1**, 3:182, 2006, doi:10.1038/nnano.2006.132.
- [23] F. STERN, *Polarizability of a Two-Dimensional Electron Gas*, Phys. Rev. Lett. **18**, 14:546, 1967, doi:10.1103/PhysRevLett.18.546.
- [24] K. S. SINGWI, M. P. TOSI, R. H. LAND, A. SJÖLANDER, *Electron Correlations at Metallic Densities*, Phys. Rev. **176**, 2:589, 1968, doi:10.1103/PhysRev.176.589.
- [25] S. DAS SARMA, W.-Y. LAI, *Screening and elementary excitations in narrow-channel semiconductor microstructures*, Phys. Rev. B **32**, 2:1401, 1985, doi:10.1103/PhysRevB.32.1401.
- [26] J. N. CRAIN, M. C. GALLAGHER, J. MCCHESENEY, M. BISSEN, F. J. HIMPSEL, *Doping of a surface band on Si(111) $\sqrt{3}\times\sqrt{3}$ -Ag*, Phys. Rev. B **72**, 4:045312, 2005, doi:10.1103/PhysRevB.72.045312.
- [27] J. A. LIPTON-DUFFIN, A. G. MARK, J. M. MACLEOD, A. B. MCLEAN, *Si(557)-Ag: A metallic quasi-one-dimensional system*, Phys. Rev. B **77**, 12:1, 2008, doi:10.1103/PhysRevB.77.125419.
- [28] U. KRIEG, C. BRAND, C. TEGENKAMP, H. PFNÜR, *One-dimensional collective excitations in Ag atomic wires grown on Si(557)*, J. Phys. Condens. Matter **25**, 1:014013, 2013, doi:10.1088/0953-8984/25/1/014013.
- [29] U. KRIEG, *1D-Plasmonen in Ag-Nanodrähten auf vicinalem Si(557)*, Doctoral Dissertation, Leibniz Universität Hannover, 2014.
- [30] U. KRIEG, T. LICHTENSTEIN, C. BRAND, C. TEGENKAMP, H. PFNÜR, *Origin of metallicity in atomic Ag wires on Si(557)*, New J. Phys. **17**, 4:043062, 2015, doi:10.1088/1367-2630/17/4/043062.
- [31] E. P. RUGERAMIGABO, T. NAGAO, H. PFNÜR, *Experimental investigation of two-dimensional plasmons in a DySi 2 monolayer on Si(111)*, Phys. Rev. B **78**, 15:1, 2008, doi:10.1103/PhysRevB.78.155402.
- [32] K. S. NOVOSELOV, A. K. GEIM, S. V. MOROZOV, D. JIANG, Y. ZHANG, S. V. DUBONOS, I. V. GRIGORIEVA, A. A. FIRSOV, *Electric Field Effect in Atomically Thin Carbon Films*, Science **306**, 5696:666, 2004, doi:10.1126/science.1102896.
- [33] K. I. BOLOTIN, K. J. SIKES, Z. JIANG, M. KLIMA, G. FUDENBERG, J. HONE, P. KIM, H. L. STORMER, *Ultrahigh electron mobility in suspended graphene*, Solid State Commun. **146**, 9-10:351, 2008, doi:10.1016/j.ssc.2008.02.024, arXiv:0802.2389.
- [34] C. TEGENKAMP, H. PFNÜR, T. LANGER, J. BARINGHAUS, H. W. SCHUMACHER, *Plasmon electron-hole resonance in epitaxial graphene*, J. Phys. Condens. Matter **23**, 1:012001, 2011, doi:10.1088/0953-8984/23/1/012001.
-

- [35] J. BARINGHAUS, M. RUAN, F. EDLER, A. TEJEDA, M. SICOT, A. TALEB-IBRAHIMI, A.-P. LI, Z. JIANG, E. H. CONRAD, C. BERGER, C. TEGENKAMP, W. A. DE HEER, *Exceptional ballistic transport in epitaxial graphene nanoribbons*, Nature **506**, 7488:349, 2014, doi:10.1038/nature12952.
- [36] P. SEGOVIA, D. PURDIE, M. HENGESBERGER, Y. BAER, *Observation of spin and charge collective modes in one-dimensional metallic chains*, Nature **402**, 6761:504, 1999, doi:10.1038/990052.
- [37] T. ABUKAWA, M. SASAKI, F. HISAMATSU, T. GOTO, T. KINOSHITA, A. KAKIZAKI, S. KONO, *Surface electronic structure of a single-domain Si(111)4 × 1-In surface: a synchrotron radiation photoemission study*, Surf. Sci. **325**, 1-2:33, 1995, doi:10.1016/0039-6028(94)00693-8.
- [38] T. FRIGGE, B. HAFKE, T. WITTE, B. KRENZER, C. STREUBÜHR, A. SAMAD SYED, V. MIKŠIĆ TRONTL, I. AVIGO, P. ZHOU, M. LIGGES, D. VON DER LINDE, U. BOVENSIEPEN, M. HORN-VON HOEGEN, S. WIPPERMANN, A. LÜCKE, S. SANNA, U. GERSTMANN, W. G. SCHMIDT, *Optically excited structural transition in atomic wires on surfaces at the quantum limit*, Nature **544**, 7649:207, 2017, doi:10.1038/nature21432.
- [39] N. ONCEL, A. VAN HOUSELT, J. HUIJBEN, A. S. HALLBÄCK, O. GURLU, H. J. W. ZANDVLIET, B. POELSEMA, *Quantum confinement between self-organized Pt nanowires on Ge(001)*, Phys. Rev. Lett. **95**, 11:1, 2005, doi:10.1103/PhysRevLett.95.116801.
- [40] H. J. W. ZANDVLIET, R. VAN GASTEL, O. GURLU, B. POELSEMA, *Coexistence of (2×1) and c(4×2) phases on Ge(001)*, Phys. Lett. A **326**, 5-6:457, 2004, doi:10.1016/j.physleta.2004.04.056.
- [41] C. LIU, T. INAOKA, S. YAGINUMA, T. NAKAYAMA, M. AONO, T. NAGAO, *Disappearance of the quasi-one-dimensional plasmon at the metal-insulator phase transition of indium atomic wires*, Phys. Rev. B **77**, 20:205415, 2008, doi:10.1103/PhysRevB.77.205415.
- [42] F. HÖTZEL, K. SEINO, S. CHANDOLA, E. SPEISER, N. ESSER, F. BECHSTEDT, A. PUCCI, *Metal-to-Insulator Transition in Au Chains on Si(111)-5×2-Au by Band Filling: Infrared Plasmonic Signal and Ab Initio Band Structure Calculation*, J. Phys. Chem. Lett. **6**, 18:3615, 2015, doi:10.1021/acs.jpcclett.5b01530.
- [43] J. E. GRIFFITH, G. P. KOCHANSKI, *The atomic structure of vicinal Si(001) and Ge(001)*, Crit. Rev. Solid State Mater. Sci. **16**, 4:255, 1990, doi:10.1080/10408439008243750.
- [44] F. TIMMER, R. OELKE, C. DUES, S. SANNA, W. G. SCHMIDT, M. FRANZ, S. APPELFELLER, M. DÄHNE, J. WOLLSCHLÄGER, *Strain-induced quasi-one-dimensional rare-earth silicide structures on Si(111)*, Phys. Rev. B **94**:1, 2016, doi:10.1103/PhysRevB.94.205431.
- [45] M. CZUBANOWSKI, A. SCHUSTER, S. AKBARI, H. PFNÜR, C. TEGENKAMP, *Adsorbate induced refacetting: Pb chains on Si(557)*, New J. Phys. **9**, 111, 2007, doi:10.1088/1367-2630/9/9/338.

- [46] T. BLOCK, C. TEGENKAMP, J. BARINGHAUS, H. PFNÜR, T. INAOKA, *Plasmons in Pb nanowire arrays on Si(557): Between one and two dimensions*, Phys. Rev. B **84**, 20:205402, 2011, doi:10.1103/PhysRevB.84.205402.
- [47] C. BRAND, *Struktur und elektronische Eigenschaften von niedrigdimensionalen Pb- und Bi-Quantenfilmen und -drähten mit starker Spin-Bahn-Wechselwirkung auf Si-Halbleiteroberflächen*, Doctoral Dissertation, Leibniz Universität Hannover, 2017.
- [48] J. A. DIONNE, K. DIEST, L. A. SWEATLOCK, H. A. ATWATER, *PlasMOStor : A Metal - Oxide - Si Field Effect Plasmonic Modulator 2009*, Nano Lett. **9**, 2:897, 2009, doi:10.1021/nl803868k.
- [49] A. N. GRIGORENKO, M. POLINI, K. S. NOVOSELOV, *Graphene plasmonics*, Nat. Photonics **6**, 11:749, 2012, doi:10.1038/nphoton.2012.262.
- [50] N. W. ASHCROFT, N. D. MERMIN, *Solid State Physics*, Cengage Learning, 1st edition, 1976.
- [51] J. K. BIENLEIN, R. WIESENDANGER, *Einführung in die Struktur der Materie*, B. G. Teubner, 1st edition, 2003.
- [52] R. GROSS, A. MARX, *Festkörperphysik*, Oldenbourg Wissenschaftsverlag Verlag, München, 2nd edition, 2012, doi:10.1524/9783486714869.
- [53] P. HOFMANN, *Surface Physics: An Introduction*, Wiley-VCH, 2nd edition, 2015.
- [54] S. HUNKLINGER, *Festkörperphysik*, De Gruyter, Berlin, Boston, 4th edition, 2014.
- [55] C. KITTEL, *Introduction to Solid State Physics*, Wiley, 8th edition, 2004.
- [56] M. P. SEAH, W. A. DENCH, *Quantitative electron spectroscopy of surfaces: A standard data base for electron inelastic mean free paths in solids*, Surf. Interface Anal. **1**, 1:2, 1979, doi:10.1002/sia.740010103.
- [57] M. HORN-VON HOEGEN, *Growth of semiconductor layers studied by spot profile analysing low energy electron diffraction*, Zeitschrift für Krist. **214**, 10:591, 1999.
- [58] H. JAGODZINSKI, W. MORITZ, D. WOLF, *Diffuse LEED intensities of disordered crystal surfaces*, Surf. Sci. **77**, 2:233, 1978, doi:10.1016/0039-6028(78)90004-3.
- [59] P. ROUS, J. PENDRY, *Diffuse LEED from simple stepped surfaces*, Surf. Sci. **173**, 1:1, 1986, doi:10.1016/0039-6028(86)90103-2.
- [60] M. HENZLER, *Quantitative evaluation of random distributed steps at interfaces and surfaces*, Surf. Sci. **73**, C:240, 1978, doi:10.1016/0039-6028(78)90499-5.

- [61] C. S. LENT, P. I. COHEN, *Diffraction from stepped surfaces - I. Reversible surfaces*, Surf. Sci. **139**, 1:121, 1984, doi:10.1016/0039-6028(84)90013-X.
- [62] J. WOLLSCHLÄGER, J. FALTA, M. HENZLER, *Electron diffraction at stepped homogeneous and inhomogeneous surfaces*, Appl. Phys. A Solids Surfaces **50**, 1:57, 1990, doi:10.1007/BF00323955.
- [63] J. WOLLSCHLÄGER, E. Z. LUO, M. HENZLER, *Diffraction characterization of rough films formed under stable and unstable growth conditions*, Phys. Rev. B **57**, 24:15541, 1998, doi:10.1103/PhysRevB.57.15541.
- [64] H. IBACH, D. L. MILLS, *Electron energy loss spectroscopy and surface vibrations*, Academic Press, 1982.
- [65] E. EVANS, D. L. MILLS, *Theory of inelastic scattering of slow electrons by long-wavelength surface optical phonons: Multiphonon processes*, Phys. Rev. B **7**, 2:853, 1973, doi:10.1103/PhysRevB.7.853.
- [66] D. MILLS, *The scattering of low energy electrons by electric field fluctuations near crystal surfaces*, Surf. Sci. **48**, 1:59, 1975, doi:10.1016/0039-6028(75)90310-6.
- [67] E. G. MCRAE, *Electronic surface resonances of crystals*, Rev. Mod. Phys. **51**, 3:541, 1979, doi:10.1103/RevModPhys.51.541.
- [68] H. FROITZHEIM, H. IBACH, D. L. MILLS, *Surface optical constants of silicon and germanium derived from electron-energy-loss spectroscopy*, Phys. Rev. B **11**, 12:4980, 1975, doi:10.1103/PhysRevB.11.4980.
- [69] P. DEBYE, *Interferenz von Röntgenstrahlen und Wärmebewegung*, Ann. Phys. **348**, 1:49, 1913, doi:10.1002/andp.19133480105.
- [70] I. WALLER, *Zur Frage der Einwirkung der Wärmebewegung auf die Interferenz von Röntgenstrahlen*, Zeitschrift für Phys. **17**, 1:398, 1923, doi:10.1007/BF01328696.
- [71] J. A. BITTENCOURT, *Fundamentals of Plasma Physics*, Springer, New York, NY, 3rd edition, 2004, doi:10.1007/978-1-4757-4030-1.
- [72] S. DAS SARMA, E. HWANG, *Dynamical response of a one-dimensional quantum-wire electron system*, Phys. Rev. B **54**, 3:1936, 1996, doi:10.1103/PhysRevB.54.1936.
- [73] J. M. PITARKE, V. M. SILKIN, E. V. CHULKOV, P. M. ECHENIQUE, *Theory of surface plasmons and surface-plasmon polaritons*, Reports Prog. Phys. **70**, 1:1, 2007, doi:10.1088/0034-4885/70/1/R01.

-
- [74] R. K. MOUDGIL, V. GARG, K. N. PATHAK, *Confinement and correlation effects on plasmons in an atom-scale metallic wire*, J. Phys. Condens. Matter **22**, 13:135003, 2010, doi:10.1088/0953-8984/22/13/135003.
- [75] W. J. SKOCPOL, L. D. JACKEL, E. L. HU, R. E. HOWARD, L. A. FETTER, *One-Dimensional Localization and Interaction Effects in Narrow (0.1- μ m) Silicon Inversion Layers*, Phys. Rev. Lett. **49**, 13:951, 1982, doi:10.1103/PhysRevLett.49.951.
- [76] W. I. FRIESEN, B. BERGERSEN, *Dielectric response of a one-dimensional electron gas*, J. Phys. C Solid State Phys. **13**, 36:6627, 1980, doi:10.1088/0022-3719/13/36/016.
- [77] T. ANDO, A. B. FOWLER, F. STERN, *Electronic properties of two-dimensional systems*, Rev. Mod. Phys. **54**, 2:437, 1982, doi:10.1103/RevModPhys.54.437.
- [78] G. D. MAHAN, *Many-Particle Physics*, Springer US, Boston, MA, 2000, doi:10.1007/978-1-4757-5714-9.
- [79] T. INAOKA, T. NAGAO, *Exchange-Correlation Effects on Low-Dimensional Plasmons in an Array of Metallic Quantum Wires*, Mater. Trans. **48**, 4:718, 2007, doi:10.2320/matertrans.48.718.
- [80] A. GOLD, A. GHAZALI, *Exchange effects in a quasi-one-dimensional electron gas*, Phys. Rev. B **41**, 12:8318, 1990, doi:10.1103/PhysRevB.41.8318.
- [81] A. GOŃI, A. PINCZUK, J. WEINER, J. CALLEJA, B. DENNIS, L. PFEIFFER, K. WEST, *One-dimensional plasmon dispersion and dispersionless intersubband excitations in GaAs quantum wires*, Phys. Rev. Lett. **67**, 23:3298, 1991, doi:10.1103/PhysRevLett.67.3298.
- [82] K. D. GRONWALD, M. HENZLER, *Epitaxy of Si(111) as studied with a new high resolving LEED system*, Surf. Sci. **117**, 1-3:180, 1982, doi:10.1016/0039-6028(82)90498-8.
- [83] M. HENZLER, *Defects at semiconductor surfaces*, Surf. Sci. **152-153**, 2:963, 1985, doi:10.1016/0039-6028(85)90511-4.
- [84] U. SCHEITHAUER, G. MEYER, M. HENZLER, *A new LEED instrument for quantitative spot profile analysis*, Surf. Sci. **178**, 1-3:441, 1986, doi:10.1016/0039-6028(86)90321-3.
- [85] D. LÜKERMANN, *Spin-Bahn-Kopplung in niedrigdimensionalen Strukturen auf Oberflächen - Wachstum und elektronischer Transport*, Doctoral Dissertation, Leibniz Universität Hannover, 2013.
- [86] E.-J. MEYER ZU HERINGDORF, M. HORN-VON HOEGEN, *Reciprocal space mapping by spot profile analyzing low energy electron diffraction*, Rev. Sci. Instrum. **76**, 8:085102, 2005, doi:10.1063/1.1988287.
-

- [87] H. CLAUS, A. BÜSSENSCHÜTT, M. HENZLER, *Low-energy electron diffraction with energy resolution*, Rev. Sci. Instrum. **63**, 4:2195, 1992, doi:10.1063/1.1143138.
- [88] T. LANGER, *Niedrigdimensionale Plasmonen in epitaktischen Graphenlagen*, Doctoral Dissertation, Leibniz Universität Hannover, 2012.
- [89] B. PERSSON, J. DEMUTH, *Inelastic scattering of slow electrons from Si(111) surfaces*, Phys. Rev. B **30**, 10:5968, 1984, doi:10.1103/PhysRevB.30.5968.
- [90] T. NAGAO, S. HASEGAWA, *Construction of an ELS-LEED: An electron energy-loss spectrometer with electrostatic two-dimensional angular scanning*, Surf. Interface Anal. **30**, 1:488, 2000, doi:10.1002/1096-9918(200008)30:1<488::AID-SIA755>3.0.CO;2-R.
- [91] G. SAUERBREY, *Verwendung von Schwingquarzen zur Wägung dünner Schichten und zur Mikrowägung*, Zeitschrift für Phys. **155**, 2:206, 1959, doi:10.1007/BF01337937.
- [92] R. A. HEISING, *Quartz crystals for electrical circuits: their design and manufacture*, D. Van Nostrand company, inc., New York, 1946.
- [93] U. BISCHLER, *Simple source of atomic hydrogen for ultrahigh vacuum applications*, J. Vac. Sci. Technol. A Vacuum, Surfaces, Film. **11**, 2:458, 1993, doi:10.1116/1.578754.
- [94] A. SUTOH, Y. OKADA, S. OHTA, M. KAWABE, *Cracking Efficiency of Hydrogen with Tungsten Filament in Molecular Beam Epitaxy*, Jpn. J. Appl. Phys. **34**, Part 2, No. 10B:L1379, 1995, doi:10.1143/JJAP34.L1379.
- [95] K. TAKAYANAGI, Y. TANISHIRO, S. TAKAHASHI, M. TAKAHASHI, *Structure analysis of Si(111)-7×7 reconstructed surface by transmission electron diffraction*, Surf. Sci. **164**, 2-3:367, 1985, doi:10.1016/0039-6028(85)90753-8.
- [96] R. J. HAMERS, U. K. KÖHLER, J. E. DEMUTH, *Nucleation and growth of epitaxial silicon on Si(001) and Si(111) surfaces by scanning tunneling microscopy*, Ultramicroscopy **31**, 1:10, 1989, doi:10.1016/0304-3991(89)90029-6.
- [97] A. KIRAKOSIAN, R. BENNEWITZ, J. N. CRAIN, T. FAUSTER, J. L. LIN, D. Y. PETROVYKH, F. J. HIMPSEL, *Atomically accurate Si grating with 5.73 nm period*, Appl. Phys. Lett. **79**, 11:1608, 2001, doi:10.1063/1.1401788.
- [98] S. A. TEYS, K. N. ROMANYUK, R. A. ZHACHUK, B. Z. OLSHANETSKY, *Orientation and structure of triple step staircase on vicinal Si(1 1 1) surfaces*, Surf. Sci. **600**, 21:4878, 2006, doi:10.1016/j.susc.2006.08.009.

-
- [99] D.-H. OH, M. K. KIM, J. H. NAM, I. SONG, C.-Y. PARK, S. H. WOO, H.-N. HWANG, C. C. HWANG, J. R. AHN, *Atomic structure model of the reconstructed Si(557) surface with a triple step structure: Adatom-parallel dimer model*, Phys. Rev. B **77**, 15:155430, 2008, doi:10.1103/PhysRevB.77.155430.
- [100] M. HENZLER, *The step structure of the Si(557) surface*, Thin Solid Films **428**, 1-2:129, 2003, doi:10.1016/S0040-6090(02)01236-1.
- [101] M. KOPCIUSZYŃSKI, P. DYNIEC, R. ZDYB, M. JAŁOCHOWSKI, *Regular step distribution of the bare Si(553) surface*, Phys. Rev. B **91**, 23:1, 2015, doi:10.1103/PhysRevB.91.235420.
- [102] A. BASKI, S. C. ERWIN, L. WHITMAN, *The structure of silicon surfaces from (001) to (111)*, Surf. Sci. **392**, 1-3:69, 1997, doi:10.1016/S0039-6028(97)00499-8.
- [103] J. N. CRAIN, J. MCCHESENEY, F. ZHENG, M. C. GALLAGHER, P. SNIJDERS, M. BISSEN, C. GUNDELACH, S. C. ERWIN, F. J. HIMPSEL, *Chains of gold atoms with tailored electronic states*, 2004, doi:10.1103/PhysRevB.69.125401.
- [104] I. SONG, J. S. GOH, S.-H. LEE, S. W. JUNG, J. S. SHIN, H. YAMANE, N. KOSUGI, H. W. YEOM, *Realization of a Strained Atomic Wire Superlattice*, ACS Nano **9**, 11:10621, 2015, doi:10.1021/acsnano.5b04377.
- [105] S. RIIKONEN, D. SÁNCHEZ-PORTAL, *Structural models for Si(553)-Au atomic chain reconstruction*, Nanotechnology **16**, 5:S218, 2005, doi:10.1088/0957-4484/16/5/015.
- [106] J. R. AHN, P. G. KANG, K. D. RYANG, H. W. YEOM, *Coexistence of Two Different Peierls Distortions within an Atomic Scale Wire: Si(553)-Au*, Phys. Rev. Lett. **95**, 19:196402, 2005, doi:10.1103/PhysRevLett.95.196402.
- [107] S. GHOSE, I. ROBINSON, P. A. BENNETT, F. J. HIMPSEL, *Structure of double row quantum wires in Au/Si(553)*, Surf. Sci. **581**, 2-3:199, 2005, doi:10.1016/j.susc.2005.02.053.
- [108] S. RIIKONEN, D. SÁNCHEZ-PORTAL, *Systematic investigation of the structure of the Si(553)-Au surface from first principles*, Phys. Rev. B **77**, 16:165418, 2008, doi:10.1103/PhysRevB.77.165418.
- [109] P.-G. KANG, J. S. SHIN, H. W. YEOM, *Point defects along metallic atomic wires on vicinal Si surfaces: Si(557)-Au and Si(553)-Au*, Surf. Sci. **603**, 16:2588, 2009, doi:10.1016/j.susc.2009.06.012.
- [110] W. VOEGELI, T. TAKAYAMA, T. SHIRASAWA, M. ABE, K. KUBO, T. TAKAHASHI, K. AKIMOTO, H. SUGIYAMA, *Structure of the quasi-one-dimensional Si(553)-Au surface: Gold dimer row and silicon honeycomb chain*, Phys. Rev. B **82**, 7:075426, 2010, doi:10.1103/PhysRevB.82.075426.
- [111] S. C. ERWIN, F. J. HIMPSEL, *Intrinsic magnetism at silicon surfaces.*, Nat. Commun. **1**, 5:58, 2010, doi:10.1038/ncomms1056.
-

- [112] M. KRAWIEC, *Structural model of the Au-induced Si(553) surface: Double Au rows*, Phys. Rev. B **81**, 11:115436, 2010, doi:10.1103/PhysRevB.81.115436.
- [113] J. N. CRAIN, A. KIRAKOSIAN, K. N. ALTMANN, C. BROMBERGER, S. C. ERWIN, J. L. MCCHESENEY, J.-L. LIN, F. J. HIMPSEL, *Fractional Band Filling in an Atomic Chain Structure*, Phys. Rev. Lett. **90**, 17:176805, 2003, doi:10.1103/PhysRevLett.90.176805.
- [114] H. W. YEOM, S. W. JUNG, J. S. SHIN, J. KIM, K. S. KIM, K. MIYAMOTO, T. OKUDA, H. NAMATAME, A. KIMURA, M. TANIGUCHI, *Direct observation of the spin polarization in Au atomic wires on Si(553)*, New J. Phys. **16**, 9:093030, 2014, doi:10.1088/1367-2630/16/9/093030.
- [115] I. BARKE, F. ZHENG, T. K. RÜGHEIMER, F. J. HIMPSEL, *Experimental Evidence for Spin-Split Bands in a One-Dimensional Chain Structure*, Phys. Rev. Lett. **97**, 22:226405, 2006, doi:10.1103/PhysRevLett.97.226405.
- [116] M. KRAWIEC, M. KOPCIUSZYŃSKI, R. ZDYB, *Different spin textures in one-dimensional electronic bands on Si(5 5 3)-Au surface*, Appl. Surf. Sci. **373**:26, 2016, doi:10.1016/j.apsusc.2015.09.219.
- [117] J. AULBACH, J. SCHÄFER, S. C. ERWIN, S. MEYER, C. LOHO, J. SETTELEIN, R. CLAESSEN, *Evidence for Long-Range Spin Order Instead of a Peierls Transition in Si(553)-Au Chains*, Phys. Rev. Lett. **111**, 13:137203, 2013, doi:10.1103/PhysRevLett.111.137203.
- [118] S. POLEI, P. C. SNIJDERS, S. C. ERWIN, F. J. HIMPSEL, K.-H. MEIWES-BROER, I. BARKE, *Structural Transition in Atomic Chains Driven by Transient Doping*, Phys. Rev. Lett. **111**, 15:156801, 2013, doi:10.1103/PhysRevLett.111.156801.
- [119] B. HAFKE, T. FRIGGE, T. WITTE, B. KRENZER, J. AULBACH, J. SCHÄFER, R. CLAESSEN, S. C. ERWIN, M. HORN-VON HOEGEN, *Two-dimensional interaction of spin chains in the Si(553)-Au nanowire system*, Phys. Rev. B **94**, 16:161403, 2016, doi:10.1103/PhysRevB.94.161403.
- [120] K. BIEDERMANN, S. REGENSBURGER, T. FAUSTER, F. J. HIMPSEL, S. C. ERWIN, *Spin-split silicon states at step edges of Si(553)-Au*, Phys. Rev. B **85**, 24:245413, 2012, doi:10.1103/PhysRevB.85.245413.
- [121] F. EDLER, I. MICCOLI, J. P. STÖCKMANN, H. PFNÜR, C. BRAUN, S. NEUFELD, S. SANNA, W. G. SCHMIDT, C. TEGENKAMP, *Tuning the conductivity along atomic chains by selective chemisorption*, Phys. Rev. B **95**, 12:125409, 2017, doi:10.1103/PhysRevB.95.125409.
- [122] K.-D. RYANG, P. G. KANG, H. W. YEOM, S. JEONG, *Structures and defects of atomic wires on Si(553)-Au: An STM and theoretical study*, Phys. Rev. B **76**, 20:205325, 2007, doi:10.1103/PhysRevB.76.205325.

- [123] P. C. SNIJDERS, S. ROGGE, H. H. WEITERING, *Competing periodicities in fractionally filled one-dimensional bands*, Phys. Rev. Lett. **96**, 7:48, 2006, doi:10.1103/PhysRevLett.96.076801, arXiv: cond-mat/0510574.
- [124] S. C. ERWIN, P. C. SNIJDERS, *Silicon spin chains at finite temperature: Dynamics of Si(553)-Au*, Phys. Rev. B **87**, 23:235316, 2013, doi:10.1103/PhysRevB.87.235316.
- [125] I. SONG, D.-H. OH, H.-C. SHIN, S.-J. AHN, Y. MOON, S.-H. WOO, H. J. CHOI, C.-Y. PARK, J. R. AHN, *Direct Momentum-Resolved Observation of One-Dimensional Confinement of Externally Doped Electrons within a Single Subnanometer-Scale Wire*, Nano Lett. **15**, 1:281, 2015, doi:10.1021/nl503558g.
- [126] M. KRAWIEC, *Protecting Au-stabilized vicinal Si surfaces from degradation: Graphene on the Si(553)-Au surface*, Appl. Surf. Sci. **304**:44, 2014, doi:10.1016/j.apsusc.2013.12.141.
- [127] L. PEDRI, L. TOPPOZINI, M. C. GALLAGHER, *Au-induced nanofaceting and the stoichiometry of the Si(775)-Au surface*, Surf. Sci. **601**, 4:924, 2007, doi:10.1016/j.susc.2006.11.031.
- [128] L. J. PEDRI, W. WU, M. C. GALLAGHER, *Au-Induced Nanostructuring of Vicinal Si Surfaces*, J. Phys. Conf. Ser. **61**:322, 2007, doi:10.1088/1742-6596/61/1/065.
- [129] M. W. DETERT, *Kollektive elektronische Anregung in Goldnanodrähten auf vizinalem Silizium*, Bachelor's Thesis, Leibniz Universität Hannover, 2016.
- [130] J. AULBACH, S. C. ERWIN, R. CLAESSEN, J. SCHÄFER, *Spin Chains and Electron Transfer at Stepped Silicon Surfaces*, Nano Lett. **16**, 4:2698, 2016, doi:10.1021/acs.nanolett.6b00354, arXiv:1601.07489.
- [131] T. LICHTENSTEIN, J. AULBACH, J. SCHÄFER, R. CLAESSEN, C. TEGENKAMP, H. PFNÜR, *Two-dimensional crossover and strong coupling of plasmon excitations in arrays of one-dimensional atomic wires*, Phys. Rev. B **93**, 16:161408, 2016, doi:10.1103/PhysRevB.93.161408, arXiv: 1601.05342.
- [132] C. BRAUN, *First Principles Investigation of Spin Ordering in Nanowires*, Master's Thesis, Universität Paderborn, 2016.
- [133] M. KISIEL, K. SKROBAS, R. ZDYB, M. JAŁOCHOWSKI, *Band structure of Au monoatomic chains on Si (335) and Si (557) surfaces*, Opt. Appl. **35**, 3:449, 2005.
- [134] M. KRAWIEC, *Spin-orbit splitting in the Si(335)-Au surface*, Surf. Sci. **609**:44, 2013, doi:10.1016/j.susc.2012.10.024.
- [135] A. PODSIADŁY-PASZKOWSKA, M. KRAWIEC, *Adsorption and diffusion of atoms on the Si(335)-Au surface*, Surf. Sci. **622**:9, 2014, doi:10.1016/j.susc.2013.11.016.

- [136] I. K. ROBINSON, P. A. BENNETT, F. J. HIMPSEL, *Structure of Quantum Wires in Au/Si(557)*, Phys. Rev. Lett. **88**, 9:096104, 2002, doi:10.1103/PhysRevLett.88.096104.
- [137] D. SÁNCHEZ-PORTAL, R. M. MARTIN, *First principles study of the Si(557)-Au surface*, Surf. Sci. **532-535**:655, 2003, doi:10.1016/S0039-6028(03)00224-3.
- [138] D. SÁNCHEZ-PORTAL, S. RIIKONEN, R. M. MARTIN, *Role of Spin-Orbit Splitting and Dynamical Fluctuations in the Si(557)-Au Surface*, Phys. Rev. Lett. **93**, 14:146803, 2004, doi:10.1103/PhysRevLett.93.146803.
- [139] T. NAGAO, S. YAGINUMA, T. INAOKA, T. SAKURAI, *One-Dimensional Plasmon in an Atomic-Scale Metal Wire*, Phys. Rev. Lett. **97**, 11:116802, 2006, doi:10.1103/PhysRevLett.97.116802.
- [140] H. W. YEOM, J. R. AHN, H. S. YOON, I. W. LYO, H. JEONG, S. JEONG, *Real-space investigation of the metal-insulator transition of Si(557)-Au*, Phys. Rev. B **72**, 3:1, 2005, doi:10.1103/PhysRevB.72.035323.
- [141] M. SAUTER, R. HOFFMANN, C. SÜRGER, H. V. LÖHNEISEN, *Temperature-dependent scanning tunneling spectroscopy on the Si(557)-Au surface*, Phys. Rev. B **89**, 7:075406, 2014, doi:10.1103/PhysRevB.89.075406.
- [142] I. BARKE, F. ZHENG, S. BOCKENHAUER, K. SELL, V. V. OEYNHAUSEN, K. H. MEIWES-BROER, S. C. ERWIN, F. J. HIMPSEL, *Coverage-dependent faceting of Au chains on Si(557)*, Phys. Rev. B **79**, 15:155301, 2009, doi:10.1103/PhysRevB.79.155301.
- [143] D. C. STREIT, F. G. ALLEN, *Thermal and Si-beam assisted desorption of SiO₂ from silicon in ultrahigh vacuum*, J. Appl. Phys. **61**, 8:2894, 1987, doi:10.1063/1.337833.
- [144] K. PHABHAKARAN, F. MAEDA, Y. WATANABE, T. OGINO, *Distinctly different thermal decomposition pathways of ultrathin oxide layer on Ge and Si surfaces*, Appl. Phys. Lett. **76**, 16:2244, 2000, doi:10.1063/1.126309.
- [145] J. VIERNOW, J. L. LIN, D. Y. PETROVYKH, F. M. LEIBSLE, F. K. MEN, F. J. HIMPSEL, *Regular step arrays on silicon*, Appl. Phys. Lett. **72**, 1998:948, 1998, doi:10.1063/1.120882.
- [146] H. MINODA, *Direct current heating effects on Si(111) vicinal surfaces*, J. Phys. Condens. Matter **15**, 47:S3255, 2003, doi:10.1088/0953-8984/15/47/005.
- [147] S. HARA, M. YOSHIMURA, K. UEDA, *Atomic Structure of Si(553) Surface Revealed by Scanning Tunneling Microscopy*, Jpn. J. Appl. Phys. **47**, 7:6102, 2008, doi:10.1143/JJAP47.6102.
- [148] H. TEIKEN, *SPA-LEED und EELS-LEED Untersuchungen an atomaren Au-Ketten auf Ge(100) und Si(553)*, Master's Thesis, Leibniz Universität Hannover, 2014.

-
- [149] C. TEGENKAMP, J. WOLLSCHLÄGER, H. PFNÜR, F.-J. MEYER ZU HERINGDORF, M. HORN-VON HOE-
GEN, *Step and kink correlations on vicinal Ge(100) surfaces investigated by electron diffraction*,
Phys. Rev. B **65**, 23:235316, 2002, doi:10.1103/PhysRevB.65.235316.
- [150] F. HÖTZEL, *Infrarotspektroskopie an quasieindimensionalen Goldatomketten auf vizinalen Siliziu-
moberfläche*, Doctoral Dissertation, Ruprecht-Karls-Universität Heidelberg, 2017.
- [151] T. LICHTENSTEIN, C. TEGENKAMP, H. PFNÜR, *Lateral electronic screening in quasi-one-dimensional
plasmons*, J. Phys. Condens. Matter **28**, 35:354001, 2016, doi:10.1088/0953-8984/28/35/
354001.
- [152] U. BACKES, H. IBACH, *Evidence for a 2D-metallic state of the clean 7×7 Si(111) surface*, Solid
State Commun. **40**, 5:575, 1981, doi:10.1016/0038-1098(81)90577-9.
- [153] J. A. SCHAEFER, J. ANDERSON, G. J. LAPEYRE, *Water adsorption on cleaved silicon surfaces*, J. Vac.
Sci. Technol. A Vacuum, Surfaces, Film. **3**, 3:1443, 1985, doi:10.1116/1.572756.
- [154] J. N. CRAIN, *End States in One-Dimensional Atom Chains*, Science **307**, 5710:703, 2005, doi:
10.1126/science.1106911.
- [155] F. HÖTZEL, N. GALDEN, S. BAUR, A. PUCCI, *One-Dimensional Plasmonic Excitations in Gold-Induced
Superstructures on Si(553): Impact of Gold Coverage and Silicon Step Edge Polarization*, J. Phys.
Chem. C, **553**:acs.jpcc.6b11753, 2017, doi:10.1021/acs.jpcc.6b11753.
- [156] H. R. PHILIPP, H. EHRENREICH, *Optical Properties of Semiconductors*, Phys. Rev. **129**, 4:1550, 1963,
doi:10.1103/PhysRev.129.1550.
- [157] C. HOGAN, E. SPEISER, S. CHANDOLA, S. SUCHKOVA, J. AULBACH, J. SCHÄFER, S. MEYER,
R. CLAESSEN, N. ESSER, *Controlling the local electronic properties of Si(553)-Au through hydro-
gen doping*, Phys. Rev. Lett. (submitted), 2017.
- [158] J. P. PERDEW, K. BURKE, M. ERNZERHOF, *Generalized Gradient Approximation Made Simple*, Phys.
Rev. Lett. **77**, 18:3865, 1996, doi:10.1103/PhysRevLett.77.3865.
- [159] J. HEYD, G. E. SCUSERIA, M. ERNZERHOF, *Hybrid functionals based on a screened Coulomb potential*,
J. Chem. Phys. **118**, 18:8207, 2003, doi:10.1063/1.1564060.
- [160] F. HÖTZEL, K. SEINO, C. HUCK, O. SKIBBE, F. BECHSTEDT, A. PUCCI, *Metallic Properties of the Si(111)
– 5×2 – Au Surface from Infrared Plasmon Polaritons and Ab Initio Theory*, Nano Lett. **15**, 6:4155,
2015, doi:10.1021/acs.nanolett.5b01279.
- [161] H. TOTSUJI, *Theory of Two-Dimensional Classical Electron Plasma*, J. Phys. Soc. Japan **40**, 3:857,
1976, doi:10.1143/JPSJ.40.857.
-

- [162] T. NAGAO, T. HILDEBRANDT, M. HENZLER, S. HASEGAWA, *Dispersion and damping of a two-dimensional plasmon in a metallic surface-state band*, Phys. Rev. Lett. **86**, 25:5747, 2001, doi:10.1103/PhysRevLett.86.5747.
- [163] T. NAGAO, T. HILDEBRANDT, M. HENZLER, S. HASEGAWA, *Two-dimensional plasmon in a surface-state band*, Surf. Sci. **493**, 1-3:680, 2001, doi:10.1016/S0039-6028(01)01282-1.
- [164] M. WOJDYR, *Fityk : a general-purpose peak fitting program*, J. Appl. Crystallogr. **43**, 5:1126, 2010, doi:10.1107/S0021889810030499.
- [165] H. J. ZANDVLIET, *The Ge(001) surface*, Phys. Rep. **388**, 1:1, 2003, doi:10.1016/j.physrep.2003.09.001.
- [166] R. E. SCHLIER, H. E. FARNSWORTH, *Structure and Adsorption Characteristics of Clean Surfaces of Germanium and Silicon*, J. Chem. Phys. **30**, 4:917, 1959, doi:10.1063/1.1730126.
- [167] D. J. CHADI, *Atomic and Electronic Structures of Reconstructed Si(001) Surfaces*, Phys. Rev. Lett. **43**, 1:43, 1979, doi:10.1016/j.susc.2007.03.035.
- [168] S. D. KEVAN, *Surface states and reconstruction on Ge(001)*, Phys. Rev. B **32**, 4:2344, 1985, doi:10.1103/PhysRevB.32.2344.
- [169] R. J. CULBERTSON, Y. KUK, L. C. FELDMAN, *Subsurface strain in the Ge(001) and Ge(111) surfaces and comparison to silicon*, Surf. Sci. **167**, 1:127, 1986, doi:10.1016/0039-6028(86)90789-2.
- [170] S. FERRER, X. TORRELLES, V. H. ETGENS, H. A. VAN DER VEGT, P. FAJARDO, *Atomic Structure of the c(4x2) Surface Reconstruction of Ge(001) as Determined by X-Ray Diffraction*, Phys. Rev. Lett. **75**, 9:1771, 1995, doi:10.1103/PhysRevLett.75.1771.
- [171] H. J. W. ZANDVLIET, B. SWARTZENTRUBER, W. WULFHEKEL, B. HATTINK, B. POELSEMA, *Spontaneous formation of an ordered c(4x2)-(2x1) domain pattern on Ge(001)*, Phys. Rev. B **57**, 12:R6803, 1998, doi:10.1103/PhysRevB.57.R6803.
- [172] H. J. W. ZANDVLIET, B. POELSEMA, *Determination of surface stress anisotropy from domain wall fluctuations*, Phys. Rev. B **59**, 11:7289, 1999, doi:10.1103/PhysRevB.59.7289.
- [173] R. J. HAMERS, R. M. TROMP, J. E. DEMUTH, *Scanning tunneling microscopy of Si(001)*, Phys. Rev. B **34**, 8:5343, 1986, doi:10.1103/PhysRevB.34.5343.
- [174] J. BENSON, J. HANSEN, M. MCELLISTREM, W. CLENDENING, J. TOBIN, *An investigation of the Au/Ge(001) interface*, Surf. Sci. **193**, 1-2:L37, 1988, doi:10.1016/0039-6028(88)90315-9.
- [175] J. WANG, M. LI, E. ALTMAN, *Scanning tunneling microscopy study of self-organized Au atomic chain growth on Ge(001)*, Phys. Rev. B **70**, 23:233312, 2004, doi:10.1103/PhysRevB.70.233312.

-
- [176] O. GURLU, O. A. O. ADAM, H. J. W. ZANDVLIET, B. POELSEMA, *Self-organized, one-dimensional Pt nanowires on Ge(001)*, Appl. Phys. Lett. **83**, 22:4610, 2003, doi:10.1063/1.1630383.
- [177] J. WANG, M. LI, E. ALTMAN, *Scanning tunneling microscopy study of Au growth on Ge(001): Bulk migration, self-organization, and clustering*, Surf. Sci. **596**, 1-3:126, 2005, doi:10.1016/j.susc.2005.09.009.
- [178] T. F. MOCKING, D. STAM, B. POELSEMA, H. J. W. ZANDVLIET, *Dynamics of Au-induced nanowires on Ge(001)*, Surf. Sci. **604**, 21-22:2021, 2010, doi:10.1016/j.susc.2010.08.015.
- [179] J. SCHÄFER, C. BLUMENSTEIN, S. MEYER, M. WISNIEWSKI, R. CLAESSEN, *New Model System for a One-Dimensional Electron Liquid: Self-Organized Atomic Gold Chains on Ge(001)*, Phys. Rev. Lett. **101**, 23:236802, 2008, doi:10.1103/PhysRevLett.101.236802.
- [180] A. VAN HOUSELT, M. FISCHER, B. POELSEMA, H. J. W. ZANDVLIET, *Giant missing row reconstruction of Au on Ge(001)*, Phys. Rev. B **78**, 23:233410, 2008, doi:10.1103/PhysRevB.78.233410.
- [181] T. F. MOCKING, *Properties of 1D metal-induced structures on semiconductor surfaces*, Doctoral Dissertation, Universiteit Twente, Enschede, the Netherlands, 2013, doi:10.3990/1.9789036501798.
- [182] C. BLUMENSTEIN, S. MEYER, S. MIETKE, J. SCHÄFER, A. BOSTWICK, E. ROTENBERG, R. MATZDORF, R. CLAESSEN, *Au-induced quantum chains on Ge(001)—symmetries, long-range order and the conduction path*, J. Phys. Condens. Matter **25**, 1:014015, 2013, doi:10.1088/0953-8984/25/1/014015.
- [183] M. C. GALLAGHER, S. MELNIK, D. MAHLER, *Temperature- and exposure-dependent study of the Ge(001)c(8×2)-Au surface*, Phys. Rev. B **83**, 3:033302, 2011, doi:10.1103/PhysRevB.83.033302.
- [184] A. SAFAEI, A. VAN HOUSELT, B. POELSEMA, H. J. W. ZANDVLIET, R. VAN GASTEL, *Dynamics of the wetting-induced nanowire reconstruction of Au/Ge(001)*, Phys. Rev. B **88**, 8:085415, 2013, doi:10.1103/PhysRevB.88.085415.
- [185] J. SCHÄFER, S. MEYER, C. BLUMENSTEIN, K. ROENSCH, R. CLAESSEN, S. MIETKE, M. KLINKE, T. PODLICH, R. MATZDORF, A. A. STEKOLNIKOV, S. SAUER, F. BECHSTEDT, *Self-organized atomic nanowires of noble metals on Ge(001): atomic structure and electronic properties*, New J. Phys. **11**, 12:125011, 2009, doi:10.1088/1367-2630/11/12/125011.
- [186] H. KODERA, *Solid Solubility of Gold in Germanium*, Jpn. J. Appl. Phys. **3**, 7:369, 1964, doi:10.1143/JJAP3.369.
- [187] S. MEYER, T. E. UMBACH, C. BLUMENSTEIN, J. SCHÄFER, R. CLAESSEN, S. SAUER, S. J. LEAKE, P. R. WILLMOTT, M. FIEDLER, F. BECHSTEDT, *Structural examination of Au/Ge(001) by surface x-ray*
-

- diffraction and scanning tunneling microscopy*, Phys. Rev. B **85**, 23:235439, 2012, doi:10.1103/PhysRevB.85.235439.
- [188] S. SAUER, F. FUCHS, F. BECHSTEDT, C. BLUMENSTEIN, J. SCHÄFER, *First-principles studies of Au-induced nanowires on Ge(001)*, Phys. Rev. B **81**, 7:075412, 2010, doi:10.1103/PhysRevB.81.075412.
- [189] S.-F. TSAY, *Au-induced deep groove nanowire structure on the Ge(001) surface: DFT calculations*, Surf. Sci. **651**:164, 2016, doi:10.1016/j.susc.2016.04.009.
- [190] S. LÓPEZ-MORENO, A. H. ROMERO, A. MUÑOZ, U. SCHWINGENSCHLÖGL, *First-principles description of atomic gold chains on Ge(001)*, Phys. Rev. B **81**, 4:041415, 2010, doi:10.1103/PhysRevB.81.041415.
- [191] D. E. P. VANPOUCKE, *Modeling 1D structures on semiconductor surfaces: synergy of theory and experiment*, J. Phys. Condens. Matter **26**, 13:133001, 2014, doi:10.1088/0953-8984/26/13/133001.
- [192] K. SEINO, F. BECHSTEDT, *Atomic configurations of Au-induced nanowires on Ge(001) stabilized by higher Au coverages*, Phys. Rev. B **93**, 12:125406, 2016, doi:10.1103/PhysRevB.93.125406.
- [193] S. MEYER, J. SCHÄFER, C. BLUMENSTEIN, P. HÖPFNER, A. BOSTWICK, J. L. MCCHESENEY, E. ROTENBERG, R. CLAESSEN, *Strictly one-dimensional electron system in Au chains on Ge(001) revealed by photoelectron k -space mapping*, Phys. Rev. B **83**, 12:121411, 2011, doi:10.1103/PhysRevB.83.121411.
- [194] N. DE JONG, R. HEIMBUCH, S. ELIËNS, S. SMIT, E. FRANTZESKAKIS, J.-S. GAUX, H. J. W. ZANDVLIET, M. S. GOLDEN, *Gold-induced nanowires on the Ge(100) surface yield a 2D and not a 1D electronic structure*, Phys. Rev. B **93**, 23:235444, 2016, doi:10.1103/PhysRevB.93.235444.
- [195] K. NAKATSUJI, R. NIIKURA, Y. SHIBATA, M. YAMADA, T. IIMORI, F. KOMORI, *Anisotropic two-dimensional metallic state of Ge(001)c(8x2)-Au surfaces: An angle-resolved photoelectron spectroscopy*, Phys. Rev. B **80**, 8:081406, 2009, doi:10.1103/PhysRevB.80.081406.
- [196] C. BLUMENSTEIN, J. SCHÄFER, S. MIETKE, S. MEYER, A. DOLLINGER, M. LOCHNER, X. Y. CUI, L. PATTHEY, R. MATZDORF, R. CLAESSEN, *Atomically controlled quantum chains hosting a Tomonaga-Luttinger liquid*, Nat. Phys. **7**, 10:776, 2011, doi:10.1038/nphys2051.
- [197] C. BLUMENSTEIN, *One-Dimensional Electron Liquid at a Surface: Gold Nanowires on Ge(001)*, Doctoral Dissertation, Julius-Maximilians-Universität Würzburg, 2012.
- [198] D. KOCKMANN, T. F. MOCKING, A. VAN HOUSELT, B. POELSEMA, H. J. W. ZANDVLIET, *Structural and Electronic Properties of Au Induced Nanowires on Ge(001)*, J. Phys. Chem. C **113**, 39:17156, 2009, doi:10.1021/jp906536a.

- [199] J. HAGER, R. MATZDORF, J. HE, R. JIN, D. MANDRUS, M. A. CAZALILLA, E. W. PLUMMER, *Non-Fermi-Liquid Behavior in Quasi-One-Dimensional Li_{0.9}Mo₆O₁₇*, Phys. Rev. Lett. **95**, 18:186402, 2005, doi:10.1103/PhysRevLett.95.186402.
- [200] J. PARK, K. NAKATSUJI, T.-H. KIM, S. K. SONG, F. KOMORI, H. W. YEOM, *Atomic scale variation of electron tunneling into a Luttinger liquid ? : High resolution scanning tunneling spectroscopy study on Au/Ge(001)* 2014, arXiv:1409.4870.
- [201] T. LICHTENSTEIN, H. TEIKEN, H. PFNÜR, J. WOLLSCHLÄGER, C. TEGENKAMP, *Au-chains grown on Ge(100): A detailed SPA-LEED study*, Surf. Sci. **632**, 100:64, 2015, doi:10.1016/j.susc.2014.09.002.
- [202] P. W. LOSCUTOFF, S. F. BENT, *Reactivity of the Germanium Surface: Chemical Passivation and Functionalization*, Annu. Rev. Phys. Chem. **57**, 1:467, 2006, doi:10.1146/annurev.physchem.56.092503.141307.
- [203] C. BLUMENSTEIN, S. MEYER, A. RUFF, B. SCHMID, J. SCHÄFER, R. CLAESSEN, *High purity chemical etching and thermal passivation process for Ge(001) as nanostructure template*, J. Chem. Phys. **135**, 6:064201, 2011, doi:10.1063/1.3624902.
- [204] K. KIANTAJ, T. K. OSBORN, A. C. KUMMEL, *Nano-Cleaning of Ge(100) Surface: A STM Study*, in *2012 Int. Silicon-Germanium Technol. Device Meet.*, 1–2, IEEE, 2012, doi:10.1109/ISTDM.2012.6222494.
- [205] J. RÄTHEL, E. SPEISER, N. ESSER, U. BASS, S. MEYER, J. SCHÄFER, J. GEURTS, *Surface phonons of Ge(001) and their correlation with the p(2×1) and c(4×2) reconstruction as shown by Raman spectroscopy*, Phys. Rev. B **86**, 3:035312, 2012, doi:10.1103/PhysRevB.86.035312.
- [206] X.-J. ZHANG, *Thermal desorption of ultraviolet–ozone oxidized Ge(001) for substrate cleaning*, J. Vac. Sci. Technol. A Vacuum, Surfaces, Film. **11**, 5:2553, 1993, doi:10.1116/1.578606.
- [207] K. SAGISAKA, D. FUJITA, G. KIDO, *Phase Manipulation between c(4×2) and p(2×2) on the Si(100) Surface at 4.2 K*, Phys. Rev. Lett. **91**, 14:146103, 2003, doi:10.1103/PhysRevLett.91.146103.
- [208] A. A. AL-FALOU, M. KAMMLER, M. HORN-VON HOEGEN, *Strain state analysis of hetero-epitaxial systems*, Europhys. Lett. **69**, 4:570, 2005, doi:10.1209/epl/i2004-10399-6.
- [209] J. ZACHARIAE, H. PFNÜR, *Surface morphology of epitaxial lattice-matched Ba_{0.7}Sr_{0.3}O on Si(001) and vicinal Si(001)-4° [110] substrates*, Surf. Sci. **600**, 13:2785, 2006, doi:10.1016/j.susc.2006.05.002.
- [210] J. CAZAUX, *Material contrast in SEM: Fermi energy and work function effects*, Ultramicroscopy **110**, 3:242, 2010, doi:10.1016/j.ultramic.2009.12.002.

- [211] H. MINODA, K. YAGI, F.-J. MEYER ZU HERINGDORF, *Gold-induced faceting on a Si (001) vicinal surface: Spot-profile-analyzing LEED and reflection-electron-microscopy study*, Phys. Rev. B **59**, 3:2363, 1999, doi:10.1103/PhysRevB.59.2363.
- [212] M. HORN-VON HOEGEN, F. J. MEYER ZU HERINGDORF, R. HILD, P. ZAHL, T. SCHMIDT, E. BAUER, *Au-induced giant faceting of vicinal Si(001)*, Surf. Sci. **433**:475, 1999, doi:10.1016/S0039-6028(99)00459-8.
- [213] M. HEYL, S. KEHREIN, F. MARQUARDT, C. NEUENHAHN, *Electron-plasmon scattering in chiral one-dimensional systems with nonlinear dispersion*, Phys. Rev. B **82**, 3:033409, 2010, doi:10.1103/PhysRevB.82.033409.
- [214] S. MELNIK, M. C. GALLAGHER, *Growth of the Au-induced $c(8 \times 2)$ structure on vicinal Ge(001)*, Surf. Sci. **606**, 1-2:L10, 2012, doi:10.1016/j.susc.2011.09.015.
- [215] P. F. WILLIAMS, A. N. BLOCH, *Self-consistent dielectric response of a quasi-one-dimensional metal at high frequencies*, Phys. Rev. B **10**, 3:1097, 1974, doi:10.1103/PhysRevB.10.1097.
- [216] H. J. SCHULZ, *Long-range Coulomb interactions in quasi-one-dimensional conductors*, J. Phys. C Solid State Phys. **16**, 35:6769, 1983, doi:10.1088/0022-3719/16/35/010.
- [217] A. GOLD, *Elementary excitations in multiple quantum wire structures*, Zeitschrift für Phys. B Condens. Matter **89**, 2:213, 1992, doi:10.1007/BF01320939.
- [218] E. P. RUGERAMIGABO, C. TEGENKAMP, H. PFNÜR, T. INAOKA, T. NAGAO, *One-dimensional plasmons in ultrathin metallic silicide wires of finite width*, Phys. Rev. B **81**, 16:165407, 2010, doi:10.1103/PhysRevB.81.165407.
- [219] W. BULLIS, *Properties of gold in silicon*, Solid. State. Electron. **9**, 2:143, 1966, doi:10.1016/0038-1101(66)90085-2.
- [220] W. G. SCHMIDT, S. WIPPERMANN, S. SANNA, M. BABILON, N. J. VOLLMERS, U. GERSTMANN, *In-Si(111)(4×1)/(8×2) nanowires: Electron transport, entropy, and metal-insulator transition*, Phys. status solidi **249**, 2:343, 2012, doi:10.1002/pssb.201100457.

Curriculum Vitae

Personal Information

Name Timo Lichtenstein
Date of Birth January 16, 1987
Place of Birth Marl, North Rhine-Westphalia, Germany

Education

2013 – 2017 Doctoral studies, Gottfried Wilhelm Leibniz Universität Hannover
Thesis: *Plasmons in Gold-Induced Quantum Wires*

2009 – 2012 Master of Science, Ruhr-Universität Bochum
Thesis: *Strukturelle und magnetische Eigenschaften von FeNi-Legierungen im Bereich des Invar-Effekts*

2006 – 2009 Bachelor of Science, Ruhr-Universität Bochum
Thesis: *Entwicklung eines Luftspulensystems zur Untersuchung von weichmagnetischen Materialien*

1997 – 2006 Abitur, Gymnasium im Loekamp, Marl

List of Publications

- [1] T. LICHTENSTEIN, H. TEIKEN, H. PFNÜR, J. WOLLSCHLÄGER, C. TEGENKAMP, *Au-chains grown on Ge(100): A detailed SPA-LEED study*, Surf. Sci. **632**, 100:64, 2015, doi:10.1016/j.susc.2014.09.002.
- [2] U. KRIEG, T. LICHTENSTEIN, C. BRAND, C. TEGENKAMP, H. PFNÜR, *Origin of metallicity in atomic Ag wires on Si(557)*, New J. Phys. **17**, 4:043062, 2015, doi:10.1088/1367-2630/17/4/043062.
- [3] T. LICHTENSTEIN, J. AULBACH, J. SCHÄFER, R. CLAESSEN, C. TEGENKAMP, H. PFNÜR, *Two-dimensional crossover and strong coupling of plasmon excitations in arrays of one-dimensional atomic wires*, Phys. Rev. B **93**, 16:161408, 2016, doi:10.1103/PhysRevB.93.161408, arXiv:1601.05342.
- [4] T. LICHTENSTEIN, C. TEGENKAMP, H. PFNÜR, *Lateral electronic screening in quasi-one-dimensional plasmons*, J. Phys. Condens. Matter **28**, 35:354001, 2016, doi:10.1088/0953-8984/28/35/354001.
- [5] I. MICCOLI, J. APROJANZ, J. BARINGHAUS, T. LICHTENSTEIN, L. A. GALVES, J. M. J. LOPES, C. TEGENKAMP, *Quasi-free-standing bilayer graphene nanoribbons probed by electronic transport*, Appl. Phys. Lett. **110**, 5:051601, 2017, doi:10.1063/1.4975205.

Acknowledgements

Dieser Abschnitt ist all denen gewidmet, die mich in den letzten Jahren auf dem wissenschaftlichen aber auch privaten Weg bei dieser Arbeit begleitet und unterstützt haben.

Ein besonderer Dank gilt Prof. Dr. Herbert Pfnür, der mich durch seine intensive Betreuung und sein offenes Ohr, aber auch kritische Fragen und lebhaften Diskussionen immer wieder motiviert hat. Gedanklich und experimentell habe ich so die wesentliche Problematik nie aus den Augen verloren. Seine gerne auch herausfordernd gestellten Fragen haben immer wieder zu neuen Erkenntnissen und Fortschritten geführt.

Des weiteren bedanke ich mich bei Prof. Dr. Christoph Tegenkamp. Seine Tür stand immer für Diskussionen und Fragen offen. Seine vielen Anregungen haben auch maßgeblich zum Verständnis der Ergebnisse beigetragen und weiterführende Messungen motiviert.

Einen großen Dank auch an Prof. Dr. Simone Sanna und Prof. Dr. Mario Rocca für die Übernahme des Korreferats der Dissertation.

Ein Dank gebührt all denjenigen mit denen ich in den letzten Jahren an der Vakuumkammer gearbeitet habe. Dazu gehört zunächst Ulrich Krieg, der mich in die Funktionsweise der Kammer eingewiesen und mir dabei viele Kleinigkeiten erklärt hat. Vielen Dank an die Studenten, die ich in meiner Zeit als Doktorand betreuen durfte: Heiko Teiken, Alina Syring und Marvin Detert. Die Arbeit mit ihnen hat mich durch viele Fragen auch aus der Reserve gelockt und angetrieben. Danke auch an meinen Nachfolger Zamin Mamiyev. Unsere manchmal doch sehr angeheizten Diskussionen haben mich definitiv im Verständnis weitergebracht. Ich danke auch Tammo Block. Seine exzellenten Elektronikkenntnisse waren bei der Reparatur der Ansteuerungen des EELS-LEED des Öfteren Gold wert.

Zudem möchte ich allen Menschen der Arbeitsgruppe ATMOS des Instituts für Festkörperphysik für die immer sehr freundliche Arbeitsatmosphäre danken. Ich denke zurück an viele konstruktive Diskussionen. Namentlich möchte ich hier Ulrich Krieg, Philipp Kröger, Jens Baringhaus, Monika Jäger und Johannes Aprojanz erwähnen. Gerade die in letzter Zeit immer öfter stattfindende nachmittägliche Kaffeepause lud zu einem ungezwungenen Dialog über die vielen auftretenden Probleme ein. Ein persönlicher Dank noch an Philipp Kröger: Du warst mir über die vielen Jahre ein guter Bürogenosse.

Ich danke der Werkstatt des Instituts, die mir immer wieder maßgefertigte Bauteile für die Kammer gezaubert hat und bei mechanischen Reparaturen mit Rat und Tat zur Seite stand.

Vielen Dank an die vielen wissenschaftlichen Diskussionen mit den Doktoranden, Postdocs und Projektleitern der 1D-Forschergruppe FOR1700. Regelmäßige Forschergruppentreffen sowie das jährliche Doktorandentreffen haben geholfen Kniffe und Tricks auszutauschen, haben aber auch zu schnellerem Erkenntnisgewinn geführt. In Erinnerung werden mir die vielen Telefonate mit Julian Aulbach und Fabian Hötzel über den Austausch neuester Ergebnisse von Si(hhk)-Au bleiben.

Ein offenes Ohr fand ich auch immer wieder bei der wöchentlichen, selbsternannten Expertenrunde im Extrakt. Hier konnten die wirklich wichtigen Dinge bei einem oder mehreren Glas (alkoholfreiem) Bier besprochen werden. Einen speziellen Dank an Tammo Block, Thomas Langer, Daniel Lükermann, Jens Baringhaus, Ulrich Krieg, Johannes Aprojanz und Monika Jäger für die großartigen Gespräche. Ich freue mich auf viele weitere Treffen.

Außerdem gebührt ein großer Dank an die vielen Freunde, die ich auf meinem Weg bisher kennenlernen durfte, die mich unterstützt haben und denen ich (vielleicht teilweise vergeblich) auch versucht habe meine Forschung etwas näherzubringen. Ich danke auch meiner Familie und insbesondere meinen Eltern mir diesen Weg ermöglicht zu haben und für den großen Rückhalt, der mir gegeben wurde.